Relatório de Actividade
ano sabático 1999/2000
Paulo Manuel Salgado Tavares de Castro

O presente relatório é um sumário de actividade desenvolvida pelo signatário no período de Outubro de 1999 a Setembro de 2000, durante o qual beneficiou do segundo ano sabático na sua carreira docente na Universidade do Porto (o primeiro teve lugar no ano lectivo de 1991/2).

Actividade docente

1º semestre de 1999/2000

- Licenciatura em Engenharia Mecânica, e em Gestão e Engenharia Industrial da FEUP, Orgãos de Máquinas I
  http://www.fe.up.pt/~ptcastro/OMA99.html
  (intervenção em OMI, cap. Engrenagens: aulas teóricas e aulas teórico-práticas de todas as 4 turmas);
- Mestrado em Estruturas de Engenharia Civil da FEUP (15ª edição), 6h de introdução à Mecânica da Fractura na disciplina Mecânica dos Meios Contínuos; (regente da disciplina: Prof J Couto Marques);
- Mestrado em Engenharia de Materiais das Universidades de Coimbra, Porto, Técnica de Lisboa, Nova de Lisboa, Aveiro e Minho (6ª edição), módulo 'Mecânica da Fractura' (6 horas) da disciplina 'Defeitos e Comportamento Mecânico', 1999/2000 (outros docentes da disciplina: Prof José Valdemar Fernandes (FCTUC), Prof Manuel Vieira (FEUP)), 26-27 de Outubro de 1999.

2º semestre de 1999/2000

- Mestrado em Engenharia Mecânica da FEUP, Disciplina Mecânica da Fractura (calendário antecipado, para possibilitar estadia do docente nos EUA como bolseiro Fulbright)

Cursos propostos

- Proposta de curso de mestrado em Design Industrial da FEUP (em colaboração com a ESAD), elaborada com A T Marques, J A Simões (Univ. Aveiro), *et al.*, apresentada à FEUP em 29 de Dezembro de 1999
- Colaboração na proposta de curso de mestrado em Terminologia e Tradução, da Faculdade de Letras da UP, promovida por Professora Belinda Maia (FLUP).

Publicações

Publicados em revistas internacionais

- J P M Gonçalves, M F S F de Moura, P M S T de Castro, A T Marques, 'Interface element including point-to-surface contraints for three-dimensional problems with damage propagation', *Engineering Computations*, vol.14, (1), 2000, pp.28-47 (**anexo**)

- L F M Silva, J P M Gonçalves, F M F Oliveira, P M S T de Castro, 'Multiple-site damage in riveted lap-joints: experimental simulation and finite element prediction', *International Journal of Fatigue*, vol.22, (4), 2000, pp.319-338 (**anexo**)
- M F S F Moura, J P M Gonçalves, A T Marques, P M S T de Castro, Prediction of compressive strength of carbon-epoxy laminates containing delamination by using a mixed-mode damage model', *Composite Structures*, vol.50, (2), 2000, pp.151-157 (**anexo**)

Artigos aceites para publicação, revistas internacionais

- M V Figueiredo, F M F Oliveira, J P Gonçalves, P M S T de Castro, A A Fernandes , 'Fracture analysis of forks of a heavy duty lift truck', *Engineering Failure Analysis*, manuscrito EFA 269, (aceitação: ofício Elsevier de 2 de Out de 2000) (**anexo**)
- A Balacó de Morais, J F Silva, A T Marques, P M S T de Castro, 'Mode II interlaminar fracture of filament wound angle-ply specimens' *Applied Composite Materials*. Ref.:ACMA308 (**anexo**)
- Abílio M P de Jesus, A S Ribeiro, A Portela, P M S T de Castro, A A Fernandes, 'Software development for the fatigue life prediction of structural components', *Welding in the World*

Artigos apresentados em conferências internacionais

- L F M Silva, J P M Gonçalves, F M F Oliveira, P M S T de Castro, 'Multiple site damage in riveted lap joint specimens', Third Joint FAA/DoD/NASA Conference on Aging Aircraft, 20-23 Setembro de 1999, Albuquerque, New Mexico, USA; proceedings publicados em cd.
- M V Figueiredo, F M F Oliveira, J P Gonçalves, P M S T de Castro, A A Fernandes, 'Fracture analysis of forks of an heavy duty lift truck', International Conference on Case Histories on Integrity and Failures in Industry, Milano, 28 Set-1 Out 1999; publicado em volume de proceedings: V Bicego et al., eds, 'Case Histoires on Integrity and Failures in Industry', EMAS 1999, pp.643-652
- M V Figueiredo, F M F Oliveira, P M S T de Castro, A A Fernandes, 'Failure analysis of a shaft belonging to a ship engine speed controller', 1999 International Mechanical Engineering Congress & Exposition, 14-19 Novembro de 1999, Session DE-11A 'Symposium on Failure Aalysis and Prevention', 16 Nov., Nashville, USA; publicado em: E C Feldy, ed., 'Mechanical Engineering Design Education: Issues and Case Studies', DE-Vol.102, ASME, 1999, pp.97-102
- A M de Jesus, A S Ribeiro, A Portela, P T de Castro, A A Fernandes, 'Software development for the fatigue life prediction of structural components', apresentado em COBEM99 - XV Congresso Brasileiro de Engenharia Mecânica, 22-26 Nov. 1999, Águas de Lindóia, São Paulo, Brasil
- A T Marques, João Francisco Silva, A Balacó de Morais, P M S T de Castro, 'Fracture Mechanics concepts and structural integrity of filament wound pipes', 13th European Conference on Fracture ECF13 , 6-9 September 2000, San Sebastian, Spain. Publicado no volume de actas: M Fuentes et al., eds., 'Fracture Mechanics: Application and Challenges ', ESIS pub. 26, Elsevier, 2000, pp.253-261
- T Novais Barbosa, F M F Oliveira, P M S T de Castro, A A Fernandes, 'Cracked stone crusher: Failure analysis and repair', presented at the 2000 ASME

International Mechanical Engineering Congress and Exhibition, Orlando, FL, Nov. 5-10, 2000. ASME paper 2000-IMECE/DE-6 (**anexo**)

Apresentações em conferências nacionais

- L F M Silva, J P M Gonçalves, F M F Oliveira, P M S T de Castro, 'Ensaio de juntas rebitadas de estruturas de aviões', 3º Encontro Nacional de Análise Experimental de Tensões e Mecânica Experimental, Porto, 24-26 de Março de 1999 (abstract publicado)
- M F S F de Moura, J P M Gonçalves, A T Marques, P M S T de Castro, 'Aplicação dum critério de modo misto ao estudo de solicitações de compressão após impacto em compósitos de carbono-epóxido', 3º Encontro Nacional de Análise Experimental de Tensões e Mecânica Experimental, Porto, 24-26 de Março de 1999 (abstract publicado)
- J P M Gonçalves, M F S F Moura, P M S T de Castro, A T Marques, 'Estudo da propagação de dano em modo I, modo II e modo misto em interfaces usando elementos finitos de interface com restrição ponto-superficie', 7as Jornadas de Fractura, UBI, Covilhã, 16-18 de Fevereiro de 2000. Livro de actas, pp.64-71
- A Balacó de Morais, A T Marques, P M S T de Castro, 'Estudo da aplicação de ensaios de fractura interlaminar de modo I a laminados compósitos multidireccionais', 7as Jornadas de Fractura, UBI, Covilhã, 16-18 de Fevereiro de 2000. Livro de actas, pp.90-95
- A M P Jesus, A S Ribeiro, A Portela, P M S T de Castro, A A Fernandes, 'Estimativa das fases de iniciação e propagação de defeitos em componentes estruturais', 7as Jornadas de Fractura, UBI, Covilhã, 16-18 de Fevereiro de 2000. Livro de actas, pp.260-269
- M V Figueiredo, F M F Oliveira, J P M Gonçalves, P M S T de Castro, A A Fernandes, 'Análise das causas de fractura de um garfo de empilhador', 7as Jornadas de Fractura, UBI, Covilhã, 16-18 de Fevereiro de 2000. Livro de actas, pp.276-281
- M F S F Moura, J P M Gonçalves, A T Marques, P M S T de Castro, 'Previsão da resistência à compressão de laminados de carbono-epóxido contendo delaminagem provocada por impacto a baixa velocidade', VI Congresso Nacional de Mecânica Aplicada e Computacional, 17-19 Abril 2000, Aveiro. Livro de actas: pp.491-499

Relatórios

- A Balacó de Morais, A T Marques, P M S T de Castro, '3rd ESIS TC4 Round robin on cross-ply laminates - report; results obtained at the University of Porto', 28th December 1999 (no quadro da participação da Universidade do Porto - INEGI nas actividades do ESIS Technical Committee 4 - Polymers, Composites and Adhesives) (**anexo**).
- A Balacó de Morais, M F S F Moura, A T Marques, P M S T de Castro, 'Mode I interlaminar fracture of carbon/epoxy cross-ply composites'
- Lucas F M Silva, F M F Oliveira, P M S T de Castro, 'Fatigue crack growth of rails for railways', INEGI report of the Part 2 tests for 'RAILCRACK' project SMT4-CT98-2240, 'Fatigue crack growth rate qualifying criteria of rails for railways: test conditions to be optimised' (versão inicial, de Março de 2000,

apresentada na reunião final deste projecto em Bruxelas, 31 Mar ; versão final, datada de Junho 2000 (**anexo**))

- Juan Luis Llorens Urrutia (*rapporteur*), E Jandl-Jaeger, G Oquist, P M S T de Castro, 'Report of the 1999 External Monitoring Panel of the IHP Programme', final report of CEC contract IHP-MP-99-04, February 2000 (**confidencial**, por exigência da UE)
- P M S T de Castro, Summary Report - visit to University of California, Berkeley, April 1 - June 30 (**anexo**)

Artigos submetidos para apresentação em conferências

- J Sabino Domingues, A Portela, P M S T de Castro, 'Mixed mode stress intensity factor determination using Trefftz complex functions', aceite para apresentação em 6th International Conference Biaxial/Multiaxial Fatigue and Fracture, ESIS, Lisboa, June 26-29, 2001 (**anexo**)
- J P M Gonçalves, M F S F Moura, P M S T de Castro, A T Marques, 'Modelling damage propagation in interfaces considering mode I, mode II and mixed mode loading conditions', aceite para apresentação em 6th International Conference Biaxial/Multiaxial Fatigue and Fracture, ESIS, Lisboa, June 26-29, 2001

Outras intervenções, palestras e participações em congressos:

- V Encuentro Internacional de Docencia de Ética Empresarial, Económica y Profesional, IESE - Universidad de Navarra, Barcelona, 5-6 de Novembro de 1999 (participação sem apresentação)
- P M S T de Castro, membro do 'Panel on Doing Engineering in the Global Marketplace: Licensing and other Regulatory Issues', ASME 1999 International Mechanical Engineering Congress & Exposition, 14-19 Novembro de 1999, Session T&S-3B, Nashville, 15 de Novembro de 1999 ; transparências para intervenção: 'Topics for intervention in the panel .... ': http://www.fe.up.pt/~ptcastro/Nashvil/sld001.htm
- Acção de formação do Gabinete de Formação Permanente da FEUP 'Dimensionamento de Estruturas Metálicas segundo o EC3', organizada por Prof Mota Freitas na FEUP, sessão: 'Uma introdução ao dimensionamento estático de ligações soldadas', 3 Fev 2000
- P M S T de Castro, 'Multiple-site fatigue damage in aircraft', seminar at the Department of mechanical Engineering, University of California at Berkeley, June 15, 2000

Projectos em curso com financiamento específico:

Científicos

- EC SMT call for proposals: Proposal PL97-1532, contract SMT4-CT98-2240, Fatigue crack growth rate qualifying criteria of rails for railways: test conditions to be optimised (RAILCRACK). Main proposer: British Steel PLC Swinden Technology Centre; CSM, Voest-Alpine, Thyssen Krupp Stahl GmbH, Sogerail, INEGI. Data de início: 1 de Janeiro de 1999

Outros

- 1999 Human Potential Monitoring Panel, CEC contract IHP-MP-99-04 (members; E Jandl-Jaeger; J L Llorens, G Oquist, P M S T de Castro)

Propostas preparadas

- proposta 'ADMIRE', programa GROWTH da Comissão Europeia, proposta GRD1-2000-25069, que viria a originar o contrato G4RD-CT-2000-00396, iniciado em 1 de Fevereiro de 2001
- programa SAPIENS Proj99, submetida 28 Janeiro 2000, 'Comportamento mecânico de juntas adesivas em materiais compósitos avançados', proposta 35975/99, aprovada, (com corte de financiamento e objectivos). Aguarda indicações do MCT para ter início.

Deslocações profissionais

- **Bruxelas**, CEC, Independent Observer, Research Training Networks Activity, CEC contract HPRE-CT-1999-00244, 13-17 de Setembro de 1999
- **Bruxelas**, CEC, Independent Observer, Research Training Networks Activity, CEC contract HPRE-CT-1999-00244, 22-24 de Setembro de 1999
- **Milano**, International Conference on Case Histories on Integrity and Failures in Industry, 28 Set-1 Out 1999
- **Bruxelas**, CEC, 1999 Human Potential Monitoring Panel, CEC contract IHP-MP-99-04, 20-21 de Outubro de 1999
- **Barcelona**, IESE - Universidad de Navarra, V Encuentro Internacional de Docencia de Ética Empresarial, Económica y Profesional, 5-6 de Novembro de 1999
- **Nashville**, ASME 1999 International Mechanical Engineering Congress & Exposition, 14-19 Novembro de 1999; ASME Board on Professional Practice and Ethics (BPPE) meeting, 13-14 de Novembro de 1999
- **Bruxelas**, CEC, 1999 Human Potential Monitoring Panel, CEC contract IHP-MP-99-04, 28-29 de Novembro de 1999
- **Bruxelas**, CEC, 1999 Human Potential Monitoring Panel, CEC contract IHP-MP-99-04, 14 -16 de Dezembro de 1999
- **Bruxelas**, 13-14 Jan 2000, 1999 Human Potential Monitoring Panel, CEC contract IHP-MP-99-04
- **Bruxelas**, 16-21 Jan 2000, assessment of cooperation projects under the SOCRATES-ERASMUS institutional contract
- **Bruxelas**, 27-29 Jan 2000, 1999 Human Potential Monitoring Pañel, CEC contract IHP-MP-99-04
- **Noordwijk**, Holanda, 28 Fev, European Space Agency, ESTEC (European Space Research and Technology Centre)
- **Amsterdam**, 29 Fev, NLR (reunião preparatória proposta ADMIRE)
- **Berkeley**, CA, 31 Mar - 30 Jun; Fulbright Scholar - Visiting Scholar, University of California at Berkeley
- **Providence**, RI, June 3-4, 2000, American Society of Mechanical Engineers, Board on Professional Practice and Ethics (BPPE) meeting
- **New York**, NY, June 5-7; American Society of Mechanical Engineers - ASME Professional Development Program short course 'The art of project management

for engineers' (instructor: David Adkins, PhD, Business Management Consultants, Ventura, California)
- **San Jose**, CA, June 13-14, 2000, 'eBusiness Conference and Expo'
- **Paris**, 4 Set: Projecto 'E4 - Enhancing Engineering Education in Europe', (proposta Thematic Network SOCRATES-ERASMUS), reunião preparatória (4th Steering Committee meeting), ENPC, (leader do projecto: Professor Alfredo Soeiro, FEUP)

Algumas outras actividades

- Concepção e responsabilidade da exposição 'Memórias da FEUP', a ter lugar no átrio da Biblioteca da FEUP em 2001. Livro correspondente:
  P M S T de Castro, coord., *'Memórias da FEUP - no Início do Funcionamento das Novas Instalações'*, FEUPedições, 2001 (ISBN 972-752-045-6)
- Presidência da Assembleia de Representantes da FEUP, que aprovou a revisão de estatutos da Faculdade, publicada em: Diário da República, II Série, 31 de Janeiro de 2001, pp.2091-2099

Porto, 1 de Abril de 2001

Paulo Manuel Salgado Tavares de Castro

Anexo: amostragem de publicações.

Nota: para mais detalhes consultor os relatórios anuais relevantes:
1999: *http://www.fe.up.pt/~ptcastro/relat99.htm*
2000: *http://www.fe.up.pt/~ptcastro/relat00.htm*

The current issue and full text archive of this journal is available at
http://www.emerald-library.com

Received January 1999
Revised September 1999
Accepted September
1999

Interface element including point-to-surface constraints for three-dimensional problems with damage propagation

J.P.M. Gonçalves, M.F.S.F. de Moura, P.M.S.T. de Castro and A.T. Marques
Faculdade de Engenharia da Universidade do Porto, Departamento de Engenharia Mecânica e Gestão Industrial, Porto, Portugal

Keywords *Finite element, 3D, Modelling*

Abstract *An interface finite element for three-dimensional problems based on the penalty method is presented. The proposed element can model joints/interfaces between solid finite elements and also includes the propagation of damage in pure mode I, pure mode II and mixed mode considering a softening relationship between the stresses and relative displacements. Two different contact conditions are considered: point-to-point constraint for closed points (not satisfying the failure criterion) and point-to-surface constraint for opened points. The performance of the element is tested under mode I, mode II and mixed mode loading conditions.*

1. Introduction

In solid mechanics, there is a growing interest in studying the behaviour of structures containing interfaces between dissimilar materials. Included in the most important examples are layered composite structures, hybrid materials and adhesive joints. In composite materials the rupture of the thin resin layer placed at the interface between two different oriented plies (delamination) can reduce the compression strength up to 60 per cent (de Moura *et al.*, 1997). Adhesive joints are being used extensively in aerospace and automotive structures. Also, hybrid materials are considered more and more for structural applications. In this context, the study of adhesive and cohesive problems becomes very important.

Various methods have been proposed to treat these problems. Some authors (Lindner and Kromp, 1988; Wang, 1980; Wu, 1987; Allix and Ladevèze, 1992) have considered, in their analyses, the interfaces in composite materials as a resin rich layer with thin thickness. Others (Spilker, 1982; Shi and Chen, 1992) employed hybrid-stress finite element methods to obtain the stress state at the interfaces. This formulation ensures the continuity of displacements and interlaminar stresses by satisfying the equilibrium equations of elasticity. Barsoum and Freese (1984) used special interlaminar shear elements for the evaluation of delamination stresses in composite materials. The introduction of a failure criterion into the finite element analysis is difficult in these

Engineering Computations,
Vol. 17 No. 1, 2000, pp. 28-47.
© MCB University Press, 0264-4401

approaches. To overcome this problem, some researchers (Zheng and Sun, 1995; Liu and Chang, 1994) included in their continuum finite element formulations appropriate tying constraints and contact conditions. A similar formulation was pursued by other authors (Cui and Wisnom, 1993) who have considered solid elements connected by discrete springs. Basically, these analyses involve a node-to-node interaction and damage propagation is also possible by using an adequate failure criterion. Another possibility is the use of interface elements as an intermediate between the different layers of dissimilar materials (Rao *et al.*, 1982; Beer, 1985; Schellekens and De Borst, 1993; Reddy *et al.*, 1997). An interface element consists of an upper and a lower plane. In contrast to continuum elements where stress-strain relations are used, relations between stresses and relative displacements of the interface surfaces govern interface elements. Generally the two planes of the interface element act as a single one until a prescribed failure criterion is satisfied. Once the failure criterion is reached, the connection is broken by creating or growing discrete damage. Some advantages of interface elements include easy implementation into standard finite element programs and direct determination of interface stresses without round-off problems.

In this context, we developed an interface finite element with 18 nodes that matches with 27 nodes isoparametric hexahedral elements available in the ABAQUS® software. Notable features of the present element include a penalty formulation, three-dimensional analysis, point-to-point and point-to-surface constraints and modelling damage initiation and growth. Before the failure criterion is satisfied, the interaction between the two planes of the interface element is made by point-to-point constraints for each pair of homologous points. When the failure criterion is met the connection is broken. At this stage the point-to-point constraint is changed to a point-to-surface interaction which simulates more accurately the physical reality. Damage propagation is simulated using two different models: the first one deals with either pure mode I or pure mode II loading conditions and the second one considers mixed mode propagation. Both of these models are based on a softening relationship between stresses and relative displacements. Finally, the numerical results for mode I, mode II and mixed mode tests are compared to closed form solutions.

2. Finite element formulation

The solution of contact problems can be formulated as the minimization of the potential energy subjected to certain kinematic constraints. Considering the variational method to obtain the equilibrium equations of a structural problem with kinematic constraints and using the penalty function method we have

$$\bar{\pi}(\mathbf{U}) = \pi(\mathbf{U}) + \frac{\varepsilon}{2}[\mathrm{G}(\mathbf{U})]^2 \qquad (1)$$

where

$$\pi(\mathbf{U}) = \frac{1}{2}\mathbf{U}^{\mathrm{T}}\mathbf{K}\mathbf{U} - \mathbf{U}^{\mathrm{T}}\mathbf{F} \tag{2}$$

being

- $\pi(\mathbf{U})$ – functional of a structural problem without constraints;
- $\bar{\pi}(\mathbf{U})$ – functional of a structural problem with kinematic constraint;
- $\mathbf{U}$ – displacement vector;
- $\mathbf{K}$ – stiffness matrix;
- $\mathbf{F}$ – nodal forces;
- $G(\mathbf{U}) = 0$ – kinematic constraint;
- ε – penalty parameter.

The state of equilibrium is achieved when the displacement field $\mathbf{U}$ minimizes the potential energy presented in equation (1). It can be shown that, when ε approaches infinity, the minimization of the functional $\bar{\pi}(\mathbf{U})$ produces a better approximation of $G(\mathbf{U}) = 0$. The kinematic constraint for a pair of points (k) in contact can be written as (Papadopoulos and Taylor, 1992; Nour-Omid and Wriggers, 1986)

$$(\mathbf{U}_{\mathrm{p}} - \mathbf{U}_{\mathrm{s}}).\mathbf{n}_k + \gamma_k = 0 \tag{3}$$

where

- $\mathbf{U}_{\mathrm{p}}$ – displacement vector of a node (p) belonging to one of the contacting surfaces;
- $\mathbf{U}_{\mathrm{s}}$ – displacement vector of the point resulting from the projection of the previous node (p) onto the opposite surface (point-to-surface interaction); for the point-to-point formulation (s) represents the node homologous to (p);
- $\mathbf{n}_k$ – unit vector normal to the surface containing (s);
- γ_k – initial distance in the normal direction $\mathbf{n}_k$.

The vectors $\mathbf{U}_{\mathrm{p}}$ and can $\mathbf{U}_{\mathrm{s}}$ be written

$$\mathbf{U}_{\mathrm{p}} = \mathbf{e}_{\mathrm{p}}^{\mathrm{T}}\mathbf{U} \tag{4}$$

$$\mathbf{U}_{\mathrm{s}} = \sum_{j=1}^{m} \alpha_j \mathbf{e}_j^{\mathrm{T}}\mathbf{U} \tag{5}$$

in which

$\mathbf{e}_p$ – the three columns of the identity matrix allowing one to obtain the displacement vector of node (p) from the global displacement vector;

$\mathbf{e}_j$ – the three columns of the identity matrix allowing one to obtain the displacement vector of node (j) from the global displacement vector;

m – number of points for definition of the displacement of (s);

α_j – set of interpolation functions used to calculate the displacement vector of point (s) from the displacement of the m points.

Rewriting (3) we have

$$(\mathbf{C}_k^{\mathrm{T}}\mathbf{U}) \cdot \mathbf{n}_k + \gamma_k = 0 \tag{6}$$

where

$$\mathbf{C}_k^{\mathrm{T}} = \mathbf{e}_p^{\mathrm{T}} - \sum_{j=1}^{m} \alpha_j \, \mathbf{e}_j{}^{\mathrm{T}} \tag{7}$$

Considering the total number of constraints (d), the functional for the problem being treated can be obtained as

$$\bar{\pi}(\mathbf{U}) = \pi(\mathbf{U}) + \frac{\varepsilon}{2} \sum_{k=1}^{d} [((\mathbf{C}_k^{\mathrm{T}}\mathbf{U}).\mathbf{n}_k + \gamma_k)^{\mathrm{T}}((\mathbf{C}_k^{\mathrm{T}}\mathbf{U}).\mathbf{n}_k + \gamma_k)] \tag{8}$$

Minimizing this equation leads to

$$\delta\bar{\pi}(\mathbf{U}) = \delta\pi(\mathbf{U}) + \varepsilon \sum_{k=1}^{d} [\mathbf{U}^{\mathrm{T}}\mathbf{C}_k\mathbf{n}_k\mathbf{n}_k^{\mathrm{T}}\mathbf{C}_k^{\mathrm{T}} + \gamma_k\mathbf{n}_k^{\mathrm{T}}\mathbf{C}_k^{\mathrm{T}}] \, \delta\mathbf{U} = 0 \tag{9}$$

or, including the differentiation of equation (2)

$$\left[\mathbf{K} + \varepsilon \sum_{k=1}^{d} \mathbf{C}_k\mathbf{n}_k\mathbf{n}_k^{\mathrm{T}}\mathbf{C}_k^{\mathrm{T}}\right]\mathbf{U} = \mathbf{F} - \varepsilon \sum_{k=1}^{d} \gamma_k\mathbf{C}_k\mathbf{n}_k \tag{10}$$

or

$$[\mathbf{K} + \mathbf{K}_r]\mathbf{U} = \mathbf{F} + \mathbf{F}_r \tag{11}$$

in which

$$\mathbf{K}_r = \varepsilon \sum_{k=1}^{d} \mathbf{C}_k\mathbf{n}_k\mathbf{n}_k^{\mathrm{T}}\mathbf{C}_k^{\mathrm{T}} \tag{12}$$

$$\mathbf{F}_r = -\varepsilon \sum_{k=1}^{d} \gamma_k \mathbf{C}_k \mathbf{n}_k \tag{13}$$

It can be stated that $\mathbf{K}_r$ and $\mathbf{F}_r$ represent the constraints contribution to the global problem. Thus, the interface finite element formulation is the determination of its contribution to the global problem by matrices $\mathbf{K}_r$ and $\mathbf{F}_r$. Two different approaches are considered in this paper:

(1) Before the failure criterion is satisfied at a certain point, the connection is not broken (closed point) and a point-to-point constraint is used.

(2) Once the failure criterion is reached the connection is broken (opened point) and a point-to-surface interaction is considered.

It must be said that in a closed point the tangential relative displacements are small. The same might not be true at an opened point, which justifies the choice of point-to-surface approach. The main difference between these approaches deals with the contact point determination. While in the first case the relative displacement is measured between homologous points, in the second one it is done between a point and its projection on to the opposite surface. Here the projection determination is a fundamental task. These two procedures are presented in the next sections.

2.1. Point-to-point constraint (Beer, 1985; de Moura *et al.*, 1996)
The element consists of 18 nodes with curved sides as shown in Figure 1.

The vector of relative displacements between two homologous points can be obtained from the displacement fields associated to the element faces (top and bottom)

$$\delta = \begin{Bmatrix} \delta_s \\ \delta_t \\ \delta_n \end{Bmatrix} = \begin{Bmatrix} u_s \\ u_t \\ u_n \end{Bmatrix}_{\text{top}} - \begin{Bmatrix} u_s \\ u_t \\ u_n \end{Bmatrix}_{\text{bot}} \tag{14}$$

where s and t represent the tangential directions and n the normal direction.

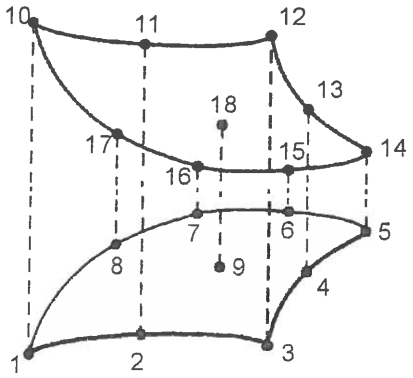

Figure 1.
The interface element

The stresses resulting from the relative displacements, defined above, are given by

$$\sigma = \mathbf{D}\delta \tag{15}$$

where

$$\mathbf{D} = \begin{bmatrix} d_s & 0 & 0 \\ 0 & d_t & 0 \\ 0 & 0 & d_n \end{bmatrix} \tag{16}$$

The parameters d_i are the shear (d_s, d_t) and normal (d_n) interface stiffnesses. The choice of these parameters is restricted by:

(1) Small values induce large interpenetrations incompatible with physical reality.

(2) Large values produce numerical errors related to the computer precision.

Thus, the optimum interface stiffnesses are the largest values that do not produce numerical problems. Some authors (Wriggers and Nour-Omid, 1986) developed a semi-empirical method to obtain an estimate for these values.

2.2. Point-to-surface constraint (Brockman, 1982; Hallquist *et al.*, 1985)
The point-to-surface procedure intends to model the behaviour of an interface between different materials during damage propagation. In fact, when rupture occurs at a point, the respective shear stiffnesses are cancelled. In such a situation, tangential displacements can occur. This means that, in some cases, the normal relative displacement between a point and its projection onto the opposite surface might be quite different from the normal relative displacement between homologous points. As this normal relative displacement is used to calculate the compressive stresses due to interpenetration constraint, a better stress field can be obtained. The aspects related with numerical integration are treated in the same way as for the point-to-point approach.

The first step of this procedure is to determine the projection (n_s) of a given point (n_p) onto the opposite surface. Thus, (n_s) is the point on the opposite surface nearest to (n_p). As can be seen in Figure 2, the vectors **T** and **R** represent, in a global system, the position of (n_p) and (n_s), respectively. The vector **R** can be defined as

$$\mathbf{R} = g_1(\xi, \eta)\mathbf{i} + g_2(\xi, \eta)\mathbf{j} + g_3(\xi, \eta)\mathbf{k} \tag{17}$$

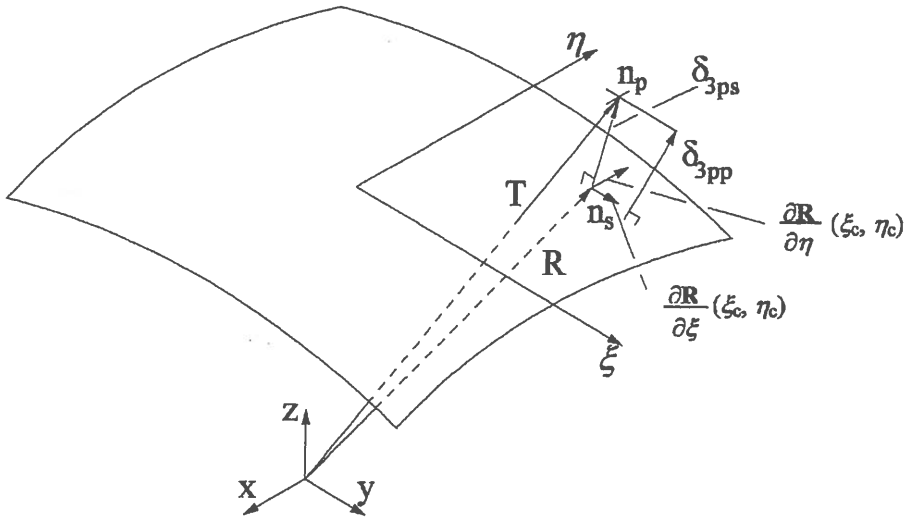

Figure 2.
Projection of (n_p) on to the opposite surface

where

$$g_1(\xi,\eta) = \sum_{j=1}^{9} N_j x_j$$
$$g_2(\xi,\eta) = \sum_{j=1}^{9} N_j y_j \qquad (18)$$
$$g_3(\xi,\eta) = \sum_{j=1}^{9} N_j z_j$$

where N_j are the shape functions of the quadratic nine-node rectangular isoparametric element (de Moura *et al.*, 1996) and (ξ, η) are the local coordinates.

The partial derivatives $\left(\frac{\partial \mathbf{R}}{\partial \xi}$ and $\frac{\partial \mathbf{R}}{\partial \eta}\right)$ represent the tangential vectors at (n_s), with local coordinates ξ_c and η_c. The main objective is the determination of these coordinates such that the vector $(\mathbf{T} - \mathbf{R})$ is perpendicular to the surface containing (n_s). Thus, the coordinates ξ_c and η_c must satisfy the following equations

$$\frac{\partial \mathbf{R}}{\partial \xi}(\xi_c, \eta_c) \cdot [\mathbf{T} - \mathbf{R}(\xi_c, \eta_c)] = 0$$
$$\frac{\partial \mathbf{R}}{\partial \eta}(\xi_c, \eta_c) \cdot [\mathbf{T} - \mathbf{R}(\xi_c, \eta_c)] = 0 \qquad (19)$$

It must be noted that this is a set of non-linear equations that must be solved numerically. The method used is known as globally convergent Newton's method (Press *et al.*, 1992).

Once the position of (n_s) is known, the vector ($\mathbf{T} - \mathbf{R}$) can be calculated. The length of this vector represents the interpenetration or gap between (n_p) and (n_s). If points are open, then friction is not considered and shear stresses are neglected. In this situation the matrix equation (15) can be reduced to

$$\sigma_n = d_n \, \delta_n \tag{20}$$

where, in this case, δ_n is the length of ($\mathbf{T} - \mathbf{R}$). It must be noted that equation (20) is only valid when $\delta_n < 0$, because for $\delta_n \geq 0$ the normal stresses are zero. It is clear that the normal displacements obtained in this way are more realistic than those calculated by the point-to-point approach, mainly when the tangential relative displacements are significant.

2.3. Element performance

Preliminary studies have shown some numerical problems related with oscillations in stress profiles. Also, some researchers (Schellekens and De Borst, 1993) have shown that large oscillations can occur in a solution if there are a coupe of degrees of freedom between different pairs of nodes. In this context, the influence of the numerical integration schemes of the linear stiffness matrix presented below was studied.

2.3.1. Stiffness matrix. The linear stiffness matrix of the element is obtained by considering the following functional

$$\pi(\mathbf{U}^e) = \frac{1}{2}\int_A \delta^T \sigma dA - \mathbf{U}^{eT}\mathbf{F}_r^e \tag{21}$$

which on minimization leads to

$$\mathbf{F}_r^e = (\int_A \mathbf{B}^T\mathbf{D}\mathbf{B}dA)\mathbf{U}^e \tag{22}$$

where $\mathbf{B}$ is the matrix relating the relative displacements and nodal displacements vectors (de Moura *et al.*, 1997). The stiffness matrix can be defined by

$$\mathbf{K}_r^e = \int_A \mathbf{B}^T\mathbf{D}\mathbf{B}dA. \tag{23}$$

2.3.2. Numerical integration. The integration scheme was previously shown (Schellekens and De Borst, 1993; Gens *et al.*, 1988) to have influence on the performance of the interface element. In those studies a better performance with the Newton-Cotes integration scheme, instead of Gauss scheme, was obtained. In the Newton-Cotes scheme the integration points are located at the nodes, which is not true for the Gauss scheme. In Gens *et al.* (1988), a 16-node element with Newton-Cotes integration was used and some difficulties were

still found. Our 18-node element that has a central pair of nodes coincident with the central integration point existing in the 3 × 3 Newton-Cotes integration scheme overcomes those difficulties. This element can be regarded as a linkage element in which the relationship between each pair of homologous nodes is independent of the rest of the element. The eigenvalue analysis performed for the linear stiffness matrix of our element is shown in Figures 3 and 4 and illustrates the uncoupling and coupling behaviours of the Newton-Cotes and Gauss schemes, respectively. This analysis was done considering only closed points, i.e. for the case where the point-to-point approach is used.

Some authors (Day and Potts, 1994) have found that stress oscillations not only are due to the integration scheme but also depend on the ratio of the stiffness of the interface element to the element adjacent to it. This dependence was not investigated in our work.

3. Damage models

When the adopted failure criterion is satisfied the sudden cancellation of the stresses transmitted at the point causes numerical problems related with convergence difficulties. To overcome this problem a damage model is used to gradually develop the failure process. Four state changes at a point must be considered:

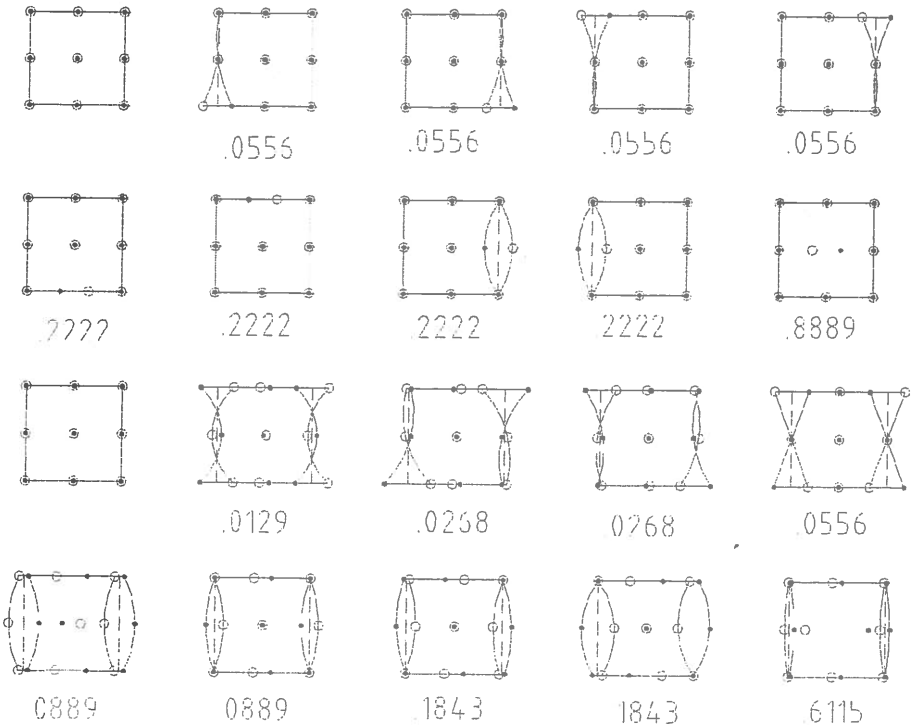

Figure 3.
The nine eigenmodes and respective eigenvalues for the 3 × 3 Newton-Cotes integration scheme

Figure 4.
The nine eigenmodes and respective eigenvalues for the 3 × 3 Gauss integration scheme

(1) Failure in presence of normal tensile stresses which implies that shear and normal stiffnesses are set to zero.

(2) Failure in presence of normal compressive stresses which implies nullification of shear stiffnesses, maintaining the normal compressive stiffness.

(3) Changing from an opened gap to a contact, which produces a normal compressive stress, to prevent interpenetration.

(4) Opposite of the previous point that implies nullification of the normal compressive stiffness.

3.1. Pure mode I or pure mode II (Reddy *et al.*, 1997; Schellekens, 1992)
The damage models used are characterised by a softening stress/relative displacements relationship, which means that the failure does not occur instantaneously. It is assumed that energy is dissipated as the crack grows. This method is based on the indirect use of fracture mechanics considering the area under the softening stress/relative displacements curve (see Figure 5) equal to the critical fracture energy.

Failure initiates once the defined strength $\sigma_{t,i}$, which corresponds to a critical relative displacement $\delta_{o,i}$, has been exceeded. The relation between $\sigma_{t,i}$ and $\delta_{o,i}$ is established by the interface stiffness d_i. The softening zone is defined by a linear decrease in the stress until it vanishes and the fracture is complete. The relative displacement $\delta_{max,i}$, for which complete failure occurs, is obtained equating the area under the softening curve to the critical fracture energy (G_{Ic} or G_{IIc}) which is a material property.

The relationship between stresses and relative displacements presented in Figure 5 can be separated in three steps:

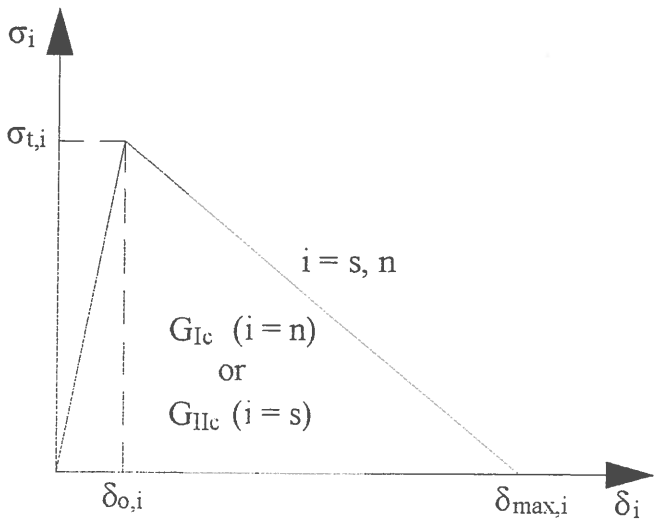

Figure 5.
Softening stress/relative displacements relationship

(1) For $\delta_i < \delta_{o,i}$ the relation is governed by equation (15).

(2) For $\delta_{o,i} \leq \delta_i \leq \delta_{max,i}$ we have

$$\sigma = (\mathbf{I} - \mathbf{E})\mathbf{D}\delta \tag{24}$$

where $\mathbf{I}$ represents the identity matrix and $\mathbf{E}$ is a diagonal matrix containing on the i-position the damage parameter,

$$e_i = \frac{\delta_{\max,i}(\delta_i - \delta_{o,i})}{\delta_i(\delta_{\max,i} - \delta_{o,i})} \tag{25}$$

corresponding to the i-direction. This parameter is obtained from the consideration that e_i goes from zero (for $\delta_i = \delta_{o,i}$) to one (for $\delta_i = _{max,i}$) in a linear manner. The other two elements of the diagonal matrix are equated to one simulating an immediate cancellation of the strength in those directions. It must be said that for pure mode problems (I or II) the two other stress components are not important.

(3) For $\delta_i = _{max,i}$ all the three components of the diagonal matrix $\mathbf{E}$ are equated to one, which means that the strengths in all directions are zero. It must be noted that, in this situation, interpenetration is prevented by reapplying the normal stiffness (d_n) whenever the crack closes.

3.2. Mixed mode

In many situations a more complex stress state is present and a mixed mode analysis is necessary instead of a single mode analysis. The mixed mode models presented below are based on the pure mode model described above. We first consider a mixed mode damage model where the three modes are included. A second model considering only mode I and mode II is obtained from the original model after a suitable simplification.

3.2.1. Mode I, mode II and mode III. This model is based on a moving plane damage surface represented in Figure 6. Initial damage at a point occurs if the resulting relative displacements lie outside the initial damage surface, which contains the three critical relative displacements ($\delta_{o,s}, \delta_{o,t}, \delta_{o,n}$). Damage propagation ends when the resulting relative displacement reaches the final damage surface containing the three maximum relative displacements ($\delta_{max,s}, \delta_{max,t}, \delta_{max,n}$). Between these two limit situations damage propagation is represented by consecutive different positions of the damage surface which is a function of the relative displacement vector δ_j. A definition of a new surface S_{j+1}, at a point, is necessary whenever the resulting relative displacements pass the current surface S_j. The new surface S_{j+1} is then obtained from the current surface and displacement increments doing,

$$\frac{\delta_{j+1,s}}{\delta^*_{j,s} + c\Delta\delta_{j+1,s}} + \frac{\delta_{j+1,t}}{\delta^*_{j,t} + c\Delta\delta_{j+1,t}} + \frac{\delta_{j+1,n}}{\delta^*_{j,n} + c\Delta\delta_{j+1,n}} = 1 \tag{26}$$

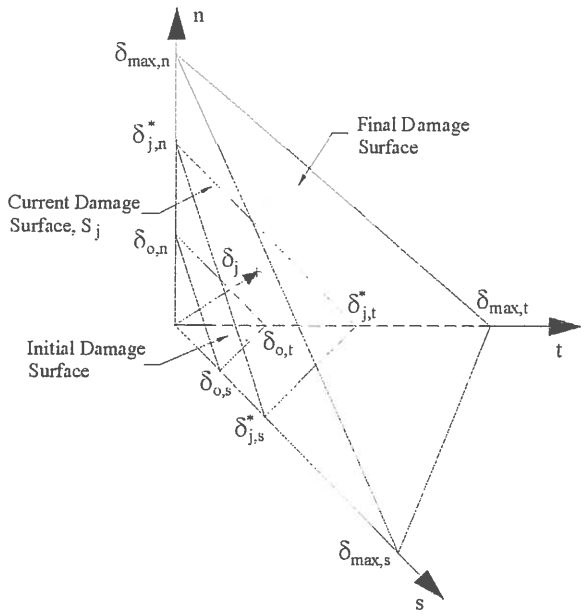

Figure 6.
Mixed mode damage model

where $\delta^*_{j,i}(i = s, t, n)$ are the intersections of the damage surface with the coordinate system and $\Delta\delta_{j+1,i}$ are the relative displacement increments. After the determination of the unknown factor c in equation (26), we obtain the new values $\delta^*_{j+1,i}$,

$$\delta^*_{j+1,i} = \delta^*_{j,i} + c(\delta_{j+1,i} - \delta_{j,i}) \tag{27}$$

The diagonal elements of matrix **E** of equation (24) are now defined by

$$e_{j+1,i} = \frac{\delta_{\max,i}(\delta^*_{j+1,i} - \delta_{o,i})}{\delta^*_{j+1,i}(\delta_{\max,i} - \delta_{o,i})} \tag{28}$$

3.2.2. Mode I and mode II (Schipperen and de Borst, 1997). For cases where mode III can be neglected, we can simplify the model presented above, considering that damage surface is represented by a straight line instead of a plane. Equation (26) can be rewritten as

$$\frac{\delta_{j+1,s}}{\delta^*_{j,s} + c\Delta\delta_{j+1,s}} + \frac{\delta_{j+1,n}}{\delta^*_{j,n} + c\Delta\delta_{j+1,n}} = 1 \tag{29}$$

The damage parameters e_s and e_n are calculated by equation (28). Because mode III is neglected, the procedure described for pure modes (see chapter 3.1) is adopted for the e_t parameter.

4. Examples

In order to study the behaviour of the proposed models some numerical tests were performed and the results obtained were compared with closed form

solutions. These examples include the double cantilever beam test (DCB) for pure mode I, the end notch flexure (ENF) for pure mode II and the mixed mode bending (MMB) for mixed mode (mode I and mode II). For these tests, two beams bonded by an adhesive (see properties in Table I) were considered.

Figure 7 shows the specimen geometry used in all tests.

Geometrically non-linear analyses were performed using the modified Riks method available in the ABAQUS® software (ABAQUS, 1996). The interface stiffnesses used in all examples were taken equal to 10^7 N/mm^3, which was considered to be a value satisfying the two conditions presented in chapter 2.1. To overcome some numerical difficulties encountered, small increments were used. However, in some cases, many iterations were needed to obtain a converged solution.

4.1. Double cantilever beam (DCB)

The loading and boundary conditions used are illustrated in Figure 8. The interface elements are located between the two layers of solid elements along the specimen length. The interface elements along the crack length were previously opened to simulate the initial crack.

Table I.
Material properties

Beams		Adhesive			
E (N/mm^2)	ν	G_{Ic} (N/mm)	G_{IIc} (N/mm)	σ_t (N/mm^2)	τ_t (N/mm^2)
69,000	0.33	0.055	1.45	20	40

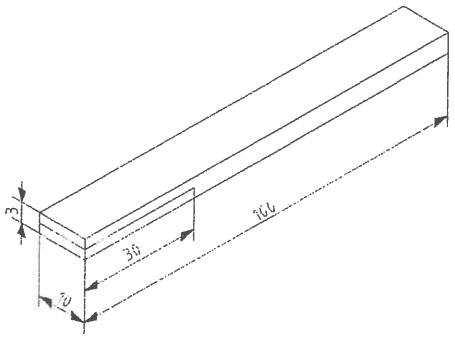

Figure 7.
Specimen geometry (dimensions in mm)

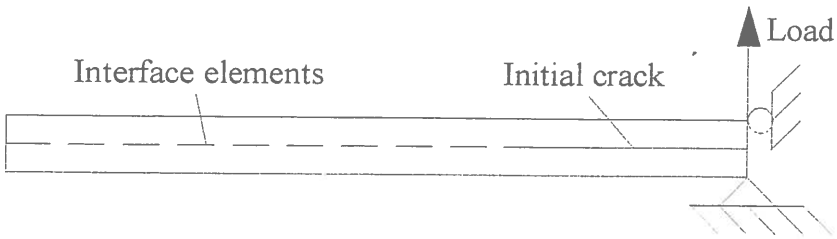

Figure 8.
Loading and boundary conditions for DCB model

The results obtained from three different meshes (50, 100 and 200 elements along the beam) were compared (see Figure 9) with closed form solutions presented in Mi and Crisfield (1996) and Mi *et al.* (1998). These solutions are based on the beam theory and fracture mechanics and they do not include the effects of shear deflection, which was shown to be insignificant (Mi and Crisfield, 1996). Two different relationships between the applied load P and the deflection Δ at the end of the DCB were considered:

(1) Before damage starts to grow,

$$\Delta = \frac{16Pa_0^3}{3EI} \tag{30}$$

(2) During damage propagation,

$$\Delta = \frac{16}{3EIP^2}\left(\frac{BG_{Ic}EI}{8}\right)^{3/2} \tag{31}$$

where:
B – width of the beam;
a_0 – initial crack length;
I – second moment of area of the beam.

Several conclusions can be drawn from Figure 9:

(1) For the coarser mesh (50 elements) the solution shows some instabilities not present in the more refined meshes. This can be explained by the small number of points undergoing the softening process at the same time, which leads to abrupt load drops when one of these points finishes the softening process.

(2) The increase in the number of elements leads to convergent solutions. The difference between the solutions for 100 and 200 element meshes is

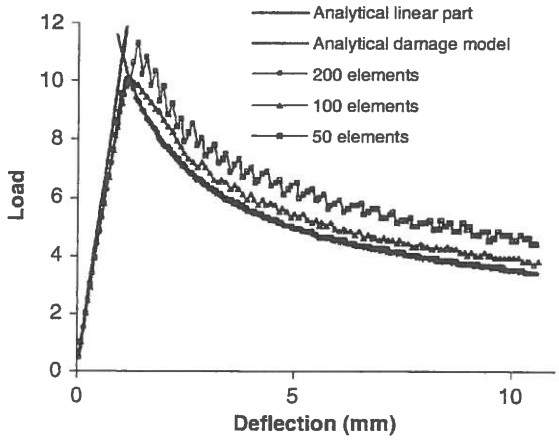

Figure 9.
Load/deflection at the end of the specimen for DCB model

negligible and smaller than the difference between the solutions for 50 and 100 element meshes. This shows a convergent process and consequently mesh independent results for adequately refined meshes.

(3) The solution for the more refined mesh (200 elements) agrees with the closed form solutions. The small difference between peak loads is explained by the geometrically non-linear analysis considered in the numerical model and the fact that some elements initiate the softening process prior to the peak load, which are not accounted for in the analytical model.

4.2. End notched flexure (ENF)

The loading and boundary conditions considered for this analysis are represented in Figure 10. The mesh with 100 elements along the beam was considered.

The numerical load/deflection relationship was also compared with closed form solutions from Mi and Crisfield (1996) and Mi *et al.* (1998), which are described by the following formulae:

(1) Before damage starts to grow,

$$\Delta = \frac{P(2L^3 + 3a_0^3)}{12EI} \tag{32}$$

where L is the half-length of the beam.

(2) During damage propagation:

- for crack length smaller than L,

$$\Delta = \frac{P}{12EI}\left(2L^3 + \frac{(8G_{IIc}BEI)^{3/2}}{\sqrt{3}P^3}\right) \tag{33}$$

- for crack length larger than L,

$$\Delta = \frac{P}{3EI}\left(2L^3 - \frac{(8G_{IIc}BEI)^{3/2}}{4\sqrt{3}P^3}\right) \tag{34}$$

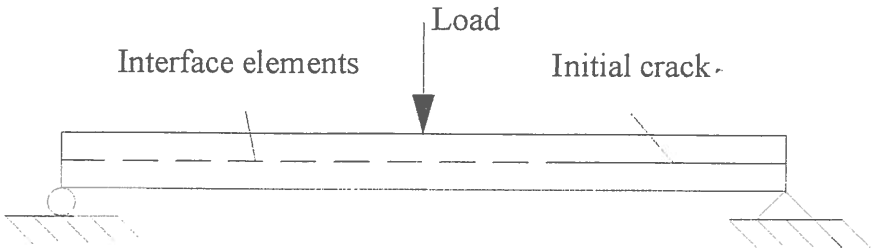

Figure 10.
Loading and boundary conditions for ENF model

Figure 11 shows the numerical and analytical results. It can be stated that the overall load/deflection solution obtained by the finite element method is in close agreement with the analytical results. The difference between peak loads is explained by the geometrically non-linear analysis considered in the numerical model and also because some elements initiate the softening process before the peak load.

4.3. Mixed mode bending (MMB)

The loading and boundary conditions considered for this analysis are represented in Figure 12. The mesh with 100 elements along the beam was

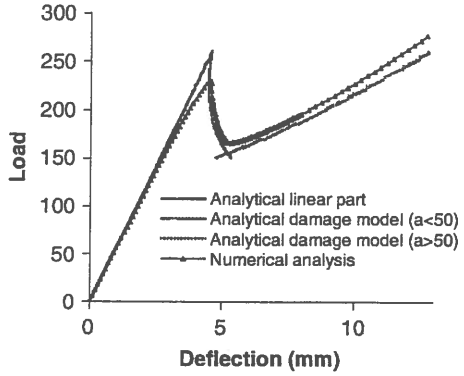

Figure 11.
Load/deflection in the middle of the specimen for ENF model

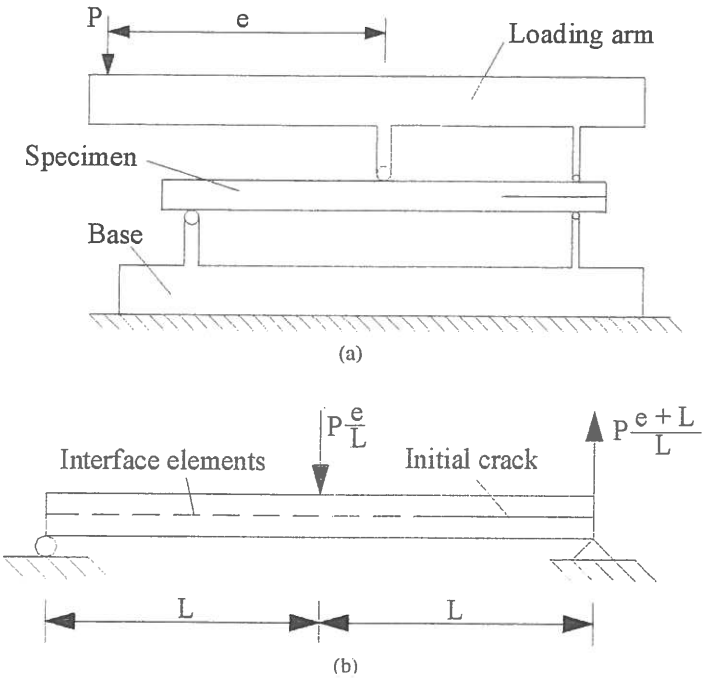

Figure 12.
Mixed mode bending: (a) test apparatus; (b) loading and boundary conditions

considered. The length e was calculated (Mi and Crisfield, 1996) as the distance (43.72mm) so that $G_I/G_{II} = 1.0$. Consequently, for having similar behaviour in the two propagation modes (I and II) the mode I material properties for the adhesive were modified so that $\sigma_t = 40\text{N/mm}^2$ and $G_{Ic} = 1.45\text{N/mm}$.

The numerical load/deflection results were compared with the analytical solution presented in Mi and Crisfield (1996). This solution is based on the superposition of the two modes (I and II). It can be seen (Mi and Crisfield, 1996) that the mode I loading is

$$P_I = \frac{3e - L}{4L} P \tag{35}$$

and the mode II loading is

$$P_{II} = \frac{e + L}{L} P \tag{36}$$

The displacement at the end of the beam is calculated in three different forms:

(1) Before damage starts to grow

$$\Delta = \frac{16 P_I a_0^3}{3EI} \tag{37}$$

(2) During damage propagation and for crack length (a) smaller than L. In this case the relation is similar to equation (37)

$$\Delta = \frac{16 P_I a^3}{3EI} \tag{38}$$

but the crack length (a) must be evaluated, which is done by considering a mixed mode linear criterion

$$\frac{G_I}{G_{Ic}} + \frac{G_{II}}{G_{IIc}} = 1 \tag{39}$$

which leads to

$$\Delta = \frac{16 P_I}{3EI} \left(\frac{BEI}{\frac{8P_I^2}{G_{Ic}} + \frac{3P_{II}^2}{8G_{IIc}}} \right)^{3/2} \tag{40}$$

(3) During damage propagation and for crack length (a) larger than L.

A similar approach to the previous case is considered. However, due to geometrical circumstances the equation for the crack length is different

$$\frac{1}{BEI}\left(\frac{8P_I^2}{G_{Ic}}+\frac{3P_{II}^2}{8G_{IIc}}-\frac{8P_IP_{II}}{G_{IIc}}\right)a^2 - \frac{1}{BEI}\left(\frac{3P_{II}^2L}{2G_{IIc}}-\frac{8P_IP_{II}L}{G_{IIc}}\right)a+\frac{3P_{II}^2L}{2BEIG_{IIc}}-1=0 \tag{41}$$

Figure 13 shows the numerical and analytical results. It can be shown that the global behaviour is in agreement. The difference observed in the peak loads can be explained by the geometrically non-linear effects, the initiation of damage before the peak load and the difference of the damage models considered. In fact, the mixed mode damage model considered in the numerical analysis is not based on the mixed mode linear criterion but on a moving damage surface defined by the relative displacements.

5. Conclusions

An interface finite element based on the penalty method and including damage propagation was presented. The aim was to model the behaviour of interfaces between dissimilar materials in three-dimensional problems. Two different approaches were considered:

(1) Before the failure criterion is satisfied a point-to-point constraint is used.

(2) After the failure criterion is met a point-to-surface constraint is considered.

The second approach requires the determination of the projection of a given point on to the opposite surface. For the quadratic elements used, this implies the solution of a set of non-linear equations, which is done by using the globally convergent Newton's method.

The damage models considered are based on the indirect use of fracture mechanics considering the area under the stress/relative displacements curve

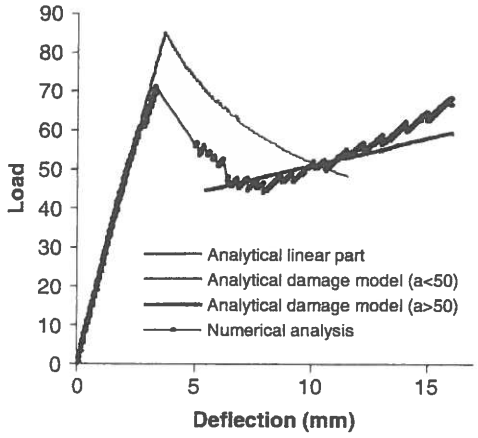

Figure 13.
Load/deflection at the end of the beam for MMB model

equal to the critical fracture energy. An advantage of this approach is to model damage propagation as well as initiation, avoiding the definition of initial flaws.

The examples presented illustrate the applicability of the element and damage models to the study of problems involving pure modes (I or II) and mixed mode (I and II). For pure modes, it can be stated that good agreement between numerical and analytical results was obtained for refined meshes. In the mixed mode the difference between peak loads is greater than in pure modes. Larger non-linear geometrical effects and different damage models used can explain it. However, the trend obtained for the mixed mode problem is in reasonable agreement with the analytical model.

References

ABAQUS (1996), *User's Manual – Version 5.6*, Hibbitt, Karlsson & Sorensen, Inc.

Allix, O. and Ladevèze, P. (1992), "Interlaminar interface modelling for the prediction of delamination", *Composite Structures*, Vol. 22, pp. 235-42.

Barsoum, R.S. and Freese, C.E. (1984), "An iterative approach for the evaluation of delamination stresses in laminated composites", *Int. J. Numer. Methods Eng.*, Vol. 20, pp. 1415-31.

Beer, G. (1985), "An isoparametric joint/interface element for finite element analysis", *Int. J. Numer. Methods Eng.*, Vol. 21, pp. 585-600.

Brockman, R.A. (1982), "Numerical solution of large deformation problems involving surface contact and impact", Winter Annual Meeting of the American Society of Mechanical Engineers, Phoenix, AZ.

Cui, W. and Wisnom, M.R. (1993), "A combined stress-based and fracture-mechanics-based model for predicting delamination in composites", *Composites*, Vol. 24 No. 6, pp. 467-74.

Day, R.A. and Potts, D.M. (1994), "Zero thickness interface elements numerical stability and application", *International Journal for Numerical and Analytical Methods in Geomechanics*, Vol. 18, pp. 689-708.

de Moura, M.F.S.F., Gonçalves, J.P.M., Marques, A.T. and de Castro, P.M.S.T. (1996), "Elemento finito isoparamétrico de interface para problemas tridimensionais", *Métodos Numéricos para Cálculo y Diseño en Ingeniería*, Vol. 12 No. 4, pp. 447-66.

de Moura, M.F.S.F., Gonçalves, J.P.M., Marques, A.T. and de Castro, P.M.S.T. (1997), "Modeling compression failure after low velocity impact on laminated composites using interface elements", *Journal of Composite Materials*, Vol. 31 No. 15, pp. 1462-79.

Gens, A., Carol, I. and Alonso, E.E. (1988), "An interface element formulation for the analysis of soil-reinforcement interaction", *Computers and Geotechnics*, Vol. 7, pp. 133-51.

Hallquist, J.O., Goudreau, G.L. and Benson, D.J. (1985), "Sliding interfaces with contact-impact in large-scale Lagrangian computations", *Computer Methods in Applied Mechanics and Engineering*, Vol. 51, pp. 107-37.

Lindner, M. and Kromp, K. (1988), "FE-calculation demonstrating the influence of the matrix interface layer on the free edge stresses in a laminated CFRC composite", *Proc. of the 2nd Int. Symp. on Brittle Matrix Composites*, Cedzina, Poland.

Liu, S. and Chang, F.-K. (1994), "Matrix cracking effect on delamination growth in composite laminates induced by a spherical indenter", *Journal of Composite Materials*, Vol. 28 No. 10, pp. 940-77.

Mi, Y. and Crisfield, M.A. (1996), "Analytical derivation of load/displacement relationships for mixed-mode delamination and comparison with finite element results", Report, Dept. of Aeronautics, Imperial College, London.

Mi, Y., Crisfield, M.A., Davies, G.A.O. and Hellweg, H.-B. (1998), "Progressive delamination using interface elements", *Journal of Composite Materials*, Vol. 32 No. 14, pp. 1246-72.

Nour-Omid, B. and Wriggers, P. (1986), "A two-level iteration method for solution of contact problems", *Computer Methods in Applied Mechanics and Engineering*, Vol. 54, pp. 131-44.

Papadopoulos, P. and Taylor, R.L. (1992), "A mixed formulation for the finite element solution of contact problems", *Computer Methods in Applied Mechanics and Engineering*, Vol. 94, pp. 373-89.

Press, W.H., Vetterling, W.T., Teukolsky, S.A. and Flannery, B.P. (1992), *Numerical Recipes in C*, 2nd ed., Cambridge University Press, Cambridge, MA.

Rao, B.N., Rao, Y.V.K.S. and Yadagiri, S. (1982), "Analysis of composite bonded joints", *Fiber Science and Technology*, Vol. 17 No. 10, pp. 77-90.

Reddy E.D. Jr, Mello, F.J. and Guess, T.R. (1997), "Modeling the initiation and growth of delaminations in composite structures", *Journal of Composite Materials*, Vol. 31 No. 8, pp. 940-77.

Schellekens, J.C.J. (1992), "Computational strategies for composite structures", PhD thesis, Technical University of Delft, Delft.

Schellekens, H. and De Borst, R. (1993), "On the numerical integration of interface elements", *Int. J. Numer. Methods Eng.*, Vol. 36, pp. 43-66.

Schipperen, J.H.A. and de Borst, R. (1997), "Mode-I and mixed mode delamination in laminated composites", in Owen, D.R.J. *et al.* (Eds), *Computational Plasticity*, CIMNE, Barcelona, pp. 1237-43.

Shi, Y.-B. and Chen, H.R. (1992), "A mixed finite element for interlaminar stress computation", *Composite Structures*, Vol. 20, pp. 127-36.

Spilker, R.L. (1982), "Hybrid-stress eight-node elements for thin and thick multilayer laminated plates", *Int. J. Numer. Methods Eng.*, Vol. 18, pp. 801-28.

Wang, S.S. (1980), "An analysis of delamination in angle-ply fiber-reinforced composites", *Journal of Applied Mechanics*, Vol. 47, pp. 64-70.

Wriggers, P. and Nour-Omid, B. (1986), "Solution methods for contact", Report number UCB/SESM-84/09, Department of Civil Engineering, University of California, Berkeley, CA.

Wu, C.M.L. (1987), "Nonlinear analysis of edge effects in angle-ply laminates", *Computers & Structures*, Vol. 25 No. 5, pp. 787-98.

Zheng, S. and Sun, C.T. (1995), "A double-plate finite-element model for the impact-induced delamination problem", *Composites Science and Technology*, Vol. 53, pp. 111-18.

ELSEVIER

International Journal of Fatigue 22 (2000) 319–338

International Journal of Fatigue

www.elsevier.com/locate/ijfatigue

Multiple-site damage in riveted lap-joints: experimental simulation and finite element prediction

Lucas F.M. Silva, J.P.M. Gonçalves, F.M.F. Oliveira, P.M.S.T. de Castro *

Department of Mechanical Engineering and Industrial Management, University of Porto, Rua dos Bragas, 4050-123 Porto, Portugal

Received 8 February 1999; received in revised form 11 November 1999; accepted 5 December 1999

Abstract

The multiple-site damage (MSD) phenomenon is discussed, and exemplified by the behaviour of riveted lap-joint specimens of aluminium alloy 2024-T3 alclad. The tests performed, on which the paper is based, are part of the contribution of IDMEC to a project on the fatigue behaviour of ageing aeronautical structures—the BRITE-EURAM project 'SMAAC', partially funded by the European Union. The study involves fatigue testing under constant amplitude loading of 1.6-mm-thick riveted lap-joints, and includes examination of the specimens during and subsequent to testing (post-mortem analysis of the fracture surface in a scanning electron microscope) in order to determine the time of occurrence, location and extent of fatigue damage. Crack growth rates are determined from periodic crack length measurements with a travelling microscope. Stress measurements are made using extensometry and the SPATE infrared technique to determine loading distribution of the lap-joints and redistribution due to cracking of fastener holes. Data on the initiation and growth of cracks and on residual static strength are used to assess the predictive model based on the finite element method. © 2000 Elsevier Science Ltd. All rights reserved.

Keywords: Multiple-site damage; Crack initiation; Crack growth; Residual strength

1. Introduction

This work is part of the BRITE/EURAM project BE95-1053, 'Structural Maintenance of Ageing Aircraft' (SMAAC) [1]. 'Ageing aircraft' is a technical term indicating that the aircraft has reached its original design goal. The light alloy structures used in commercial aircraft could be susceptible to widespread fatigue damage (WFD). WFD as an effect of multiple-site damage (MSD) can be regarded as the major problem of ageing aircraft. This problem may be divided roughly into three parts:

- the initiation of MSD (which assesses the initial damage scenario),
- the crack propagation of MSD (simultaneously at different sites), and
- the residual strength in the presence of MSD and possible further deteriorating effects like corrosion, debonding or manufacturing defects.

The objective is to generate basic material crack propagation data; to study the initiation and growth of cracks in laboratory specimens which simulate the key features of aircraft joints in which WFD is present; and to derive data on crack initiation, crack growth and residual static strength which will be used to assess the predictive model based in the FRANC2D/L finite element programme. This bring us to focus the literature review on four points: loading and stress distribution of a longitudinal fuselage splice, crack initiation, crack growth and residual static strength. Although the specimens tested are simple riveted lap-joints, it is important to be aware of the loading present in practice.

2. Literature review

2.1. Loading and stress distribution of a longitudinal fuselage splice

Eastaugh et al. [2] present a comprehensive description of this aspect. Fuselage pressurisation is the main

* Corresponding author. Tel.: +351-22-204-1719; fax: +351-22-205-9125.

E-mail address: ptcastro@fe.up.pt (P.M.S.T. de Castro).

0142-1123/00/$ - see front matter © 2000 Elsevier Science Ltd. All rights reserved.
PII: S0142-1123(99)00129-2

fatigue load on a longitudinal fuselage splice (around 55 kPa once per flight). This pressure subjects a splice to a combination of hoop tension, longitudinal tension, and out-of-plane bending. There are two effects associated with the out-of-plane bending: pillowing of the skin between stiffeners and distortion, known as secondary bending, caused by the action of hoop tension on the eccentricity inherent in single lap- or butt-joints.

The hoop stress, rivet load and out-of-plane bending stress are generally all higher at the extreme rows than at other rows: row A in the countersunk sheet and row B in the non-countersunk sheet. Fig. 1 shows a lap-joint often used in fuselages, along with the location of the critical rows. As reported by Schijve [3], fatigue cracks may be expected in row A. On an aircraft, this is the upper row in the outer sheet. The main reason why fatigue cracking tends to start here rather than in row B (lower row of the inner sheet) is that the countersink increases the stress concentration at the holes. The edge of the countersink rivet hole acts as a stress concentration site and can elevate the local stresses by a factor of 3 or more [4]. If cracks are in row A, inspection can then be done. The other critical row of the inner skin cannot be inspected visually. Unfortunately, experiments have shown that row B can be critical, which is not easy to understand.

The stress distribution within a splice is a difficult matter. The load transfer in the lap-joint is done by rivet shear and also through friction between the sheets. This uneven load transfer combined with the stress concentration due to holes and the secondary bending gives a complex, three-dimensional stress distribution. Eastaugh et al. [2] illustrate the complexity in a photoelastic image. They noticed that the bending stress is greatest along a line roughly tangential to the rivet holes. They also used strain gauges due to the limitation of the photoelasticity technique. The specimens comprised two sheets of 1-mm-thick aluminium alloy 2024-T3 alclad held by three rows of 4-mm-diameter rivets of aluminium alloy 2117-T4, with continuous straps bonded across its width above and below the splice. The strain gauges were placed on both sides of a sheet, to distinguish between membrane and bending stresses. The non-cracked hoop stress distribution is flat over the central 4 inches of the specimen, and then curves gradually downwards to a value at the outer rivets which is 90% of the maximum value. The authors report that these results are representative of those published by Miller et al. [5] for Boeing narrow-body aircraft. Samavedam et al. [6] tested curved panels with an uninterrupted frame-bay of 51 cm (20 in). The value of the skin hoop stress at the frames and straps varies by 35% of mid-bay stress.

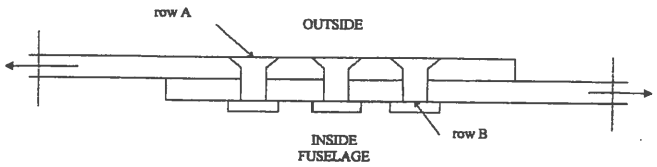

Fig. 1. Critical locations in the lap-joint.

Another full-scale study, carried out by Jeong et al. [7] on a Boeing 737, reported the following points:

- the lower rivet row of the inner skin experiences the same peak strains as the upper rivet row of the outer skin. Thus, as reported by Schijve [3], two critical planes must be considered in fatigue and damage tolerance analysis,
- hoop stresses in the frames were as much as 50% lower than those in the adjacent lap splice skin.

As regards the secondary bending, Schutz and Lowak [8] found a bending ratio (bending stress/local membrane stress), on actual fuselage splices, ranging from 0.2 to 1.8. Eastaugh et al. [2] measured 0.45.

Fatigue cracks start in or close to the rivet holes. The stress distribution around a rivet hole is therefore of prime importance. It is the result of several loading conditions, as reported by Eastaugh et al. [2]:

- biaxial tension in the sheet,
- pin-loading at the hole due to load transfer through rivet shear,
- clamping load applied by the rivet,
- surface shear within the clamping zone of the rivet due to load transfer through friction,
- internal pressure in the hole due to expansion of the rivet, possibly causing yielding,
- out-of-plane bending due to skin pillowing and joint eccentricity.

The combination of these effects and the stress concentration due to the hole raise the stress above the yield strength under normal operating conditions.

2.2. Crack initiation

In an aircraft splice, fatigue cracking usually starts in the upper rivet row in the outer sheet. However, cracking can occur in the inner lap depending on the skin thickness: thicker skins, used in wide-body aircraft, favour cracking in the outer lap, while in thinner skins, used in narrow-body aircraft, cracks can occur in the inner lap [2]. Cracks typically initiate at hidden locations—at the edge of a rivet hole, or at the faying surface of the sheets [2]. This tendency is promoted by firm clamping, which depends on the applied riveting force [9] and also the type of rivet. Experiments have shown that fatigue cracks initiate in cladding layers because of their lower strength [10,11], but the details of crack initiation are still not completely understood.

According to Piascik et al. [12], fatigue crack

initiation occurs in regions of high stress concentration factors located at or near rivet holes. Typically, cracks were found to initiate at rivet hole corners, surface discontinuities (burrs, dents, etc.) and abraded (fretted) surfaces. Evidence of fretting fatigue was noted by a black oxide deposit on the mating surface between the inner and outer skin around each rivet hole. The role of fretting is not clear. It may be the result of cracking or the cause, increasing the local stress and hence the crack driving force during early crack growth [13].

Wang [14] and Potter and Yee [15] reported on examinations of fracture surfaces of cracks starting from fastener holes. Crack nucleation occurred at inclusions, tool marks and other small damage. A remarkable result was reported when a poor drilling technique was replaced by an improved technique [15]. It increased the spectrum fatigue life by a factor of almost 2. This confirms that the initiation can be a matter of small initial surface damage.

The environment also plays an important role. Fatigue cracks tend to initiate earlier and crack growth tends to be faster in moist environments [2]. Moisture promotes pitting and intergranular corrosion. Sealant applied to the faying surfaces and rivets prior to assembly can keep moisture out of the splice. Surface chemical treatments, inhibitors, paints, drainage, ventilation and effective maintenance tend to slow its effects.

Visual and high-frequency eddy current techniques are currently used for inspecting fuselage skin splices. These techniques cannot reliably detect cracks until they are through the sheet and clear of the rivet head. Initiation is often considered as the appearance of a crack of size 0.02 in [16]. At this size, the crack generally just emerges from under a typical fastener head and becomes inspectable.

The crack initiation stage and early crack growth (up to visible cracks) may cover the major part of the fatigue life [3]. Striation counts on the Aloha 737 provided evidence of crack growth underneath rivet heads for at least 25% of the total airframe fatigue life [17], while cracks have appeared beyond rivet heads during full-scale tests after approximately 50% of airframe life [18].

As regards the distribution in initiation life, Eastaugh et al. [2] report that there is a relation between the uniformity of cracks within an MSD cluster and the growth period from first link-up to critical length. In the 747, this period seems to vary from about 10 000 pressurisation cycles for a small, non-uniform cluster of cracks down to 1000 cycles for a larger, more uniform cluster spanning most of the frame-bay [2].

2.3. Crack growth

Based on published in-service and test data [2,12,16,19,20], the general characteristics of crack growth in fuselage splices are the following:

1. There is a period of relatively slow growth under the rivet heads followed by faster growth beyond the rivet heads. Due to out-of-plane bending the crack nuclei grow and coalesce to form a part-through crack. The shape is roughly quarter- or semi-elliptical, depending on the proximity of a rivet hole. The cracks tend to grow faster in the direction of the row of the rivet holes than through the skin towards the outer surface. When cracks reach the outer surface of a lap, they become through-cracks. However, the crack fronts remain slanted to some extent, because of the out-of-plane bending.
2. Cluster of cracks develop in one or more frame-bays, away from frames and straps. The clusters may be broad, i.e. distributed along most of the width of a frame-bay, or they may be narrow, i.e. two or three cracked rivet holes in close proximity.
3. Then, two adjacent cracks may link-up to form a lead crack. This lead crack grows much faster than other, unlinked cracks and tends to dominate subsequent crack growth within a frame-bay. The link-up of the remaining cracks and uncracked holes proceeds one ligament at a time until there is a linked crack spanning most of the frame-bay. This is, in other words, the problem of MSD. The critical size for MSD based on the size of the outlying cracks can be much smaller than that of a single crack, making it harder to detect the critical cracks by inspection.
4. All fatigue cracks initiate at the rivet hole horizontal centreline or in the upper half of the rivet row. Cracks grow longitudinally, along the rivet row, in most cases. In some cases they grow obliquely, indicating the presence of in-plane shear stress.
5. A large MSD cluster and uniform crack lengths result in a relatively short period between the first link-up and the development of a linked crack across the full frame bay. On the other hand, either small uniform clusters or non-uniform cracks will result in a relatively long growth period after the first link-up.

The mechanism of link-up involves a complex pattern of plastic deformation and necking across the full width of the ligament prior to fracture. Eastaugh et al. [2] studied this mechanism in their simple specimen tests and did not observe fast fracture prior to yielding. Link-up occurred at small crack separations of 1.5 to 4.5 mm, and the size of the final ligament prior to link-up increased with crack size. Molent and Jones [21] found that link-up of MSD generally occurred when the distance between the adjacent crack tips was approximately 2 mm. During link-up, cracks may overlap, curve towards and eventually intersect the opposing crack. Crack link-up of long to short cracks exhibits less curvature.

2.4. Residual static strength

Due to fatigue cracks the residual strength of the structure degrades during the life of the aircraft, and more rapidly in the presence of WFD.

Broek [22] published a report on the residual strength behaviour of 2024-T3 alclad sheet panels. The failure scenarios for a lead crack and more small MSD cracks showed that small MSD cracks can significantly reduce the load for unstable crack extension. For single-crack panels, the data are well represented by a net section failure criterion, but for panels with central crack and MSD, there is a significant loss.

Nesterenko [23] presents test data on residual strength of various types of airframes with multiple-site fatigue cracks. He reports that residual strength is affected by structural design features, holes, component bending stresses, material plasticity, arrangement of multiple-site cracks and stable growth of cracks under single static loading. Structures with MSD fail when stress intensity factors are within a range from the plane-strain fracture toughness (K_{Ic}) to plane-stress fracture toughness and when net stresses are 30 to 90% of the yield stress.

Full-scale tests reveal that the presence of MSD adjacent to a lead crack reduces the residual strength by 15% [6].

3. Experimental work

This section is a synthesis of data obtained in the experimental work of IDMEC-FEUP in the context of the BRITE-EURAM 'SMAAC' project. Lap-joint specimens were supplied by Daimler–Benz Aerospace Airbus (DASA). The specimens were fatigue tested in an MTS, model 312.31, servo-hydraulic machine with a capacity of 250 kN. The fatigue crack initiation and propagation were measured with a travelling microscope. The post-mortem fracture surface analysis was done using scanning electronic microscopy (SEM). Some stress pattern analysis by thermal emission (SPATE) scans were done in order to assess the capability of this system to detect hidden cracks in the lap-joint.

3.1. Load conditions

The load for SPATE analysis is F_{med}=16 000 N, ΔF=28 000 N, σ_{max}=42 MPa, σ_{min}=2.8 MPa, $\Delta\sigma$=39.2 MPa and f=6 Hz. For the fatigue tests, F_{med}=38 720 N, ΔF=63 360 N, σ_{max}=100 MPa, σ_{min}=10 MPa, $\Delta\sigma$=90 MPa, and f=6 Hz.

3.2. Specimen geometry

The specimen geometry is presented in Fig. 2. Specimens #1 to #5 have two rows of rivets and specimens #6 to #10 have three rows of rivets.

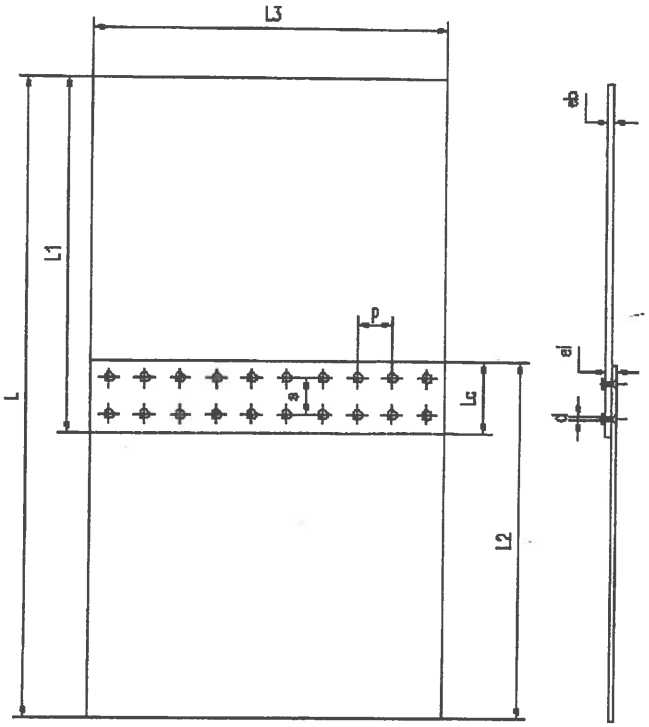

Number of rows	2	3
L	555	534
L1	299,5	300
L2	299,5	300
L3	440	440
Lc	44	66
ei	3,2	3,2
eb	1,6	1,6
Number of columns	20	20
p	22	22
s	22	22
d	4,8	4,8

Fig. 2. Specimen geometry, schematic representation (dimensions in mm).

3.3. Loading history

The loading history is summarized in Table 1.

There is an apparent relation between the specimen type and the critical row (it could be just a coincidence):

- the five specimens with three rows of rivets failed in the countersunk sheet,
- four of the specimens with two rows failed in the non-countersunk sheet.

The literature reports that there are two critical planes depending on the thickness of the sheets, the squeezing force, the type of rivet, etc. It is difficult to predict the critical row and to explain why.

For specimen #3 at 100 000 and 205 000 cycles, R=0.8 was used (instead of R=0.1), maintaining the maximum load constant, for 25 000 cycles, in order to

Table 1
Loading history[a]

Specimen	Critical row[b]	Initial defects[c]	N_{SPATE}	N_f	N_{i_f}	% N_{i-f}	$N_{1st\ link\text{-}up\_f}$[f]	$N_{1st\ link\text{-}up\_f}$[g]	% $N_{1st\ link\text{-}up}$[f]	% $N_{1st\ link\text{-}up}$[g]	Observations
#1	B		234000	257841							
#2	B			215034	10000	4.65	3034	6319	1.41	2.94	One lead crack starting at hole 8
#3	B			298737	63750	21.34	2085	162	0.70	0.05	3 MSD cracks, hole 9, hole 12, hole 13
#4	B	B		130000 [d]							
#5	A	B		399620 [d]	11542 [e]		6620 [h]	750 [i]	1.66	0.19	2 MSD cracks, hole 7, hole 15
#6	A			672277							
#7	A		560450	572000	22000	3.85					2 MSD cracks, hole 13, hole 20
#8	A			805450	95450	11.85	1051	4950	0.13	0.61	2 MSD cracks, hole 10, hole 13
#9	A	B		323350	26471	8.19		12350		3.82	One lead crack starting at hole 11
#10	A	B		237750	21750	9.15	2750	1150	1.16	0.48	One lead crack starting at hole 13

[a] Specimens #1 to #9 have two rows of rivets and specimens #6 to #10 have three rows of rivets. N_{SPATE} is the number of cycles under load for SPATE readings. N_f is the number of cycles, under fatigue test load conditions, to failure. N_{i-f} is the number of cycles between the initiation of the crack and the failure under fatigue test load conditions. % N_{i-f} is the percentage of number of cycles between the initiation of the crack and the failure, under fatigue test load conditions, in terms of the number of cycles to failure. $N_{1st\ link\text{-}up\_f}$ is the number of cycles, under fatigue test load conditions, between the 1st link-up and the failure under fatigue test load conditions. % $N_{1st\ link\text{-}up\_f}$ is the percentage of number of cycles between the 1st link-up and the failure, under fatigue test load conditions, in terms of the number of cycles to failure.

[b] Fig. 2 shows the location of the critical rows: row A in countersunk sheet and row B in the non-countersunk sheet.

[c] row containing initial (artificial) defects is presented.

[d] followed by residual strength test.

[e] between initiation and residual strength test.

[f] between visible cracks.

[g] between an internal crack and a visible crack.

[h] between 1st link-up (two visible cracks) and residual strength.

[i] between 1st link-up (visible and internal) and residual strength.

eventually mark the fatigue cracks. However, this attempt was unsuccessful. Schijve [3] reports that Wang [14] and Potter and Yee [15] got crack growth curves from striation-type markings. Willard [24] studied the fatigue crack propagation of hidden cracks in a full-scale fuselage article with marker bands. Every 10 000 cycles coded marker block loading sequences were used to mark the fracture surfaces of the fatigue cracks propagating within the panel. The loading sequences consisted of series of underloads combined with a series of full pressurisation. The combination of loads and underloads marked the fracture surfaces with marker bands that could later be used to reconstruct the fatigue crack growth history of selected regions within the test article.

A selection of the most important results is presented.

3.4. Loading and stress distribution

Within a splice, load is transferred from one sheet to the other mainly through rivet shear, but also through friction between the sheets. The load transfer, the stress concentrations due to holes, and the bending give rise to a complex stress distribution as illustrated in Fig. 3. This is a SPATE image which gives the first stress invariant. The legend contains the stress in MPa. The regions of low stress between the rivets result from out-of plane bending, and the associated contours suggest that the bending stress is greatest along a line roughly tangential to the rivet holes.

It is difficult to measure the stress distribution within a splice. SPATE images only indicate the first stress invariant. Therefore, strain gauges are also used. These are placed on both sides of a sheet, to distinguish between traction and bending stresses, at 21 mm from the rivet row. Plotting the remote stress vs σ_t (traction stress) and σ_b (bending stress), Figs. 4 and 5, for the loads used in the calibration, the bending component is higher for specimens with two rows of rivets (#5) than for specimens with three rows of rivets (#6). The bending ratio (bending stress/traction stress) is 0.32 for specimens with two rows and 0.18 for specimens with three rows, for a remote stress of 100 MPa.

The strain gauge analysis suggested that there are various contributions to the specimen behaviour as illus-

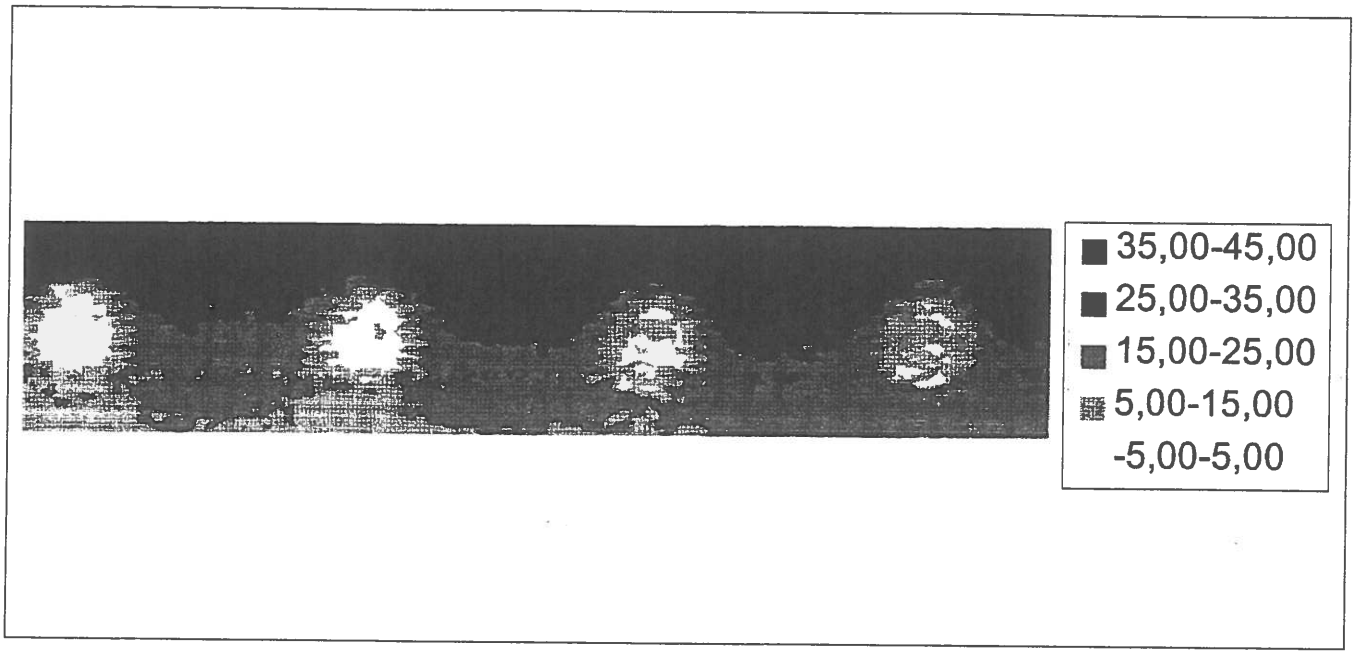

Fig. 3. SPATE image.

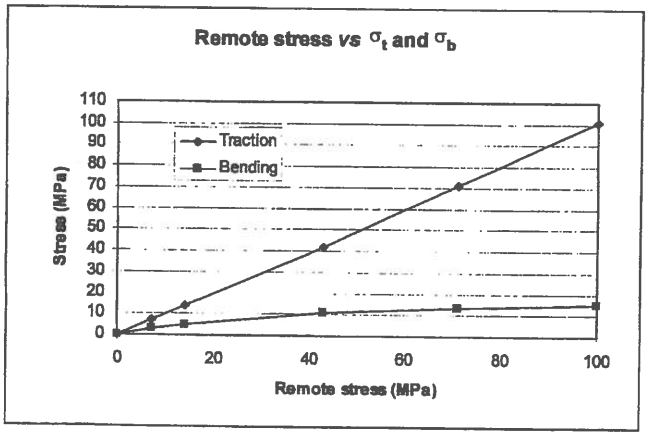

Fig. 4. Remote stress vs σ_t and σ_b, specimen #6 (with three rows of rivets).

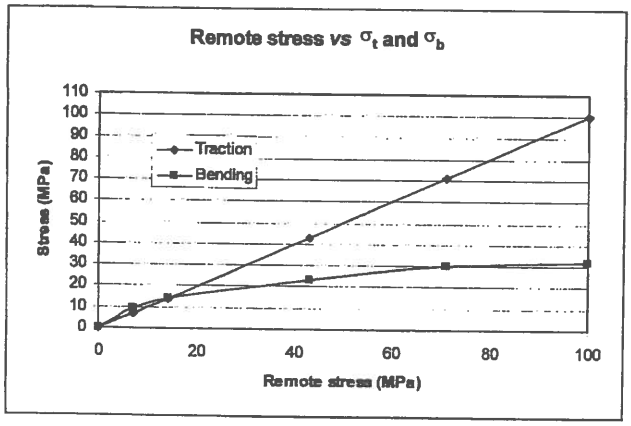

Fig. 5. Remote stress vs σ_t and σ_b, specimen #5 (with two rows of rivets).

trated in Fig. 6. Three contributions must be taken into account:

1. the irregular stress distribution applied remotely,
2. the bending stress due to the eccentricity of the lap-joint,
3. the bending stress due to the twist of the specimen.

According to the literature [2], the stress distribution in the immediate vicinity of a rivet hole is the result of several superimposed loading conditions, which were already mentioned in the second section of this paper.

3.5. Fatigue crack growth

The general characteristics of crack growth described in the Crack growth subsection of the Literature review above were also found in our study.

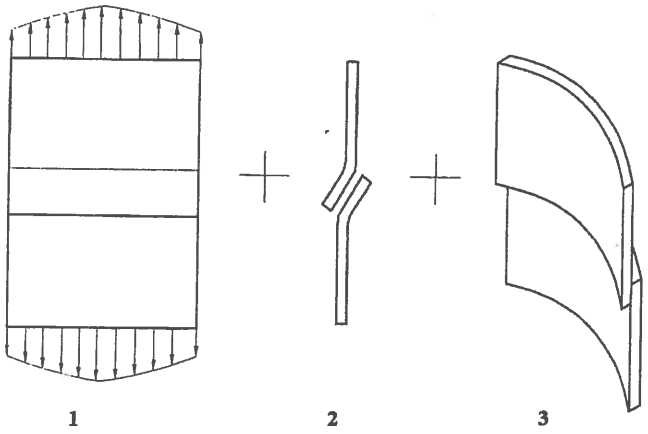

Fig. 6. Various contributions to the phenomenon.

All fatigue cracks initiated at the rivet hole horizontal centreline or in the upper half of the rivet row. Cracks grow longitudinally, along the rivet row, in most cases. In some cases they grow obliquely, indicating the presence of in-plane shear stress. In either case, cracks that have overlapped generally curve towards and eventually intersect the opposing crack (see specimen #5 at 393 000 cycles between holes 7 and 8, Fig. 7). Crack link-up of long to short cracks exhibited less curvature (see specimen #8 at 804 399 cycles between holes 11 and 12, Fig. 8).

Clusters of cracks or a single crack develop. The cracks may be uniform or non-uniform to various degrees. The cluster may be broad (see specimen #3, Fig. 9), i.e. separated by three holes, or narrow, i.e. separated by one or two holes (most of the specimens).

Eventually two adjacent cracks link-up to form a lead crack. This lead crack grows faster than other unlinked cracks, and tends to dominate subsequent crack growth. The link-up of the remaining cracks and uncracked holes proceeds one ligament at a time until there is a linked crack spanning most of the specimen. A good example is specimen #10, Fig. 10.

The combination of a large MSD cluster and uniform crack lengths results in a relatively short period between the first link-up and the development of a linked crack across the full frame-bay. This situation is well illustrated by the behaviour of specimen #3. On the other hand, either small uniform clusters or non-uniform cracks will result in a relatively long growth period after first link-up. This is the case of specimens #2 and #9 (see Table 1).

The mechanism of link-up involves a complex pattern of plastic deformation and necking across the full width of the ligament prior to fracture. Fast fracture prior to yielding was not observed. Link-up occurred at fairly small crack separation and the size of the final ligament prior to link-up increased with crack size.

The following mechanism of link-up (Fig. 11), based on SEM results, is suggested:

(i) initiation of a fatigue crack at a rivet hole,
(ii) by fatigue, this crack grows until it reaches the outer surface,
(iii) another crack initiates at the next rivet, smaller than the first crack and not visible,
(iv) the two cracks grow by fatigue and the one that was not visible shows up suddenly and links with the visible one.

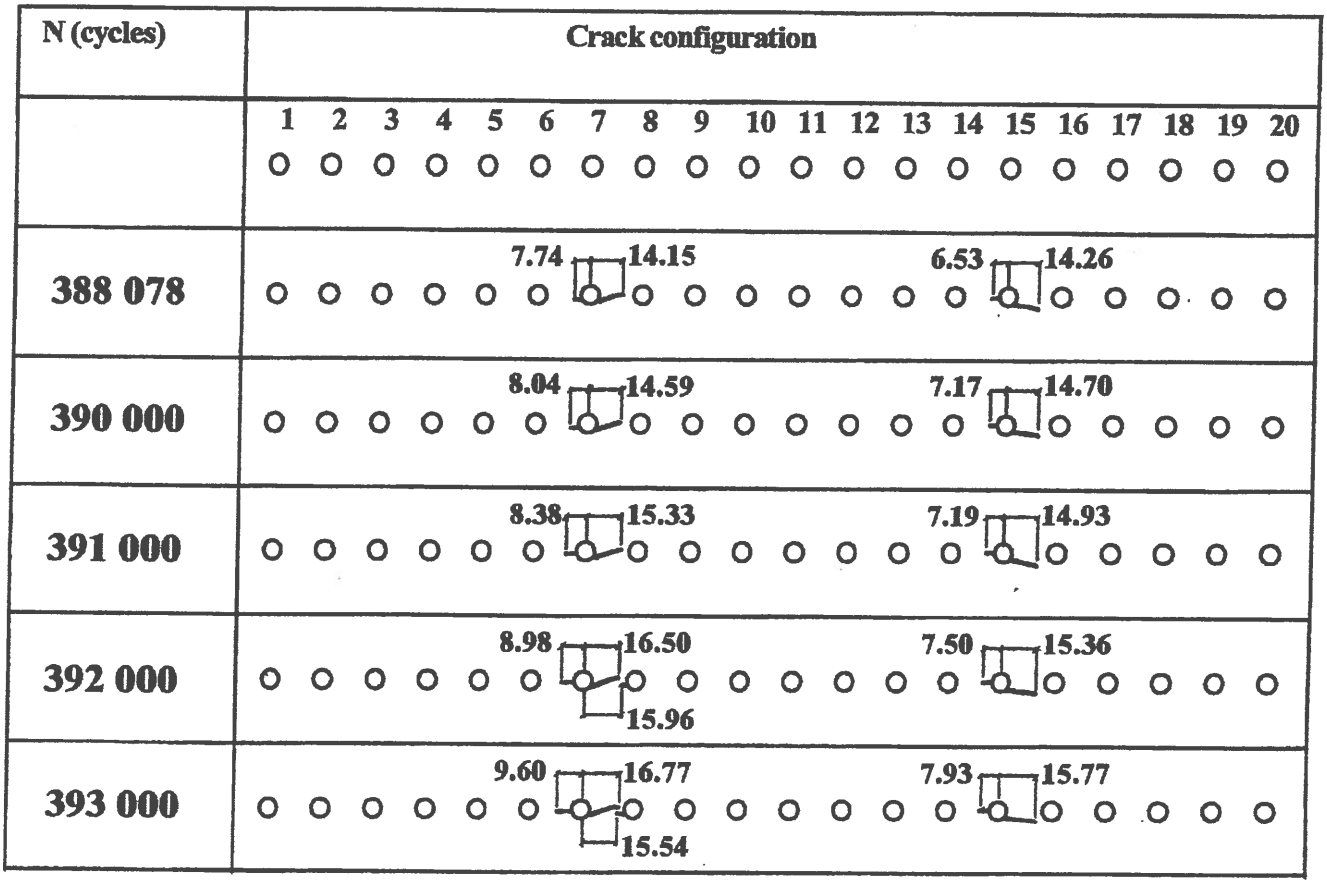

Fig. 7. Cracks that have overlapped generally curve towards and eventually intersect the opposing crack (specimen #5).

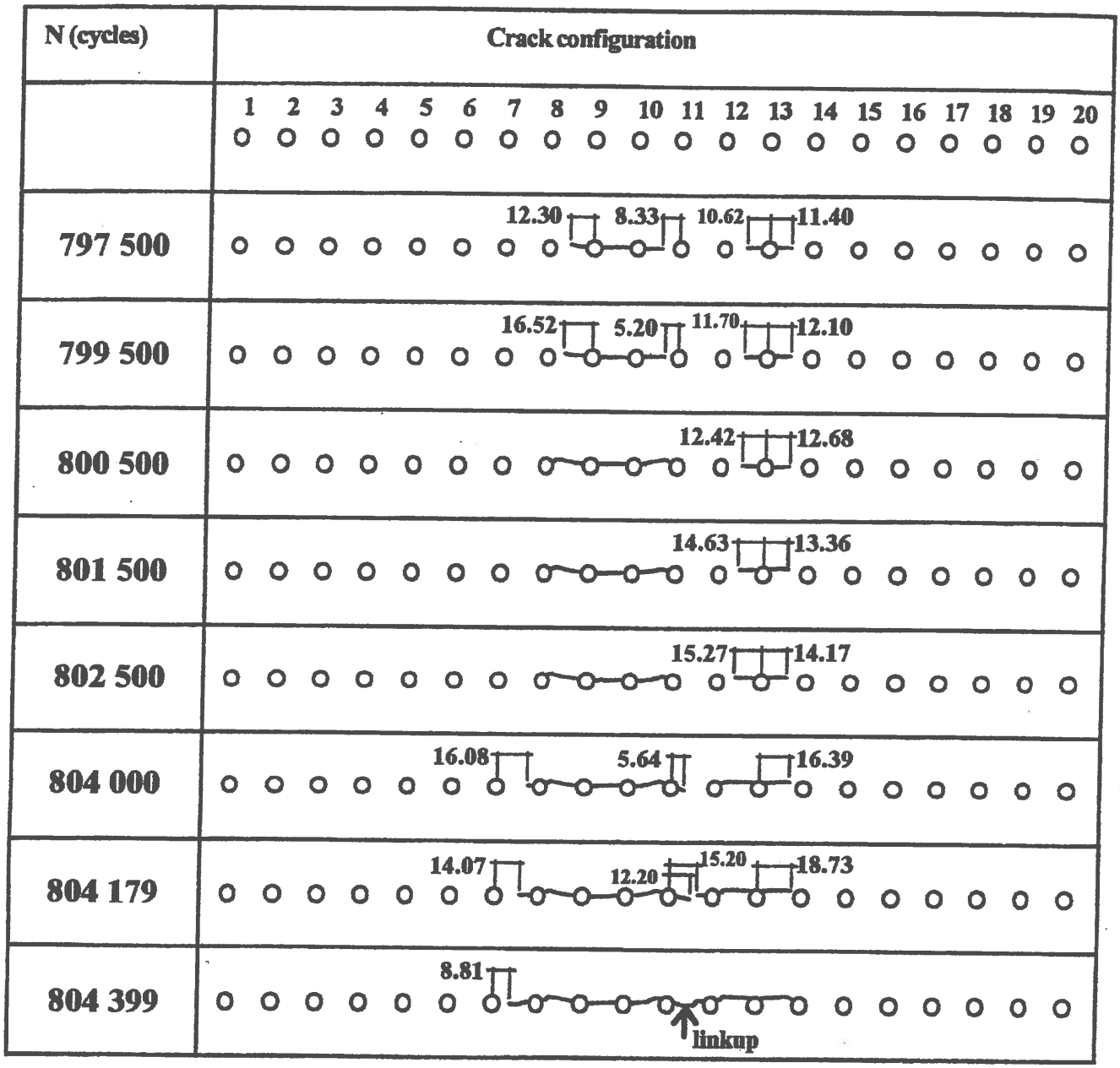

Fig. 8. Crack link-up of long to short cracks exhibited less curvature (specimen #8).

The variation in the fatigue lives of the specimens was partially due to the nature of the cracking. In general, the shortest life occurred when the largest cracks grew towards each other from adjacent fastener holes. A longer life occurred when cracks initiated and grew from widely separated holes.

In each case the number of cycles required to achieve initial failure did not differ significantly from that to final failure of the specimen (see Table 1). In fact the percentage of the number of cycles between the first visible crack and failure varies from 4% for specimen #7 to 20% for specimen #3.

3.6. Residual static strength

The first three specimens were subjected to a fatigue test until failure under σ_{max}=100 MPa. Thus, it is clear that the residual strength for these specimens is 100 MPa. A travelling microscope was set up to measure the crack growth. The initiation of the cracks took place inside the joint so that the measurements correspond to the crack propagation once it reaches the outer surface. A multi-site crack configuration was verified. An SEM analysis of the fracture surface enabled us to estimate the total non-resistant area (fatigue plus rivet holes)

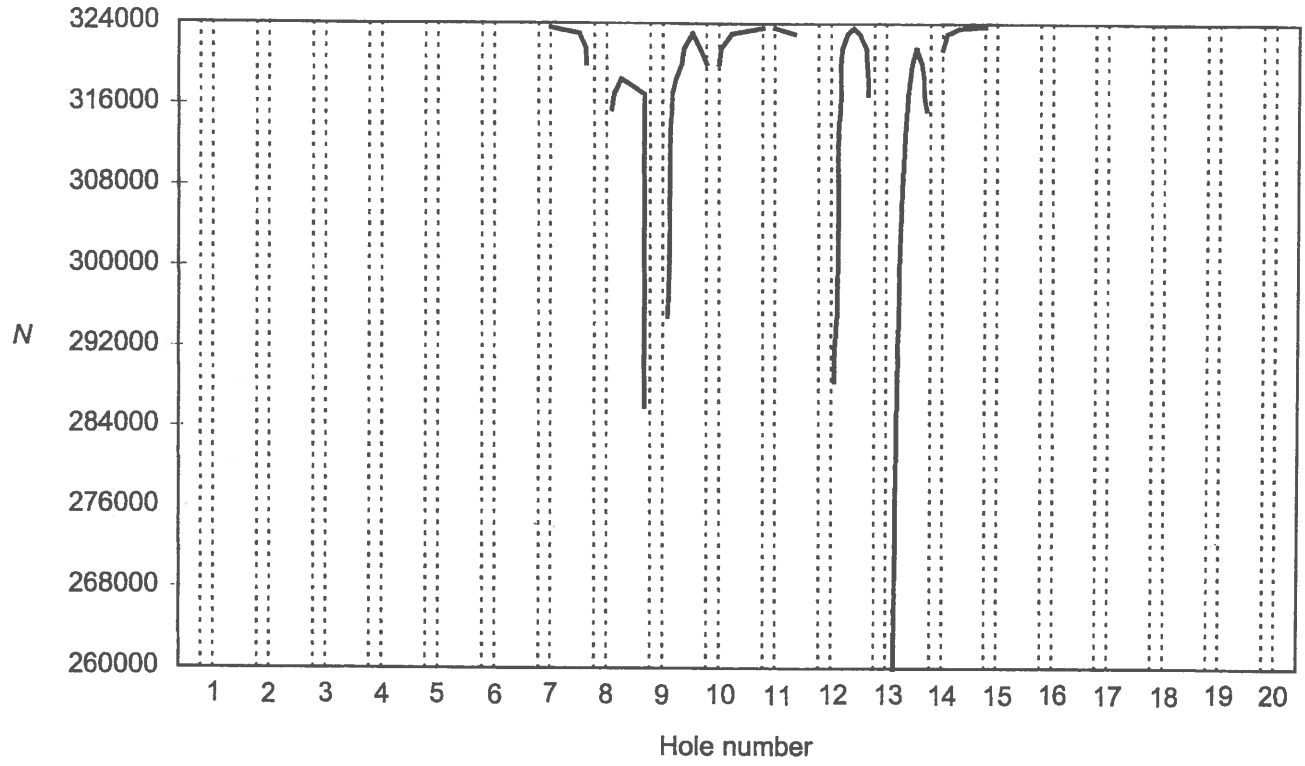

Fig. 9. Crack growth (the lines are the crack lengths) in the whole specimen (specimen #3).

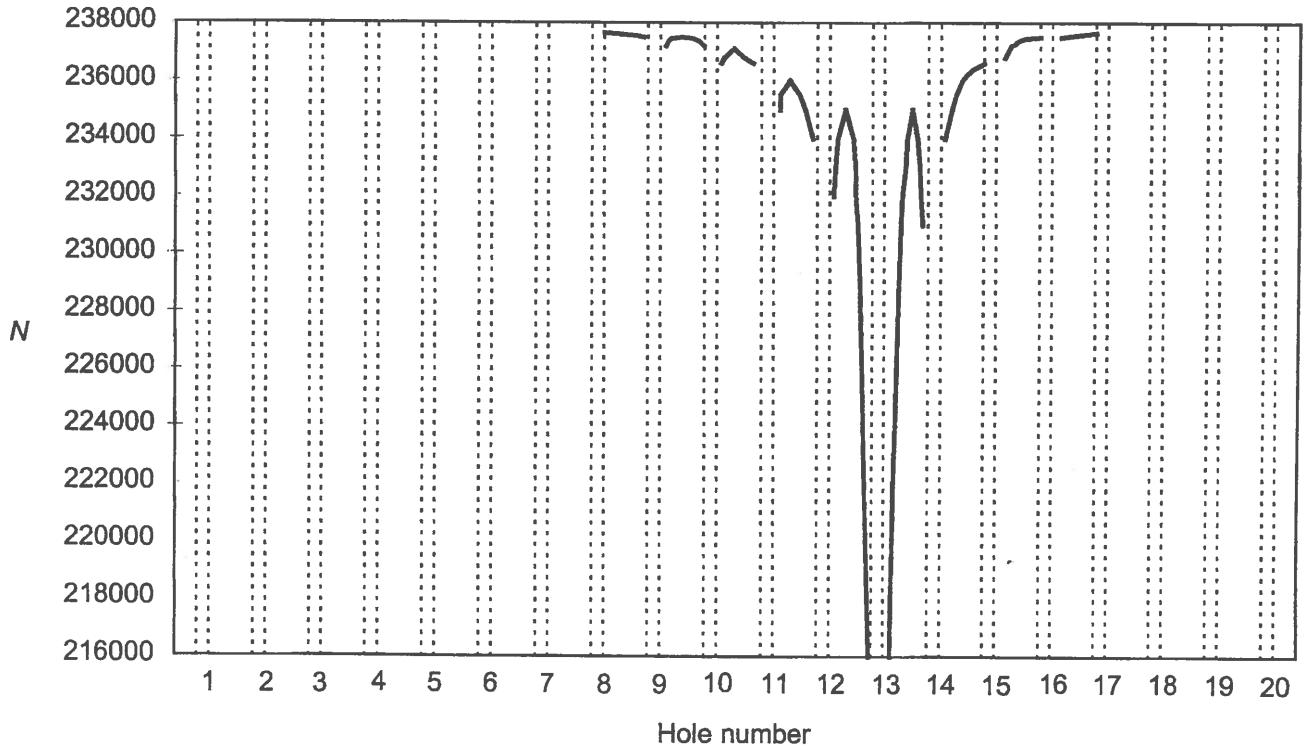

Fig. 10. Crack growth (the lines are the crack lengths) in the whole specimen (specimen #10).

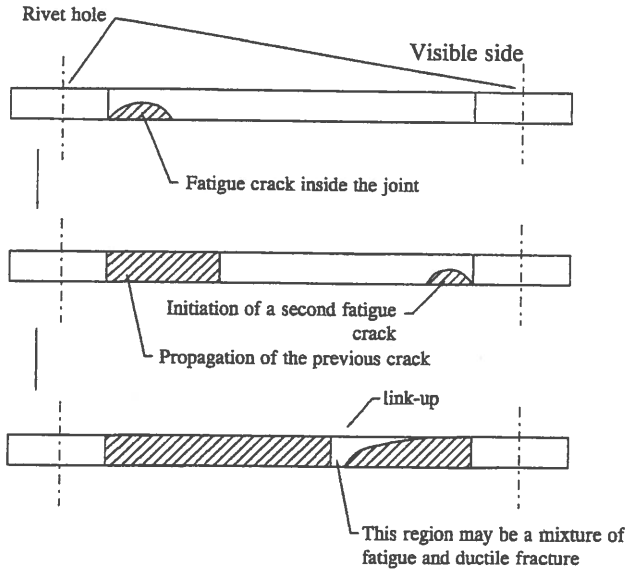

Fig. 11. Suggested mechanism of link-up.

when the specimens failed. Two techniques were used: image processing and precise weighing. The results of the two techniques proved to be similar.

Specimen #4 was subjected to 50% of the mean N_f (number of cycles corresponding to failure), based on the first three specimens which is about 260 000 cycles. Stopping the cyclic loading after 50% of 260 000 cycles was thought to be enough to guarantee the presence of fatigue cracking. However, the SEM analysis proved the opposite. Nevertheless, it was possible to detect the presence of initial defects, representing 2.3% of the total area. The total non-resistant area is 25% of the total area. The static loading of the specimen #4 gave a residual strength of 241 MPa.

Specimen #5 was fatigue tested under the same loading conditions. After extensive propagation of cracks (visible cracks), the specimen was statically loaded. The residual strength is 139 MPa. The total non-resistant area was estimated only by the image processing of the fracture surface obtained by the SEM analysis.

Let us consider (Fig. 12) the residual strength vs crack size for specimens #1, #2, #3, #4 and #5, with a net stress equal to the yield strength of the material 2024-T3, σ_{net}=296 MPa, and a net stress equal to $\sigma_{net}=(\sigma_t+\sigma_y)/2$=361 MPa (material characterisation tests were undertaken in our laboratory). The presence of fatigue cracking drastically reduce the residual strength.

3.7. Fracture surface

Cracks typically initiate at hidden locations, at the edge of a rivet hole, or at the faying surface of the sheets. Fatigue crack initiation occurs in regions of high stress concentration located at or near rivet holes. It can be at rivet hole corners, or at abraded (fretted) surfaces [12].

The MSD cracks are hidden for 80% (specimen #3) to 96% (specimen #7) of the total fatigue life (see Table 1).

The scanning electron micrographs shown in Fig. 13 illustrate the typical transgranular morphology and location of fatigue cracks observed in the countersunk and non-countersunk sheets.

Fig. 14 shows the fracture morphology of fatigue cracks (situated in the countersunk sheet) at different stages of propagation. From Fig. 14b, 14c and 14d, a pattern of fatigue crack propagation has been derived as illustrated in Fig. 14a. These results show that cracks initiate at the interface and propagate in the subsurface manner depicted in Fig. 14a.

Complex loading during fatigue cracking was noted by scratches on the fracture surface (specimens #8, #9 and #10) oriented transverse to the direction of the crack propagation. This was verified for a relatively long crack length. Presumably, out-of-plane motion of the upper portion of the fracture surface occurred. Piascik et al. [12] also observed this phenomenon. This motion rubbed the mating fracture surfaces, forming the transverse scratches. Based in fractographic analysis, significant out-of-plane (Mode III) motion is likely only when cracks are long and no longer captured by the rivets heads.

Figs. 13c and 14 suggest that crack initiation is associated with localised damage due to fretting. Evidence of fretting fatigue was noted by a black oxide deposit on the mating surface around each rivet hole.

On the fracture surface of many fatigue cracks, ridges and several crack initiation nuclei were observed. It seemed as if one crack was composed of several cracks that were initiated and had grown on different levels independently of each other. van der Hoeven and Schra [25] observed this and report that during a later stage of the fatigue test, the individual cracks must probably coalesce by static failure of the bridges between cracks.

The SEM analysis proved the presence of three different mechanisms of fracture (see, for example, specimen #3, Figs. 15 and 16): ductile fracture, fatigue and a mixture of ductile and fatigue fracture.

In addition, fatigue striations in the clad layer imply a mixture of ductile and fatigue fracture in the middle part of the sample. The striations in the cladding are very near the fatigue cracks. As the striations go far from the fatigue cracks, the distance between striations becomes larger.

4. Finite element analysis

The FRANC2D/L finite element program was used. This is an extension of FRANC2D, which was originally written by Paul Wawrzynek at Cornell University for the analysis of crack growth. At present, Kansas State University is being funded by NASA, as part of the

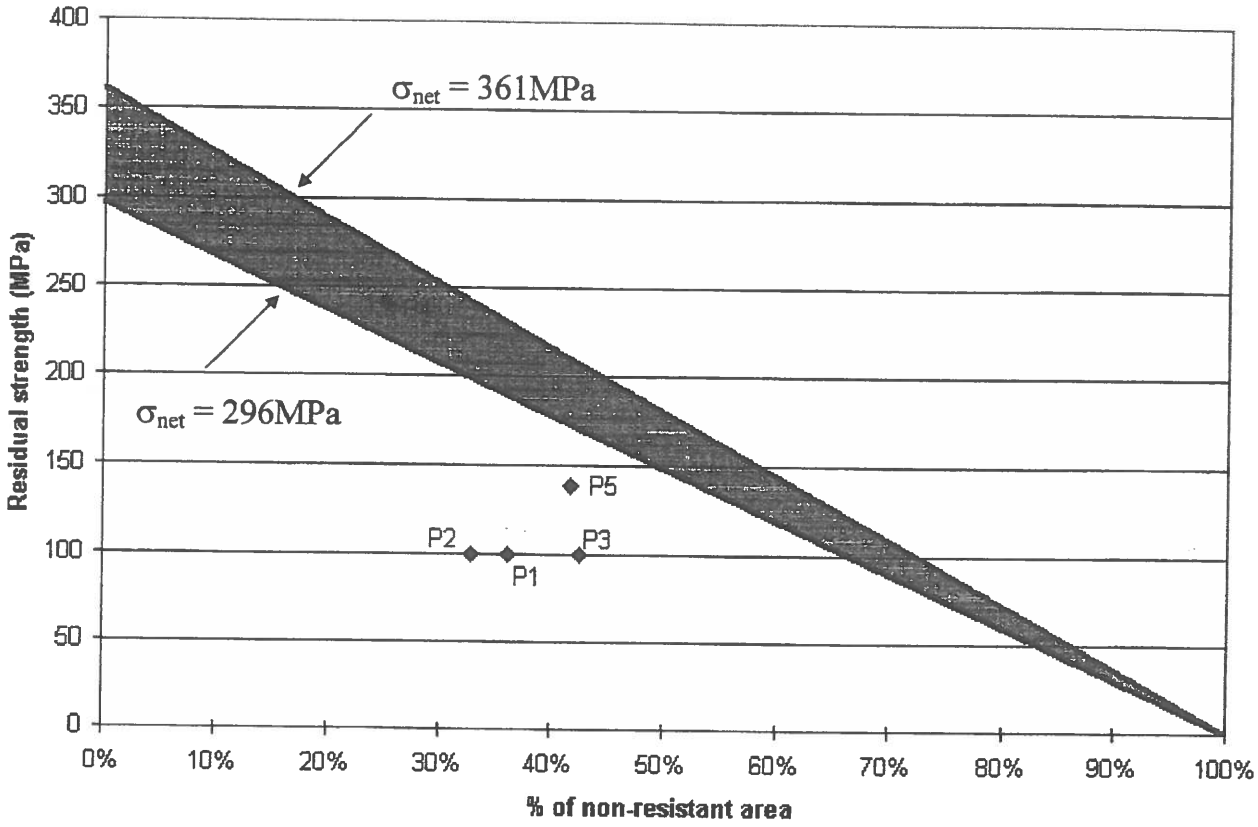

Fig. 12. Residual strength with σ_{net} = yield strength (296 MPa), and $\sigma_{net} = \frac{\sigma_t+\sigma_y}{2}$ (361 MPa).

Aging Aircraft Program, to extend the code to simulate crack growth in layered structures.

FRANC2D/L is a finite element program for the small deformation analysis of two-dimensional structures. As such, the lap-joint is modelled in two dimensions, without considering the bending effect. Linear elastic fracture mechanics (LEFM) analyses can be performed with automatic re-meshing as the crack grows. The layered capability allows the user to model riveted and adhesively bonded structures, such as lap-joints and bonded repairs.

It was decided to model crack growth during the fatigue test carried out in specimen #3, particularly crack growth between 295 000 and 318 500 cycles. Initiation of cracks (in left or right sides) of rivets is taken as the first visual observation of a crack.

The test for the problem of residual strength corresponds to specimen #5. Maximum load is to be determined. The data are analysed by three procedures:

1. the net section plastic collapse approach: $\sigma=\sigma_y(1-X)$, where X is the 'total cracked area' divided by 'total cross-section area' (total cross-section area does not include rivet holes),
2. the failure criterion for a plane strain structure: $K \geq K_{Ic}$,
3. the R-curve.

4.1. MSD crack growth

Data used for this exercise are $C=5.3\times10^{-8}$, $n=3.335$ (Paris law with da/dN in mm/cycle and ΔK in MPa $m^{1/2}$), obtained by the present authors. $E=75$ GPa and $\nu=0.32$.

In FRANC2D/L simplifying assumptions are made which still allow us to capture the essential features of the response. The assumptions include:

- Each layer is considered as an individual two-dimensional structure under a state of plane-stress or plane-strain condition.
- Individual layers are connected with rivets.
- A rivet is treated as an elastic shear spring between two nodes of each layer.

The stiffness of the spring elements is available from empirically based formulae, such as those published by Swift [26].

The algorithm to determine the crack propagation, based on the Paris law, is described in Fig. 17. The algorithm in Fig. 17 is designated as the cycle-by-cycle summation technique, best suited for incorporation with crack growth interaction models to account for load interactions effects.

Fig. 18 compares the experimental results with the FRANC2D/L prediction. The analysis is done only until

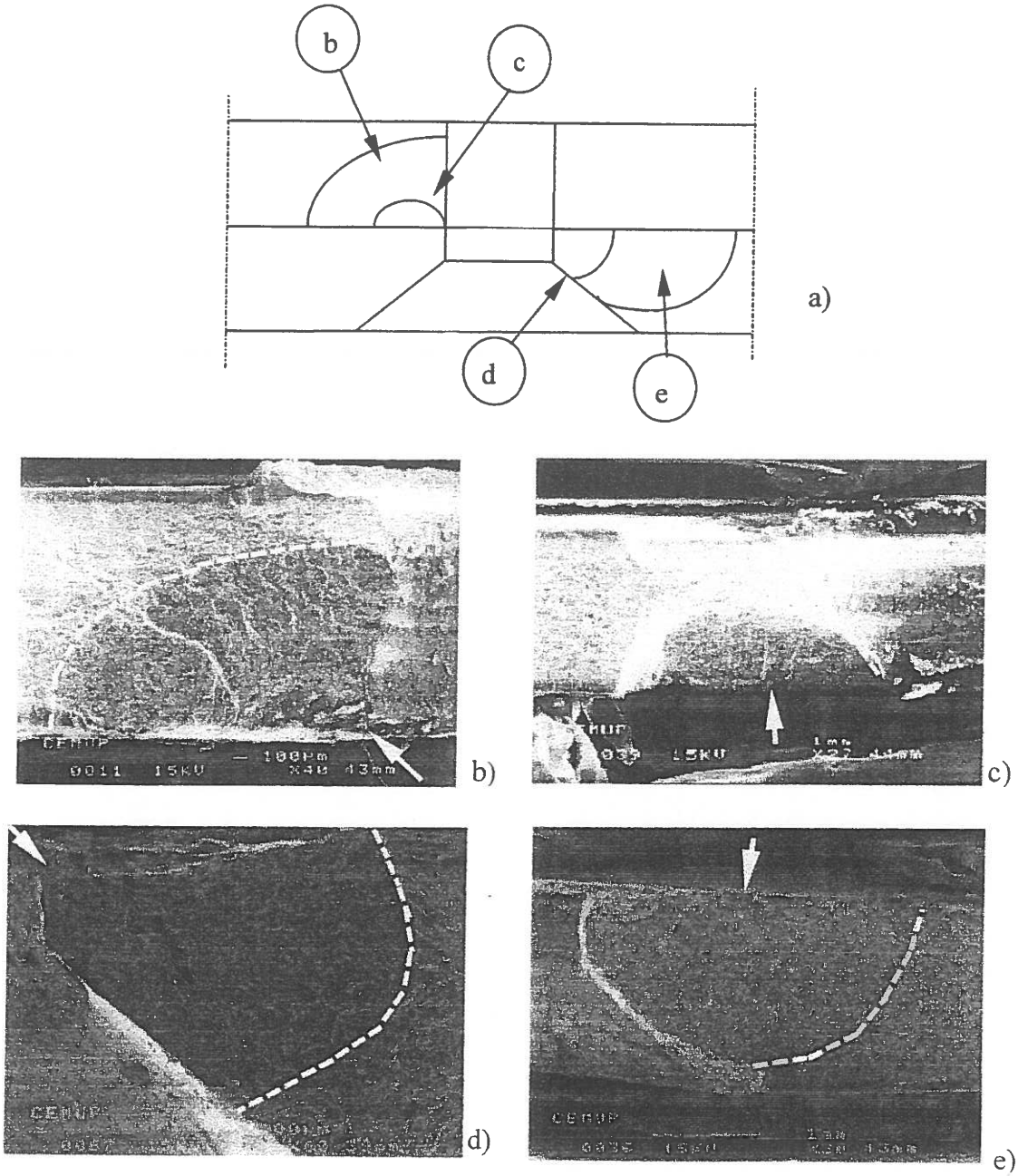

Fig. 13. Schematic and scanning electron micrographs showing the location of fatigue cracking, crack initiation site (arrows) and fracture morphology of fatigue cracks.

315 500 cycles so the problem of the interaction of two cracks is not treated. An attempt was made to include the interaction effects, but FRANC2D/L could not remesh the situation of two very close crack tips.

The first comment on the results is the fact that there is good agreement between the experimentation and the prediction of FRANC2D/L. The exception is the right crack of hole 9. There are many factors which can explain this:

- First of all, the experimental readings of the crack propagation are affected by an error that is difficult to assess. The travelling microscope measurements are dependent on the operator.
- Another point is the fact that as the crack grows, internal cracks can develop which have an evident influence on the stress distribution on the crack tips. This fact is ignored in the FRANC2D/L analysis.
- The rivets are treated as spring elements, a simplification that has its limitations. The problem is in fact closer to a lap-joint fastened by welded points than to a riveted lap-joint. The typical stress distribution of a hole is not considered.
- FRANC2D/L allows only a 2D model of a joint, so

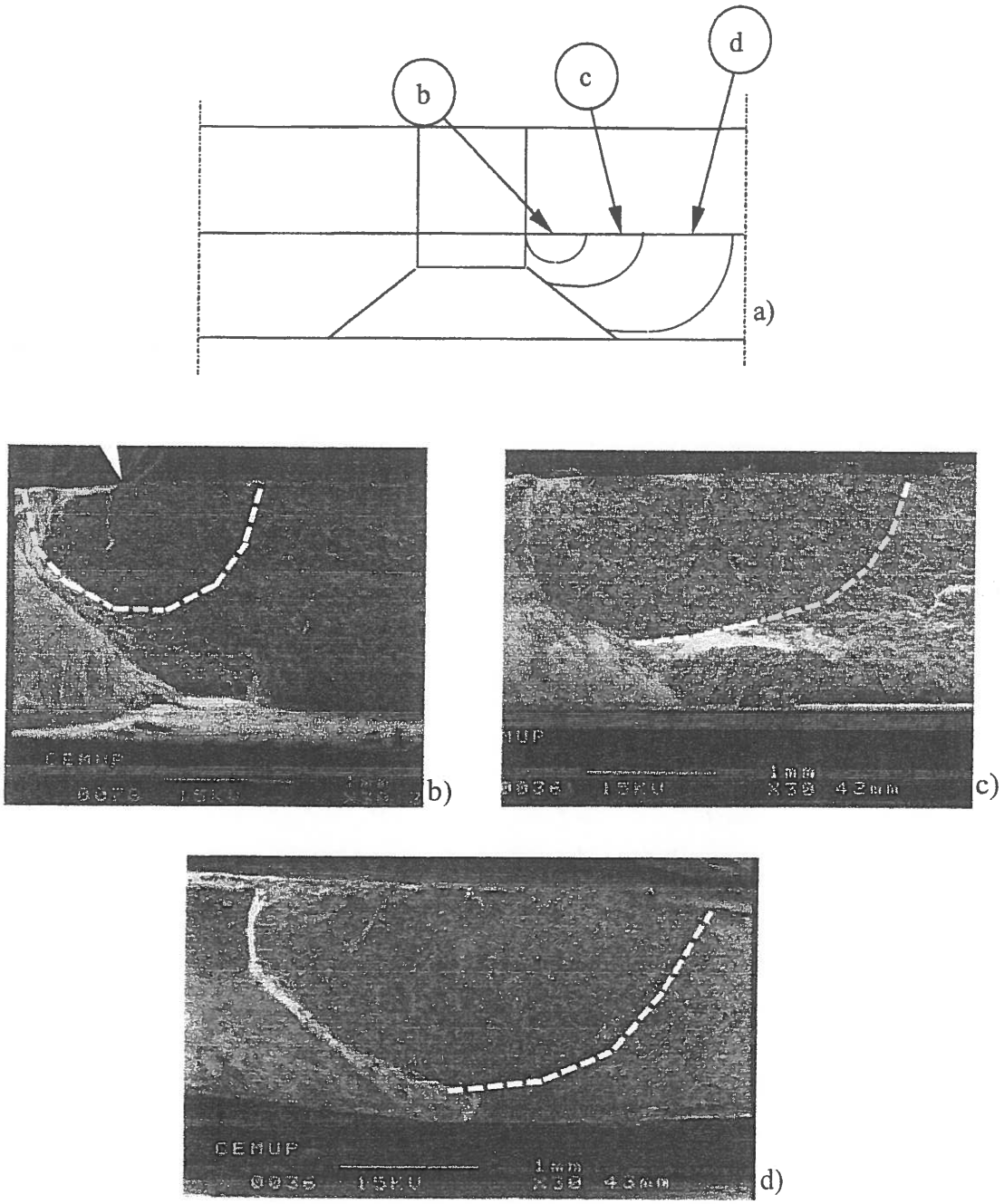

Fig. 14. Schematic and scanning electron micrographs illustrating the location of fatigue crack initiation (arrows) and sequence of crack propagation in the countersunk sheet.

the secondary bending stresses one expects in a typical lap-joint cannot be modelled. There is no doubt that a 2D model gives a very good indication of lap-joint stresses but there is still controversy about how important the bending stresses in the joint are—clearly they affect the detailed crack growth. Secondary bending may not be required for an overview of the stresses, and consequent fatigue life or strength. But detailed modelling of crack growth—crack positions and crack linkage—will not be accurate without the secondary bending.

- The last point is about the remote stress distribution. Since the specimen support is not infinitely rigid, the load is not exactly constant along the edge of the specimen, and it probably has some influence on the crack propagation.

4.2. MSD residual strength

The prediction of the net section collapse does not need finite element analysis. It is based upon the use of

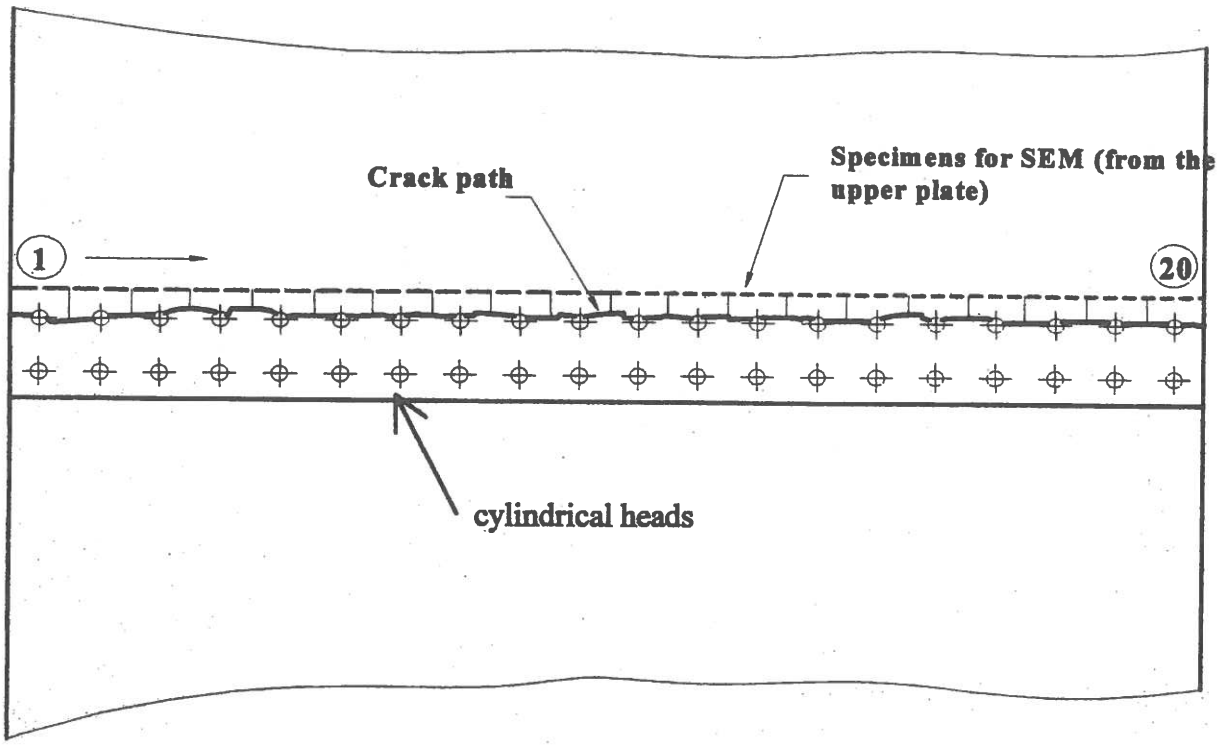

Fig. 15. Fracture path and samples for SEM examination, specimen #3.

$\sigma=\sigma_y(1-X)$, where X is the 'total cracked area' divided by the 'total cross-section area'. Fig. 12 shows the results obtained. The specimen we are dealing with corresponds to the point P5. According to Fig. 12, the residual strength is around 170 MPa for σ_{net}=296 MPa and 210 MPa for σ_{net}=361 MPa. These values are well above the true residual strength of the specimen (139 MPa). The net section plastic collapse procedure is to be taken as just a rough estimation.

The failure criterion for plane strain fracture, $K \geq K_{Ic}$, is supposed to give a conservative failure load prediction since the fracture toughness in plane strain (K_{Ic}) is less than the true fracture toughness of the material. It is an approach which uses a single parameter (K) to predict the response of a crack to applied loads. Often, this parameter can be compared to a single material parameter (K_{Ic}), and reasonably accurate failure prediction can be made so long as plain strain condition is verified [27].

According to the Advisory Group for Aerospace Research and Development [28] (AGARD), K_{Ic} is 34 MPa $m^{1/2}$ for a thickness of 25.4 mm.

The next step is to determine the stress intensity factors in FRANC2D/L and use the maximum stress intensity factor. Supposing that LEFM is applicable, then we have: for σ=100 MPa, K_{max}=1486.0 MPa $mm^{1/2}$. For K_{Ic}=34 MPa $m^{1/2}$, the failure load is then $(100\times34)/(1486/1000^{1/2})$=72.4 MPa. This value is well below the true failure load of the specimen, as we expected.

The failure criterion for plane strain condition is not valid for the case of thin metal sheet structures. The existence of extensive slow stable growth (under monotonic loading) prior to instability and catastrophic failure results in a significant complication. Here, rather than a single material parameter, a material curve (R-curve or K_r) representing essentially an infinity of points is apparently necessary to make an accurate failure prediction. Not only is the necessary input information more extensive, but the actual failure prediction is more complex due to the presence of an unknown in addition to the failure load. The crack length (or alternatively the stress intensity factor) at instability is not known a priori. Thus, rather than the single failure criterion for plane strain condition, two criteria must be satisfied in structures for which a significant amount of slow stable growth takes place [27]:

$$K \geq K_r \text{ and } \frac{\partial K}{\partial a} \geq \frac{\partial K_r}{\partial a}$$

The R-curve in terms of stress intensity factors is described by Ewalds and Wanhill [29].

The data for this problem consist of the R-curve of the material and the geometry of the specimen. The equation of the R-curve, obtained by DASA in the 'TL' direction, is $K=18.08\Delta a^{0.52}-0.51\Delta a+21.49$ with K in MPa $m^{1/2}$ and Δa in mm.

Due to the complex geometry there is not a crack driving force curve available. Thus, an iterative process is needed which involves the R-curve and the determi-

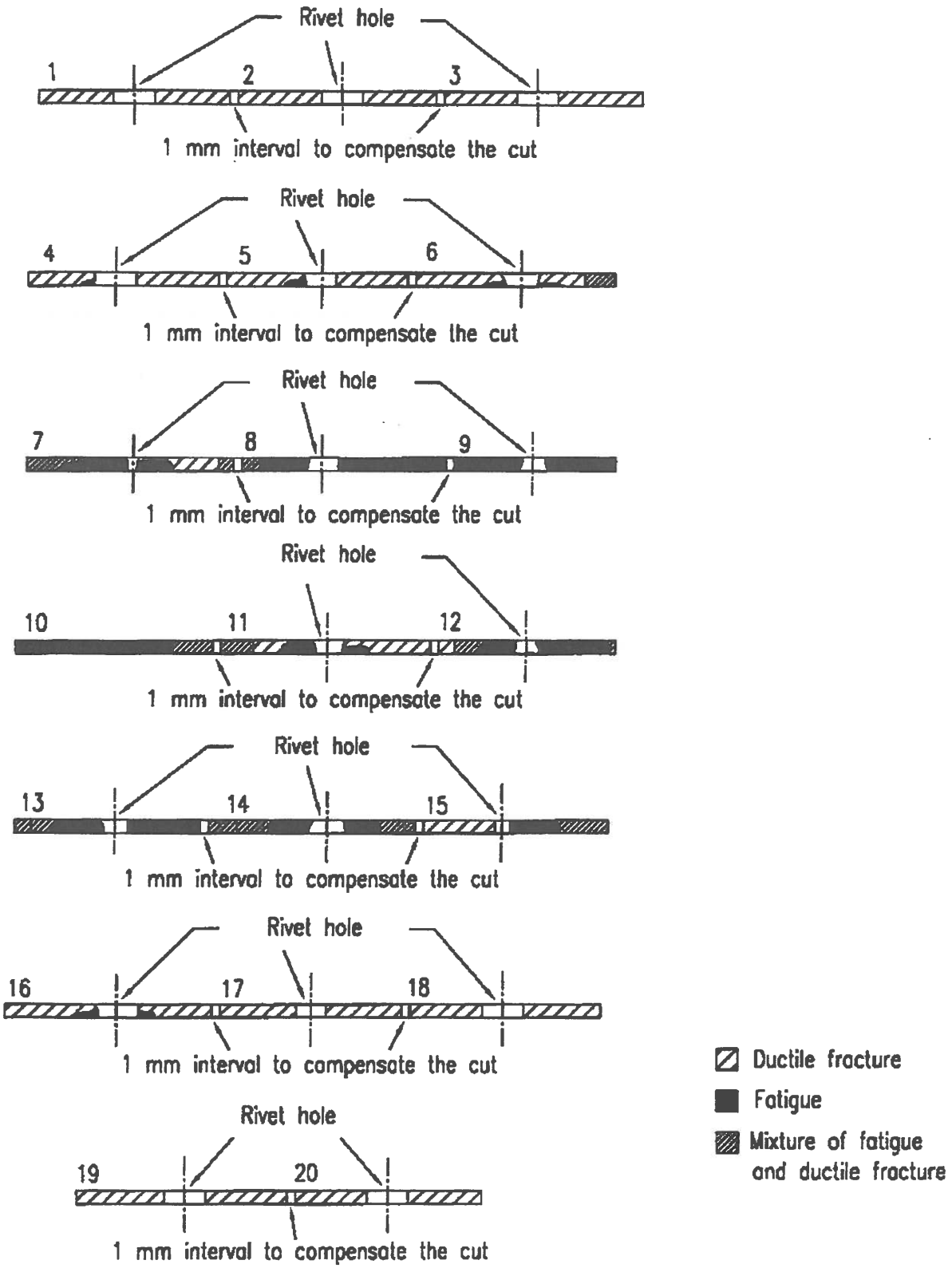

Fig. 16. Fracture surface, specimen #3. The vertical lines in the regions of mixture of fatigue and ductile fracture correspond to a change in the orientation of striations in the clad layer.

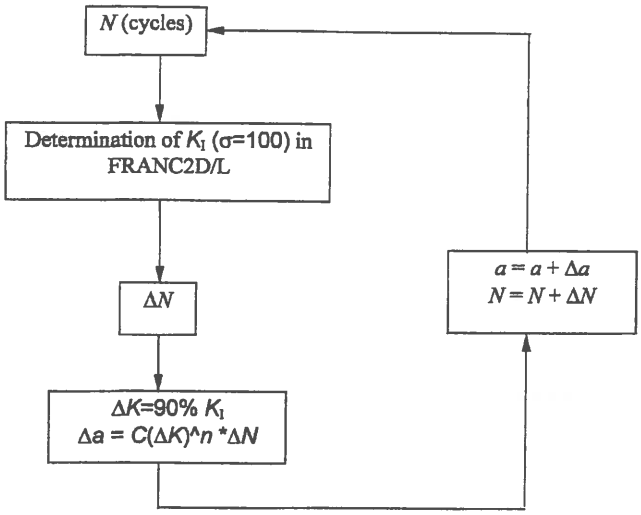

Fig. 17. Algorithm for the crack propagation.

nation of the stress intensity factors in FRANC2D/L. The iterative procedure is described in Fig. 19.

Yet there is still one question to solve. Which is the criterion to stop the algorithm?

The link-up of two cracks may be modelled using the Swift model. The basic concept is that the residual strength in the presence of MSD depends on the criterion that an MSD crack will be absorbed by the main crack when their two plastic zones meet, and the ligament then fails by collapse [30], Fig. 20.

The present case is more complicated. There is a main crack from hole 10 to hole 6 but the presence of the rivets has a strong effect on the crack propagation. The

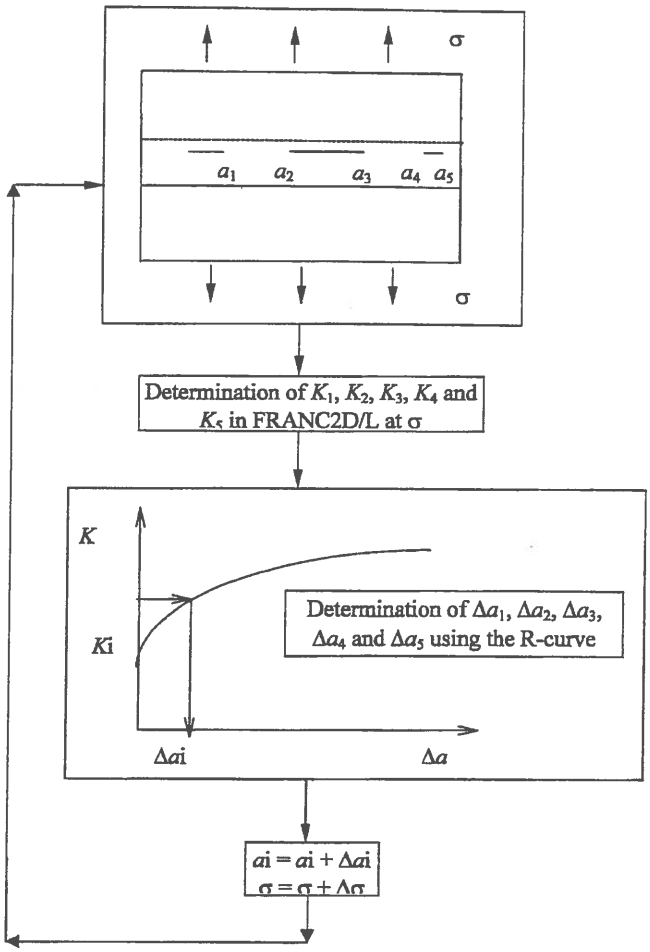

Fig. 19. Algorithm for the prediction of the slow stable crack growth.

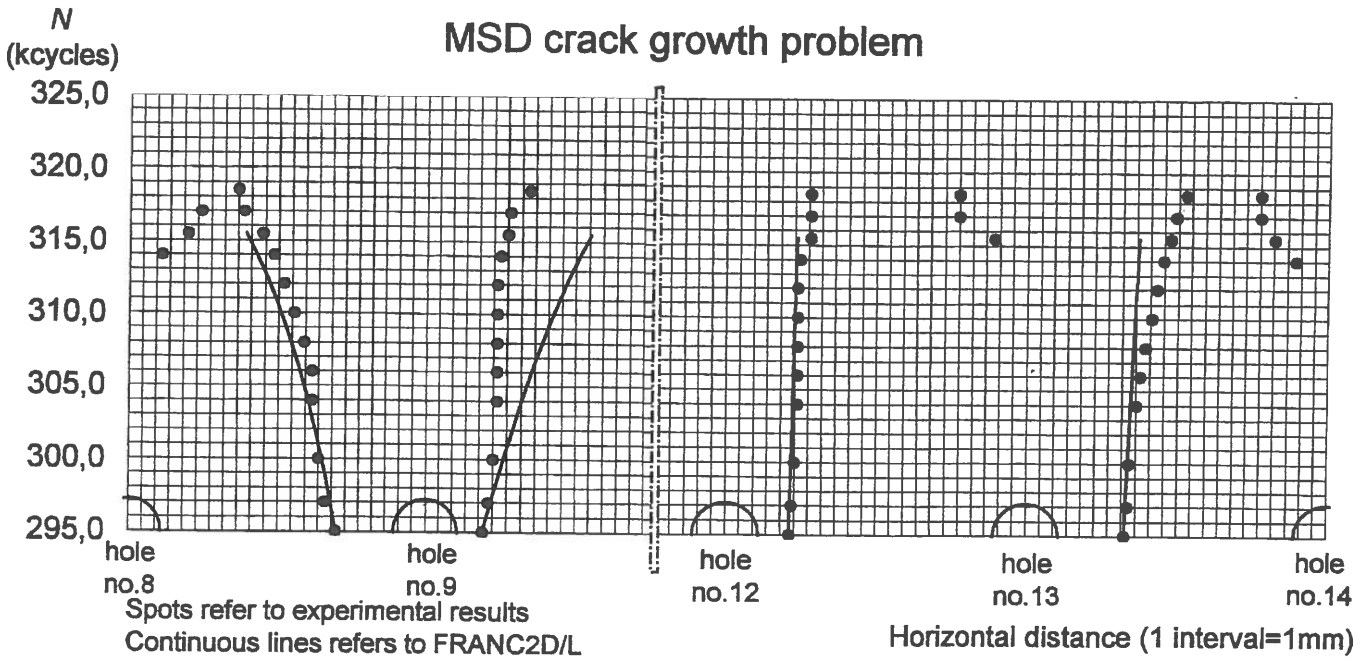

Fig. 18. Comparison of experimental and analytical data.

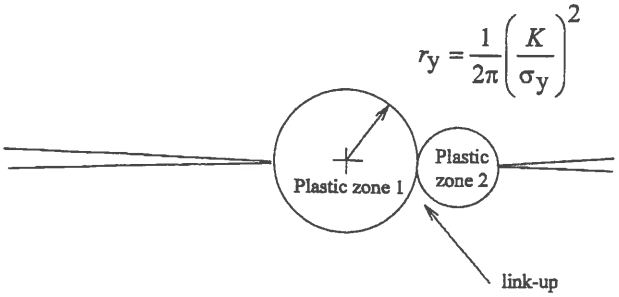

Fig. 20. The link-up criterion [30].

procedure described in Fig. 19 is valid until cracks reach a rivet, Fig. 21.

Two interpretations are possible:

1. apply the algorithm until a crack reaches a rivet and then use the net section plastic collapse criterion, or
2. use directly the net section plastic collapse criterion assuming that the cracks first grew until the next rivet.

The first possibility implies that after one crack meets a rivet, there is no more stable growth of the cracks and the specimen collapses.

For σ=100 MPa, the maximum value of K is 1486 MPa mm$^{1/2}$ or 47 MPa m$^{1/2}$. From the R-curve equation K_o (the point of initial crack extension) is approximately 30 MPa m$^{1/2}$. Supposing LEFM, the crack will start to propagate at 63 MPa. The first iteration starts with 63 MPa.

Table 2 summarises the results obtained for each crack tip. The R-curve gives Δa effective which means Δa physical plus the plastic zone. Therefore, there is no need to calculate r_y.

There is stable crack growth only for the main crack (tip 3 and 4). The dimensions of the other two smaller cracks remain constant since the stress intensity factor is below K_o. At σ=98 MPa, the dimension of the crack from hole 6 ($a+\Delta a_{ef}$=19.66 mm>19.6 mm) is big enough to meet hole 5. There is a link-up between crack tip 3 and hole 5.

Next the net section plastic collapse is applied considering the crack sizes indicated in Table 2 in bold (iteration 8), Fig. 22.

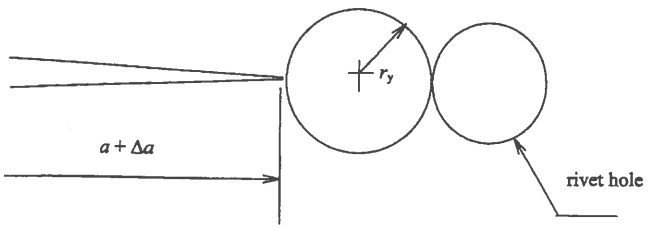

Fig. 21. Link-up between a crack and a rivet.

The criterion is $\sigma=\sigma_y(1-X)$, and it gives a failure load of 146 MPa. This result is very close to the measured residual strength (139 MPa). However, the procedure used is more an academic exercise than a rigorous method of prediction; perhaps the very good result is no more than coincidence. The interpretation is very questionable and must be analysed carefully. The model in FRANC2D/L is subjected to many simplifications. The problem is treated in 2D, without bending. The shape of the cracks through the thickness and the internal cracks (see Fig. 16) are other aspects which have not be considered.

The second interpretation (use directly the net section plastic collapse criterion assuming that the cracks first grew until the next rivet) is very simple and does not need the use of the R-curve. The crack configuration is in this case described in Fig. 23:

The criterion is $\sigma=\sigma_y(1-X)$, and it gives a failure load of 121 MPa. This value is also not too bad so this interpretation is worth taking into account.

4.3. Discussion

As regards FRANC2D/L, the main advantages are:

- Each layer is considered as an individual two-dimensional structure
- Individual layers can be connected with rivets
- A crack mesh generation is very easy (one just needs to introduce two points)
- The determination of the stress intensity factors is also easy (just pick on the crack tip location on the mesh)
- Simulation of rivets by spring elements is very useful
- The analysis time is very short (10 sec)

The main disadvantages are:

- The simulation of rivets by spring elements (the hole is ignored and there are some limitations regarding the propagation of cracks)
- Bending is ignored

5. Conclusions

As regards the stress distribution, the complex stress distribution was found along with three loading conditions:

1. the irregular stress distribution applied remotely,
2. the bending stress due to the eccentricity of the lap-joint,
3. the bending stress due to the pillowing of the specimen.

Table 2
Stable crack growth prediction: based on DASA ('TL') R-curve

Iteration no.	σ (MPa)	$\Delta\sigma$ (MPa)	a (mm)	$K_I(\sigma)$ (MPa m$^{1/2}$)	Δa_{cf} (mm)
Tip no. 1—Hole no. 15—Right tip					
1	63	5	11.07	14.40	0.00
2	68	5	11.07	15.55	0.00
3	73	5	11.07	16.71	0.00
4	78	5	11.07	17.90	0.00
5	83	5	11.07	19.08	0.00
6	88	5	11.07	20.28	0.00
7	93	5	11.07	21.50	0.00
8	**98**		**11.07**		
Tip no. 2—Hole no. 10—Left tip					
1	63	5	6.15	29.61	0.22
2	68	5	6.37	31.69	0.34
3	73	5	6.71	34.09	0.52
4	78	5	7.23	35.96	0.68
5	83	5	7.91	38.07	0.89
6	88	5	8.80	40.03	1.11
7	93	5	9.91	42.22	1.39
8	**98**		**11.30**		
Tip no. 3—Hole no. 6—Right tip					
1	63	5	16.24	26.58	0.09
2	68	5	16.33	28.78	0.18
3	73	5	16.51	30.84	0.29
4	78	5	16.80	33.17	0.45
5	83	5	17.25	35.32	0.62
6	88	5	17.87	36.84	0.77
7	93	5	18.64	39.24	1.02
8	**98**		**19.66**		
Tip no. 4—Hole no. 1—Left tip					
1	63	5	6.23	9.15	0.00
2	68	5	6.23	9.89	0.00
3	73	5	6.23	10.62	0.00
4	78	5	6.23	11.38	0.00
5	83	5	6.23	12.14	0.00
6	88	5	6.23	12.91	0.00
7	93	5	6.23	13.71	0.00
8	**98**		**6.23**		
Tip no. 5—Hole no. 1—Right tip					
1	63	5	5.07	9.91	0.00
2	68	5	5.07	10.70	0.00
3	73	5	5.07	11.50	0.00
4	78	5	5.07	12.32	0.00
5	83	5	5.07	13.14	0.00
6	88	5	5.07	13.96	0.00
7	93	5	5.07	14.82	0.00
8	**98**		**5.07**		

Specimens with two rows of rivets have a higher bending component than specimens with three rows of rivets.

The variation in the fatigue lives of the specimens was partially due to the nature of the cracking. In general, the shortest life occurred when the largest cracks grew towards each other from adjacent fastener holes. A longer life occurred when cracks initiated and grew from widely separated holes. The MSD cracks are hidden for 80% (specimen #3) to 96% (specimen #7) of the total fatigue life; therefore, the number of cycles required to achieve initial failure did not differ significantly from that to final failure of the specimen.

The presence of fatigue cracking drastically reduce the residual strength.

Cracks typically initiate at hidden locations, at the edge of a rivet hole, or at the faying surface of the sheets. Fatigue crack initiation occurs in regions of high stress concentration located at or near rivet holes. It can be at rivet hole corners with the shape of the crack a quarter-ellipse, or at abraded (fretted) surfaces with the shape of the crack a semi-ellipse. The results show that cracks initiate at the interface and propagate in a subsurface manner.

The FRANC2D/L modelling of the crack propagation

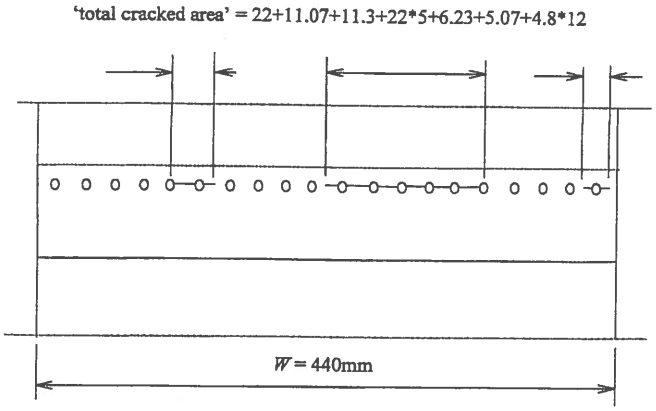

Fig. 22. Crack configuration for the net section plastic collapse (first interpretation).

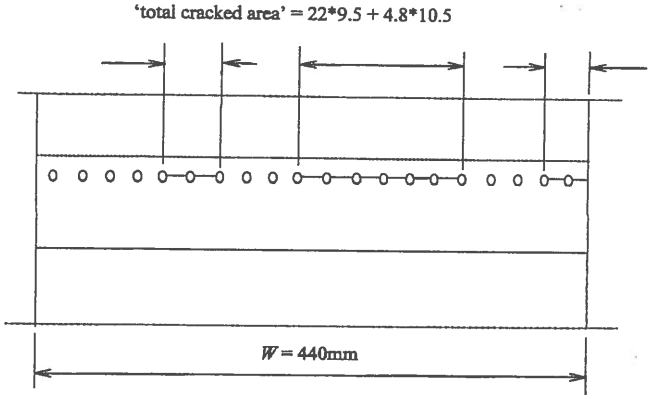

Fig. 23. Crack configuration for the net section plastic collapse (second interpretation).

problem is acceptable. The exception is the right crack of hole 9.

Three methods were used for residual strength prediction: the net section plastic collapse approach, the failure criterion for plane strain structure and the R-curve. The third method gave the best results.

Acknowledgements

The SEM work of Dr Carlos Moreira de Sá (CEMUP—Universidade do Porto) is greatly acknowledged. This paper is based on work carried out at the Faculdade de Engenharia da Universidade do Porto—IDMEC in the context of the BRITE-EURAM project BE95-1053 'Structural Maintenance of Ageing Aircraft', partially funded by the European Commission.

References

[1] Structural maintenance of ageing aircraft. BRITE-EURAM project number BE95-1053, Synthesis report, March 1999.
[2] Eastaugh GF, Simpson DL, Straznicky PV, Wakeman RB. A special uniaxial coupon test specimen for the simulation of multiple site fatigue crack growth and link-up in fuselage skin splices. NASA 96N24261, December 1995.
[3] Schijve J. Fatigue of aircraft materials and structures. Int J Fatigue 1994;16(1):21–32.
[4] Dawicke DS, Phillips EP, Swenson DV, Gondhalekar S. Crack growth from loaded countersunk rivet holes: durability of metal aircraft structures. In: Atluri SN, Harris CE, Hoggard A, Miller N, Sampath SG, editors. Proceedings of the International Workshop on Structural Integrity of Aging Airplanes, 31 March–2 April; Atlanta: Springer Verlag, 1992. p. 75–90.
[5] Miller M, Gruber ML, Wilkins KE, Worden RE. Full-scale testing and analysis of fuselage structure. In: FAA/NASA International Symposium on Advanced Structural Integrity Methods for Airframe Durability and Damage Tolerance, NASA CP 3274, September 1994:481–96.
[6] Samavedam G, Hoadley D, Thomson D. Full-scale testing and analysis of curved aircraft fuselage panels. FAA, DOT/FAA/CT-93/78, December 1993.
[7] Jeong DY, Roach DP, Canha JV, Brewer JC, Flournoy TH. Strain fields in Boeing 737 fuselage lap splices: field and laboratory measurements with analytical correlations. FAA, DOT/FAA/CT-95/25, June 1995.
[8] Schutz D, Lowak H. The effect of secondary bending on the fatigue strength of joints. Laboratorium fur Betriebsfestigkeit Report FB-113 (1974), RAE library translation no. 1858, August 1975.
[9] Schra L, Ottens HH, Vlieger H. Fatigue crack growth in simulated Fokker 100 lap joints under MSD and SSD conditions. NLR CR 95279 C, National Aerospace Laboratory NLR, Amsterdam, June 1995.
[10] Forsyth PJE. The effect of cladding condition on the stages of fatigue crack formation and growth: problems with fatigue in aircraft. In: Proceedings of the Eighth ICAF Symposium. Emmen: Swiss Federal Aircraft Establishment (F+W), 1975, pp. 2.5/1–2.5/23.
[11] Schijve J, Jacobs FA, Tromp PJ. Flight-simulation tests on notched elements. NLR TR 74033 U, National Aerospace Laboratory NLR, Amsterdam, February 1974.
[12] Piascik RS, Willard SA, Miller M. The characterisation of widespread fatigue damage in fuselage. NASA 95N14920, September 1994.
[13] Rooke DP. Fracture mechanics analysis of short cracks at loaded holes: behaviour of short cracks in airframe components. In: AGARD Conference Proceedings No. 328. Neuilly-sur-Seine: Advisory Group for Aerospace Research and Development, 1983, pp. 8-1–8-6.
[14] Wang DY. A study of small crack growth under transport spectrum loading. AGARD-CP-328, paper 14, 1983. Shorter version in ASTM STP 761, American Society for Testing and Materials, 1982:181–211.
[15] Potter JM, Yee BGW. Use of small crack data to bring about and quantify improvements to aircraft structural integrity. AGARD-CP-328, paper 4, 1983.
[16] Pitt S, Jones R. Multiple-site and widespread fatigue damage in aging aircraft. Eng Failure Anal 1997;4(4):237–57.
[17] Part 2 of the U.S. National Transportation Safety Board Report on the Fuselage Failure of an Aloha Airlines Boeing 737-200 in April 1988. In: Aviation Week and Space Technology, 4 September–15 September 1989.
[18] Maclin JR. Performance of fuselage pressure structure. In: International Conference on Aging Aircraft and Structural Airworthiness, NASA CP 3160, 1991:67–74.
[19] Wanhill RJH. Some practical considerations for fatigue and corrosion damage assessment of ageing aircraft. NLR Technical Publication TP 96253 L, 1996.
[20] Gruber ML, Mazur CJ, Wilkins KE, Worden RE. Investigation

of fuselage structure subject to widespread fatigue damage. FAA, DOT/FAA/AR-95/47, February 1996.
[21] Molent L, Jones R. Crack growth and repair of multi-site damage of fuselage lap joints. Eng Fract Mech 1993;44(4):627–37.
[22] Broek D. The effects of multi-site damage on the arrest capability of aircraft fuselage structures. FractuREsearch, TR 9302, 1993.
[23] Nesterenko GI. Multiple site fatigue damages of aircraft structures. NASA, N96-24270, December 1995.
[24] Willard SA. A record of all marker bands found in the upper rivet rows of 2 adjacent bays from a fuselage lap splice joint. NASA, N96-16272, November 1995.
[25] van der Hoeven W, Schra L. Document SMAAC-TR-3.1-01-1.3/NLR, NLR-TR-98195, March 1998.
[26] Swift T. The application of fracture mechanics to the development of the DC-10 fuselage. AGARD-AG-176. January 1974:234.
[27] Creager M. A note on the use of a simple technique for failure prediction using resistance curves, fracture toughness evaluation by R-curve methods. ASTM STP 527, American Society for Testing and Materials, 1973:105–12.
[28] Liebowitz H, editor. AGARDograph No. 176: Fracture mechanics of aircraft structures. January 1974.
[29] Ewalds HL, Wanhill RJH. Fracture mechanics. London: Edward Arnold, 1985.
[30] DeWit R, Fields RJ, Low III SR, Harne DE, Foecke T. Fracture testing of large-scale thin-sheet aluminum alloy. Federal Aviation Administration, Report No. DOT/FAA/AR-95/11, February 1996.

ELSEVIER

Composite Structures 50 (2000) 151–157

COMPOSITE STRUCTURES

www.elsevier.com/locate/compstruct

Prediction of compressive strength of carbon–epoxy laminates containing delamination by using a mixed-mode damage model

M.F.S.F. de Moura *, J.P.M. Gonçalves, A.T. Marques, P.M.S.T. de Castro

Departamento de Engenharia Mecânicae Gestão Industrial, Faculdade de Engenhariada, Universidade do Porto, Rua dos Bragas, 4050-123 Porto, Portugal

Abstract

It is well known that composite laminates are easily damaged by low-velocity impact. The internal delaminations can drastically reduce the compressive strength of laminates. In this study, a numerical analysis for predicting the residual compressive strength of delaminated plates is proposed. The delaminated interfaces are modelled by using interface elements connecting the three-dimensional solid elements modelling the composite layers. Delamination propagation is modelled by using a damage model based on the indirect use of fracture mechanics. Due to the complex stress state of the problem, a mixed-mode analysis including the three modes of fracture was considered. Experimental studies were performed on carbon–epoxy $[0_4, 90_4]_s$ and $[90_4, 0_4]_s$ laminates. They included low-velocity impact tests, followed by X-ray damage characterisation and compression tests. Good agreement between experimental and numerical analysis was obtained. © 2000 Elsevier Science Ltd. All rights reserved.

Keywords: Composites; Delamination propagation; Interface elements; Mixed-mode damage model

1. Introduction

Delamination is one of the most severe problems concerning laminated composites. In fact, the mechanical properties of these materials can be drastically reduced in presence of delamination that may develop between adjacent plies with different orientation. This kind of damage is based on the failure of the thin resin layer existing between two different oriented plies and usually is a result of low-velocity impact or manufacturing defects. Of all mechanical properties of composite materials, the most affected by delamination is the compressive strength that can be reduced up to 60%. Consequently, the development of numerical tools to predict the behaviour of composite laminates containing delamination and submitted to compression is very important.

Several authors have investigated the behaviour of delaminated composite materials under uniaxial compression loads. Whitcomb [1] studied the behaviour of a post-buckled embedded circular delamination, considering geometrically nonlinear three-dimensional finite element analysis. He also considered an approximate contact analysis and concluded that, for moderate strain levels, the strain energy release rates can be calculated with reasonable accuracy without including contact effects. However, for other configurations and high strain rates, the contact effects must be included preventing overlap of the delamination faces. Mukherjee et al. [2] considered a three-dimensional analysis including contact conditions for studying the stress field and strain energy release rates for an embedded delamination. They concluded that interpenetration must be prevented and that strain energy release rates varies considerably along the delamination front, which shows the limitation of the bidimensional models. Suemasu and Kumagai [3] studied the compressive behaviour of rectangular composite plates with multiple delaminations. Three-dimensional block elements were adopted to accurately obtain energy release rates G_I, G_{II} and G_{III} along the delamination fronts based on virtual crack closure method. The contact problem of the delaminated surfaces was considered by introducing a spring element between the nodes of the upper and lower surfaces of the delaminations. Good agreement was obtained between finite element and Raleigh–Ritz analyses for buckling loads. Kyoung et al. [4] studied the effect of multiple delaminations under compressive loading. To avoid overlapping between delaminated layers, the contact node pair was considered to apply displacement

* Corresponding author. Fax: +351-2220-59125.
E-mail address: mfmoura@fe.up.pt (M.F.S.F. de Moura).

0263-8223/00/$ - see front matter © 2000 Elsevier Science Ltd. All rights reserved.
PII: S0263-8223(00)00091-X

constraints between contacted sublayers. They obtained accurate results for the buckling and post-buckling behaviour of composite laminates.

With the purpose of studying the composite material behaviour under compression after impact, avoiding difficult and expensive experimental testing, a numerical model was developed. A first step towards a general assessment of the effects of embedded delamination on compression failure of composite materials was pursued by de Moura et al. [5], by using an interface finite element with 18 nodes [6] compatible with 27 node isoparametric hexahedral elements. This analysis was based on three characteristics that were considered to be fundamental for modelling the compression failure of delaminated composites:

- three-dimensional analysis,
- contact constraints,
- delamination propagation.

The delamination propagation was modelled by considering a stress failure criterion and the results agreed, reasonably well, with the experimental ones.

The objective of the present work is to obtain the failure compressive load of $[0_4, 90_4]_s$ and $[90_4, 0_4]_s$ laminates containing delamination caused by low-velocity impact. This is done using interface elements and a damage model based on the indirect use of fracture mechanics, by considering the area under the stress/relative displacements curve equal to the critical fracture energy. With this approach, it is possible to model damage propagation as well as initiation, avoiding the definition of initial flaws. Due to the complex stress state, characteristic of this kind of problems, a mixed-mode analysis including the three modes is considered.

2. Theory

The interface finite element formulation, detailed in [5,6], can be viewed as a contact problem. Basically, the solution of the equations arising in contact problems consists on the minimisation of the potential energy subjected to certain kinematic constraints. This is done considering the variational method with penalty function formulation. The formulated interface element consists of 18 nodes with curved sides as shown in Fig. 1.

The vector of relative displacements between two homologous points can be obtained from the displacement fields of the element faces (top and bottom)

$$\boldsymbol{\delta} = \begin{Bmatrix} \delta_s \\ \delta_t \\ \delta_n \end{Bmatrix} = \begin{Bmatrix} u_s \\ u_t \\ u_n \end{Bmatrix}_{\text{top}} - \begin{Bmatrix} u_s \\ u_t \\ u_n \end{Bmatrix}_{\text{bot}}, \tag{1}$$

where s and t represent the tangential directions and n the normal direction.

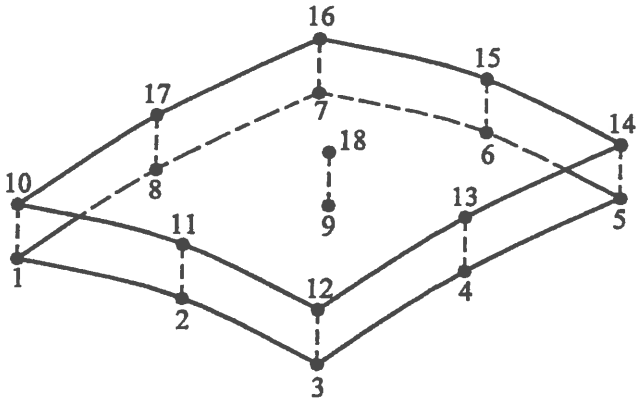

Fig. 1. The interface element.

The stresses resulting from the relative displacements, defined above, are given by

$$\boldsymbol{\sigma} = \mathbf{D}\boldsymbol{\delta}, \tag{2}$$

where

$$\mathbf{D} = \begin{bmatrix} d_s & 0 & 0 \\ 0 & d_t & 0 \\ 0 & 0 & d_n \end{bmatrix}, \tag{3}$$

d_i being the shear (d_s, d_t) and normal (d_n) interface stiffnesses. They represent the penalty parameter (N/m^3) introduced by the user and they have to be carefully chosen to obtain a good performance of the model. As small values induce large interpenetrations and large values induce numerical problems, the optimum interface stiffnesses are the largest values that do not produce numerical problems.

3. Damage model [7]

Some researchers [8–11] have already modelled the behaviour of interfaces with damage. Schellekens [8] used a mixed-mode delamination model based on orthotropic hardening/softening plasticity. The model was applied to investigate the onset and growth of free edge delamination in laminated composite strips subjected to uniaxial tension and compression. Good agreement between computations and experimental results was obtained. Allix and Ladevèze [9] introduced an interface damage model, using a few intrinsic characteristics of the interface, to predict the tendency of a structure to delaminate. This modelling has been used for the prediction of delamination initiation and growth in the case of static loading without buckling. Two applications of this model are presented by Daudeville et al. [10]. The authors studied, under static loading, the delamination in the vicinity of a straight edge of a specimen under tension or compression and near a hole of a perforated plate under tension. They considered degradations of

layers and of connections between layers and predicted the onset of delamination and its propagation on a short distance. Comparisons between numerical simulations and experimental results are encouraging on the prediction of damaged areas and onset strains. However, a possible dependence of interface characteristic parameters on the relative angle between layers was not studied. Mi et al. [11] developed a progressive mixed-mode delamination including Modes I and II based on the use of interface elements in conjunction with softening relationships between the stresses and relative displacements. By considering a scalar parameter in their damage model, the authors simulate linear or quadratic interactions between Modes I and II. Some simple examples were presented and good agreement between numerical and analytical results was obtained.

The damage model considered in this work is detailed in [7]. It is based on the indirect use of fracture mechanics and is characterised by a softening stress/relative displacement relationship (see Fig. 2). When the stresses at a point, calculated by Eq. (2), satisfy the adopted criterion, the failure process must be gradual because the abrupt cancellation of the stresses induces numerical instabilities. Physically, it means that the failure may not occur instantaneously and the failure energy is dissipated as crack grows. If we have single mode propagation (Mode I, II or III), the area under the stress/relative displacement curve can be equated to the critical fracture energy. As the strength ($\sigma_{t,i}$) and the critical fracture energy (G_c) are material properties experimentally determined, we can obtain the maximum relative displacement ($\delta_{\max,i}$).

Eq. (2) represents the relation between stresses and relative displacements up to the defined strength ($\sigma_{t,i}$) is attained. The points ($\delta_{0,i}$, $\sigma_{t,i}$) and ($\delta_{\max,i}$, 0) correspond to the initiation and complete failure, respectively. The decrease between these two points is the softening relationship represented by

$$\sigma = (\mathbf{I} - \mathbf{E})\mathbf{D}\delta, \tag{4}$$

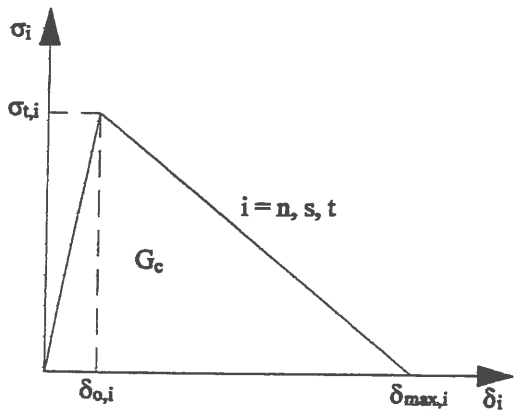

Fig. 2. Softening stress/relative displacements relationship for pure Modes (I, II or III).

where I represents the identity matrix and E is the diagonal matrix containing on the i-position the damage parameter

$$e_i = \frac{\delta_{\max,i}(\delta_i - \delta_{0,i})}{\delta_i(\delta_{\max,i} - \delta_{0,i})}, \tag{5}$$

corresponding to the i-direction. In pure modes, the other two components of stress are not important and can be abruptly cancelled equating to one the respective elements of the diagonal matrix E.

The mixed-mode model is an extension of the pure modes model presented above. This model is based on a damage surface moving between two limit situations (see Fig. 3). The initial damage surface is defined by the critical relative displacements ($\delta_{0,s}$, $\delta_{0,t}$, $\delta_{0,n}$), which correspond to ($\delta_{0,i}$) in the pure mode model, and the final damage surface by the maximum relative displacements ($\delta_{\max,s}$, $\delta_{\max,t}$, $\delta_{\max,n}$), which correspond to ($\delta_{\max,i}$) in the pure mode model. Between these extremes, damage propagation is simulated by consecutive different positions of the damage surface, which are function of the relative displacement vector δ_j. A definition of a new surface at a point is necessary whenever the relative displacement vector passes the current surface. The new surface is then obtained from the current surface and displacements increments doing

$$\frac{\delta_{j+1,s}}{\delta^*_{j,s} + c\Delta\delta_{j+1,s}} + \frac{\delta_{j+1,t}}{\delta^*_{j,t} + c\Delta\delta_{j+1,t}} + \frac{\delta_{j+1,n}}{\delta^*_{j,n} + c\Delta\delta_{j+1,n}} = 1, \tag{6}$$

where $\Delta\delta_{j+1,i}$ are the relative displacement increments and $\delta^*_{j,i}$ ($i = s, t, n$) are the intersections of the damage surface with the coordinate system. These parameters

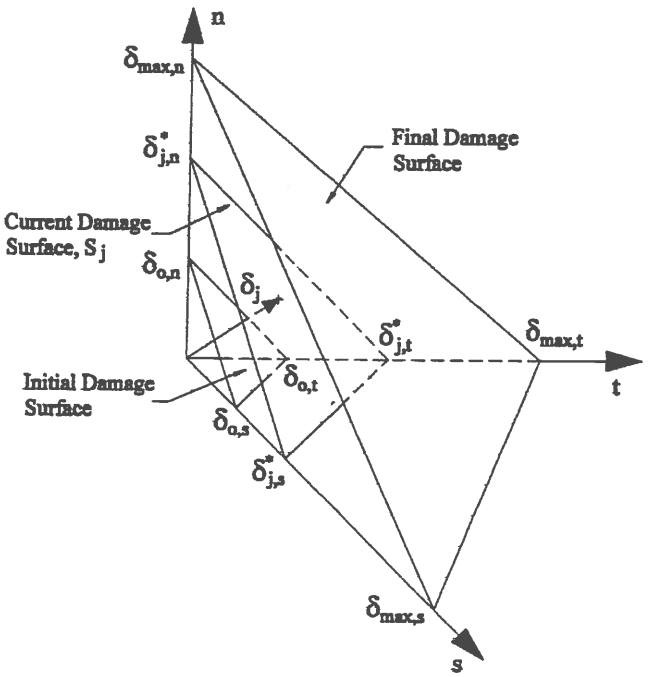

Fig. 3. Mixed-mode damage model.

Table 1
Mechanical properties of the unidirectional carbon–epoxy material[a]

E_{11} (GPa)	$E_{22} = E_{33}$ (GPa)	$\nu_{12} = \nu_{13}$	ν_{23}	$G_{12} = G_{13}$ (GPa)	G_{23} (GPa)	Y_t (MPa)	S_i (MPa)
109.34	8.82	0.342	0.52	4.32	3.2	59	54

[a] E_{ii}, G_{ij}, ν_{ij} – Elastic mechanical properties; Y_t – Transverse tensile strength; S_i – Interlaminar shear strength.

($\delta^*_{j,i}$) represent the position in the softening process for each mode. After the determination of the unknown factor c in Eq. (6), we obtain the new values $\delta^*_{j+1,i}$

$$\delta^*_{j+1,i} = \delta^*_{j,i} + c(\delta_{j+1,i} - \delta_{j,i}). \tag{7}$$

The diagonal elements of matrix **E** (e_s, e_t and e_n) of Eq. (4) can then be obtained from

$$e_{j+1,i} = \frac{\delta_{\max,i}(\delta^*_{j+1,i} - \delta_{0,i})}{\delta^*_{j+1,i}(\delta_{\max,i} - \delta_{0,i})}. \tag{8}$$

4. Experiments

The material used for the experimental testing was a common brittle carbon–epoxy from ICI (Fib 150/42), whose mechanical properties are listed in Table 1 [5].

The fracture toughnesses for Modes I and II were taken from [12] for a 0/90 interface of a brittle carbon–epoxy material (see Table 2). Although the test methods for Modes I and II fracture toughnesses are very well established [7], the same is not true for G_{IIIc}. However, recently some authors have dedicated their attention to this problem. Liao and Sun [13] showed that in the edge crack torsion test (ECT), the fracture is dominated by Mode III, which is not true in the split cantilever beam (SCB) test, where substantial Mode II components are generated near the free edge [14]. They also concluded that G_{IIIc} values for different kinds of angle-ply laminates are very close, and of the same order of magnitude of G_{IIc}. As they used the same material used in [12], we took their results for G_{IIIc} (see Table 2).

Two different laminates were studied: $[0_4, 90_4]_s$ and $[90_4, 0_4]_s$. The 140 mm × 60 mm specimens were clamped in order to produce a central circular area ($\phi = 50$ mm) and were submitted to low-velocity impact (velocities ranging from 1.5 to 2.5 m/s) using a drop weight testing machine. The impact test produced a peanut-like shape delamination located at the outermost interface between different oriented plies, with its major axis oriented on the fibres direction of the lower ply of the interface [15].

The compression after impact tests were performed on those specimens using a fixture system [16], adjusted to leave a testing area of 60 mm × 60 mm (see Fig. 4). The compression strength was considered as the maximum recorded load in the load–displacement curve.

Table 2
Fracture toughnesses (J/m^2) for 0/90 interface

G_{Ic}	G_{IIc}	G_{IIIc}
306	632	817

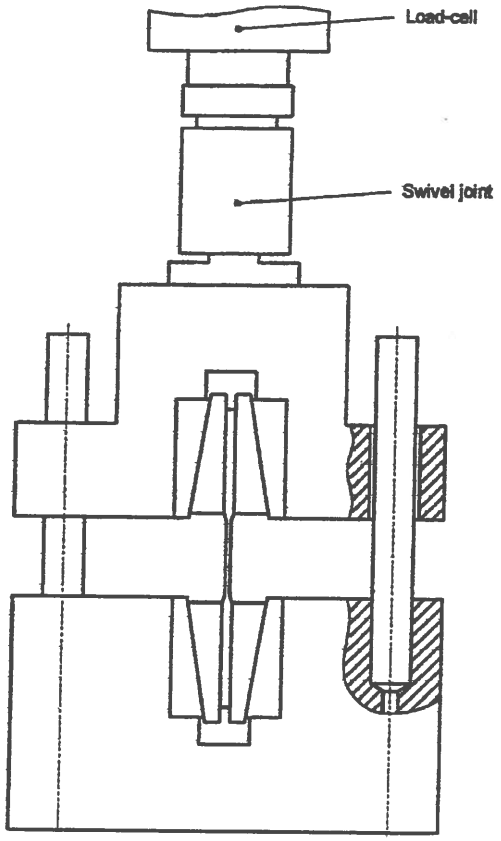

Fig. 4. Fixture system used for the compression tests.

5. Results

The main objective of the numerical model is to predict the maximum load that damaged composite plates can sustain under compression tests. Considering the geometrical and material symmetry of the problem, only one-fourth of the plate was considered. Three hundred three-dimensional elements modelled the three different sets of equally oriented layers. At the damaged interface, the adjacent layers of solid elements are contacting each other by interface elements that present two different states:

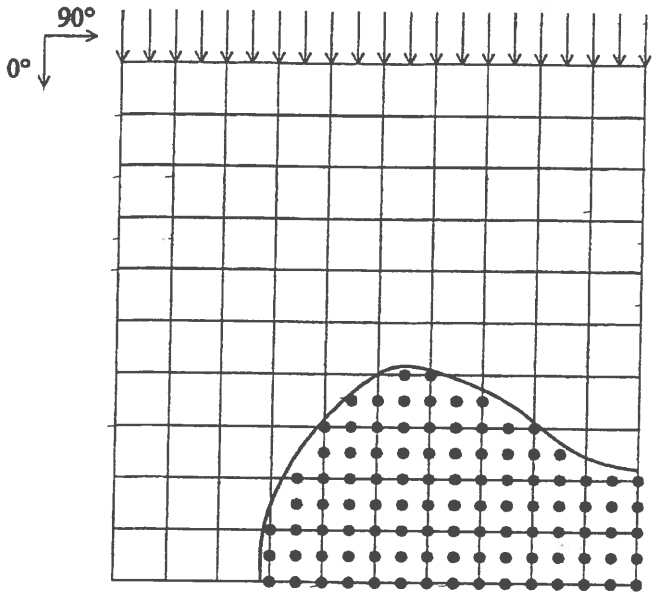

Fig. 5. Peanut like shape delamination (maximum dimensions of 26 mm × 42 mm) for $[90_4, 0_4]_s$ laminate.

- In the undamaged area the points are closed, restraining any relative movement between the two layers of the solid elements; in this case the three interlaminar stresses are totally transmitted.
- In the damaged area the points are open, allowing the relative movement between the two layers of solid elements; in this case only normal compressive stresses can be transmitted between the contacting surfaces, because friction is not included in the model.

The loading condition was performed by imposing a displacement (see Fig. 5). A geometrically nonlinear analysis using the modified Newton–Raphson method was considered. The interface stiffnesses used in the interface elements were considered equal to 10^7 N/mm^3. An initial imperfection at the point nearest to the center of the plate was considered. The imperfection is simulated considering the homologous nodes located at the central point of the damaged area, separated by a quantity of the same order of magnitude of the thin resin layer (0.0125 mm) existing between two composite layers. This quantity was considered equal to 10% of the ply thickness [5]. The consideration of this imperfection is important for numerical reasons and physically represents the rupture of this thin resin layer.

The real delaminated area was introduced in the interface elements by considering the points, located inside of the peanut-like shape delamination, open (see Fig. 5). This is a better approach relatively to previous studies [5], where the peanut-like shape delamination was replaced by a rectangle involving that area. The experimental and numerical results are listed in Table 3. In this table the delaminations are identified by the maximum dimensions of the delamination in each direction.

The analysis of Table 3 shows that the errors between the numerical and experimental results range between 0.2% and 3.8%, which can be considered excellent. It must be noted that there was a significant reduction in the relative errors compared with previous work [5].

It must be stated that the different compression behaviour experimentally observed between the two kinds of laminates was also obtained numerically (see Figs. 6 and 7). The $[0_4, 90_4]_s$ laminate showed local buckling of the damaged region and a sudden drop of load at collapse. On the other hand, the $[90_4, 0_4]_s$ laminate presented global buckling and a smooth behaviour at collapse. Moreover, in the $[0_4, 90_4]_s$ laminate, the delamination mainly propagated perpendicular to the applied displacement (see Fig. 8), before maximum load was attained. This was also experimentally observed in [17]. The $[90_4, 0_4]_s$ laminate did not show significant delamination propagation. The differences between local and global buckling are related to the product between the Young's modulus in the direction of compression

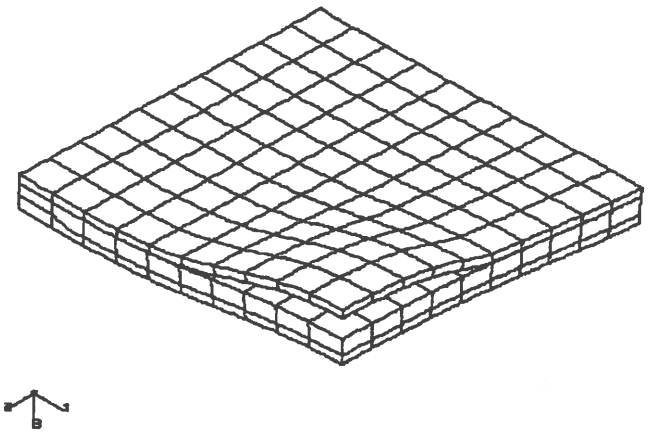

Fig. 6. Local buckling behaviour observed in $[0_4, 90_4]_s$ laminates.

Table 3
Failure load (N) for $[0_4, 90_4]_s$ and $[90_4, 0_4]_s$ plates

	$[0_4, 90_4]_s$		$[90_4, 0_4]_s$				
Del. size (mm)	48 × 32	50 × 36	13 × 30	18 × 39	26 × 42	38 × 50	40 × 54
Experimental	29,230	27,870	16,600	16,500	15,910	15,640	15,240
Numerical	30,350	28,306	16,050	16,036	15,980	15,612	15,540
Error (%)	3.8	1.6	−3.3	−2.8	0.4	−0.2	2.0

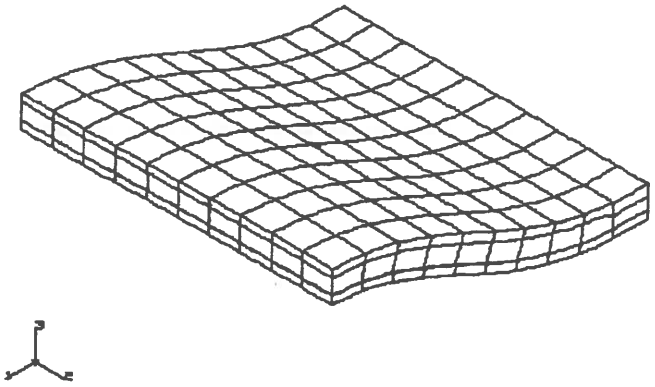

Fig. 7. Global bukling behaviour observed in $[90_4, 0_4]_s$ laminates.

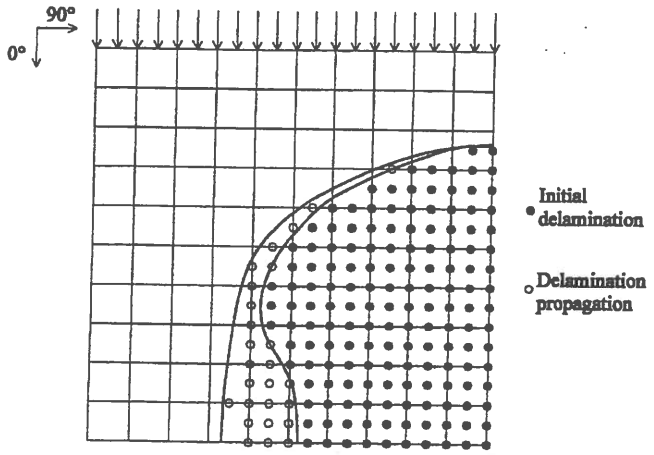

Fig. 8. Delamination propagation for $[0_4, 90_4]_s$ laminate with initial damage of maximum dimensions equal to 48 mm × 32 mm.

(E_{xx}) and the second moment of an area (I), as discussed in [5]. In $[0_4, 90_4]_s$ laminates, the delamination propagation, observed before buckling, is more pronounced that in $[90_4, 0_4]_s$ laminates. These two issues may explain the less sensitivity of $[90_4, 0_4]_s$ laminates to the delamination size observed in Table 3.

6. Conclusions

A numerical model for predicting the residual compressive strength of delaminated composite plates due to low-velocity impact was developed. The model is based on interface finite elements compatible with three-dimensional solid finite elements and includes a specific damage model. The damage model uses an indirect fracture mechanics approach considering the area under the stress/relative displacement curve equal to the fracture energy. Due to the complexity of the stress state, the damage model was extended to mixed-mode analysis considering the three modes. The initial delaminated area was introduced by opening the points of the interface elements located inside the peanut shape delamination considered.

Numerical modelling of $[0_4, 90_4]_s$ and $[90_4, 0_4]_s$ laminates was performed. Different behaviours were observed between these laminates which are justified by different flexural stiffnesses and delamination propagation. Good agreement between the experimental data and numerical results was obtained for the prediction of maximum load. Also, the numerical model showed the different compression behaviour experimentally observed for the two kinds of laminates. This is a good indication of the applicability of the model in predicting the residual compressive strength in impacted composite plates.

References

[1] Whitcomb JD. Analysis of a laminate with a post-buckled embedded delamination, including contact effects. J Compos Mater 1992;26(10):1523–35.
[2] Mukherjee YX, Gulrajani SN, Mukherjee S, Netravali AN. A numerical and experimental study of delaminated layer composites. J Comp Mater 1994;28(9):837–70.
[3] Suemasu H, Kumagai T. Compressive behaviors of multiply delaminated rectangular composite plates. In: Proceedings of the Eleventh International Conference on Composite Materials (ICCM-11), Australia, vol. V, 1997. p. 776–85.
[4] Kyoung WC, Kim CG, Hong CS. Modeling of composites laminates with multiple delaminations under compressive loading. J Comp Mater 1998;32(10):951–68.
[5] de Moura MFSF, Gonçalves JPM, Marques AT, de Castro PMST. Modeling compression failure after low velocity impact on laminated composites using interface elements. J Comp Mater 1997;31(15):1462–79.
[6] de Moura MFSF, Gonçalves JPM, Marques AT, de Castro PMST. Elemento Finito Isoparamétrico de Interface Para Problemas Tridimensionais. Métodos Numéricos Para Cálculo y Diseño en Ingeniería 1996;12(4):447–66.
[7] Gonçalves JPM, de Moura MFSF, de Castro PMST, Marques AT. Interface element including point-to-surface constraints for three-dimensional problems with damage propagation. Eng Comp: Int J Computer-Aided Eng Software 2000;17(1):28–47.
[8] Schellekens JCJ. Computational strategies for composite structures. PhD thesis, Technical University of Delft, Delft, 1992.
[9] Allix O, Ladevèze P. Interlaminar interface modelling for the prediction of delamination. Comp Struct 1992;22:235–42.
[10] Daudeville L, Allix O, Ladevèze P. Delamination analysis by damage mechanics: some applications. Comp Eng 1995;5(1):17–24.
[11] Mi Y, Crisfield MA, Davies GAO. Progressive delamination using interface elements. J Comp Mater 1998;32(14):1246–72.
[12] Lammerant L, Verpoest I. Modelling of the interaction between matrix cracks and delaminations during impact of composite plates. Comp Sci Technol 1996;56:1171–8.
[13] Liao WC, Sun CT. The determination of Mode III fracture toughness in thick composite laminates. Comp Sci Technol 1996;56:489–99.
[14] Donaldson LD. Mode III interlaminar fracture characterization of composite materials. Comp Sci Technol 1988;32:225–49.
[15] de Moura MFSF, Marques AT. Numerical and experimental studies of low velocity impact damage in carbon–epoxy laminates. In: Science, technologies and applications, Proceedings of the

European Conference on Composite Materials (ECCM-8), Naples, vol. 1, 1998. p. 77–85.
[16] Morais AB. Report NT-1401-U/1. Project Brite/Euram, Contract No. BRE2-CT92/0314, 1995.
[17] Gao SL, Kim JK, Xian XJ. Characterization of impact damage in CFRPS using a scanning acoustic microscope. In: Proceedings of the International Conference on Composite Materials (ICCM-1), Australia, vol. VI, 1997. p. 185–92.

EFA 269p Disk used DTD=4.1.0

PERGAMON

Engineering Failure Analysis □ (2000) 1–11

ENGINEERING FAILURE ANALYSIS

Fracture analysis of forks of a heavy duty lift truck

M.V. Figueiredo, F.M.F. Oliveira, J.P.M. Gonçalves, P.M.S.T. de Castro *, A.A. Fernandes

INEGI, Instituto de Engenharia Mecânica e Gestão Industrial, Faculdade de Engenharia da Universidade do Porto, Rua dos Bragas, 4050-123 Porto, Portugal

Received 30 November 1999; accepted 3 July 2000

Abstract

The fracture of the two forks of a heavy duty lift truck in operation at a harbour is described and discussed. The failure analysis included: mechanical tests for characterisation of the material, including tensile and Charpy tests; the study of a previous repair by welding carried out in one of the forks and the identification of consequential weld defects; the detection of fatigue cracks in the other fork; detailed metalographical analysis; stress analysis using the finite element method; and fracture mechanics and plastic collapse analyses. This case study illustrates the methodology for failure analysis, through systematic and sequential consideration of the evidence, generation of data, and use of models of behaviour. © 2000 Elsevier Science Ltd. All rights reserved.

Keywords: Welds; Failure analysis; Metallography; Overload; Fatigue

1. Introduction

The accident occurred in March 1997, and consisted of the fracture of the two forks of the fork lift truck that was moving a transformer of 22.6 t weight. Consequential loss concerning damage to the transformer is of the order of US$35,000, and the cost of replacement of the broken forks is of the order of US$70,000. Other damages are to be considered, such as delays in the supply of the transformer, and unavailability of the lift truck during repair.

The forks are represented in Fig. 1. The fracture occurred when the truck passed over a shallow channel in the road surface. It was verified that the left fork had been subjected to an earlier welding repair; the present fracture surface was close to that repair. The repair procedure included the following steps:

- joint preparation with arc-air in double tulip, followed by deburring,
- welding with austenitic electrode AWS E312-16, diameter 2.5 and 3.25 mm,
- pre-heating at 150°C,
- post heating at 200°C; slow cooling of the fork, with mineral wool protection,
- .control of weldment with dye penetrant.

* Corresponding author. Tel.: +351-22-205-1241; fax; +351-22-205-9125.
E-mail address: ptcastro@fe.up.pt (P.M.S.T. de Castro).

1350-6307/00/$ - see front matter © 2000 Elsevier Science Ltd. All rights reserved.
PII: S1350-6307(00)00040-6

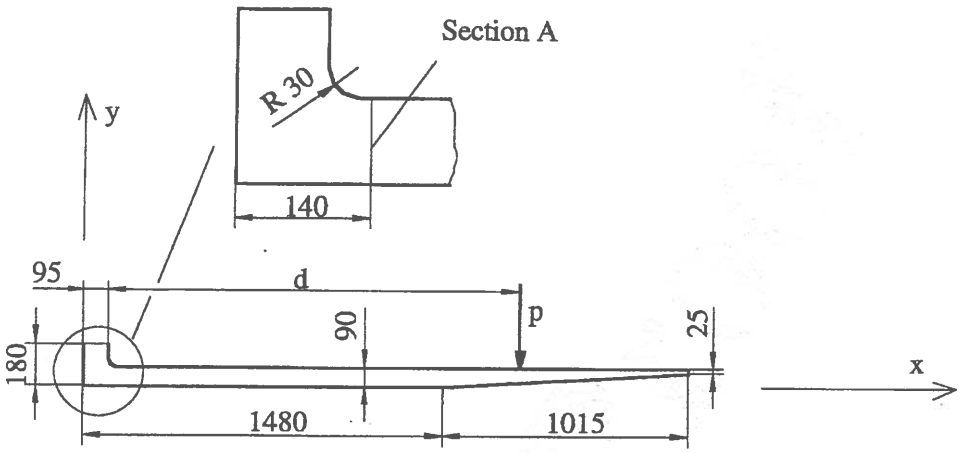

Fig. 1. Schematic representation of the fork.

The chemical composition of the forks' steel is given in Table 1. The chemical composition of the weld metal used in the mentioned earlier repair is given in Table 2.

The material of the fork can be considered equivalent to low alloy steel 35NiCrMoV12.5, see Table 3 [1]. Tensile and Charpy tests were performed in order to characterise the mechanical properties of the parent and weld metals for the repair in the left fork. The results are presented in Table 4, and the location and references of the samples are shown in Fig. 2.

Table 1
Chemical composition of the forks' steel

%C	%Si	%Mn	%P	%S	%Cr	%Mo	%Ni	%Al	%Cu	%V
0.34	0.19	0.63	0.011	0.012	1.31	0.55	3.31	0.014	0.092	0.12

Table 2
Chemical composition of the weld metal

%C	%Si	%Mn	%P	%S	%Cr	%Mo	%Ni	%Al	%Cu
0.14	0.84	0.94	0.02	0.007	25.9	0.18	8.31	0.004	0.11

Table 3
Chemical composition of the steel 35 NiCrMoV 12 5 according to DIN, Ref. [1]

0.30–0.40%C	0.15–0.35%Si	0.40–0.70%Mn	< 0.015%P	< 0.015%S
1.10–1.40%Cr	0.35–0.60%Mo	2.50–3.50%Ni	0.08–0.20%V	⩽0.015%Al

Table 4
Mechanical properties

	σ_r Nmm^{-2}	σ_y Nmm^{-2}	El %	KCV J
Parent metal	1446	1305	11.7	22.5
Weld metal	764	531	27	38.6
HAZ	–	–	–	23

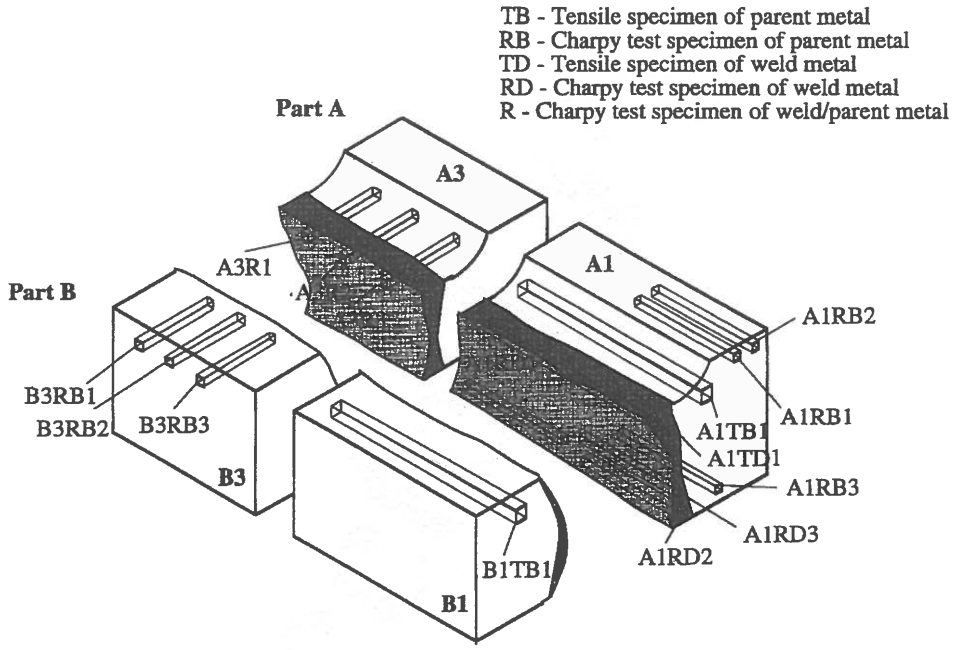

Fig. 2. Location and references of the samples.

2. Fractography

In Fig. 1 the crack plane (A) is shown. The crack surface of the right fork shows the existence of previous cracks with the appearance of fatigue cracks, due to the cyclic nature of the loading. Several initiation sites were identified, and the larger defects have the dimensions presented in Fig. 3.

In the left fork a lack of fusion defect (in the repair weldment) with the dimensions indicated in Fig. 4 was found.

A scanning electron microscope examination of the fracture surfaces was attempted but was unsuccessful, due to the damage and extensive oxidation suffered by the surfaces.

The fracture surface of the left fork shows an extensive lack of fusion defect. Fig. 5 shows the location of samples for the different examinations conducted. Fig. 6 is a macrograph of the earlier repair weldment, revealing that the fracture progressed along the fusion line except for the last weld passes. Another feature displayed by this figure is the narrow joint gap and access difficulty, which complicated the welding operation.

Vickers hardness was measured in three positions of sample A2, in the longitudinal direction, Fig. 7 a, b and c. Average hardness for the parent and weld metals is 460 and 250 HV, respectively. Hardness of weld metal is considerably smaller than hardness of the parent metal as expected; this implies that the tensile

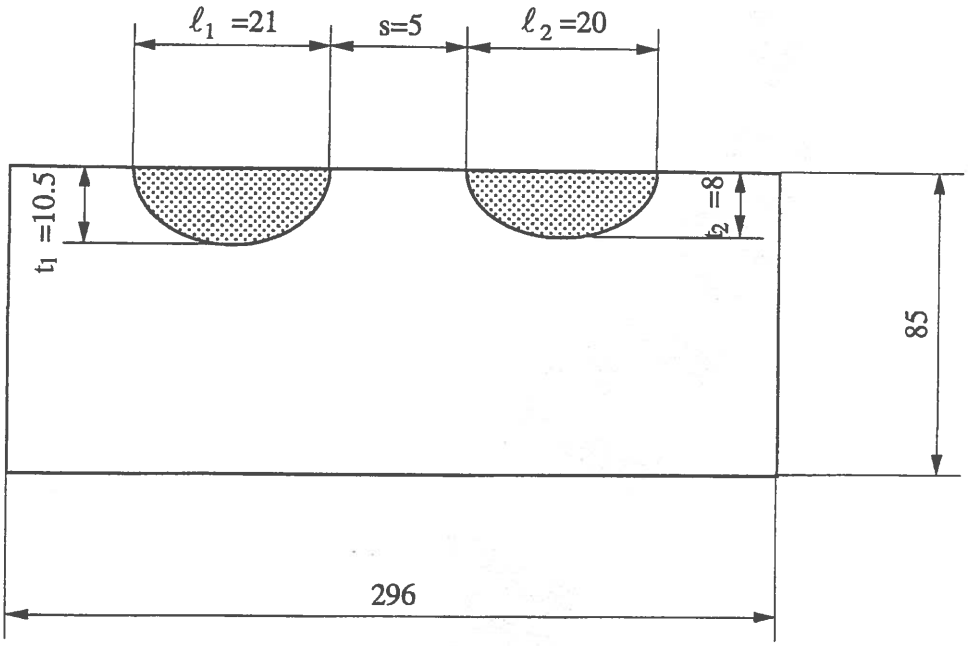

Fig. 3. Fatigue cracks in the right fork.

properties of the weld metal will be much lower than those of the parent metal. Fig. 7 shows that the HAZ hardness in sample B2 is higher than in sample A2, implying that during the welding process the thermal balance was not equal on both sides of the weldment.

This may be due to difficulties with handling the electrode or to the fact that both parts to be welded were not at the same temperature.

Samples subjected to 5% Nital attack revealed a tempered martensitic microstructure with average hardness of 460 HV in the parent metal (Fig. 8) and an austenitic-ferritic microstructure with average hardness of 250 HV in the weld metal (Fig. 9).

In summary, the macrographic examination gave the following results:

- fracture occurred along the fusion line in the interior of the fork, suggesting bad connection on side B, as shown by the lack of fusion,
- slag inclusions were found, suggesting difficulties in the welding operation or with cleaning due to the narrow gap used,
- the fork not subjected to earlier repair (right) displayed fatigue crack initiation sites,
- the HAZ of sample B2 shows greater hardness levels than sample A2.

The following points resulted from micrographic examination:

- weld metal with an austenitic-ferritic microstructure of average hardness of 250 HV and parent metal with a tempered martensitic microstructure of average hardness of 460 HV,
- the weld metal has considerably lower strength than the parent metal,
- sample B2 shows HAZ with maximum hardness levels higher than those of sample A2.
- HAZ of sample B2 shows in the interior of the fork a microstructure of refined grains only, indicating that in that zone there was not enough heat input for adequate fusion.

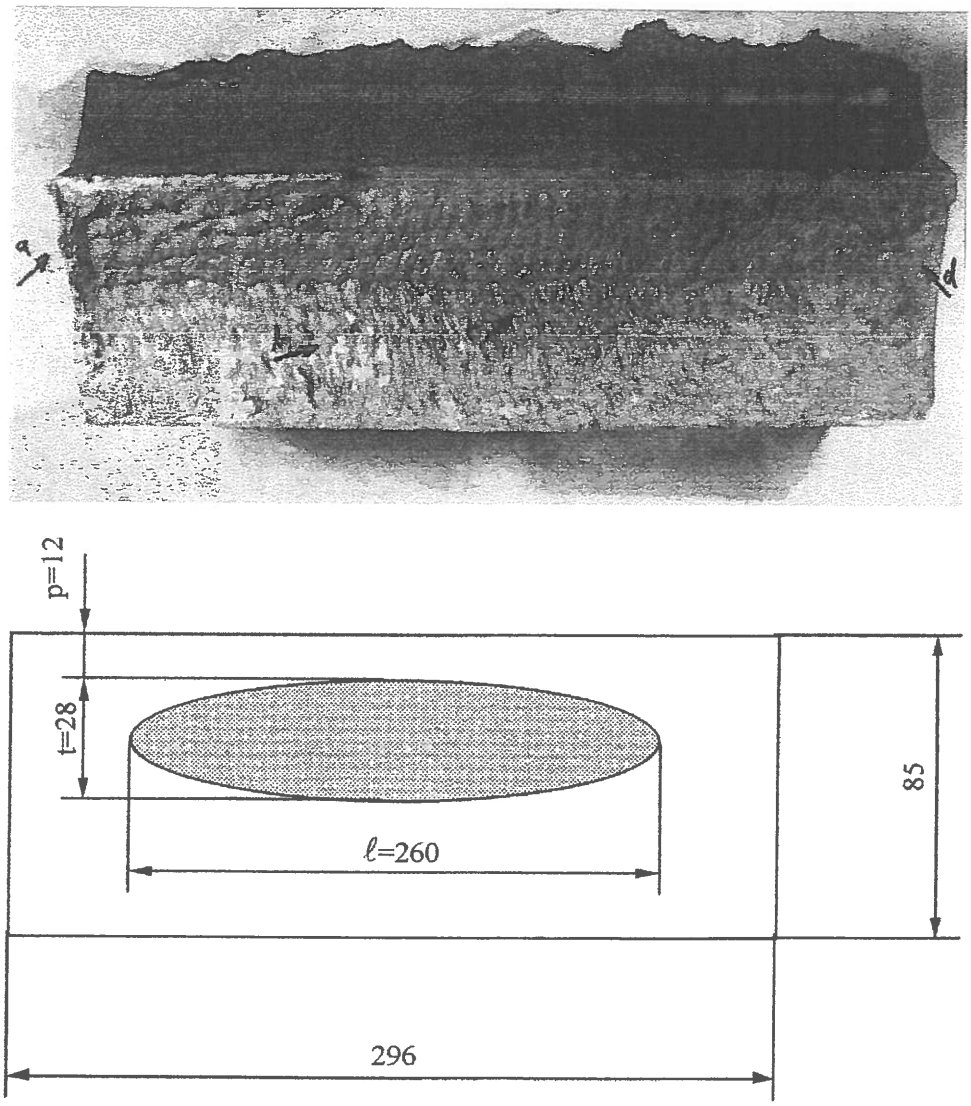

Fig. 4. Lack of fusion defect in the left fork.

3. Stress analysis in the fracture surface region

A finite element stress analysis of the fork was performed. Two situations were studied: the design maximum load scenario, i.e. a force of 25 t at the distance $d=1200$ mm (Fig. 1), and the actual circumstances of the accident, *i.e.* transformer weight (22.6 t) acting at the distance $d=1700$ mm. The result for the stress along the crack plane, in the absence of crack, is shown in Fig. 10, corresponding to the transformer load (22.6 t) at $d=1700$ mm.

Taking into account the measured values of tensile strength for parent and weld metals, and using safety factors of 1.5 or 2.35 for yield or rupture stress, the admissible stresses are 615 and 325 Nmm^{-2}, respectively. This implies an admissible load, at design distance $d=1200$ m, of 11,700 kg for the left and 22,000 kg for the right forks, respectively.

A3, A1, B3, B1 - specimens for determination of mechanical properties
A2, B2 - specimens for chemical composition and microstructure analyses

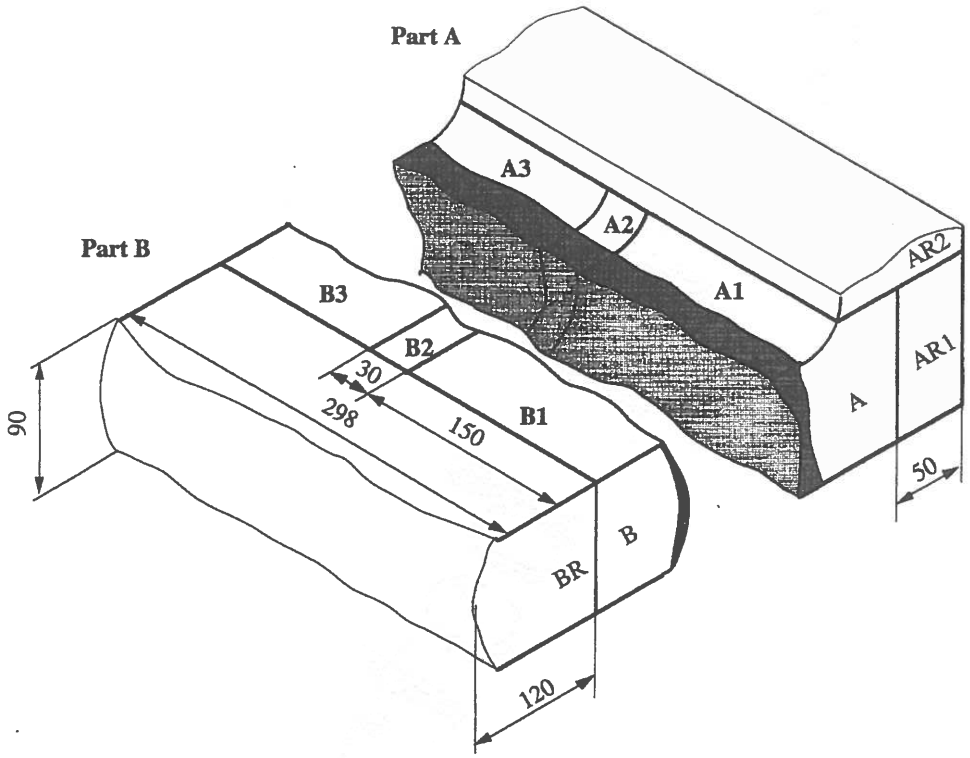

Fig. 5. Location of samples taken from left fork.

An obstacle with 20 cm height (such as the mentioned shallow channel), causes a dynamic intensification of stress of the order of 2.5 [2]. Taking this into account, then the maximum load for the left fork (subjected to earlier repair) was estimated as 4700 kg, and for the right fork was 8900 kg.

The analysis above assumes that there are no defects in the fork. The influence of defects was analysed using fracture mechanics concepts adopted by BS PD6493 [3]. The estimated fracture toughness of the parent metal, based upon empirical correlations with Charpy values given by Rolfe and Barsom in [4] is $K_{Ic} = 2700\ \mathrm{Nmm}^{-3/2}$. Following [3], the stress intensity factor may be estimated as

$$K_I = ((a^{1/2})/Q_0)(\sigma_m M_m + \sigma_b M_b) \quad (1)$$

or, since the principal stresses are bending stresses,

$$K_I = ((a^{1/2})/Q_0)(\sigma_b M_b) \quad (2)$$

where $a = t$ for surface defects, or $a = t/2$ for internal defects, and Q_0 and M_b are calibration factors, with values of 0.575 and 0.65 for the left fork.

Therefore, K_I is given as $K_I = 4.23\sigma_b$. With $\sigma_b = 450\ \mathrm{Nmm}^{-2}$, as given by the finite element analysis, the applied stress intensity factor is $K_I = 4.23 \times 450 = 1904\ \mathrm{Nmm}^{-3/2}$, higher than K_I admissible $= 0.7\ K_{Ic}$, i.e. $0.7 \times 2700\ \mathrm{Nmm}^{-3/2} = 1890\ \mathrm{Nmm}^{-3/2}$. Parent metal toughness was used in this analysis, since the rupture occurred close to the fusion line. The propagation path of the crack of the left fork can be observed in

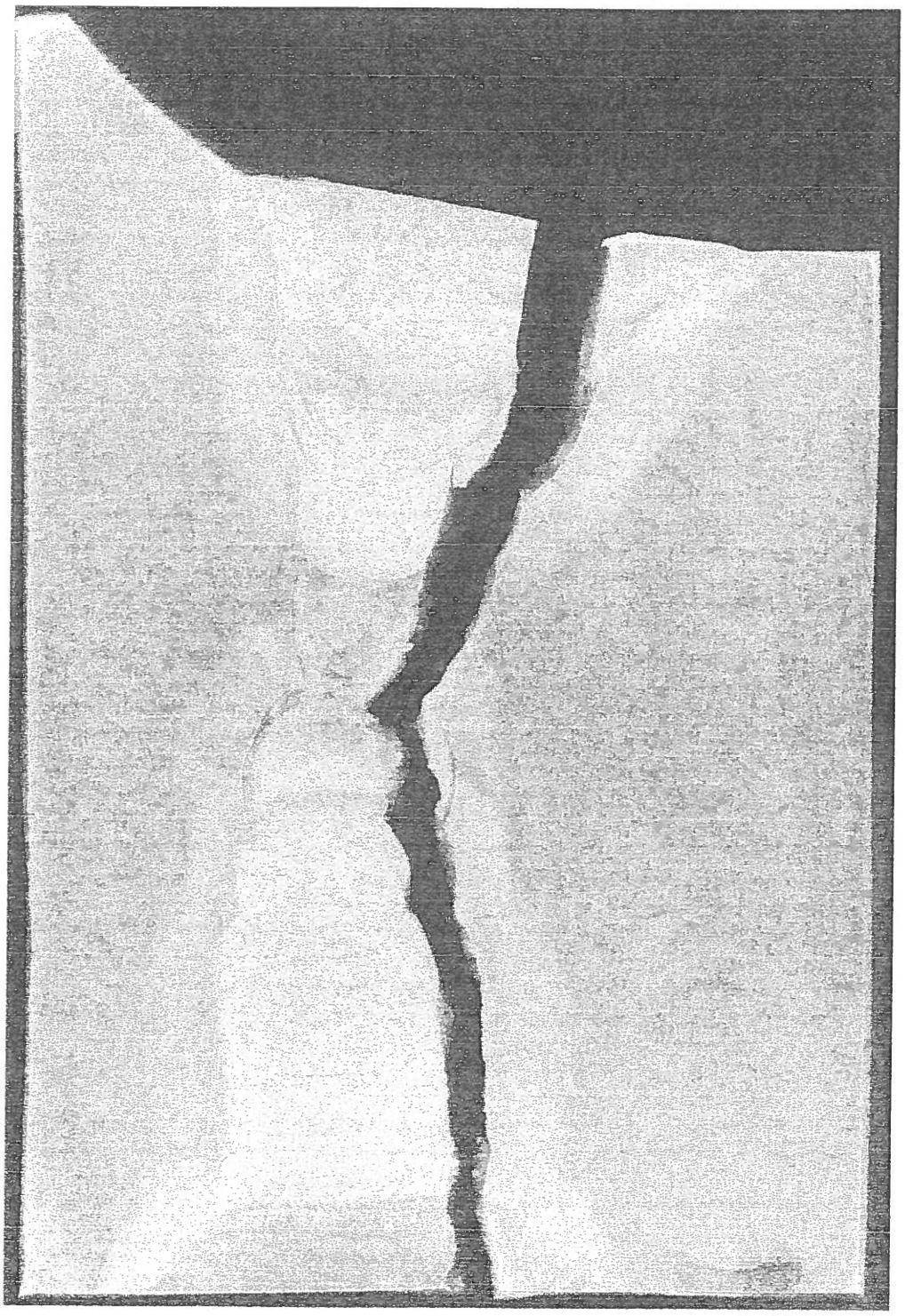

Fig. 6. Macrograph of the welding joint of the left fork.

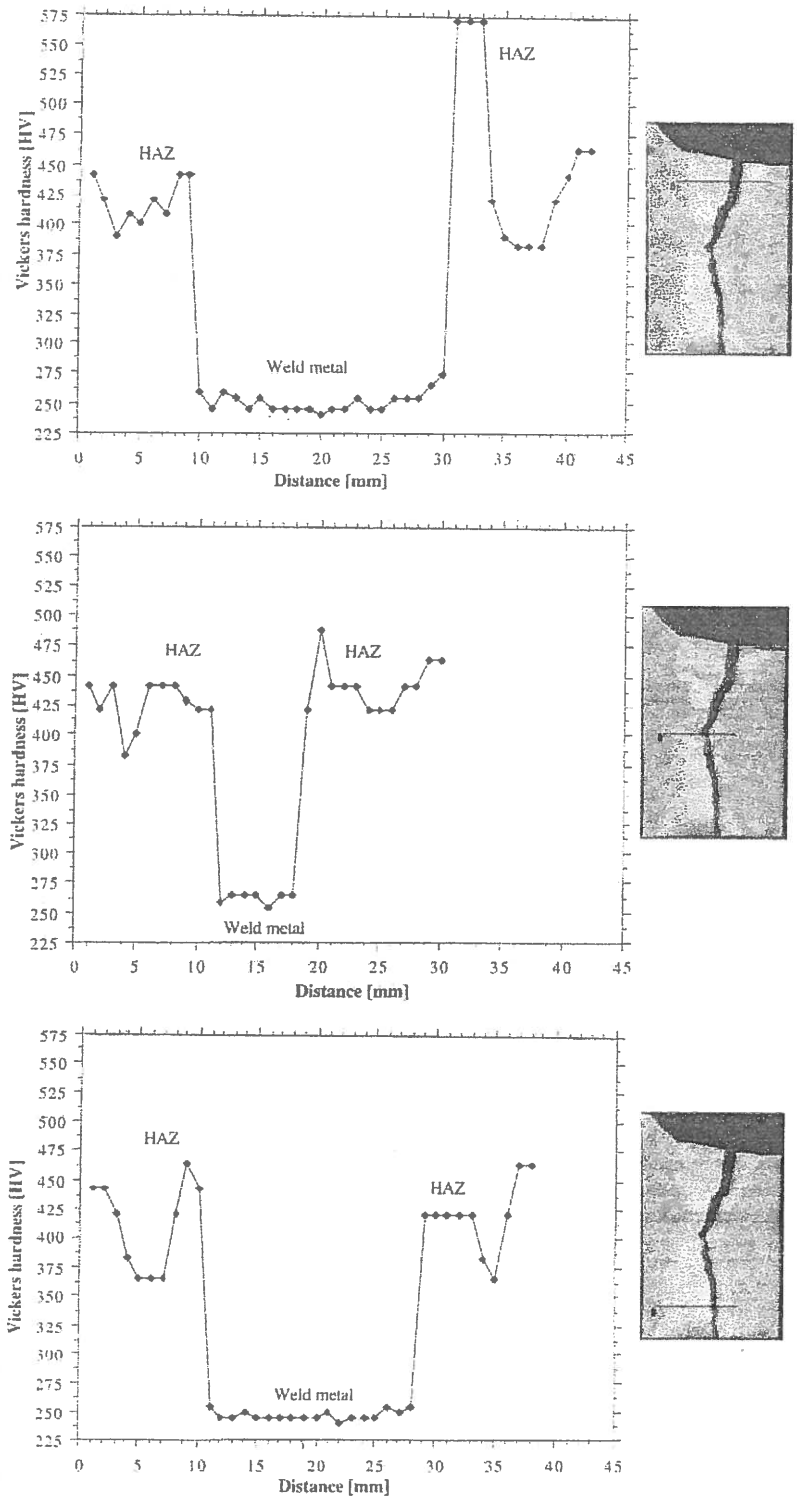

Fig. 7. Vickers hardness in the fork's longitudinal direction.

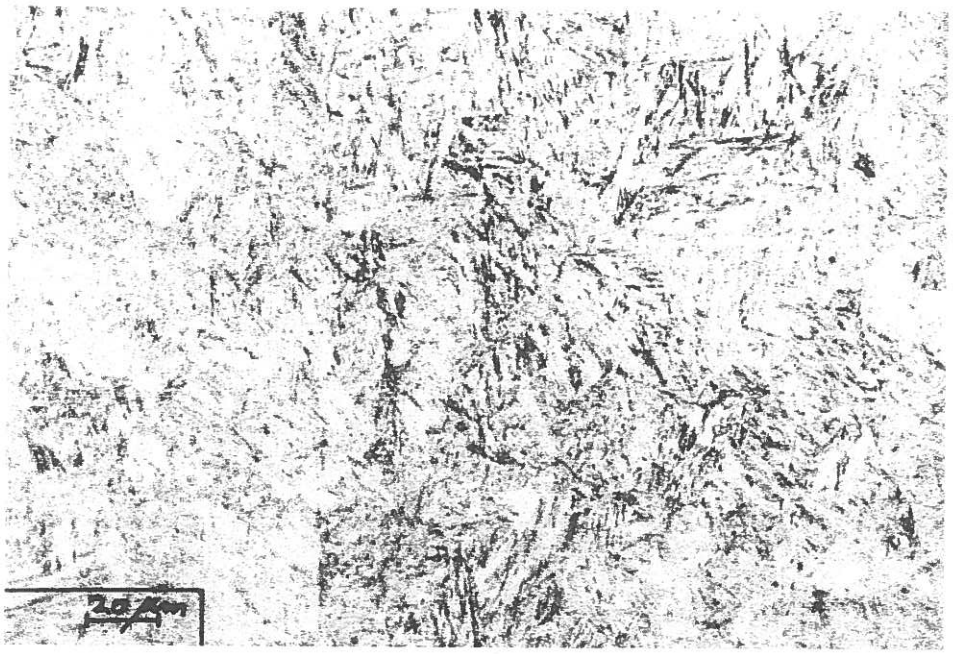

Fig. 8. Tempered martensitic microstructure of the parent metal.

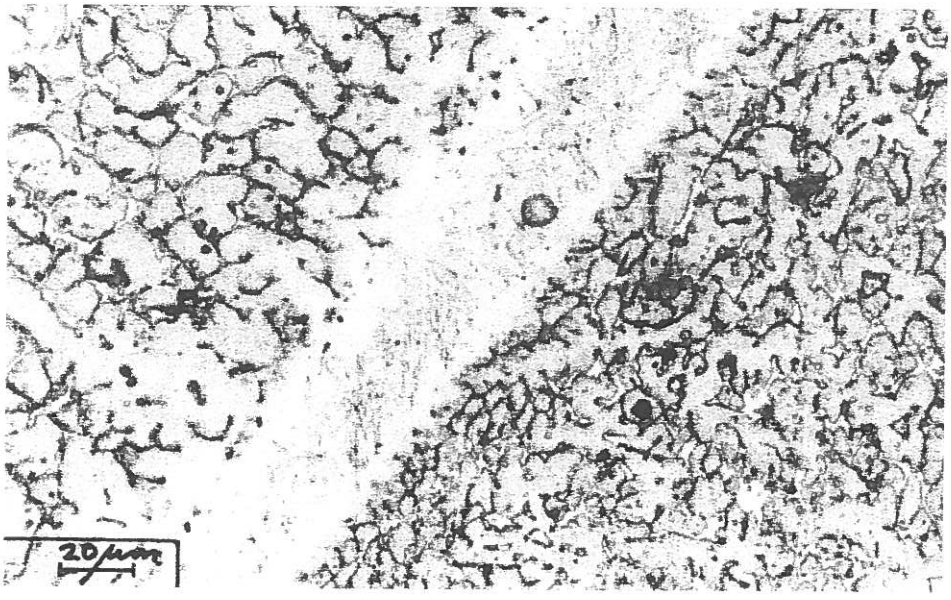

Fig. 9. Austenitic-ferritic microstructure of the weld metal.

Fig. 6. Except for the last weld passes, this path is close to the fusion line, where large local increases in hardness were detected, see Fig. 7.

In the presence of the lack of fusion defect, the fork was not able to withstand the applied load. Of course, this conclusion is reinforced if the dynamic effect of the obstacle is taken into account.

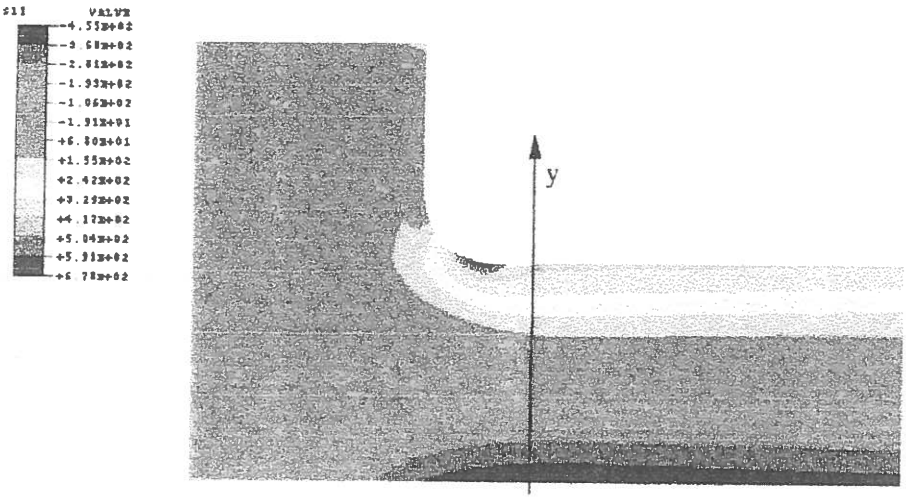

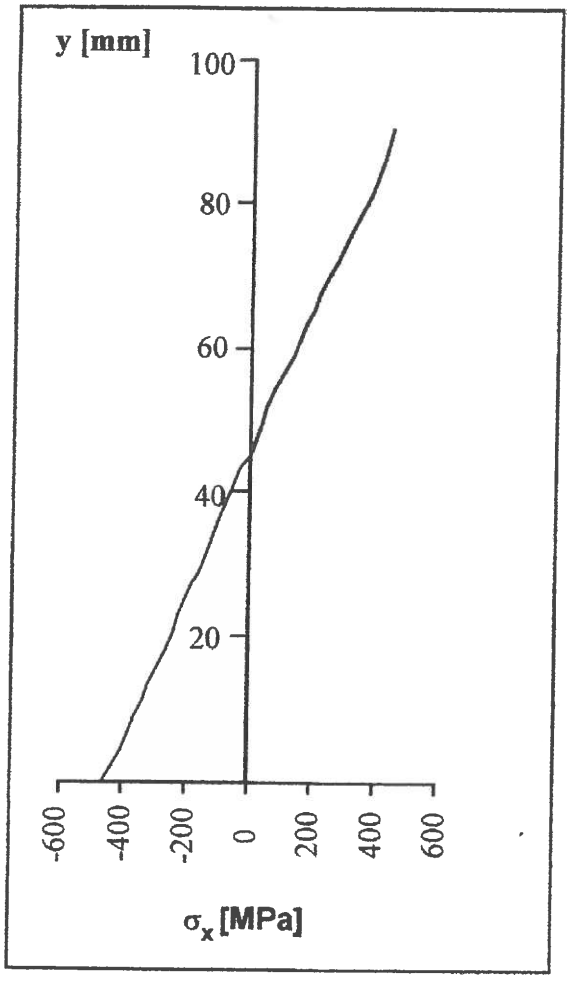

Fig. 10. Stress distribution along the crack plane, in the absence of crack.

An analysis using the methodology of [3] was also conducted with the data of the right fork. In this case interaction between both cracks (see Fig. 3) was specified by [3], leading to an equivalent crack of dimensions $t = t_1 = 10.5$ mm, $\lambda\ell = \lambda\ell_1 + \lambda\ell_2 + s = 46$ mm. In this case $Q_0 = 0.665$ and $M_b = 1.055$, leading to $K_I = 5.14\sigma_b$. and implying that the rupture of the right fork was also predictable.

A plastic collapse analysis, taking into account the important lack of fusion crack-like internal defect in the left fork, was carried out. For this purpose the fracture section of the left fork was approximated by three rectangles of 296 mm length, and 12, 28 and 45 mm height. In this approximation, the first and last rectangles correspond to the load bearing section, whereas the second rectangle corresponds to the lack of fusion crack-like defect. Taking into account the yield strength of the weld metal, the normal force corresponding to the yielding of the upper load bearing section is 54 kg mm^{-2}×12 mm×296 mm, corresponding to a bending moment in the section of approximately 11.1×10^3 kgm, and to a load of 6500 kg acting at the distance 1700 mm, lower than the actual applied load. The same conclusion of predictable failure was thus reached.

4. Concluding remarks

The left fork was subjected to an earlier welding repair for a rupture most probably due to fatigue cracking, as suggested by the existing fatigue cracks in the right fork.

The use of an austenitic electrode for the repair, although justifiable from the standpoint of control of hydrogen induced cold cracking [5], is inadequate from the standpoint of the strength of the joint. Indeed, the base material admissible tensile strength is almost double that of the weld metal, implying that even in the absence of defects the load carrying capacity of the left fork was almost halved. A more appropriate solution for this repair would consist of using a weld metal similar to the parent metal, provided a suitable weld procedure was specified, namely as concerns:

- adequate joint preparation,
- pre-heating and temperature control during welding,
- post-welding heat treatment (tempering).

The important lack of fusion internal defect (only detectable by ultrasound or X-ray techniques), further reduced the load carrying capacity of the fork, justifying the accident analysed.

The initiation of fatigue cracks, visible in the right fork, indicates that periodic non-destructive inspections with dye penetrant should be performed in this type of equipment.

References

[1] Wegst CW. Stahlschlüssel, Verlag Stahlschlüssel Wegst GmbH, 1995. p. 457.
[2] Pawlowski J. Vehicle body engineering. Business Books, 1969.
[3] BS PD6493. Guidance on some methods for the derivation of acceptance level for defects in fusion welded joints. British Standards Institute, 1980.
[4] Rolfe ST, Barson JM. Fracture and fatigue control in structures. Prentice Hall, 1977. p. 178.
[5] Bailey N, Coe FR, Gooch TG, Hart PHM, Jenkins N, Pargeter RJ. Welding steels without hydrogen cracking. 2nd ed. ASM International and Abington Publishing, 1973.

MODE II INTERLAMINAR FRACTURE OF FILAMENT WOUND ANGLE-PLY SPECIMENS

A. B. de Morais [a,*], J. F. Silva [b], A. T. Marques [c], P. T. de Castro [c]

[a] University of Aveiro, Department of Mechanical Engineering, Campus Santiago, 3810 Aveiro, Portugal
[b] Polytechnic Institute of Engineering of Porto, Department of Mechanical Engineering, Rua de S. Tomé, 4200 Porto, Portugal
[c] University of Porto, Faculty of Engineering, Department of Mechanical Engineering and Industrial Management, Rua Dr. Roberto Frias, 4200-465 Porto, Portugal

[*] Corresponding author. Tel.: 351 234 370830; Fax: 351 234 370953; E-mail: abm@mec.ua.pt)

ABSTRACT

This paper presents a study of the interlaminar fracture of filament wound composites. Mode II end notched flexure (ENF) tests were performed on flat glass/polyester specimens. The tested specimens had asymmetric $[\pm\theta]_4$ angle-ply stacking-sequences, with θ values from 0.8º (hoop winding) to 30º. Due to the low stiffness and probable high toughness, it was not possible to propagate the crack in $[\pm 60º]_4$ specimens before they suffered considerable permanent deformations. A short support span had to be employed for $[\pm 30º]_4$ specimens in order to obtain crack propagation. Nevertheless, the results for those specimens should be viewed with caution, as some non-linear behaviour and small permanent deformations were detected. No other unusual features, such as crack jumping to other interface, were observed. The scatter in the critical strain energy release rate values (G_{IIc}) was higher for $[\pm 10º]_4$ and $[\pm 30º]_4$ specimens than for the quasi-unidirectional ones. G_{IIc} values from the insert were generally lower than those from mode II pre-cracks, except for quasi-unidirectional specimens. A plot of average G_{IIc} values against θ showed a minimum at $\theta = 5º$.

Keywords: interlaminar fracture; filament wound composites; glass/polyester composites; angle-plies; mode II; end notched flexure (ENF) tests; permanent deformations.

1. INTRODUCTION

There has been considerable interest in the characterisation of the delamination resistance of laminated composites [1-3]. On the other hand, very few studies have been conducted on the interlaminar fracture of filament wound composites [4-7]. In filament wound pipes, interlaminar fracture may occur associated to matrix cracking, leading to significant stiffness losses and to increased probability of buckling.

In principle, more difficulties can be expected in the study of interlaminar fracture of filament wound composites than of autoclaved laminates. Firstly, the larger heterogeneity of filament wound composites can result in increased scatter, which is already relatively high for laminated composites. Secondly, typical applications of filament wound composites involve angle-ply $[\pm\theta]_n$ stacking sequences. The interlaminar fracture of multidirectional composites has already received considerable attention e.g. [5-12]. There are, however, several features that complicate toughness measurements. Multidirectional composite specimens often exhibit elastic membrane-bending and bending-bending couplings, which result in non-uniform through-the-width energy release rate distributions. This may lead to highly curved delamination fronts and to local mixed-mode effects [13-15]. Residual stresses may also contribute significantly to measured toughnesses [16]. A major problem in the testing of multidirectional laminates seems to be the high susceptibility to crack jumping and to non-linear behaviour. The toughness of multidirectional laminates remains an important research subject. Thirdly, filament wound parts have curved shapes. Ozdil et al [5-7] have recently

used curved filament wound specimens for mode I, mode II and mixed-mode tests. As the specimens were cut parallel to the cylinder axis, curved supports and loading anvil had to be used. A modified data reduction analysis was also developed to handle specimen through-the-width curvature.

In this work, we have used flat specimens in view of the simplicity of testing and data reduction and of the relatively incipient state-of-the-art, requiring that several basic issues be addressed. Obviously, one may question whether a flat region is representative of an actual curved shape. Truth is, however, that actual applications involve an enormous variety of curvatures, so that the same question of representativity can be put for any specimen curvature.

We have also limited ourselves to the well-known mode II end notched flexure (ENF) test (figure 1). The current mode II test methods have been reviewed in [2,3]. The ENF test has been the most used, in spite of the unstable crack propagation. Stabilisation of the ENF test has been achieved via servo-control, which is unavailable in most testing machines. On the other hand, the ELS test (figure 1) is intrinsically stable if the a/L ratio exceeds 0.55. It is, however, more susceptible to large displacements, and the flexural moduli calculated from the test data are generally much lower than those measured in bending tests. This discrepancy is due to the clamping effects, which are also an undesirable source of scatter. Considering the low bending stiffness of the angle-ply filament wound specimens and the lack of experience in the testing of these materials, we have chosen the ENF test.

Presently, the most comparable data has been obtained by Ozdil et al [5], who showed that the critical strain energy release rate (G_{IIc}) of $[\pm\theta]_{12}$ glass/epoxy specimens increased when θ varied from 30° to 55°. The validity of their results is, however, questionable because of the non-linear load-displacement curves and of the permanent deformations visible after

unloading [5]. Similar results have been reported for angle-ply glass/polyester laminates [8]. The present results seem to agree with those previous studies, except for small θ values.

2. EXPERIMENTAL PROCEDURES

Glass/polyester parts were manufactured by filament winding using a CNC PULTREX machine. The process is schematically depicted in figure 2. Winding was performed at 30 rpm mandrel rotational speed and 0.3 g/Tex fibre tension. The E-glass roving (2400 Tex), sized for Polyester resins, was supplied by VETROTEX. Band-width was 5 mm. The resin was an isophtalic polyester CRYSTIC 272, formulated with 2% catalyst (BUTANOX M50) and less than 0.05 % accelerator (0.4 % diluted Cobalt salt). A 25 μm MELINEX film was inserted at half-thickness to generate the starter crack. Actually, the current mode I standards recommend that the starter film thickness should be less than 13 μm, as it was observed that the G_{Ic} initiation values decreased with decreasing starter film thickness [1-3]. This requirement was also incorporated in mode II test protocols, in spite of the lack of experimental data [2]. The starter film thickness is, in principle, less important in mode II tests, because the G_{IIc} initiation values from the insert are generally higher than those from mode I or mode II pre-cracks [2,3].

Angle-ply $[\pm\theta]_4$ stacking sequences were used, with θ = 5, 10, 30 and 60°. A quasi-unidirectional plate, with θ = 0.8°, was also manufactured by hoop winding. After winding, each part was wrapped by a peel-ply and put into an oven for post-cure at 80 °C during 24 h. Fibre volume fraction was near 50 %. The mandrel was then removed and 20 mm wide specimens were cut perpendicular to the mandrel rotation axis, except the $[\pm 60°]_4$ specimens, which were cut from the $[\pm 30°]_4$ plate.

The ENF tests were initially carried out with a support span $2L$ = 100 mm and with a/L = 0.5 (figure 1), as recommended by the ESIS protocol [17]. This proved to be an excessively

large span for $[\pm 30°]_4$ and $[\pm 60°]_4$ specimens, as they would undergo very large displacements and significant permanent deformations before any sign of crack propagation. The span was therefore reduced to 40 mm, while keeping the a/L ratio at 0.5. Bending tests performed prior to the ENF tests proved that transverse shear effects were negligible: less than 2 % for $[\pm 30°]_4$ specimens. This could be expected from the relatively low bending-to-shear moduli ratio of those specimens when compared to that of unidirectionals. Nevertheless, reducing the support span does decrease the accuracy of toughness measurements by increasing the uncertainty around the true crack length. Unfortunately, it was still impossible to obtain crack propagation for $[\pm 60°]_4$ specimens. Toughness measurements of $-\theta/+\theta$ interfaces at high θ angles should be carried out using stiffer specimens, obtained by increasing the number of layers or by incorporating 0° layers in the stacking sequence. In [5], however, some non-linearity and permanent deformations were still observed with much thicker (12 mm) specimens.

Loading and unloading were performed at 3 and 6 mm/min, respectively, when the span was 100 mm. When the shorter 40 mm span was employed, the above rates were reduced to 1 and 2 mm/min. Unloading curves were recorded to detect any possible non-linearity or permanent deformations, since the test results should then be considered dubious. By sliding the specimens across the supports, three toughness measurements have generally been made: the first from the insert, and the others from the cracks generated in the previous loading cycles. Test results were not considered when the crack jumped from the initial half-thickness plane. This, however, rarely occurred. After each loading cycle, the crack tended to be arrested below the loading anvil, leading to a fairly straight crack front. Such observations agree with the analysis of the elastic couplings. According to [13-15], the magnitude of crack front curvatures and mixed-mode effects is characterised by the parameters $D_c = D_{12}^2/(D_{11}D_{22})$ and $s = D_{16}/D_{11}$, where D_{ij} represent the Classical Lamination Theory bending stiffness

coefficients, computed for each specimen leg, i.e. below and above the crack. Assuming typical layer properties of glass reinforced polymers with 50 % fibre volume fraction (E_1 = 38 GPa, E_2 = 8 GPa, ν_{12} = 0.28, G_{12} = 3 GPa and 0.44 mm layer thickness), one obtains $s = 0$ for all specimens and the D_c ratios of table 1. In all cases, D_c does not exceed the 0.25 "bound" suggested in [15].

Prior to the ENF tests, the flexural modulus (E) of each specimen was measured (table 2). The compliance calibration coefficient m [17] was also determined for some of the specimens. This requires that the compliance C is measured in bending tests with variable crack lengths a, and that m is subsequently determined from the regression

$$C = C_0 + ma^3 \tag{1}$$

with

$$E = \frac{L^3}{4C_0 bh^3} \tag{2}$$

This method, known as experimental compliance calibration (ECC) [17], can be used to obtain the critical strain energy release rate

$$G_{IIc} = \frac{3ma^2 P_c^2}{2b}\frac{F}{N} \tag{3}$$

where P_c is the critical load and F and N are large displacement correction factors [17]. Compliance calibration is strongly recommended when testing from a mode II pre-crack, since the crack front position may be difficult to define. The actual crack length in the ENF test can then be determined using the measured compliance C and the regression (1). In the present case, the crack position was easily visible, because of the near-transparency of the specimens. The ECC method was only used for verification purposes, and was always in good agreement with the corrected beam theory value [17]

$$G_{IIc} = \frac{9a^2 P_c^2}{16Eb^2 h^3} \frac{F}{N} \tag{4}$$

The effect of residual stresses on the toughness measurements will not be considered here. Nairn [16] showed that residual stresses may have a significant contribution to the mode I toughness of multidirectional laminates. In [5], however, the effect of residual stresses on ENF tests of angle-ply filament wound composites was found to be negligible. Actually, the evaluation of residual stresses in filament wound composites is complex, because they depend on the winding parameters e.g. fibre tension. In present study, it seems unlikely that the residual stresses play a relevant role, since most of the resin curing process took place at room temperature. Furthermore, the subsequent post-cure was performed at a relatively low temperature.

The data reduction schemes require the load-displacement point corresponding to crack initiation. ESIS has also suggested two alternative criteria to define the critical point (figure 3): the non-linearity (NL) and the 5 % offset or maximum load (5 %/Max). In the first case, the critical point is the one where the load-displacement curve deviates from linearity. It has been shown, however, that the NL point depends on the plot scale, and that the deviation from linearity is often due to large displacements, leading to unrealistically low G_{IIc} values [2,3]. The 5 %/Max criterion stipulates that a line corresponding to a compliance 5 % larger than the initial one is intersected with the actual load-displacement curve (figure 3). This intersection point will be taken as the critical point, unless it occurs at a larger displacement than the maximum load point. In this case, the critical point is precisely the one of maximum load. This criterion usually results in higher G_{IIc} values than the visual detection ones, and may still be affected by large displacements. We have therefore used the visual detection criterion to define crack initiation, in spite of the inevitable uncertainties. Nevertheless, it is worth mentioning that the observations were facilitated by the near-transparency of the specimens.

3. RESULTS AND DISCUSSION

Figures 4 to 8 show typical load-displacement curves. Considerable fibre bridging was observed on all specimens. No relevant non-linearities or permanent deformations were visible for $[\pm\theta]_4$ specimens with θ up to 10° (figures 4 to 6). Some non-linearity and small permanent deformations were detected in the $[\pm 30°]_4$ specimens (figure 7). The G_{IIc} results for those specimens should therefore be viewed with caution. As mentioned above, even at a reduced span, no crack propagation was achieved for $[\pm 60°]_4$ specimens. The load-displacement curve of figure 8 shows the highly non-linear behaviour of those specimens and the significant permanent deformations after unloading.

Figures 9 to 11 show the results obtained for all tested specimens, while figures 12 and 13 summarise the data in terms of averages and standard deviation-to-average ratios. The scatter is generally higher for the measurements from the insert, except for $[\pm 10°]_4$ specimens, whose G_{IIc} values presented unusually low scatter from the insert and high scatter from the pre-cracks. The scatter for $[\pm 30°]_4$ specimens is also clearly higher than for the quasi-unidirectionals.

The G_{IIc} values from the insert for the quasi-unidirectional specimens are only slightly higher than those obtained from the mode II pre-cracks. The reverse happens for angle-ply specimens, indicating a significant R-curve. Therefore, the problem of crack initiation must be studied in detail, in order to evaluate the effects of the starter film thickness and of the type

and size of the pre-crack. The lower G_{IIc} values obtained for $[\pm 5^\circ]_4$ specimens seem to show that the common ENF tests on unidirectional specimens may not yield the desired conservative toughness values for filament wound composites. The G_{IIc} values then increased with θ for $\theta \geq 5^\circ$. A possible explanation for the influence of θ lies on its effects on the toughening efficiency of fibre bridging and on the size of the plastic zone behind the crack tip. Bridged fibres at an increasing angle can be expected to offer less resistance to crack propagation. On the other hand, specimens with larger θ will have larger matrix plasticity zones behind the crack tip, leading to higher toughness.

4. CONCLUSIONS

A study of the mode II interlaminar fracture of filament wound composites was presented. End notched flexure (ENF) tests were performed on flat glass/polyester specimens. The tested specimens had asymmetric $[\pm\theta]_4$ angle-ply stacking-sequences, with θ values from 0.8° (hoop winding) to 30°. Due to the low stiffness and probable high toughness, it was not possible to propagate the crack in $[\pm 60^\circ]_4$ specimens, which instead suffered significant permanent deformations. It was also necessary to use a short support span for $[\pm 30^\circ]_4$ specimens to actually obtain crack propagation. Nevertheless, the validity of the results for those specimens is somewhat questionable, as some non-linear behaviour and small permanent deformations were detected.

When compared to the quasi-unidirectionals, higher scatter was found in the toughness values of $[\pm 10^\circ]_4$ and $[\pm 30^\circ]_4$ specimens. G_{IIc} values from the insert were generally lower than those from mode II pre-cracks, except for the quasi-unidirectionals. This calls for a detailed study on the influence of the starter film thickness and of the pre-crack type and size.

Average G_{IIc} values decreased from $\theta = 0.8°$ to $\theta = 5°$ and then increased again until $\theta = 30°$. It seems therefore that the common ENF tests on unidirectional specimens may not give conservative toughness values for filament wound composites. The conflicting effects of the layer angle θ on the toughening efficiency of fibre bridging and on the size of the plastic zone behind the crack tip could explain the observed toughness variation.

5. REFERENCES

1. Williams, J.G., Davies, P. and Brunner, A.J., 'Standard tests for the toughness of composite laminates - some bones of contention', Proceedings of the 10th International Conference on Composite Materials (ICCM-10), 1995, Vol. I, 71-75.
2. Davies, P., Ducept, F., Brunner, A.J., Blackman, B.R.K. and Morais, A.B., 'Development of a standard mode II shear fracture test procedure', Proceedings of the 7th European Conference on Composite Materials (ECCM-7), 1996, Vol. 2, 9-15.
3. Davies, P., Blackman, B.R.K. and Brunner, A.J., 'Standard test methods for delamination resistance of composite materials: current status', Applied Composite Materials, **5**, 1998, 345-364.
4. Davies, P. and Rannou, F., 'The effect of defects in tubes: part 1. Mode I delamination resistance', Applied Composite Materials, **1**, 1995, 333-347.
5. Ozdil, F., Carlsson, L.A. and Li, X., 'Characterization of mode II delamination growth in glass/epoxy composite cylinders', Journal of Composite Materials, **34**, 2000, 274-298.
6. Ozdil, F. and Carlsson, L.A., 'Characterization of mode I delamination growth in glass/epoxy composite cylinders', Journal of Composite Materials, **34**, 2000, 398-419.

7. Ozdil, F. and Carlsson, L.A., 'Characterization of mixed mode delamination growth in glass/epoxy composite cylinders', Journal of Composite Materials, **34**, 2000, 420-448.
8. Ozdil, F., Carlsson, L.A. and Davies, P., 'Beam analysis of angle-ply laminate end-notched flexure specimens', Composites Science and Technology, **58**, 1998, 1929-1938.
9. Laksimi, A., Benyahia, A.A., Benzeggagh, M.L. and Gong, X.L., 'Initiation and bifurcation mechanisms of cracks in multi-directional laminates', Composites Science and Technology, **60**, 2000, 597-604.
10. Choi, N.S., Kinloch, A.J. and Williams, J.G., 'Delamination fracture of multidirectional carbon-fiber/epoxy composites under mode I, mode II and mixed-mode I/II loading', Journal of Composite Materials, **33**, 1999, 73-100.
11. Tao, J.X. and Sun, C.T., 'Influence of ply orientation on delamination in composite laminates', Journal of Composite Materials, **32**, 1998, 1933-1947.
12. Polaha, J.J., Davidson, B.D., Hudson, R.C. and Pieracci, A., 'Effects of mode ratio, ply orientation and precracking on the delamination toughness of a laminated composite', Journal of Reinforced Plastics and Composites, **15**, 1996, 141-173.
13. Davidson, B.D. and Schapery, R.A. 'Effect of finite width on deflection and energy release rate of an orthotropic double cantilever beam specimen', Journal of Composite Materials, **22**, 1988, 640-656.
14. Sun, C. T. and Zeng, S. 'Delamination characteristics of double cantilever beam and end-notched flexure composite specimens', Composite Science and Technology, **56**, 1996, 451-459.
15. Davidson, B.D., Krüger, R. and König, M. 'Three dimensional analysis and resulting design recommendations for unidirectional and multidirectional end-notched flexure tests', Journal of Composite Materials, **29**, 1995, 2108-2133.

16. Nairn, J.A. 'Energy release rate analysis for adhesive and laminate double cantilever beam specimens emphasizing the effect of residual stresses', International Journal of Adhesion and Adhesives, **20**, 2000, 59-70.

17. Protocols for interlaminar fracture testing of composites. ESIS-Polymers & Composites Task group. Edited by P. Davies, 1993.

A. B. de Morais. Mode II interlaminar fracture of filament wound angle-ply specimens.

FIGURES CAPTIONS

Figure 1: Schematic representation of the ENF and ELS tests.

Figure 2: Illustration of the filament winding manufacturing of the parts from where specimens were cut.

Figure 3: Alternative ESIS crack initiation criteria [17].

Figure 4: Typical load-displacement curve for a quasi-unidirectional specimen.

Figure 5: Typical load-displacement curve for a $[\pm 5^{\circ}]_4$ specimen.

Figure 6: Typical load-displacement curve for a $[\pm 10^{\circ}]_4$ specimen.

Figure 7: Typical load-displacement curve for a $[\pm 30^{\circ}]_4$ specimen.

Figure 8: Typical load-displacement curve for a $[\pm 60^{\circ}]_4$ specimen.

Figure 9: Results obtained from the insert for all tested specimens.

Figure 10: Results obtained from the first mode II pre-crack for all tested specimens.

Figure 11: Results obtained from the second mode II pre-crack for all tested specimens.

Figure 12: Comparison of the average results.

Figure 13: Comparison of the standard deviation-to-average ratio results.

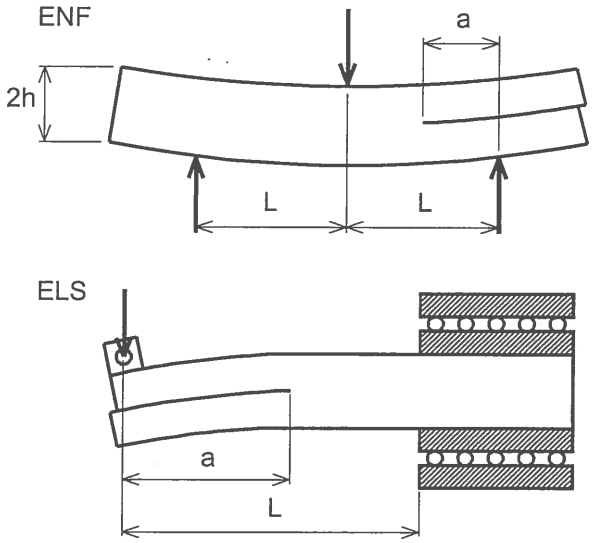

Figure 1

A. B. de Morais. Mode II interlaminar fracture of filament wound angle-ply specimens.

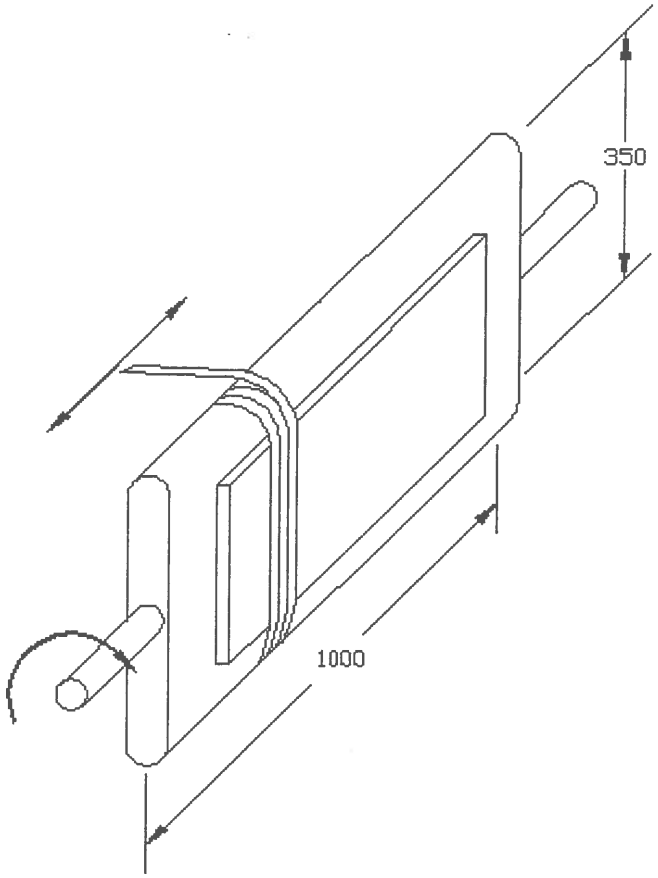

Figure 2

A. B. de Morais. Mode II interlaminar fracture of filament wound angle-ply specimens.

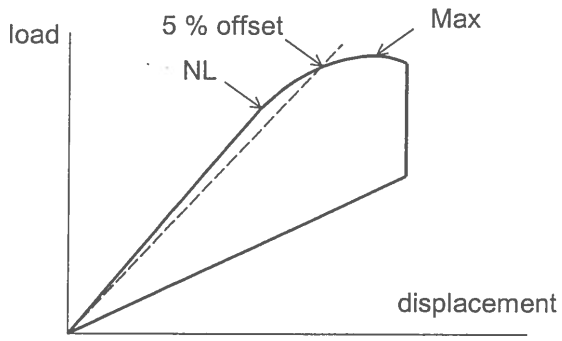

Figure 3

A. B. de Morais. Mode II interlaminar fracture of filament wound angle-ply specimens.

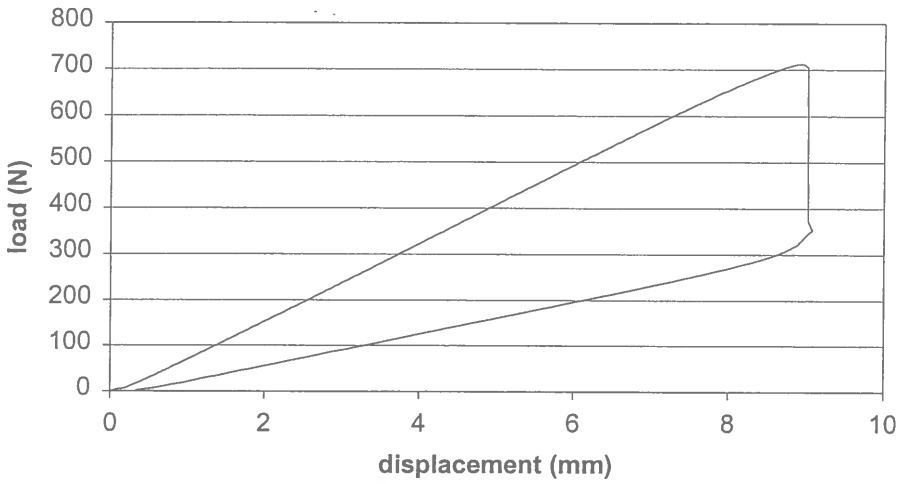

Figure 4

A. B. de Morais. Mode II interlaminar fracture of filament wound angle-ply specimens.

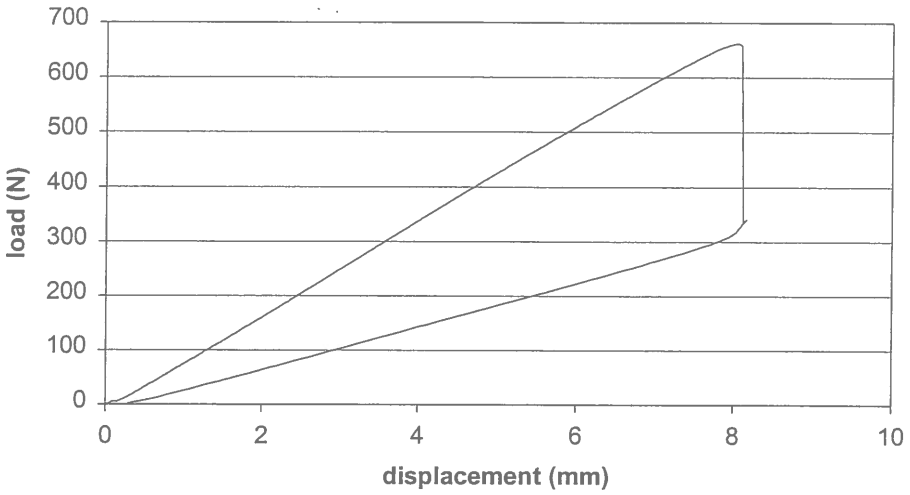

Figure 5

A. B. de Morais. Mode II interlaminar fracture of filament wound angle-ply specimens.

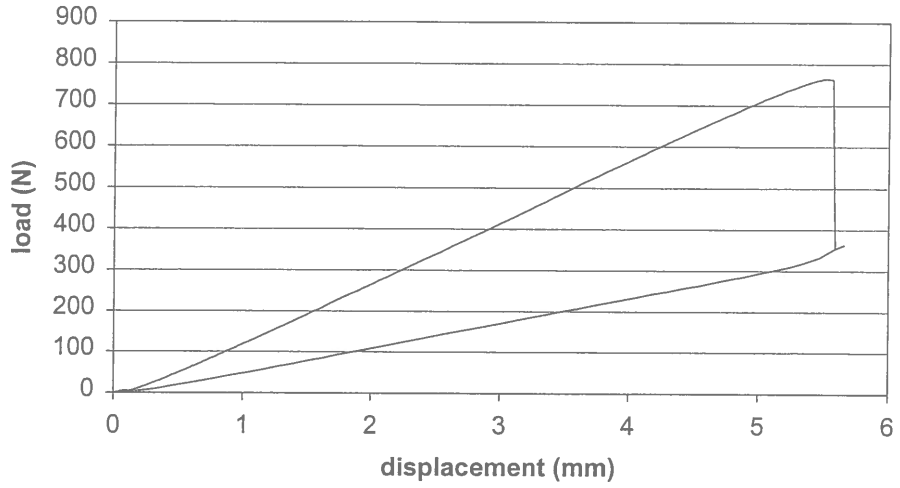

Figure 6

A. B. de Morais. Mode II interlaminar fracture of filament wound angle-ply specimens.

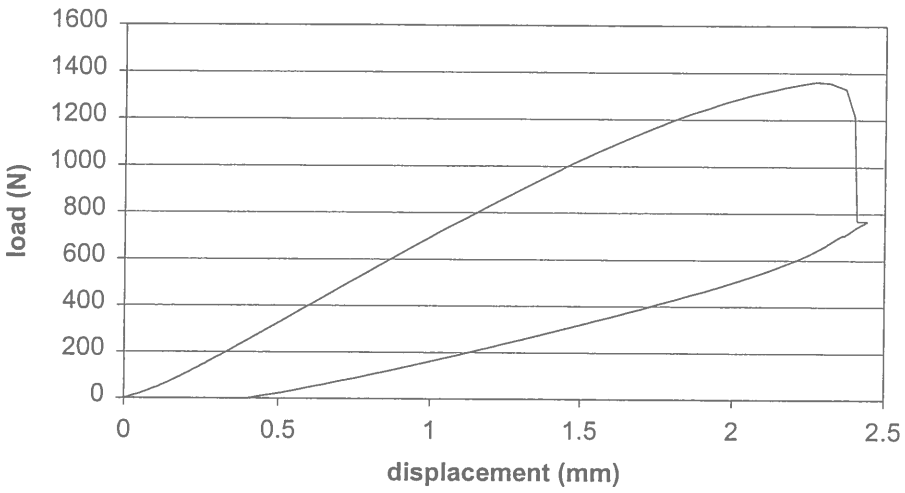

Figure 7

A. B. de Morais. Mode II interlaminar fracture of filament wound angle-ply specimens.

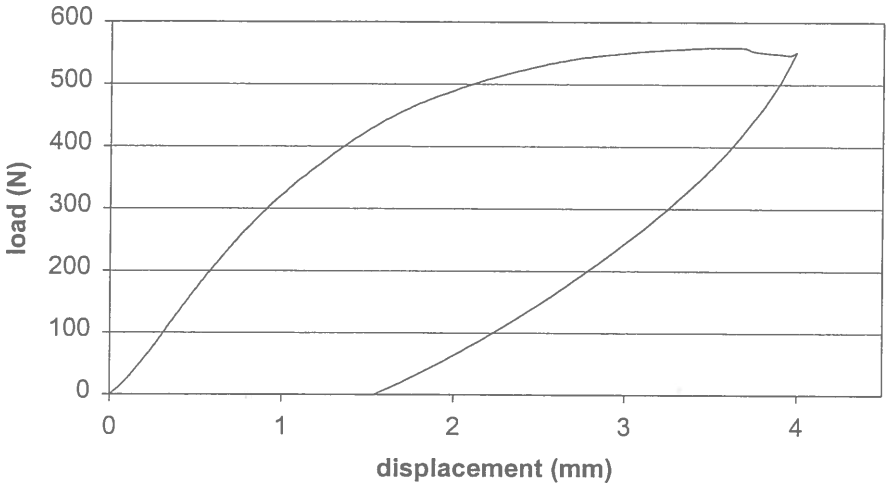

Figure 8

A. B. de Morais. Mode II interlaminar fracture of filament wound angle-ply specimens.

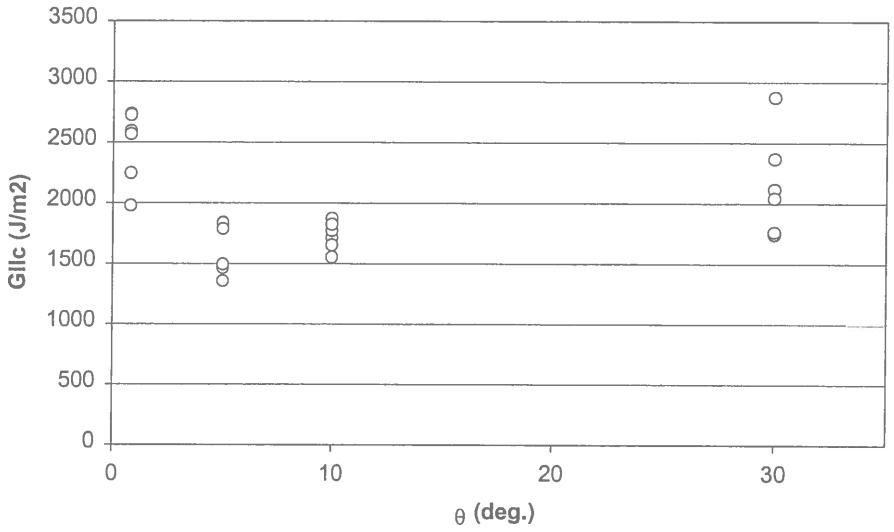

Figure 9

A. B. de Morais. Mode II interlaminar fracture of filament wound angle-ply specimens.

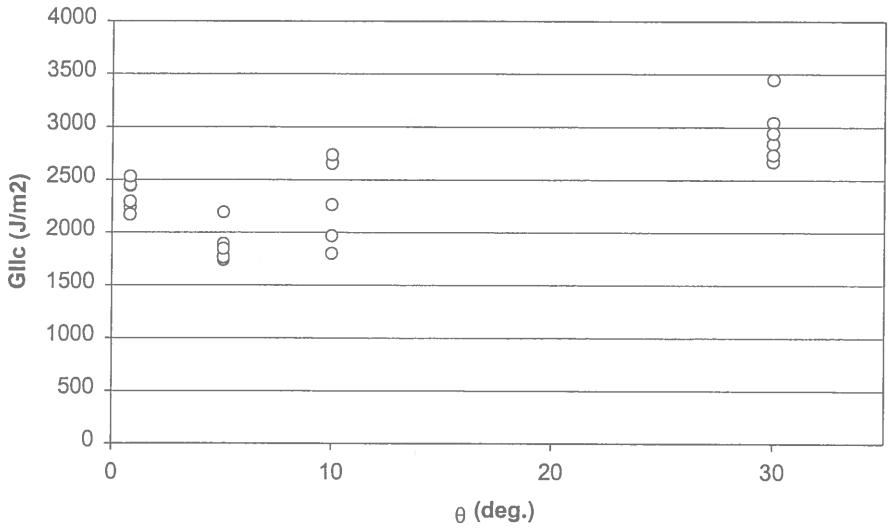

Figure 10

A. B. de Morais. Mode II interlaminar fracture of filament wound angle-ply specimens.

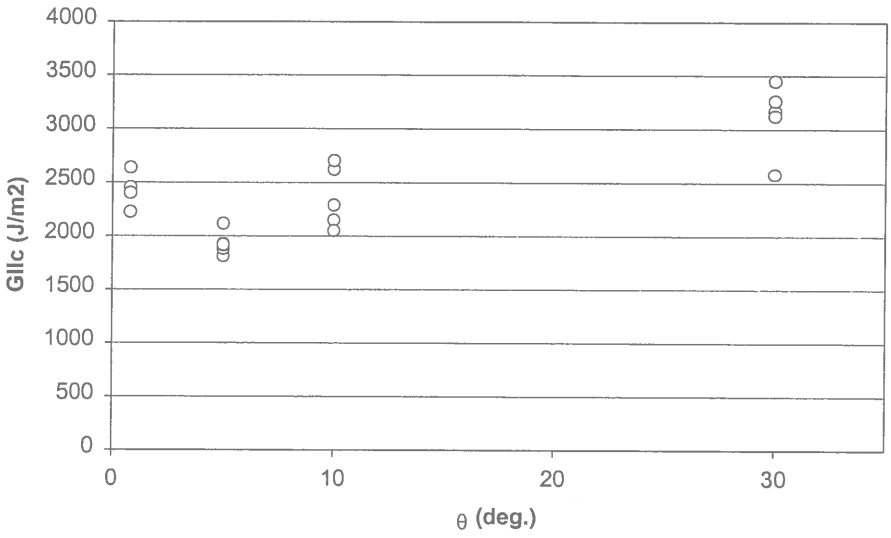

Figure 11

A. B. de Morais. Mode II interlaminar fracture of filament wound angle-ply specimens.

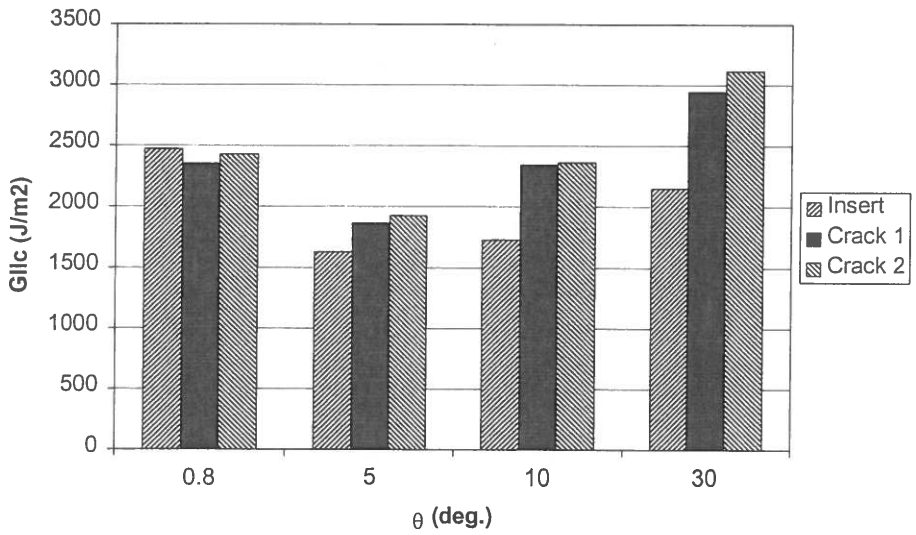

Figure 12

A. B. de Morais. Mode II interlaminar fracture of filament wound angle-ply specimens.

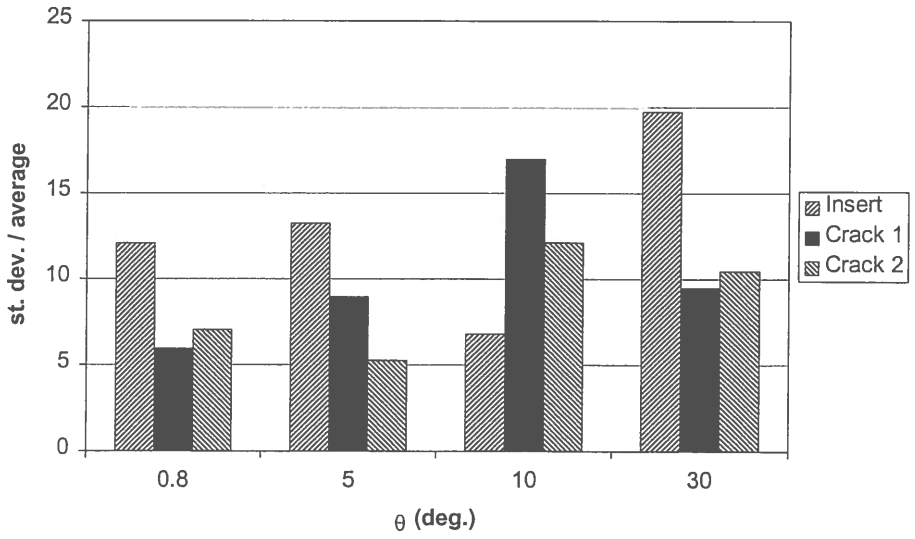

Figure 13

A. B. de Morais. Mode II interlaminar fracture of filament wound angle-ply specimens.

Table 1: Values of the D_c ratio for each leg of the tested specimens.

lay-up	$[\pm 0.8^\circ]_2$	$[\pm 5^\circ]_2$	$[\pm 10^\circ]_2$	$[\pm 30^\circ]_2$
D_c	0.017	0.020	0.033	0.247

Table 2: Thicknesses and moduli of each type of specimen.

Specimen lay-up	$[\pm 0.8^\circ]_4$	$[\pm 5^\circ]_4$	$[\pm 10^\circ]_4$	$[\pm 30^\circ]_4$
thickness (mm)	3.46 ± 0.13	3.49 ± 0.07	3.55 ± 0.17	3.62 ± 0.08
flex. modulus (GPa)	37.02 ± 0.74	35.45 ± 0.61	33.07 ± 1.12	15.02 ± 0.83

THE AMERICAN SOCIETY OF MECHANICAL ENGINEERS
Three Park Avenue, New York, N.Y. 10016-5990

2000-IMECE/DE-6

The Society shall not be responsible for statements or opinions advanced in papers or discussion at meetings of the Society or of its Divisions or Sections, or printed in its publications. Discussion is printed only if the paper is published in an ASME Journal. For authorization to photocopy material for internal or personal use under those circumstances not falling within the fair use provisions of the Copyright Act, contact the Copyright Clearance Center (CCC), 222 Rosewood Drive, Danvers, MA 01923, tel: 978-750-8400, www.copyright.com. Requests for special permission or bulk reproduction should be addressed to the ASME Technical Publishing Department.

Copyright © 2000 by ASME All Rights Reserved Printed in U.S.A.

CRACKED STONE CRUSHER: FAILURE ANALYSIS AND REPAIR

T Novais Barbosa,
F M F Oliveira,
P M S T de Castro,
A A Fernandes

INEGI - Instituto de Engenharia Mecânica e Gestão Industrial
Faculdade de Engenharia da Universidade do Porto
Rua dos Bragas, 4050-123 Porto, Portugal
email: ptcastro@fe.up.pt

ABSTRACT

This paper concerns the progressive failure and the repair of a heavy duty, very large, stone crusher of tronco-conical shape. A crack developed in service due to dynamic loading. The damage is a through thikness crack, visible on the outside of the equipment, but not visible on the inside because of the anti-wear lining used.

The crack progressed slowly over a number of years. The structural integrity analysis of the cracked stone crusher taking into account the service conditions was carried out. The objective of the work is the specification of a repair procedure which might arrest or delay crack propagation, in order that the remaining life of the stone crusher is at least similar to the remaining life of the quarry.

Several alternative solutions for repair were studied, such as the complete welding of the crack, or the reinforcement of the cracked crusher using reinforcement rings or localised welded clamps.

Reasons for the preferred alternative for repair and the metallurgical and mechanical analysis of the proposed solution are presented and discussed.

1. INTRODUCTION AND OBJECTIVE OF THE STUDY

The stone crusher is schematically described in Figure 1. Stones to be crushed are fed from the top, and crushed by the large shaft rotating eccentrically (crusher). The crushed stones are evacuated through the bottom of the cone (vessel). The maximum and minimum inside diameter of the cone are 3.05m and 1.83m, respectively, and its height is 1.71m. This vessel is protected by an interior anti-wear lining, which is replaced periodically. The vessel of the heavy-duty stone crusher presented a crack with an overall length of 1.27m, as schematically shown in Figure 2. This crack has been growing slowly, during years, as a result of the dynamic loading applied to this component in service. The crack is a through thickness crack, clearly visible on the outside, but not visible on the inside, because of the anti-wear lining used.

The main characteristics of the stone crusher are as follows:

- power: 250 CV
- speed: 750 rpm
- shaft speed reduction: 1 - 5.6
- shaft eccentricity: 50mm
- average size of stones at entry: 1000mm - 1200mm
- average size of stones at exit: <300mm
- weight of shaft: 21 t
- weight of crusher vessel: 37 t
- production: 600 to 900 t / hour

The objective of the present study is to perform a structural integrity analysis of the stone crusher, taking into consideration the service conditions, and to propose a cost effective repair solution which will arrest or retard the crack propagation, so that the stone crusher may continue operating until the foreseen end of the quarry.

A finite element modeling of the vessel was performed with I-DEAS finite element method (fem) software. Simplifying assumptions for the boundary conditions of that stress analysis are presented and discussed.

Several alternative solutions for repair were then studied, such as repair by welding of the crack, reinforcement of the cracked vessel using reinforcement rings, or localized welded clamps.

A detailed Fracture Mechanics crack propagation analysis was not carried out, since relevant conclusions could be reached using approximate considerations and engineering judgment as will be explained later.

Presented at the 2000 ASME International Mechanical Engineering Congress & Exhibition
Orlando, FL — November 5– 10, 2000

2. STRUCTURAL ANALYSIS

The definition of the loading imposed upon the stone crusher in service is difficult because of the complex service conditions. In these circumstances, the characterization of the crack tip stress state, relevant for crack propagation studies, is subjected to great imprecision. Bearing in mind these limitations, a finite element stress analysis was performed using the I-DEAS software. The boundary conditions used were the following:

- no rotations or displacements in the base, because of the high stifness of that region and of its connection with the rest of the equipement;
- distributed load, applied on the top, corresponding to the weight of the spider, ie the structure above the vessel, which guides the eccentric shaft - crusher;
- concentrated load, applied at mid-height of the interior of the vessel, simulating a situation of crushing of stones of large dimension against the vessel wall, and with an area of 2500 mm^2.

The maximum applied load (F_{max}) was evaluated taking into account the knowledge of the engine power, and the eccentricity of the shaft.

- Engine power P:
  P = 250 CV = 184 kW

- Maximum torque M_m:
  n = 750 rpm
  $M_m = P / \omega = P / (2\pi n/60) = 2344$ Nm

- Speed reduction i:
  $M_m / M_{appl} = 1 / i$
  i = 5.6
  $M_{appl} = M_m\, i = 13126$ Nm

- Eccentricity e:
  e = 50mm
  $M_{appl} = e\, F$
  $F = M_{appl} / e = 262.5$ kN

Taking into account the dynamic nature of loading, characterized by permanent impacts, the maximum force estimated above was multiplied by a factor of 3. Then, maximum force for analysis is estimated as:

$F_{max} = 788$ kN

I-DEAS Master Series 2.1 fem software was used. Elements were 4-node tetrahedrons with linear interpolation. Several analyses were carried out, starting with the damaged state of the equipment (10135 elements, 7204 nodes) and analyzing several repair alternatives:

1. welding of the crack (12976 elements, 11487 nodes),
2. reinforcement of the cracked vessel using one reinforcement ring (11508 elements, 8065 nodes),
3. localized welded clamps (13296 elements, 11546 nodes).

Because of economic considerations, a welding with lack of penetration was considered as repair solution '1' , where joint preparation and welding would be carried out at the two faces of the crack, but the weld would not extend through all the thickness.

Figure 3 shows the finite element mesh for the repair with a reinforcement ring, whereas Figure 4 shows the mesh for the analysis of the welded clamps repair.

These analyses show that the use of welded clamps reduces very considerably the maximum stress obtained in the crack tip region. For the damaged, non-repaired, equipment, the maximum von Mises stress at the crack tip region was 278 MPa, whereas for the vessel subjected to the repair consisting in welded clamps, the equivalent value is 18.7 MPa, more than ten times smaller.

This very substantial reduction of the calculated stress level, together with the fact that this is a straightforward repair procedure, justified the choice of welded clamps repair. Figure 5 is a perspective of the solid finite element model used, showing the clamps.

A detailed Fracture Mechanics crack propagation analysis was not carried out, since relevant conclusions could be reached using approximate considerations as follows.

A precise identification of stress levels at the crack tip, which would require a very refined mesh or the use of specific techniques to determine stress intensity factor K (or strain energy release rate G or J integral), was not carried out; however, with the level of mesh refinement used, crack tip region stress levels were found to decrease by more than an order of magnitude with the proposed repair (crack tip stress state for the repaired vessel more than 10 times smaller than the state for the un-repaired cracked vessel).

Crack growth has been occurring under conditions which can be described using the simple Paris law approach (ref. 1), since there is no macroscopic plasticity, and they are not 'short crack' behavior.

In these conditions, a decrease of the stress state at the crack tip implies a similar reduction of the amplitude of the stress intensity factor at the crack tip, ΔK:

$$\Delta K = Y \Delta\sigma (\pi a)^{1/2}$$

where Y is a geometry dependent non-dimensional factor.

A reduction of ΔK by an order of magnitude implies a reduction of fatigue crack growth rate by more than an order of magnitude (see for example refs.1 and 2). Such a reduction of crack growth rate was shown to be compatible with the continued operation of the stone crusher at least until the end of the useful exploitation of the quarry

The clamps were designed for the maximum stress levels estimated. The fillet welds for the connection clamp / vessel were designed following the rules for the design of fillet welded connections, as described in a later section of this paper.

3. REPAIR PROCEDURE

The choice of the solution consisting on the use of welded clamps requires the definition of a suitable welding procedure, to be strictly followed by the welders.

The welding procedure is a function of the material of the vessel and of the clamps. Chemical composition of the steel used in the vessel is given in Table 1.

Table 1 – Chemical composition of the vessel's steel

C	0.34
Si	0.35
Mn	0.76
P	0.015
S	0.025
Cr	0.1
Mo	0.03
Ni	0.089
Al	0.073
Cu	0.084

Taking into consideration this chemical composition of the base material, as well as the stress state of the clamps as determined by the fem analysis, it is recommended that the clamp material should be St52.3 steel according to DIN 17100 (ref.3), or an equivalent steel.

Because of the thickness of the vessel (75mm), and the chemical composition of its steel, the use of a fusion weld repair may originate hydrogen induced cracking. Preventive steps must be taken in order to avoid this problem. These steps consist of the control of the thermal energy exchange and the choice of adequate weld metals. In general, cooling is controlled through pre-heating in the area close to the welded connection.

Using the well known carbon equivalent (CE) formula, ref.4:

$$CE = C+(Mn/6)+((Cr+Mo+V)/5)+((Ni+Cu)/15)$$

where quantities of the various elements are given in percentage weights, carbon equivalent was found to be CE = 0.51

Since CE is lower than 0.54, the methodology for determination of pre-heating temperatures of British standard BS 52135:1984, ref. 5, will be used. It was determined that for the equivalent thickness of 200mm, relevant for the welded connection region, the pre-heating temperature should be 175 °C.

The welding procedure recommended under these circumstances is the following:

- manual welding with basic electrodes previously baked or at least taken directly from an unused package;
- pre-heating of the welded region at 175 °C with temperature control using digital thermometer, or thermo-chrome pencil at a distance of 75mm from the welded connection, and after temperature stabilization;
- temperature between passes: 175 °C;
- electrodes of AWS E7018 type, with diameter of 4mm.

4. DESIGN OF THE CLAMP'S WELDED CONNECTIONS

Figure 6 is a sketch of the clamp, highlighting the two surfaces (A and B) where stresses were determined in order to derive the loading on the clamp for the design of the fillet weld connections, see Figure 7.

The design criteria was based on the identification of the components of stress n , $t_\perp$, $t_{//}$ on the throat section, following an approach to design of fillet similar to that of Eurocode 3 (refs. 6, 7), or specified in national codes such as the Portuguese, ref.8. As explained in Figure 8,

- n is stress normal to the rebutted throat section,
- $t_\perp$ is shear stress on the throat section, perpendicular to the fillet weld root, and
- $t_{//}$ is shear stress on the throat section, parallel to the fillet weld root.

The design equation is

$$1.4\,(n^2 + t_\perp^2) - 0.8\,n\,t_\perp + 1.8\,t_{//}^2 = \sigma_e^2$$

where σ_e is $(2/3)\sigma_y$, and σ_y is the yield stress of the base metal. With the input presented before, the specified throat of the welded connections is 17mm.

5. CONCLUDING REMARKS

- A structural integrity case involving the assessment of a cracked vessel of a stone crusher was presented;
- Finite element modeling and structural analysis of the cracked vessel and of several alternative repairs were performed;
- An approximate Fracture Mechanics analysis, based upon simple engineering considerations, justified the solution of repairing the cracked vessel using welded clamps;
- The welding procedure and the design of the weldments was presented;
- This case illustrates the use of finite element structural analysis and engineering judgment based upon Fracture Mechanics considerations, for the purpose of structural integrity assessments.

6. REFERENCES

1. H O Fuchs, R I Stephens, 'Metal Fatigue in Engineering', John Wiley & Sons, 1980
2. N E Frost, K J Marsh, L P Pook, 'Metal Fatigue', Clarendon Press, Oxford, 1974
3. DIN 17100 'Acero para construcciones en general - norma de calidad', Spanish translation in: 'DIN Acero y hierro - normas de calidad', tomo II, Editorial Balzola, Bilbao.
4. J G Hicks, 'Welded Joint Design', John Wiley & Sons, New York, 1979, p.12
5. British Standards Institution, British standard BS 52135:1984
6. Eurocode 3: Design of steel structures; European prestandard ENV 1993-1-1, Feb. 1992; Portuguese translation, version dated March 1998
7. R Arguelles Alvarez, R Arguelles Bustillo, F Arriaga Martitegui, J R Atienza Reales, 'Estruturas de Acero', in Spanish, Bellisco, Madrid, 1999, p.4.17
8. 'Regulamento de Estruturas de Aço para Edifícios', in Portuguese, Imprensa Nacional de Lisboa, 1968, p.61

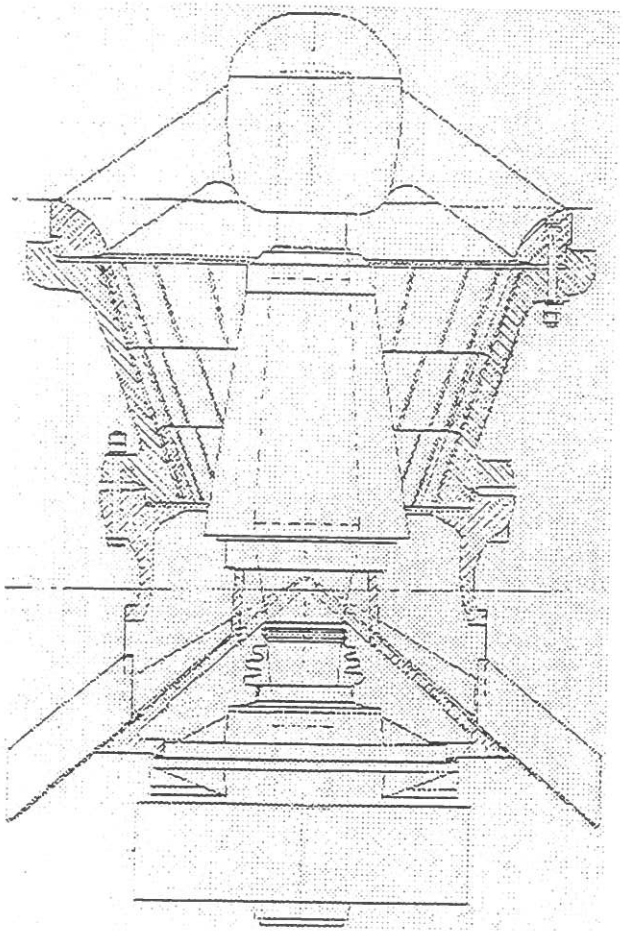

Figure 1 - Schematic representation of the heavy-duty stone crusher

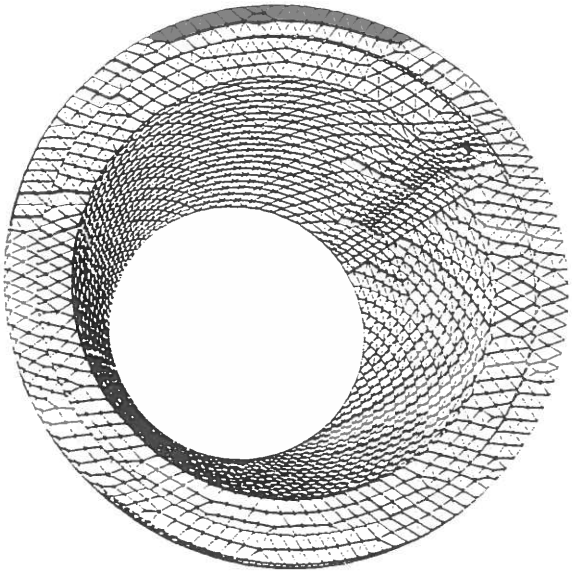

Figure 2 - Finite element model of the cone (vessel). Region containing the crack has a refined mesh.

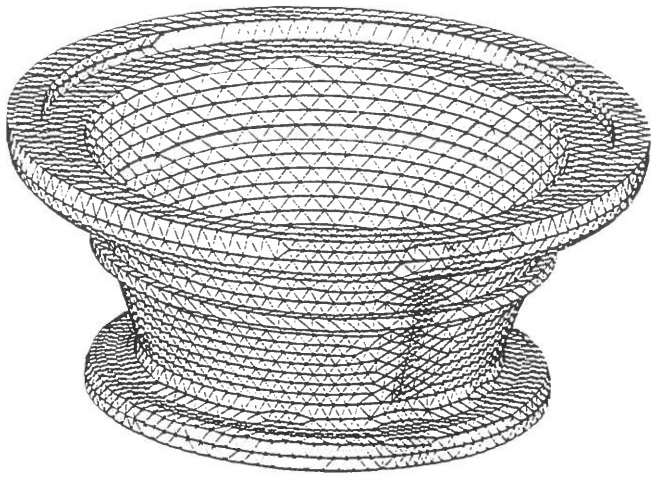

Figure 3 - Finite element model of the repair with a reinforcement ring

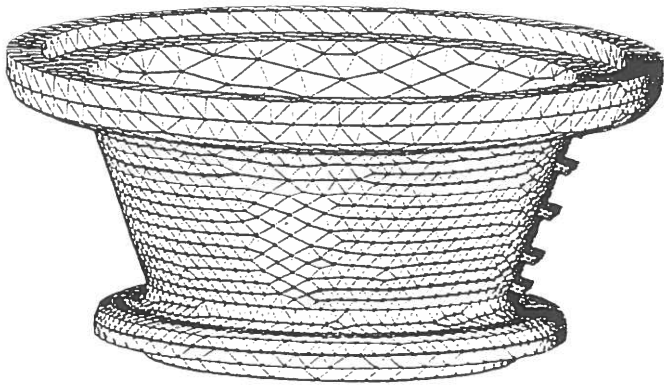

Figure 4 - Finite element model of the repair with clamps.

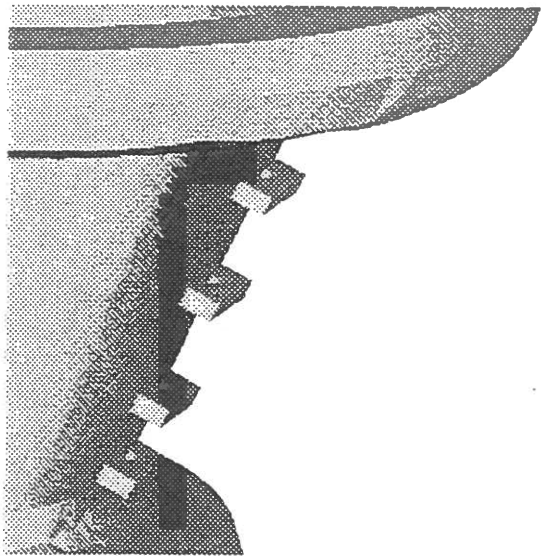

Figure 5 - Perspective of the solid finite element model used, showing the clamps.

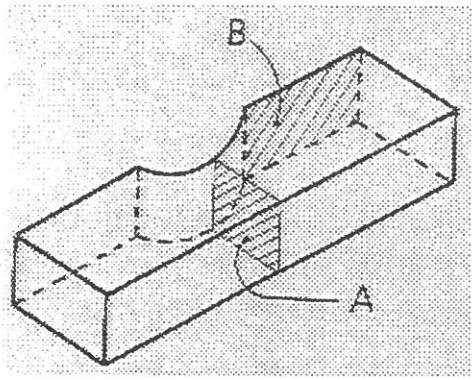

Figure 6 - Schematic representation of the clamps for repair. Stress analysis in sections A and B used to derive the loading on the clamp for design of the fillet weld connections.

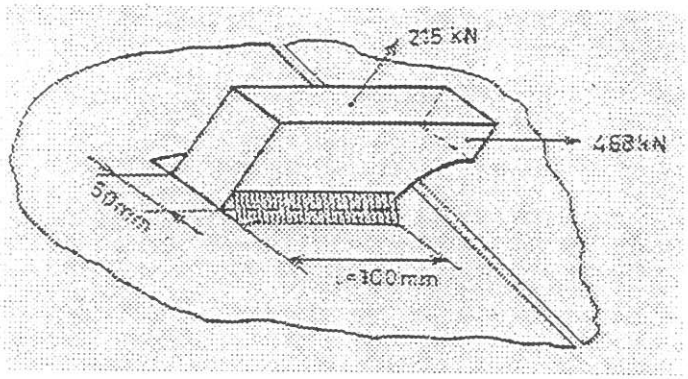

Figure 7 - Schematic representation of the welded clamp, with forces considered for the design of the welded connections.

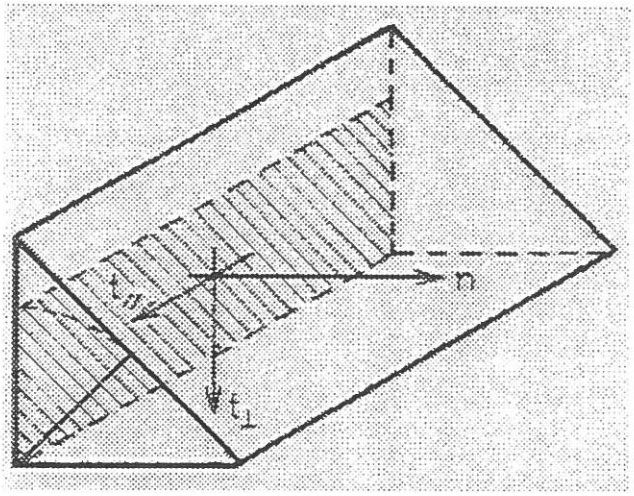

Figure 8 - Stress components for design of fillet welds, acting upon the rebutted throat weld section:

- n is stress normal to the throat section,
- $t_{\perp}$ is shear stress on the throat section, perpendicular to the fillet weld root, and
- $t_{//}$ is shear stress on the throat section, parallel to the fillet weld root.

3RD ESIS TC4 ROUND ROBIN ON CROSS-PLY LAMINATES

REPORT

Results obtained at the University of Porto.

28/12/99

A.B. Morais, A.T. Marques, P.T. Castro

EXPERIMENTAL PROCEDURES

We followed ISO/DIS 15024 as much as possible. The specimens were dried at 75 °C during 24 h, and then stored in a dessicator for no longer than 24 h before testing. Tests were performed using an INSTRON 4208 machine at a 3 mm/min crosshead speed.

RESULTS AND DISCUSSION

In pre-cracking of $[0°/90°]_{6s}$ specimens, the crack jumped to one of the closer 0°/90° interface. Initiation was unstable, but it was possible to keep the pre-crack size below 5 mm. Extensive stick-slip occurred during subsequent propagation, resulting in a "saw-tooth" shaped load-displacement curve (figure 1). We would have to measure successive initiation and arrest values, instead of initiation and propagation values. We therefore concluded that the current ISO/DIS test procedures are not applicable to those specimens. Unusual events were also observed, such as occasional crack jumps and more than one crack propagating at different locations. A slight permanent deformation was also visible.

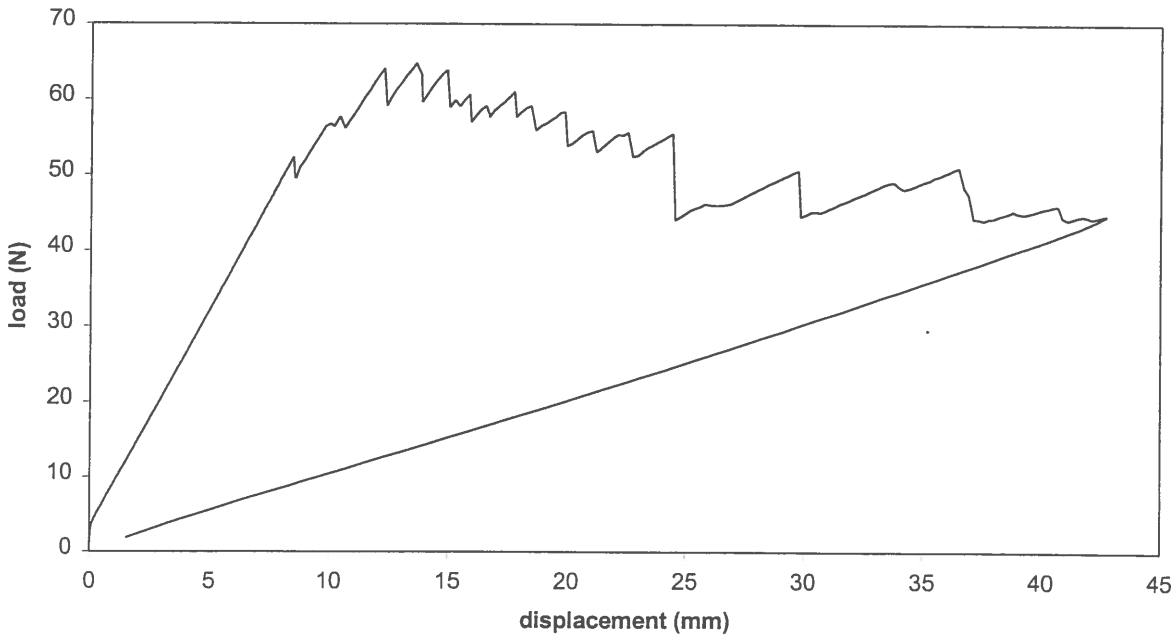

Figure 1: Load-displacement curve for a $[0°/90°]_{6s}$ specimen.

As to $[0°/90°]_{12}$ specimens, crack propagation was relatively easy to follow since there was only occasional stick-slip. Figure 2 shows a typical load-displacement curve during propagation. We observed that the crack "wandered" between two neighbour 0°/90° interfaces, as is schematically depicted in figure 3.

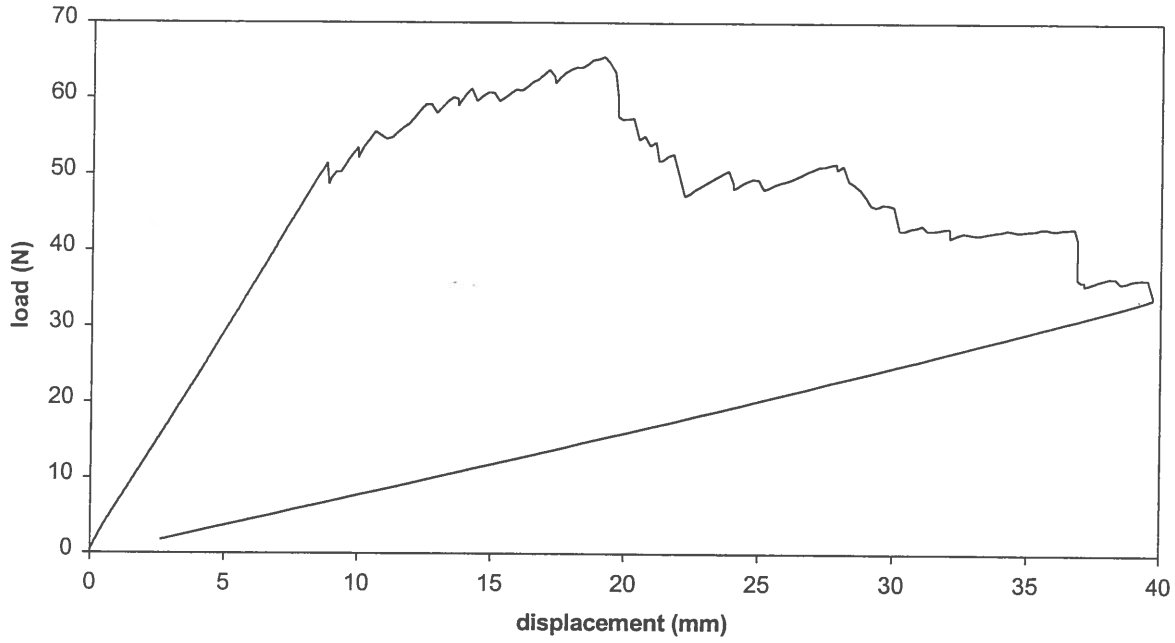

Figure 2: Load-displacement curve for a $[0°/90°]_{12}$ specimen.

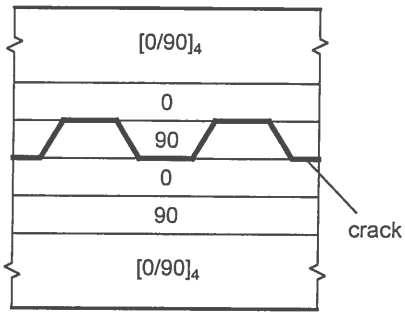

Figure 3: Scheme illustrating crack propagation in $[0°/90°]_{12}$ specimens.

We could nevertheless apply the data reduction worksheets, and actually we obtained apparently consistent results e.g. good $C^{1/3}$.vs.a linear fits, acceptable E-moduli variations, etc. Tables 1 and 2 summarise the main results obtained with $[0°/90°]_{12}$ specimens, and compares them with those of $[0°]_{24}$ specimens. Figures 4 and 5 show typical R-curves. It is clear that, in general, G_{Ic} values of $[0°/90°]_{12}$ specimens are higher than those of $[0°]_{24}$. The difference is particularly large for propagation as a result of the pronounced R-curves of $[0°/90°]_{12}$ specimens, but the scatter is also significant. Shear corrections were relatively small, considering the initial crack sizes.

Table 1: Obtained G_{Ic} values (J/m2).

#Spec.	Initiation				Propagation	
	Film		DCB pre-crack		(maximum)	
	$[0]_{24}$	$[0/90]_{12}$	$[0]_{24}$	$[0/90]_{12}$	$[0]_{24}$	$[0/90]_{12}$
1	275	288	302	513	370	1522
2	267	302	308	500	358	1105
3	263	333	286	483	366	1351
4		321		540		1159
Avg.:	**268**	**311**	**298**	**509**	**365**	**1284**

Table 2: Obtained E-moduli and Δ-transverse shear correction factor. The initial film crack size (a_o) is also shown.

#Spec.	E-modulus (GPa)		a_0 (mm)		Δ (mm)	
	$[0]_{24}$	$[0/90]_{12}$	$[0]_{24}$	$[0/90]_{12}$	$[0]_{24}$	$[0/90]_{12}$
1	151	76.3	55.2	56.9	5.8	7.2
2	156	76.1	56.1	54.3	6.4	6.2
3	162	74.1	54.9	55.1	8.7	6.5
4		64.0		55.4		2.4
Avg.:	**156**	**72.6**	**55.4**	**55.4**	**7.0**	**5.6**

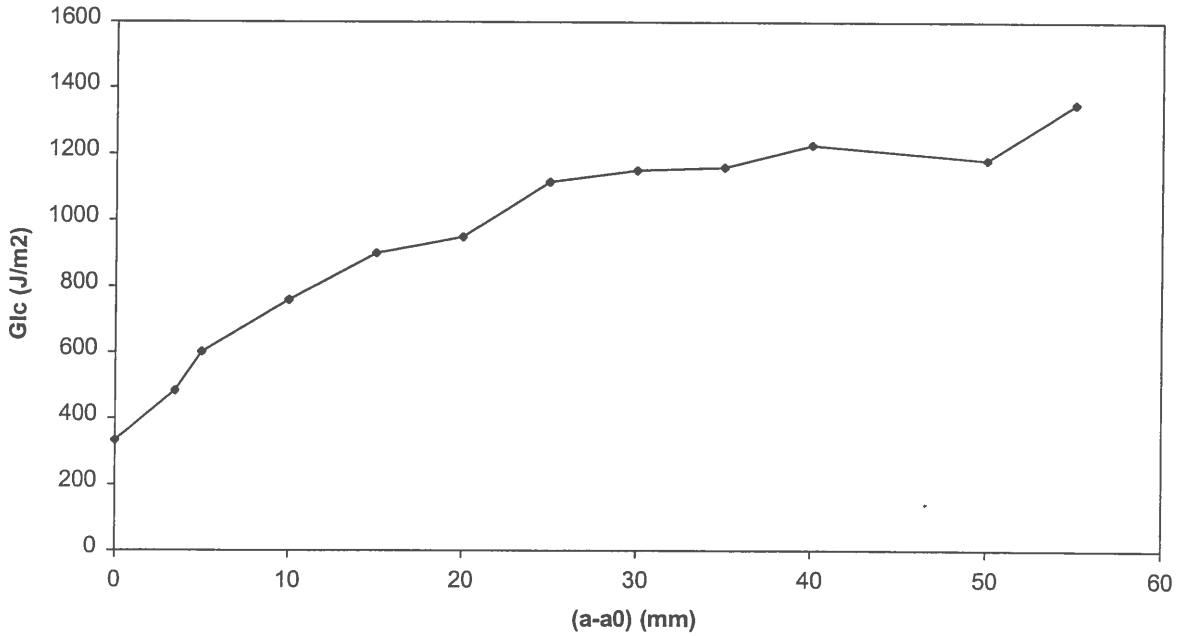

Figure 4: R-curve of a $[0°/90°]_{12}$ specimen.

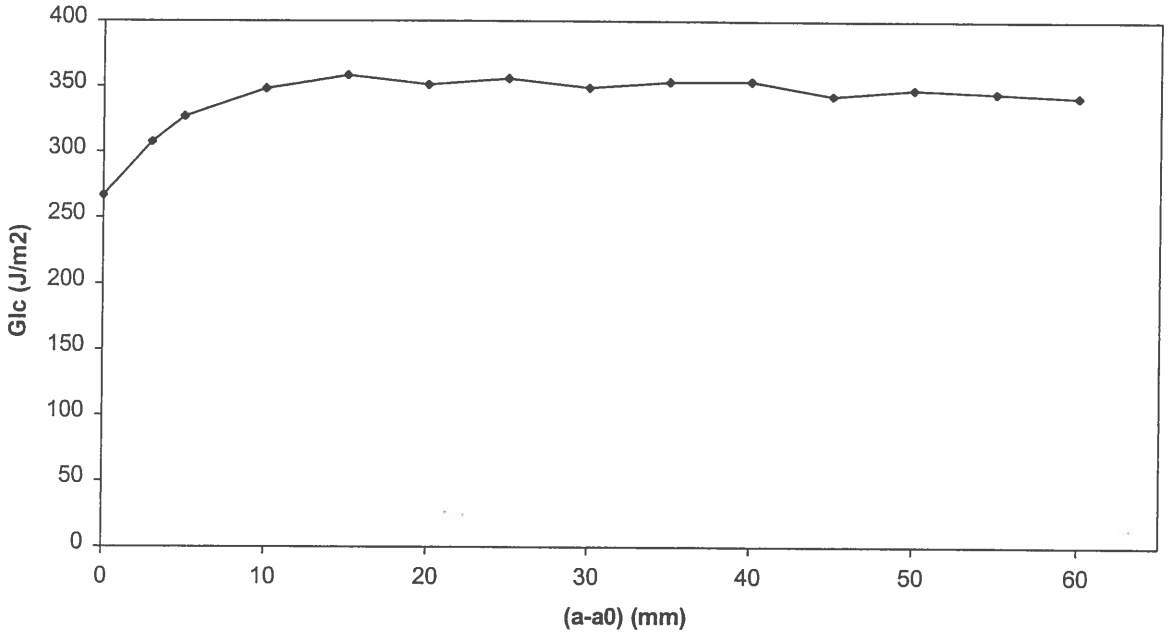

Figure 5: R-curve of a $[0°]_{24}$ specimen.

In spite of the apparent consistency of the above results, we have considerable doubts about the validity of the results, specially in view of the "wavy" crack propagation trajectory. We think there may be two arguments in favour of the validity of the results. First, data reduction assumes a linear crack path, and does not take into account the referred "waviness". The computed G_{IC} could therefore be viewed as an "apparent" interlaminar strain energy release rate. It could be argued that this kind of crack propagation is, in practice, unavoidable. This is confirmed by other studies available in the references.

Second, due to the very low contribution of the near-the-crack 90° plies to flexural stiffnesses of both specimen arms, the crack wandering does not result in a significant flexural stiffness mismatch. Otherwise, a mode II component would arise. This is confirmed by a very simple study we performed. As shown in figure 3, the specimen arms can be either both $[0°/90°]_6$ or $[(0°/90°)_5/0°]$ and $[90°/(0°/90°)_6]$. We assumed typical carbon/epoxy laminate layer properties: E_1 = 150 GPa, E_2 = 11 GPa, ν_2 = 0.25, G_{12} = 6 GPa and 0.165 mm layer thickness. Using Classical Lamination Theory, we obtained the flexural stiffness (EI) for the typical 20 mm wide specimen arms:

- 995 kNmm^2 for $[(0°/90°)_5/0°]$;
- 1066 kNmm^2 for $[90°/(0°/90°)_6]$;
- 1046 kNmm^2 for $[0°/90°]_6$.

When the crack propagates in the initial mid-plane, the flexural E-modulus would be 80.9 GPa. For crack propagation between $[(0°/90°)_5/0°]$ and $[90°/(0°/90°)_6]$ laminates, we can obtain the apparent flexural stiffness

$$2(1/EI) = (1/EI)_1 + (1/EI)_2$$

and then an apparent 79.5 GPa flexural E-modulus, which is quite close to the other value. This explains why we obtained consistent E-moduli for each specimen.

Fatigue Crack Growth of Rails for Railways

Lucas F M Silva, F M F Oliveira, P M S T de Castro

June 2000

INEGI report of the Part 2 Tests for 'Railcrack' Project SMT4 – CT98 – 2240 'Fatigue crack growth rate qualifying criteria of rails for railways: Test conditions to be optimised'

Table of contents

Abstract 3
1 Introduction 4
2 Test procedure 4
3 Data reduction techniques 6
4 Test results and analysis 10
4.1 Specimen 1B4 10
4.2 Specimen 2B9 14
4.3 Specimen 3B14 18
4.4 Specimen 4B19 22
4.5 Specimen 4B20 26
5 Comparison and conclusion 29
Annex 1 - A basic computer program that utilises the seven point incremental polynomial technique 31
Annex 2 – Tensile and hardness testing 34

Abstract

According to the Report of the Part 1 Tests for 'Railcrack' Project SMT4 - CT98 – 2240:

The purpose of this project was to determine the effects of stress ratio and relative humidity of laboratory air on the fatigue crack growth rates of grade 260 rail steel of the draft European Rail Standard, and to measure the scatter in fatigue crack growth rates measured in six laboratories in different countries within the European Union under conditions within this draft standard.

The rails from four manufacturers were machined to produce ten single edge notched bend specimens, as described in the draft standard, from each rail. Part 1 of the project determined the effects of different factors, namely laboratory, rail source, stress ratio and relative humidity on the fatigue crack growth rate by carrying out twenty tests using an experimental design. Two laboratories carried out ten tests each under test conditions using two levels of stress ratio, 0.2 and 0.5, and three levels of relative humidity, < 10%, ~ 35% and ~ 60%.

Based on the findings of the Part 1 results, the conditions for the Part 2 tests have been set at a stress ratio of 0.5, with test temperature and relative humidity recorded but not controlled beyond the ambient laboratory condition, with cyclic test frequency added as a factor in the experimental design. Test frame and crack monitoring details also will be reported, but will not be explicitly studied.

This report presents the da/dN *vs* ΔK curve determination of five specimens under the conditions set for the Part 2 of the railcrack project.

1 Introduction

The secant method and the seven point incremental polynomial technique based on the ASTM E 647 standard were used for analysing the experimental data. In the third section of this report, these procedures are described and applied to a set of raw data, treated by all partners.
Fatigue crack growth rates are presented for specimens 1B4, 2B9, 3B14, 4B19 and 4B20 under the conditions set for the Part 2 of the railcrack project.
Firstly, in section 2 (Test procedure), the factor settings are presented along with the test frame and crack monitoring details.
In the test results and analysis section, both raw data and treated data (secant method and seven point incremental polynomial technique) are given for each specimen.
The fatigue test of specimens 2B9, 3B14 and 4B19 was stopped before failure and the specimens were loaded in tension in order to determine the load at failure.
Finally, some comments on the results are drawn in the conclusion section.

2 Test procedure

The specimens were fatigue tested in a servo-hydraulic MTS testing machine 312.31 with a capacity of 250 kN. The machine contains two columns.
The tests rig is presented in figure 1. The two travelling microscopes to measure the crack length on both sides of the specimen can be seen in this figure. The amplifications of the microscopes are 30x for side 1 and 40x in side 2. The resolution is 0.01 mm for both sides.

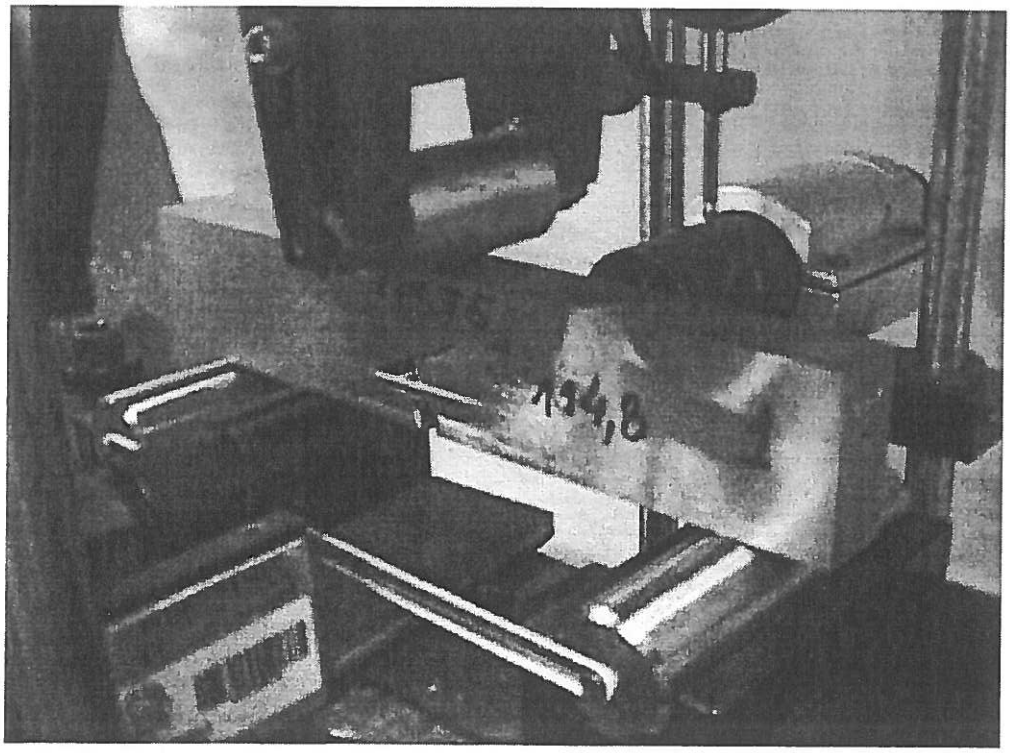

Figure 1 – Test rig

The specimens are of the single edge notched bend type with dimensions of W = 45 mm, B = 20 mm and L = 230 mm. However specimen 1B4 is smaller because the original specimen failed before fatigue crack measurements could be carried out, and one smaller specimen was machined from one of the broken parts.
Figure 2 shows the specimens geometry and Table 1 gives the dimensions for each specimen.

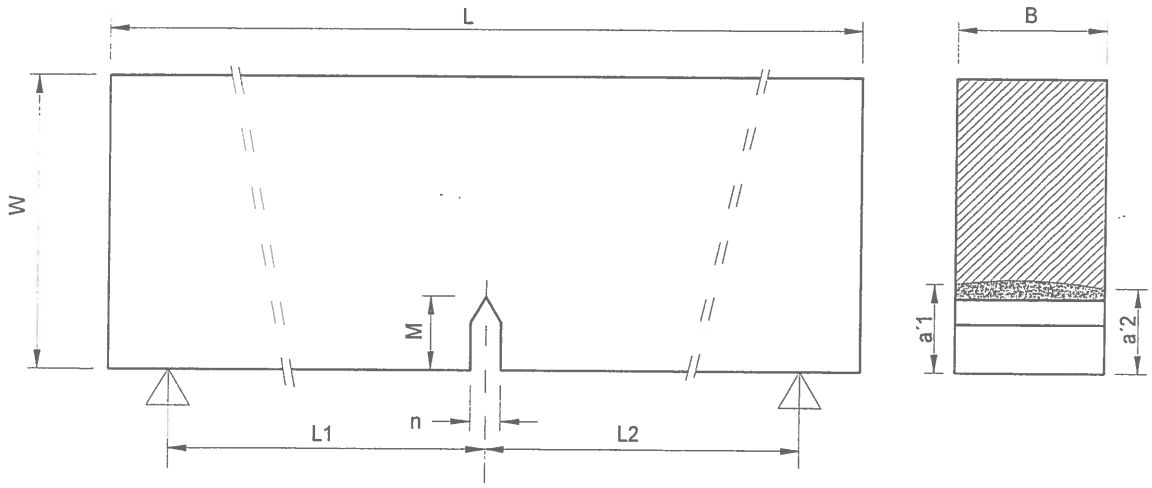

Figure 2 – Specimens geometry

	W	B	L	M	n	L_1	L_2
1B4	27.00	12.05	114.80	6.09	2.11	54.00	54.00
2B9	45.05	20.00	229.50	9.97	3.96	90.00	90.00
3B14	45.05	20.00	229.75	10.07	4.05	90.00	90.00
4B19	45.00	20.04	229.50	9.81	4.03	90.00	90.00
4B20	45.00	20.05	229.50	9.82	4.02	90.00	90.00

Table 1 – Dimensions for each specimen (mm)

The factor settings for each specimen are given in Table 2.

Specimen ref.	Rail manufacturer	Stress ratio (R)	Frequency (Hz)	Temperature	Relative humidity
1B4	1	0.5	10	record	record
2B9	2	0.5	10	record	record
3B14	3	0.5	15	record	record
4B19	4	0.5	10	record	record
4B20	4	0.5	15	record	record

Table 2 – Factor settings

3 Data reduction techniques

The data is analysed by two procedures: the secant method and the seven point incremental polynomial technique.

For the secant method, da/dN at crack length a_i is calculated as follows:

$$\frac{da}{dN}(\text{m/cycle}) = \frac{a_{i+1} - a_{i-1}}{N_{i+1} - N_{i-1}} \times 10^{-3}$$

where

a_{i+1} is the crack length (in mm) of the next record;
a_{i-1} is the crack length (in mm) of the previous record;
N_{i+1} is the count of individual cycles for the next record;
N_{i-1} is the count of the individual cycles of the previous record.

ΔK is calculated from a_i, using the following equation:

$$\Delta K = \frac{\Delta P\, Y}{B\sqrt{W}}$$

where

ΔP is the force range (P_{max}-P_{min}) (in kN);

$$Y = \sqrt{1000} \times \frac{6\sqrt{\alpha}\left\{1.99 - \alpha(1-\alpha)(2.15 - 3.93\alpha + 2.7\alpha^2)\right\}}{(1+2\alpha)(1-\alpha)^{1.5}}$$

with $\alpha = a/W$ (see BS 6835 standard);
B is the specimen thickness (in mm);
W is the specimen width (in mm).

The seven point incremental polynomial method (see ASTM E 647 standard) for computing da/dN involves fitting a second-order polynomial (parabola) to sets of (2n+1) successive data points, where n is 3. The form of the equation for the local fit is as follows:

$$\hat{a}_i = b_0 + b_1\left(\frac{N_i - C_1}{C_2}\right) + b_2\left(\frac{N_i - C_1}{C_2}\right)^2$$

where

$$-1 \le \left(\frac{N_i - C_1}{C_2}\right) \le +1$$

and b_0, b_1, and b_2 are the regression parameters that are determined by the least squares method (minimisation of the square of the deviations between observed and fitted values of crack length) over the range $a_{i-n} \le a \le a_{i+n}$. The value $\hat{a}_i$ is the fitted value of crack length at N_i. The parameters $C_1 = 1/2(N_{i-n} + N_{i+n})$ and $C_2 = 1/2(N_{i+n} - N_{i-n})$ are used to scale the input data, thus avoiding numerical difficulties in determining the

regression parameters. The rate of crack growth at N_i is obtained from the derivative of the above parabola, which is given by the following expression:

$$(da/dN)_{\hat{a}i} = b_1/C_2 + 2b_2(N_i-C_1)/C_2^2$$

The value of ΔK associated with this da/dN value is computed using the fitted crack length, $\hat{a}_i$, corresponding to N_i.

A computer program that utilises the above scheme is given in Annex 1.

Table 3 contains the raw data given for treatment by all partners, in order to compare their data reduction techniques.

Cycles	a
	mm
0	13.51
117054	13.96
198092	14.41
270125	14.86
324150	15.31
391682	15.76
450209	16.21
513238	16.66
546554	17.12
596076	17.57
642898	18.02
682517	18.47
706828	18.92
761753	19.37
795969	19.82
828384	20.27
858098	20.72

Cycles	a
	mm
890513	21.17
912123	21.62
927430	22.07
957144	22.52
975152	22.97
990459	23.42
1005767	23.87
1017472	24.32
1026476	24.77
1037281	25.22
1046285	25.67
1052588	26.12
1061592	26.57
1065194	27.02
1066094	27.47
1071497	27.92

Table 3 – Raw data to be analysed by all partners for comparison

Figures 3 and 4 present the da/dN *vs* ΔK curve using the secant method and the seven point incremental polynomial technique respectively. The da/dN *vs* ΔK curve determined with the seven point incremental polynomial technique is very smooth compared with the secant method, as it could be expected.

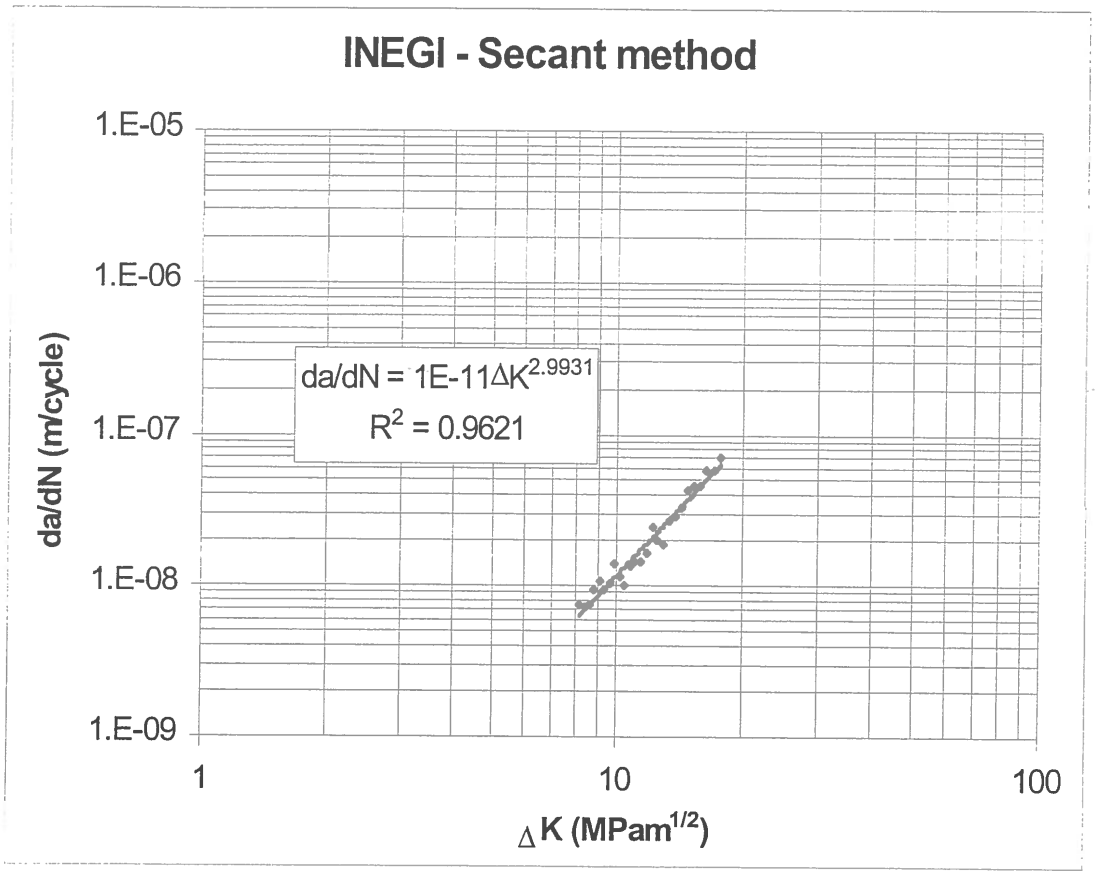

Figure 3 – da/dN *vs* ΔK curve with the secant method (raw data of table 3)

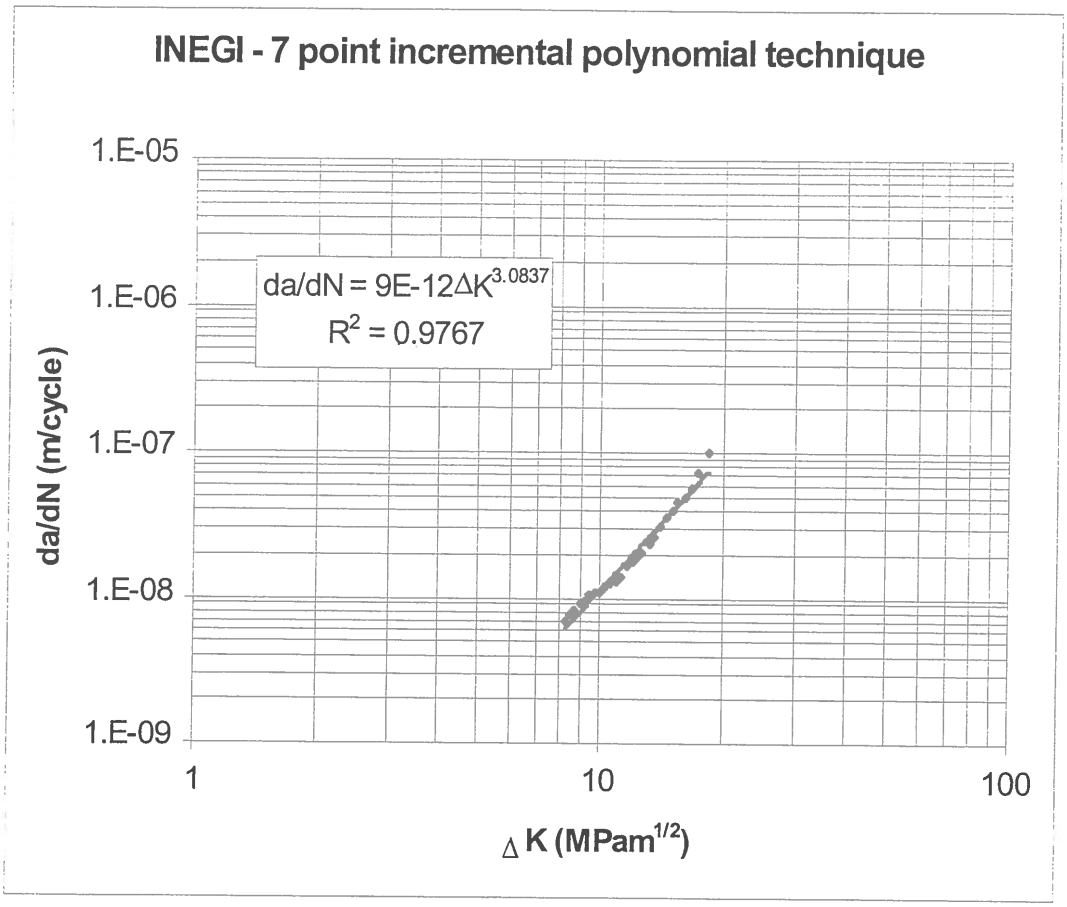

Figure 4 – da/dN *vs* ΔK curve with the seven point incremental polynomial technique (raw data of table 3)

4 Test results and analysis

The raw data, i.e. the number of cycles and the crack length, is given for each specimen in a table and graphically. The crack length is the average of the crack length measured on sides 1 and 2. The table indicates also the relative humidity and the temperature. Then the data is analysed by two procedures: the secant method and the seven point incremental polynomial technique.

4.1 Specimen 1B4

Specimen 1B4 failed before we could get any points for the da/dN *vs* ΔK curve. Then, a smaller specimen was manufactured from one of the broken parts (dimensions indicated in table 1). The localisation of the smaller specimen is shown in Figure 5.

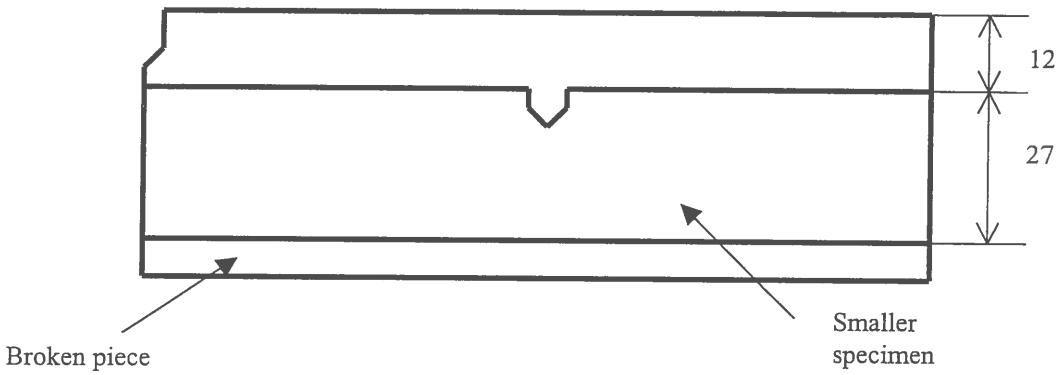

Figure 5 – Localisation of the smaller specimen (in mm)

For the fatigue crack growth rate determination of specimen 1B4, P_{max} = 4.6 kN and P_{min} = 2.3 kN.
Table 4 and figure 5 give the raw data, figure 6 the da/dN *vs* ΔK curve with the secant method and figure 7 the da/dN *vs* ΔK curve with the seven point incremental polynomial technique.
At 514000 cycles an overload occurred (the maximum load should be 4.6 kN and it went to around 6 kN). So the points after that number of cycles should not be considered. However they are indicated in table 4 and figure 5.
The specimen failed at 542854 cycles.

Cycles	a	RH	T
	mm	(%)	(°C)
0	9.47	47	24
30000	9.60		
70000	9.74		
120000	9.99		
160000	10.31	44	23
190000	10.43		
220000	10.59		
250000	10.78		
280000	11.07		
300000	11.25		
320000	11.39	48	24
345000	11.67	42	21
365000	11.97		
380000	12.20		
395000	12.34		
410000	12.43		
435000	12.65		
460000	13.05		
475000	13.27		
490000	13.60	46	22
502000	13.82		
514000	14.11		
524000	14.69		
534000	15.72		
539000	16.25		
541000	16.48	44	23

Table 4 – Specimen 1B4, raw data

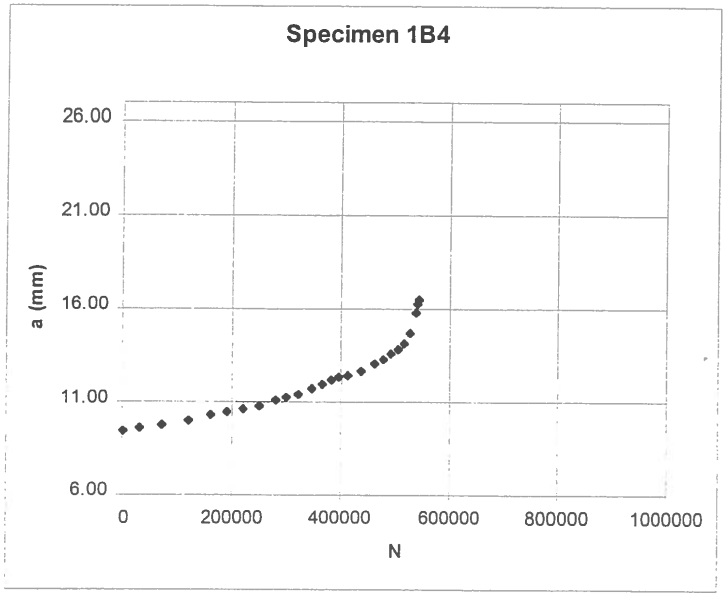

Figure 6 – a *vs* N, specimen 1B4

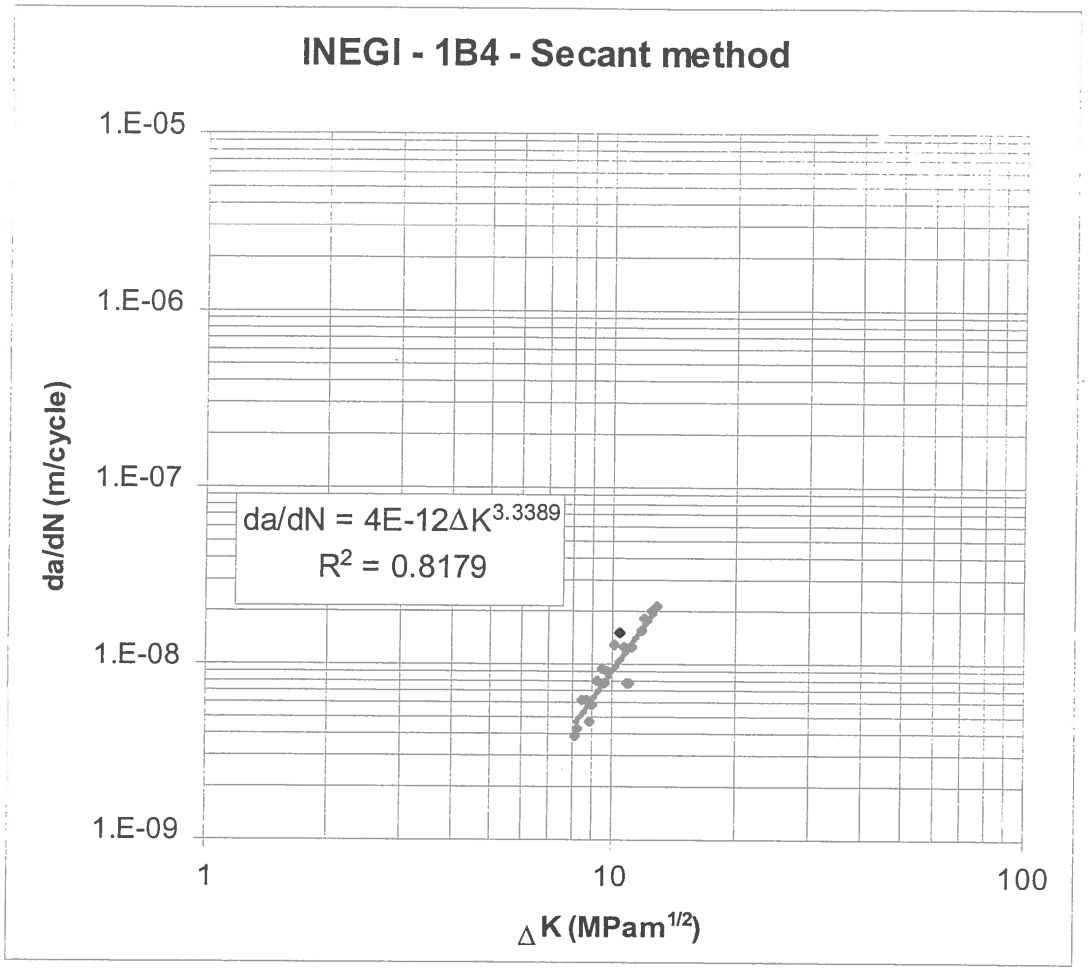

Figure 7 - da/dN *vs* ΔK curve with the secant method, specimen 1B4

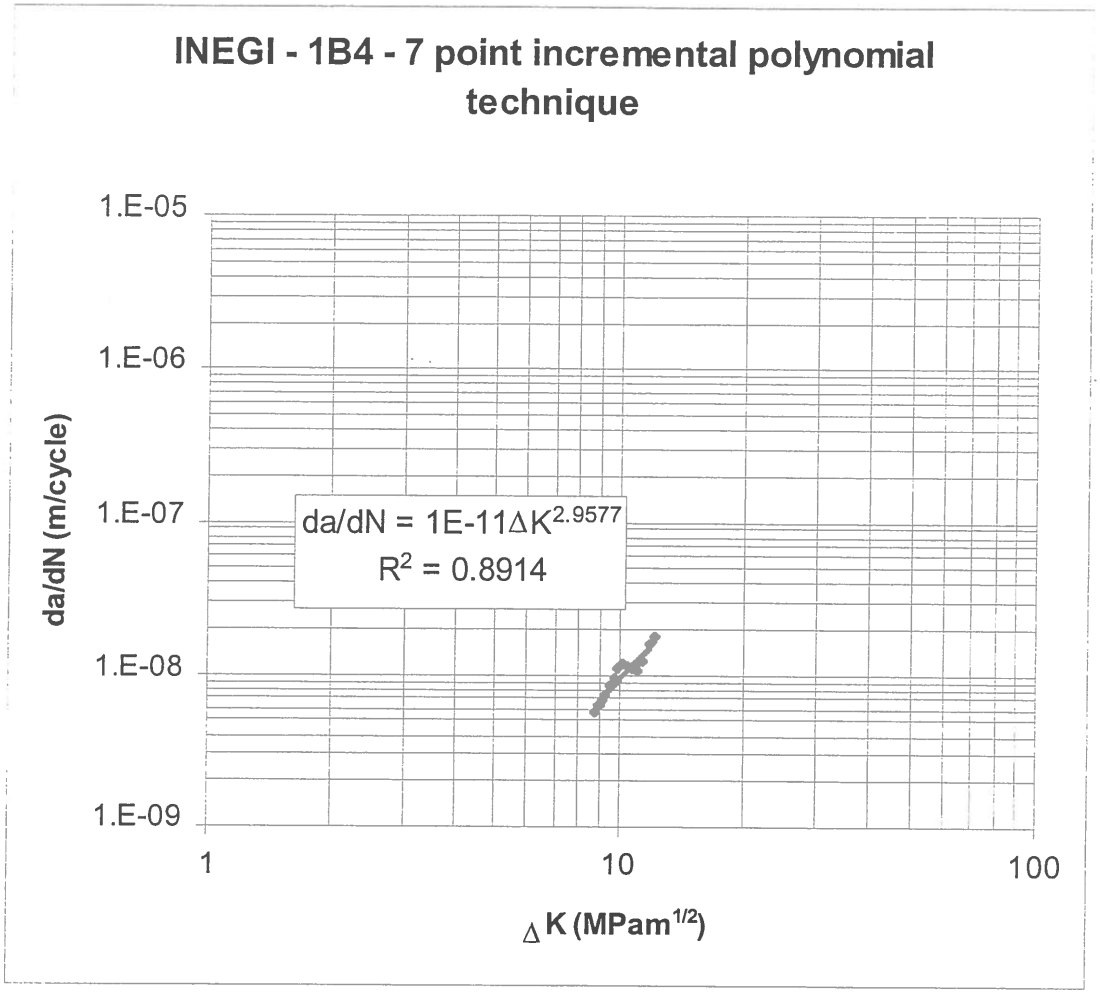

Figure 8 - da/dN *vs* ΔK curve with the seven point incremental polynomial technique, specimen 1B4

Figure 8 represents the fracture surface of the original specimen with a completely brittle fracture and figure 9 is the fracture surface of the small specimen with fatigue and brittle fractures. It should be noted that for the fatigue and brittle fracture, the terminal area of the fatigue has brittle parts indicating that the crack growth was unstable. This is true for all the other specimens.

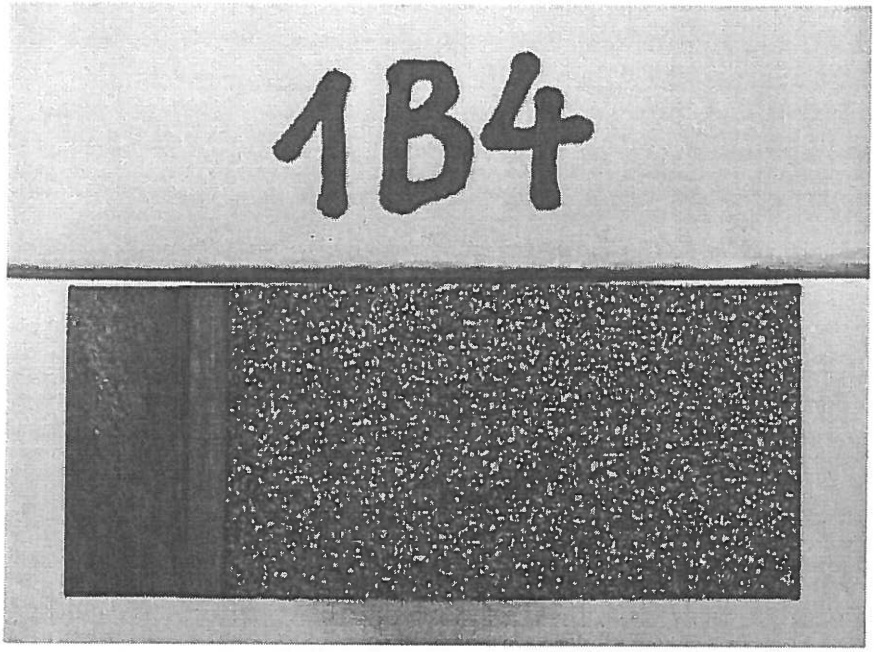

Figure 9 – Specimen 1B4 fracture surface (original specimen)

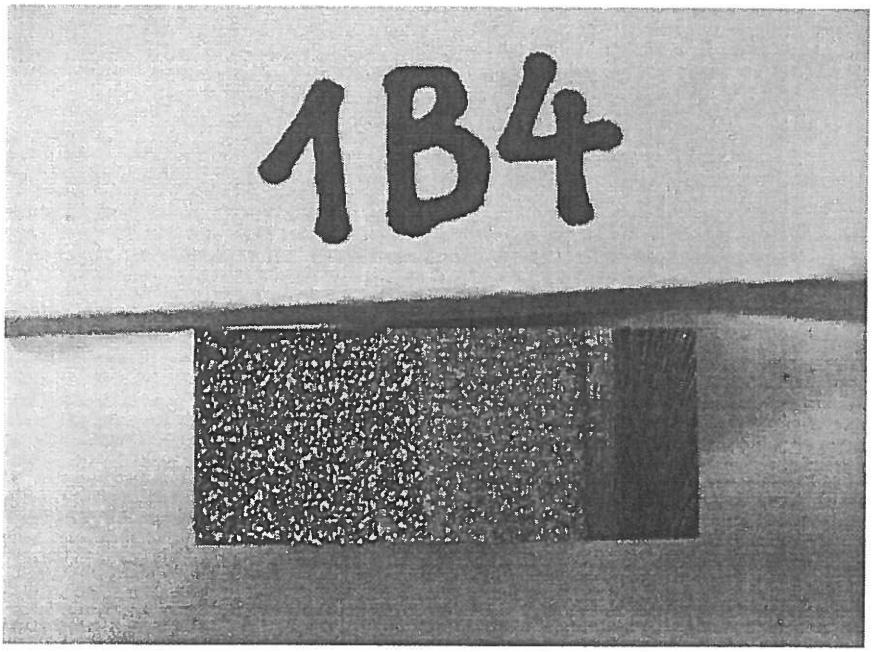

Figure 10 – Specimen 1B4 fracture surface (small specimen)

4.2 Specimen 2B9

For the fatigue crack growth rate determination of specimen 2B9, the P_{max} = 11 kN and P_{min} = 5.5 kN.
Table 5 and figure 10 give the raw data, figure 11 the da/dN *vs* ΔK curve with the secant method and figure 12 the da/dN *vs* ΔK curve with the seven point incremental polynomial technique.
It should be noted that from 0 to 787500 cycles the crack lengths differ by more than 0.1a so this data is not presented here.

Cycles	a	RH	T
	mm	(%)	(°C)
787500	22.47		
797500	22.72		
807500	22.98	60	21
817500	23.24		
827500	23.50		
837500	23.84	60	21
845000	24.01		
852500	24.29		
860000	24.65		
865000	24.84		
870000	24.97	60	21
875000	25.13		
880000	25.35		
885000	25.49		
890000	25.74		
895000	25.99		
900000	26.22	60	21
905000	26.44		
910000	26.74		
913000	26.92		
916000	27.14		
919000	27.37		
921000	27.59		
923000	27.86		
924000	28.04		
925000	28.14		

Table 5 – Specimen 2B9, raw data

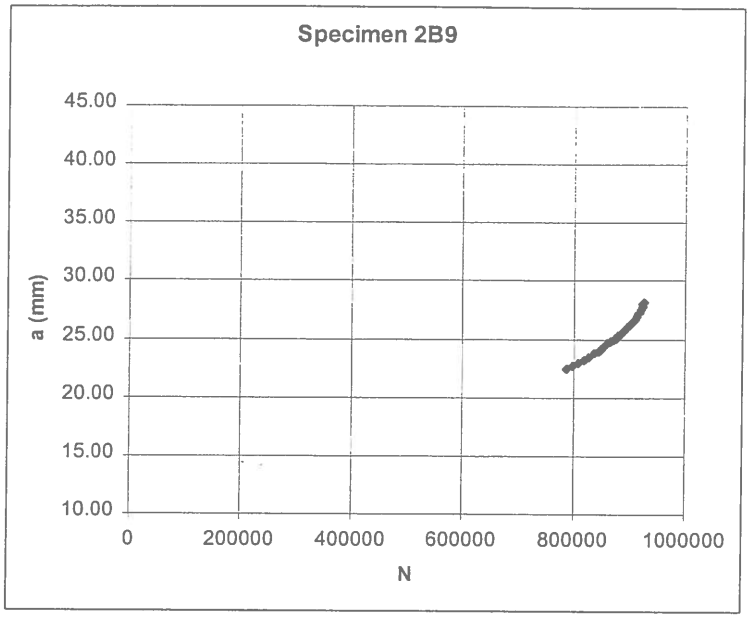

Figure 11 - a *vs* N, specimen 2B9 (scale is the same of figures 15, 20 and 25 for purpose of comparison)

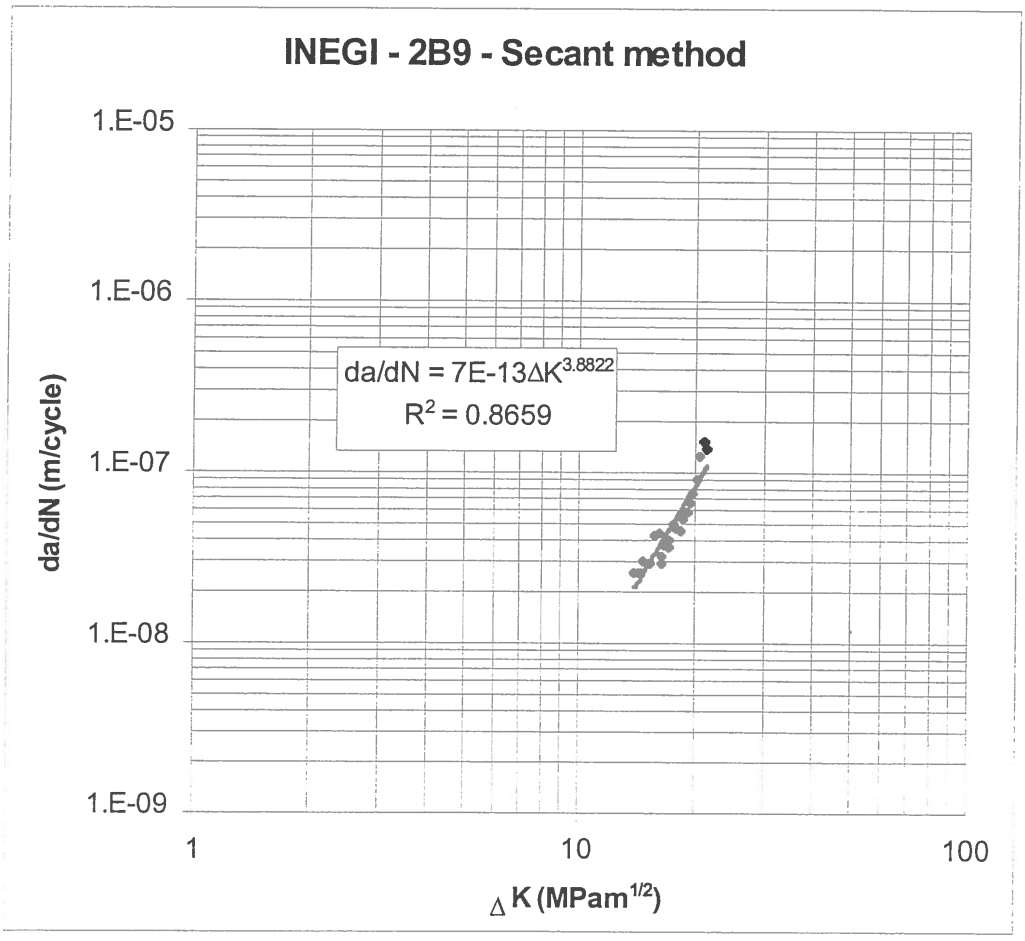

Figure 12 - da/dN *vs* ΔK curve with the secant method, specimen 2B9

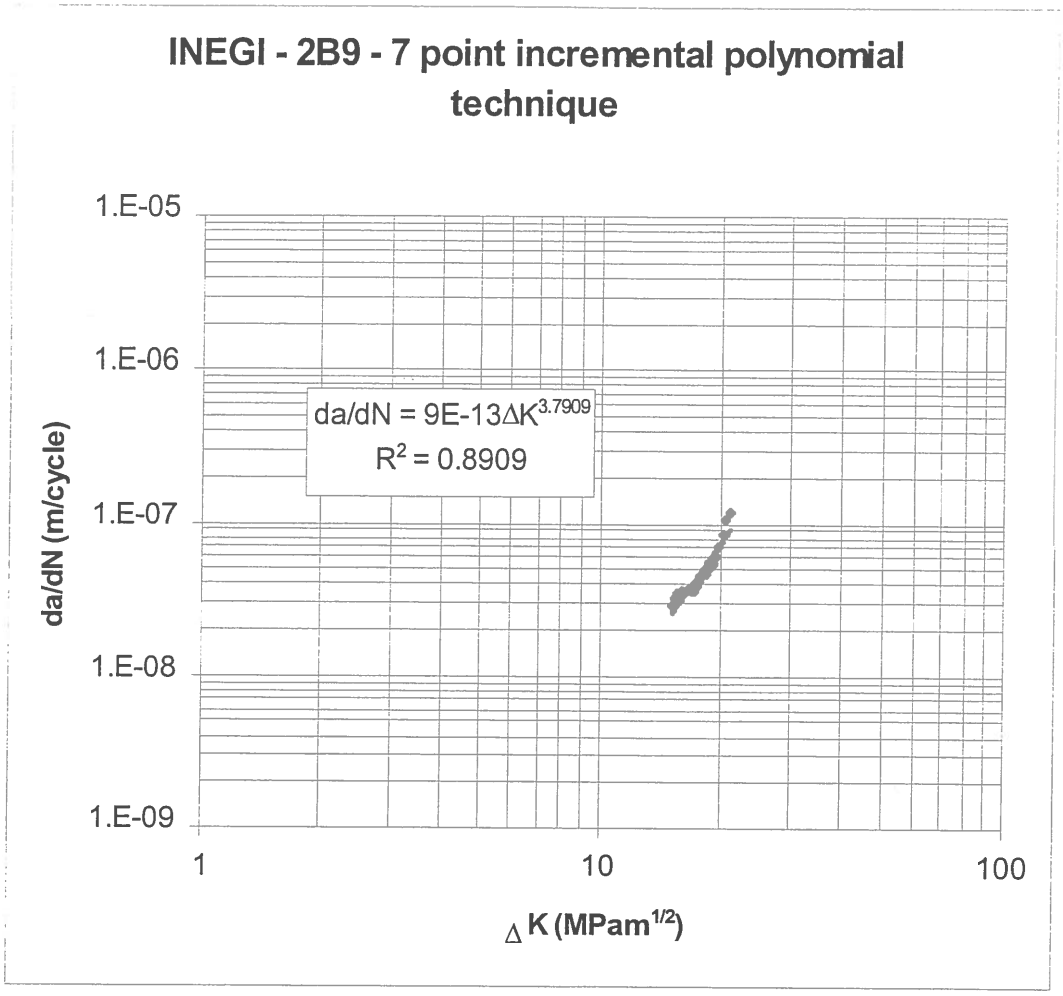

Figure 13 - da/dN *vs* ΔK curve with the seven point incremental polynomial technique, specimen 2B9

The fatigue test was stopped after 925000 cycles, and then statically loaded in tension. Figure 13 gives the load *vs* displacement. This is a typically brittle type of failure. With BS 7448 standard Part 1 (Method for determination of K_{Ic}, critical CTOD and critical J values of metallic materials), an estimate of K_{Ic} can be found. For the maximum load, $F_Q = 13677$ N, $K_Q = 53$ MPam$^{1/2}$. However for K_Q to be equal to K_{Ic}, the following conditions must be satisfied:
$W = 2B$, $0.45 < a/W < 0.55$ and $a, B, (W-a) < 2.5(K_Q/\sigma_{YS})^2$).
Neither of these conditions is satisfied for all the specimens, so we just can report the value of K_Q. For the determination of K_Q the formula in BS 6835 standard was used because the dimensions of the specimen are in accordance with that standard. For the other specimens, the value of K_Q is presented.

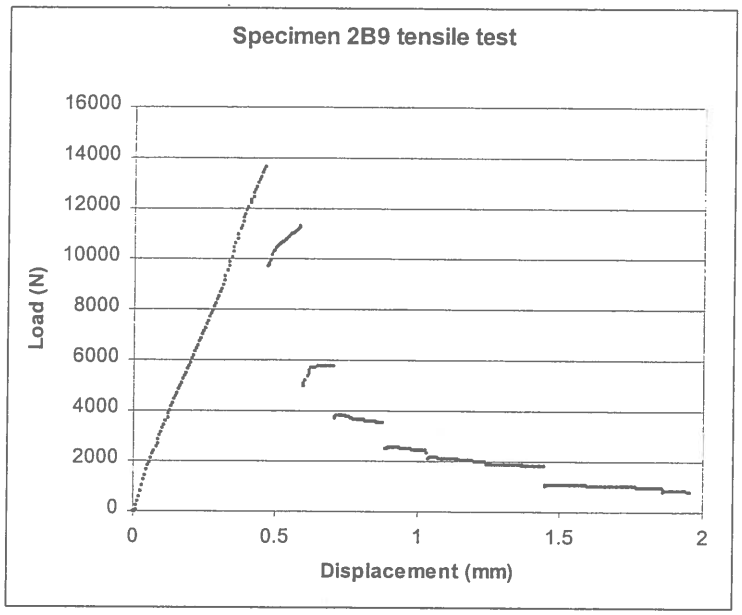

Figure 14 – Tensile test, specimen 2B9

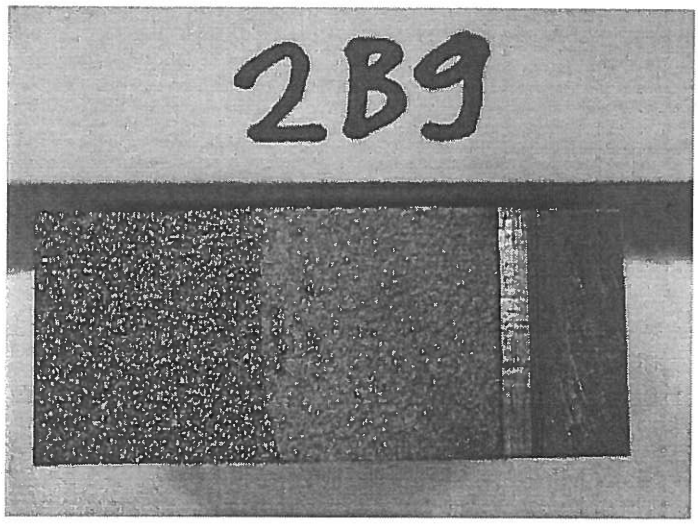

Figure 15 – Specimen 2B9 fracture surface

4.3 Specimen 3B14

For the fatigue crack growth rate determination of specimen 3B14, the P_{max} = 10.4 kN and P_{min} = 5.2 kN.
Table 6 and figure 15 give the raw data, figure 16 the da/dN *vs* ΔK curve with the secant method and figure 17 the da/dN *vs* ΔK curve with the seven point incremental polynomial technique.

Cycles	a	RH	T
	mm	(%)	(°C)
0	15.86	58	21
50000	16.22		
100000	16.64		
130000	16.88	58	20
160000	17.13		
190000	17.39		
220000	17.64		
250000	17.91	58	20.5
280000	18.20		
310000	18.47		
340000	18.79		
360000	19.01	58	21
380000	19.24		
400000	19.46		
420000	19.77		
435000	19.96		
450000	20.17		
465000	20.38		
480000	20.59		
495000	20.85		
510000	21.09	58	21
525000	21.35		
540000	21.60		
555000	21.90		
565000	22.08		

Cycles	a	RH	T
	mm	(%)	(°C)
575000	22.32		
585000	22.54	58	21
595000	22.83	58	20
605000	23.12		
615000	23.37		
625000	23.61		
635000	23.98		
641000	24.18		
647000	24.46		
653000	24.67		
659000	25.00		
663000	25.19		
667000	25.46		
671000	25.68		
675000	25.89	58	20
679000	26.10		
683000	26.46		
685000	26.59		
687000	26.79		
689000	27.01		
691000	27.22		
693000	27.39		
695000	27.60		
697000	27.87		
698000	28.30	58	20.5

Table 6 – Specimen 3B14, raw data

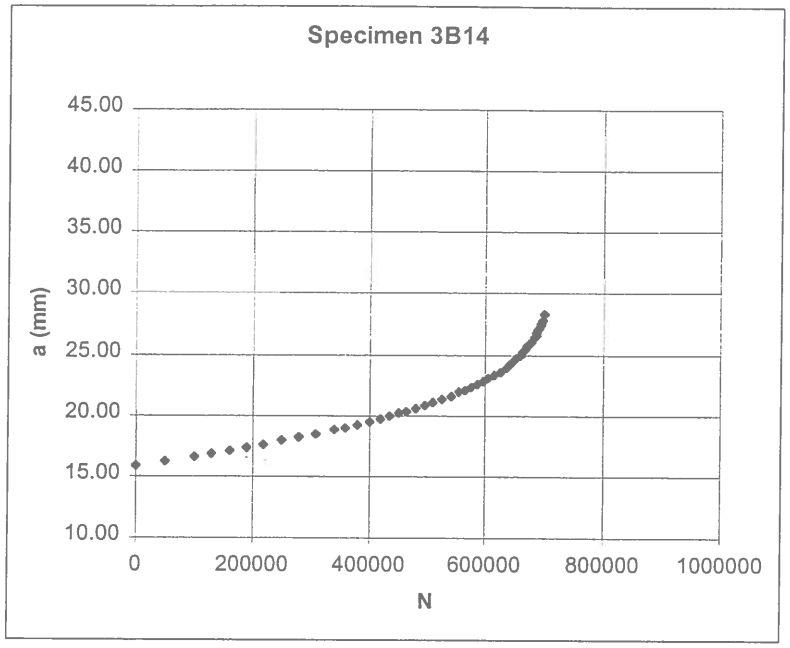

Figure 16 - a *vs* N, specimen 3B14

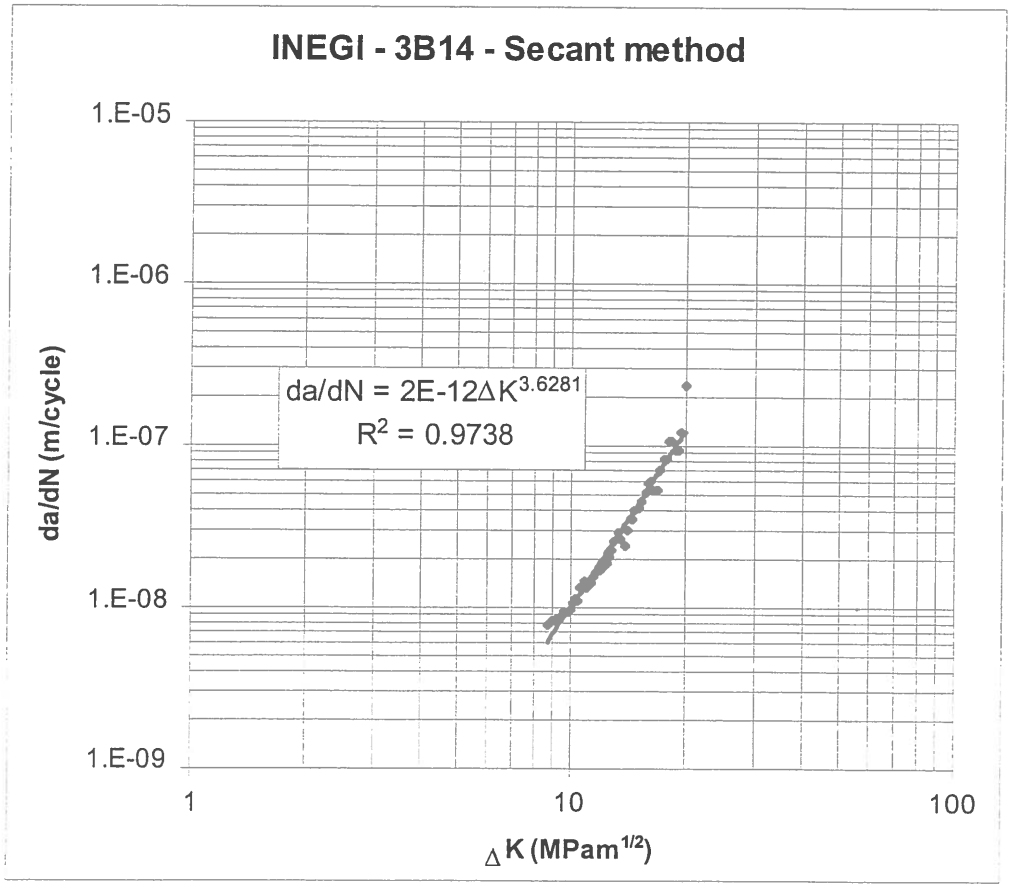

Figure 17 - da/dN *vs* ΔK curve with the secant method, specimen 3B14

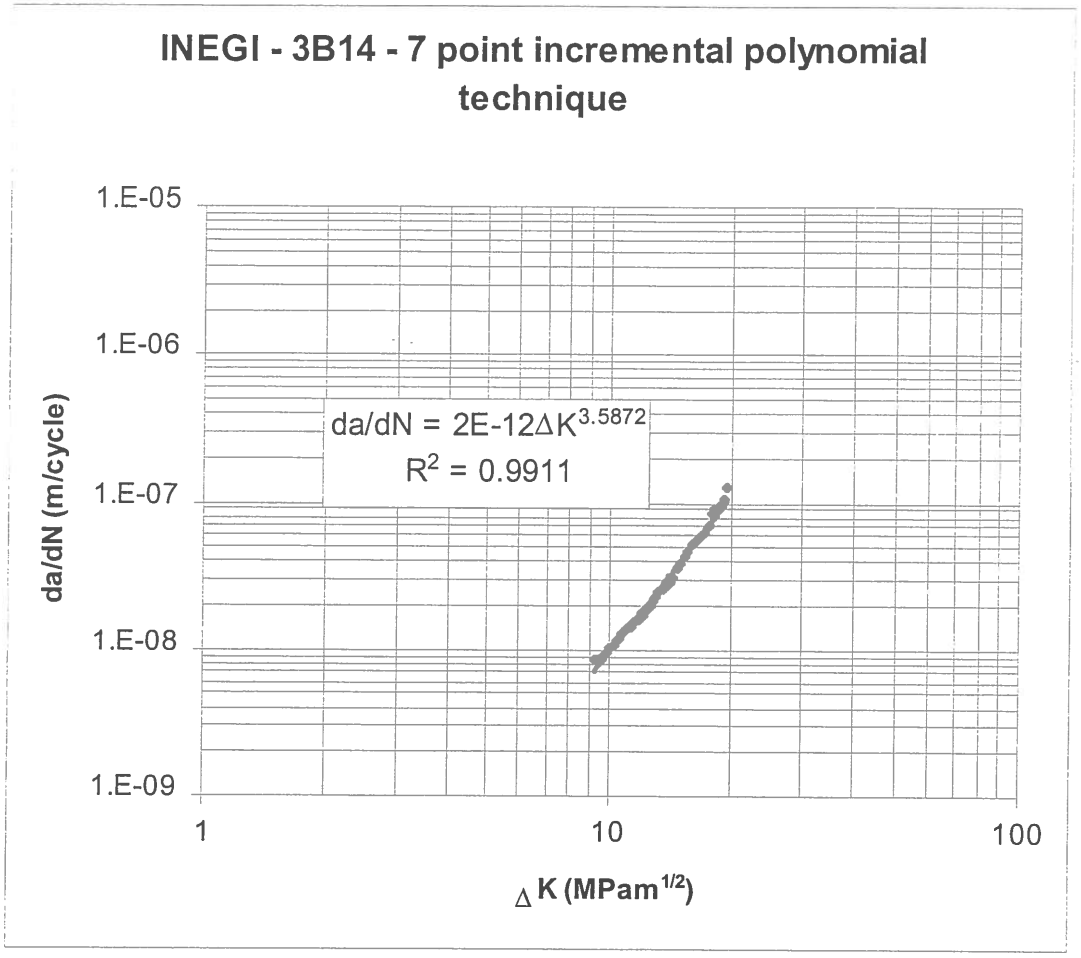

Figure 18 - da/dN *vs* ΔK curve with the seven point incremental polynomial technique, specimen 3B14

The fatigue test was stopped after 698000 cycles, and then statically loaded in tension. Figure 18 gives the load *vs* displacement. This is a typically brittle type of failure. For the maximum load, F_Q = 10794 N, K_Q = 43 MPam$^{1/2}$.

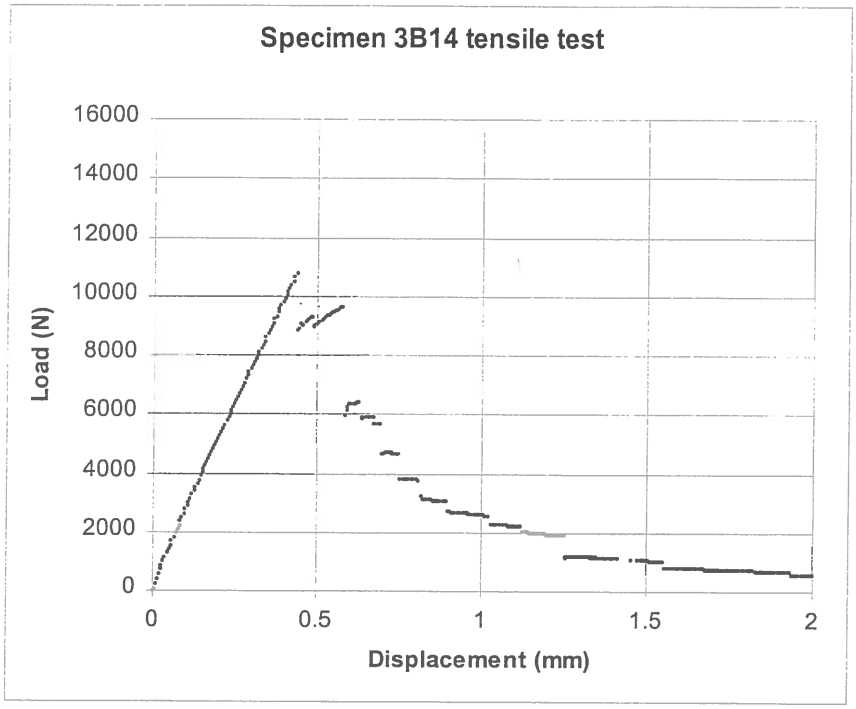

Figure 19 – Tensile test, specimen 3B14

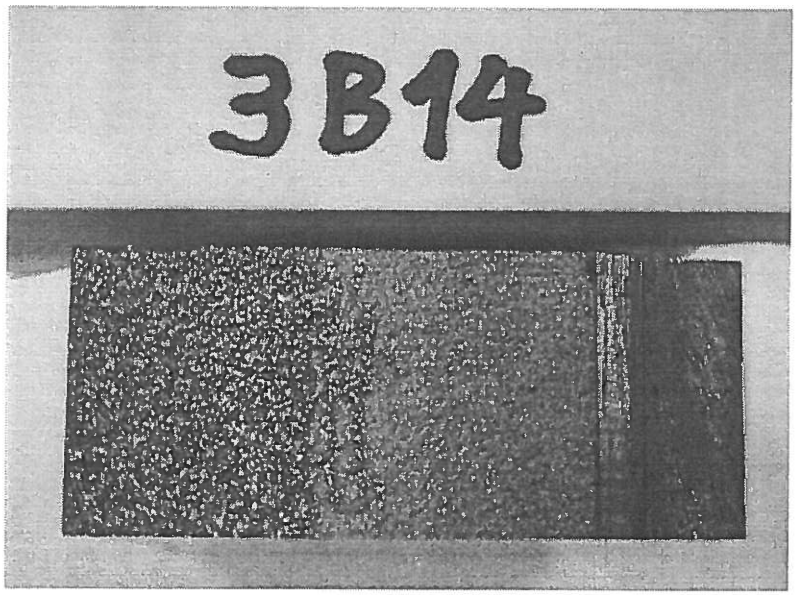

Figure 20 – Specimen 3B14 fracture surface

4.4 Specimen 4B19

For the fatigue crack growth rate determination of specimen 4B19, the P_{max} = 10.4 kN and P_{min} = 5.2 kN.
Table 7 and figure 20 give the raw data, figure 21 the da/dN *vs* ΔK curve with the secant method and figure 22 the da/dN *vs* ΔK curve with the seven point incremental polynomial technique.

Cycles	a	RH	T
	mm	(%)	(°C)
0	14.95	62	21
30000	15.13		
60000	15.29		
90000	15.44		
130000	15.68	62	20
170000	15.94		
210000	16.16		
250000	16.37		
290000	16.66	63	21.5
330000	16.90		
370000	17.17		
410000	17.44	60	21
450000	17.77		
480000	18.00		
510000	18.31		
530000	18.47	59	22
555000	18.67		
580000	18.97		
605000	19.22		
630000	19.58		
650000	19.82		
670000	20.05		
690000	20.30		
710000	20.60	57	22
725000	20.78		
740000	21.04		
755000	21.31		
770000	21.58		

Cycles	a	RH	T
	mm	(%)	(°C)
785000	21.88	54	22
795000	22.05		
805000	22.22		
815000	22.38		
825000	22.64		
835000	22.83	54	22
845000	23.07		
855000	23.29		
865000	23.53		
875000	23.79		
885000	24.05		
895000	24.37		
902000	24.58		
909000	24.86	53	23
916000	25.12		
923000	25.36		
930000	25.76		
935000	26.05		
939000	26.30		
942500	26.47		
946000	26.68		
949500	26.96		
953000	27.39		
955000	27.69		
956000	27.78		
958000	27.98		
960000	28.17		
962000	28.73	53	23

Table 7 – Specimen 4B19, raw data

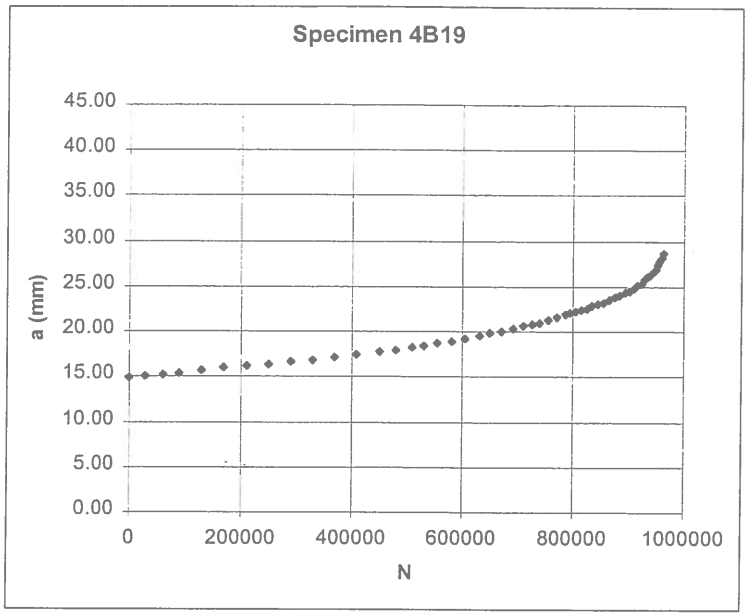

Figure 21 - a *vs* N, specimen 4B19

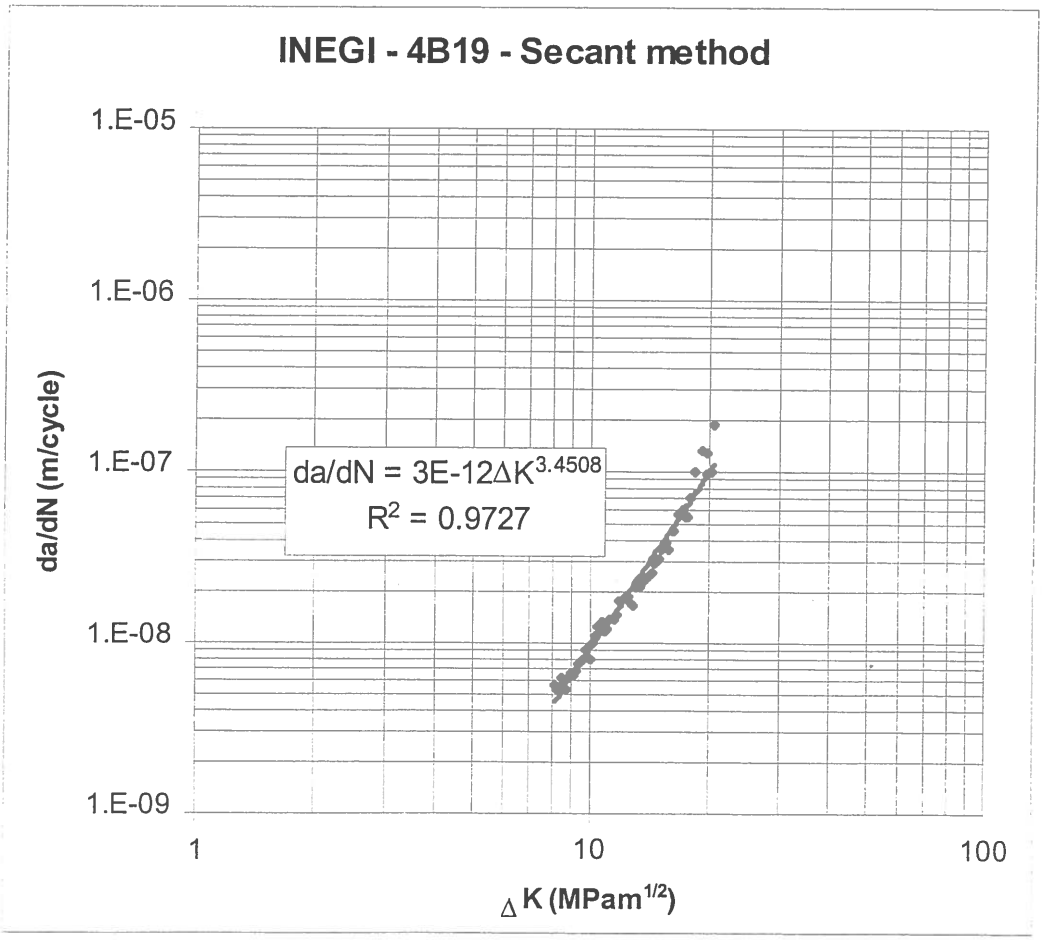

Figure 22 - da/dN *vs* ΔK curve with the secant method, specimen 4B19

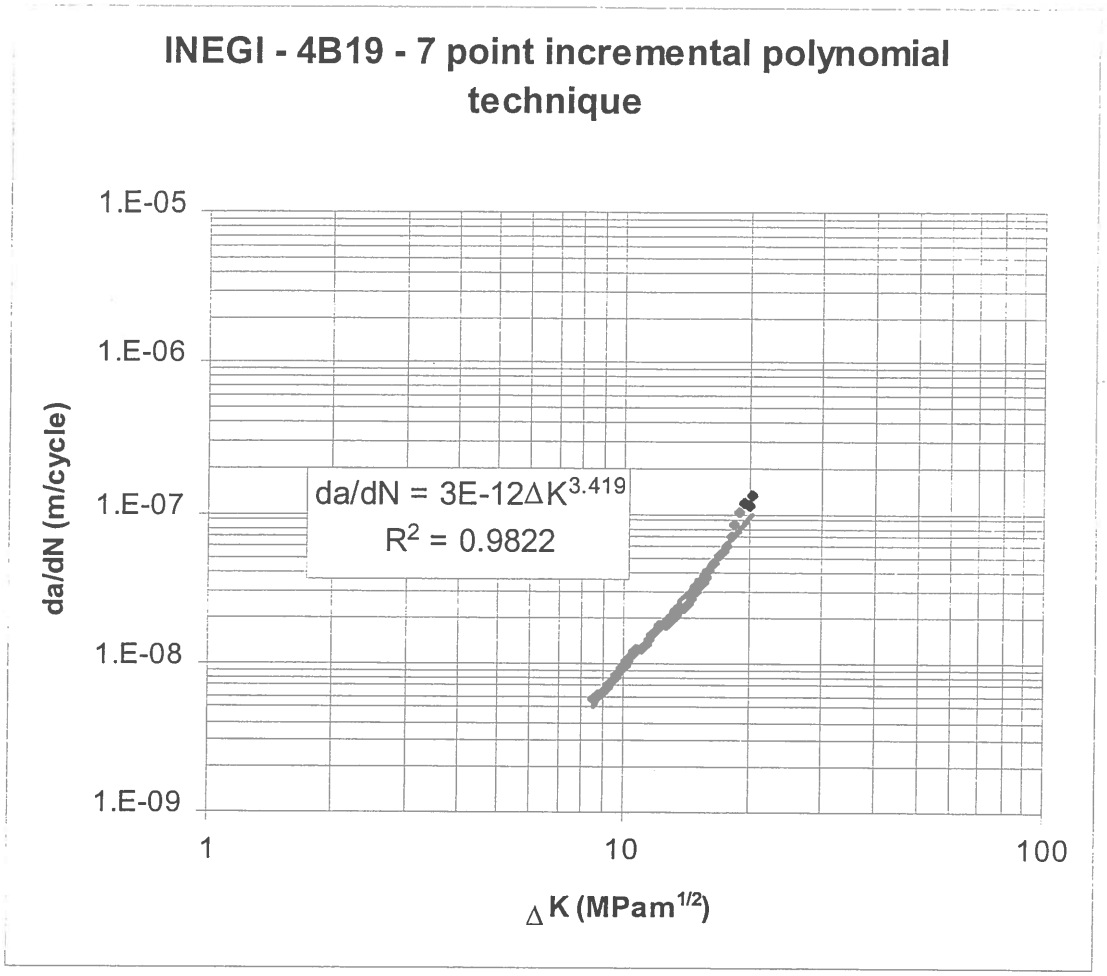

Figure 23 - da/dN *vs* ΔK curve with the seven point incremental polynomial technique, specimen 4B19

The fatigue test was stopped after 962000 cycles, and then statically loaded in tension. Figure 23 gives the load *vs* displacement. This is a typically brittle type of failure. For the maximum load, $F_Q = 10138$ N, $K_Q = 42$ MPam$^{1/2}$.

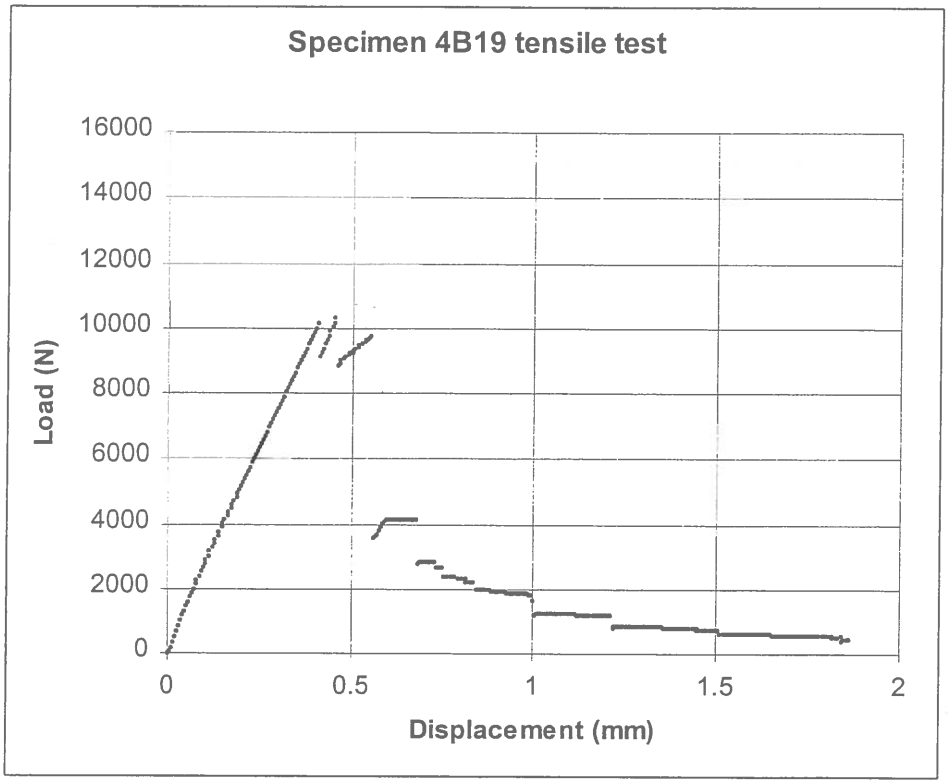

Figure 24 – Tensile test, specimen 4B19

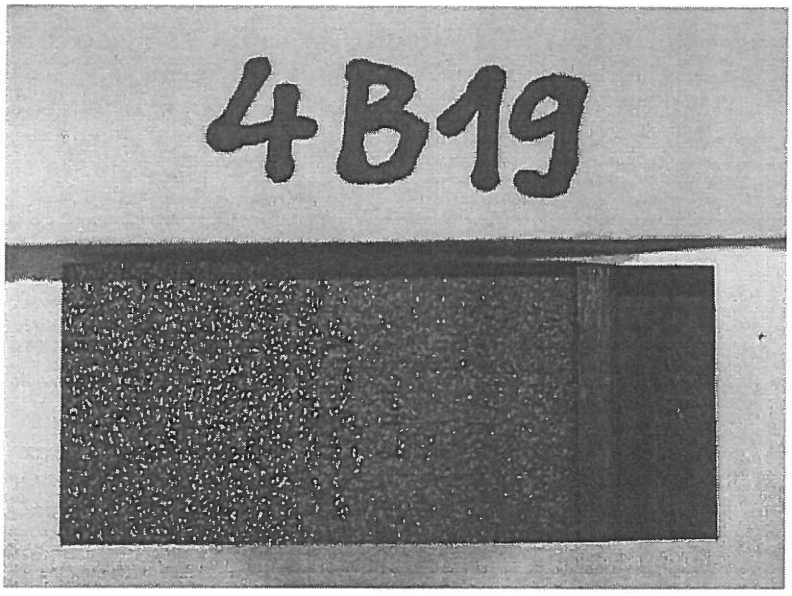

Figure 25 – Specimen 4B19 fracture surface

4.5 Specimen 4B20

For the fatigue crack growth rate determination of specimen 4B20, the P_{max} = 10.4 kN and P_{min} = 5.2 kN.
Table 8 and figure 25 give the raw data, figure 26 the da/dN *vs* ΔK curve with the secant method and figure 27 the da/dN *vs* ΔK curve with the seven point incremental polynomial technique.
The specimen failed at 704420 cycles.

Cycles	a	RH	T
	mm	(%)	(°C)
0	16.34		
30000	16.55	55	23
60000	16.77		
90000	16.98		
120000	17.22		
150000	17.43		
180000	17.70		
210000	17.93		
240000	18.22		
270000	18.46		
300000	18.75		
330000	19.04		
360000	19.34		
390000	19.68	54	24
410000	19.95	50	22
430000	20.16		
450000	20.50		
465000	20.70		
480000	20.92		
495000	21.13		
510000	21.41		
525000	21.64		
540000	21.88		
555000	22.26		
565000	22.41	48	23

Cycles	a	RH	T
	mm	(%)	(°C)
575000	22.59		
590000	23.00		
600000	23.21		
610000	23.42		
620000	23.76		
627000	23.95		
634000	24.16		
641000	24.39		
648000	24.60		
655000	24.97		
660000	25.21		
665000	25.45		
670000	25.68		
675000	25.93		
680000	26.26		
683000	26.50		
686000	26.75		
689000	26.95		
692000	27.50		
694000	27.78		
696000	27.99		
698000	28.18		
700000	28.41		
702000	28.69		
704000	28.90	50	24

Table 8 – Specimen 4B20, raw data

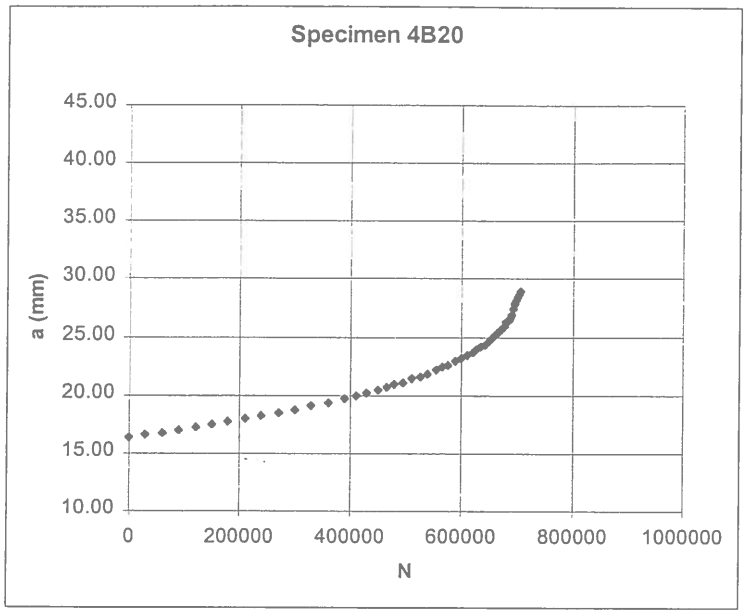

Figure 26 - a *vs* N, specimen 4B20

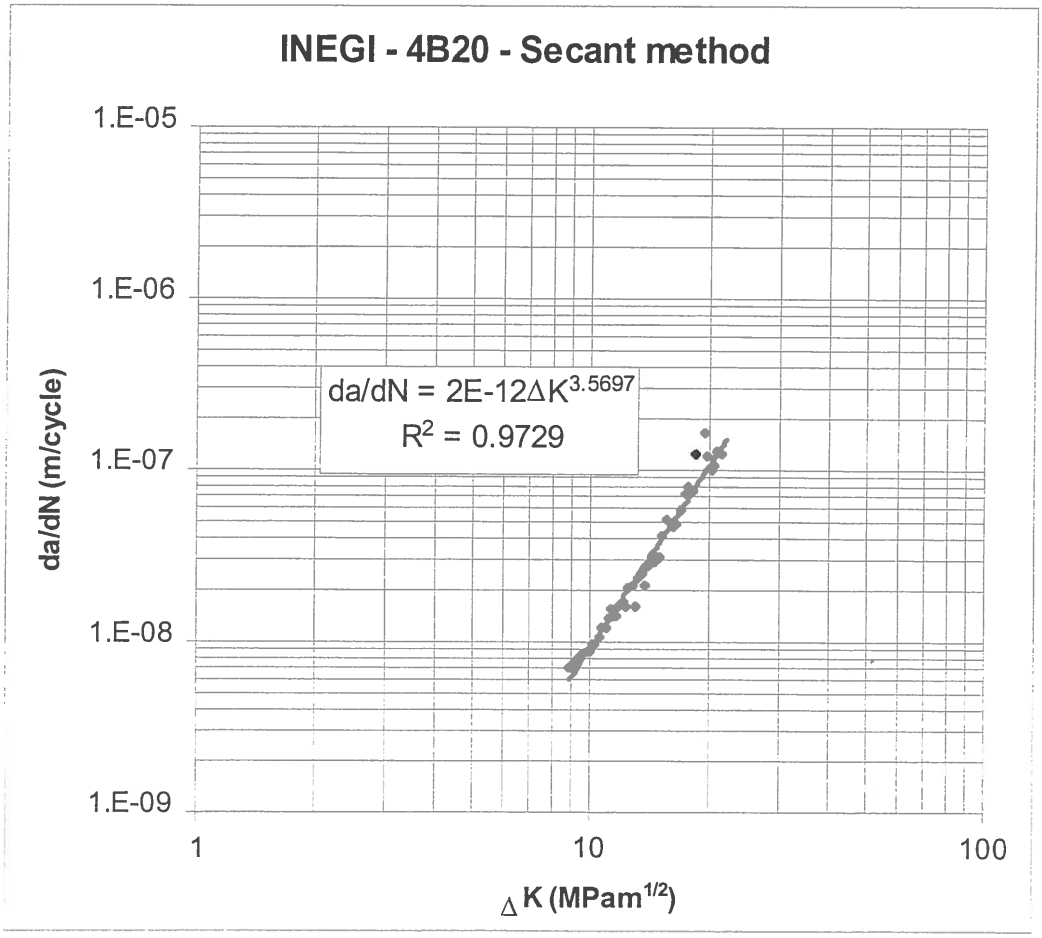

Figure 27 - da/dN *vs* ΔK curve with the secant method, specimen 4B20

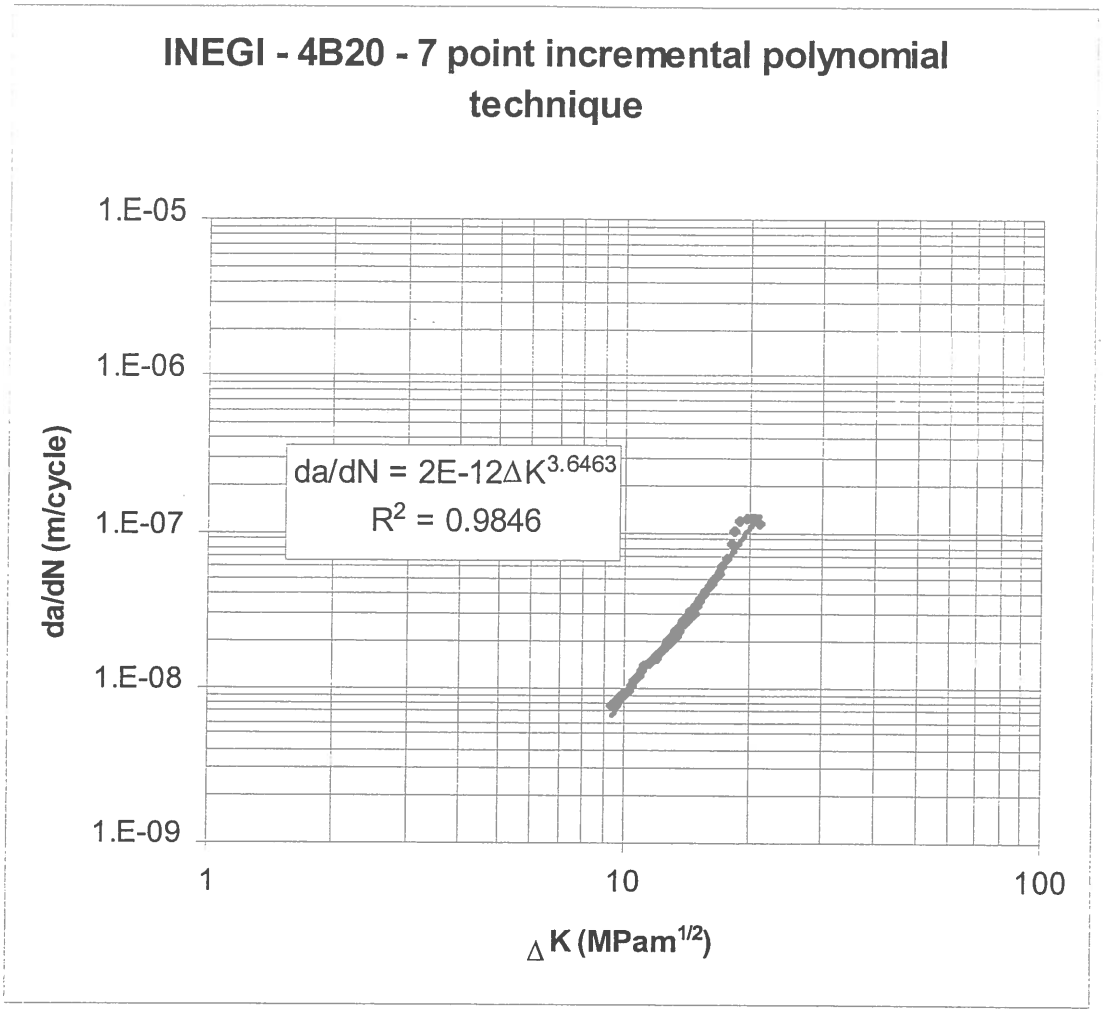

Figure 28 - da/dN *vs* ΔK curve with the seven point incremental polynomial technique, specimen 4B20

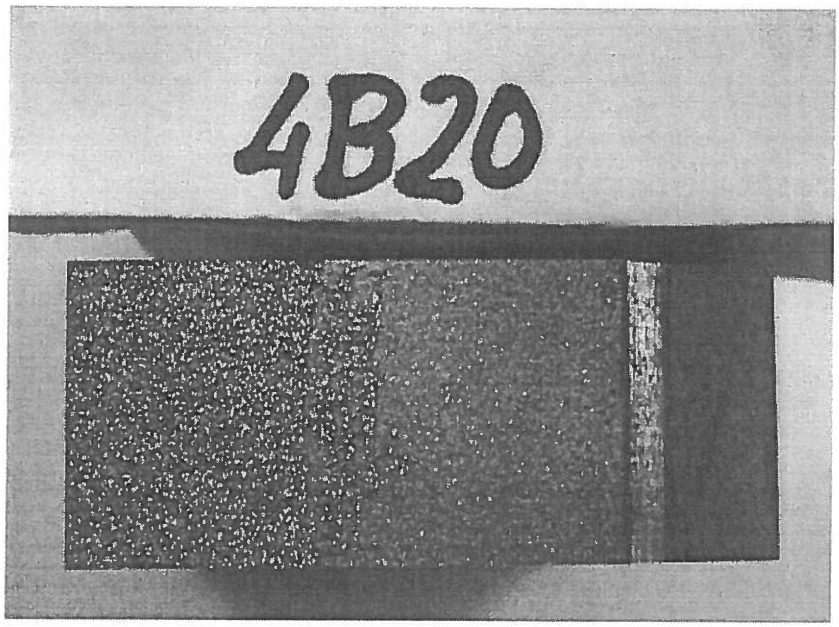

Figure 29 – Specimen 4B20 fracture surface

5 Comparison and conclusion

The constants of the Paris law $da/dN = C\ \Delta K^m$ (da/dN in m/cycle and ΔK in $MPam^{1/2}$) for each specimen are presented in table 9, determined with the seven point incremental polynomial technique.

Specimen ref	C	m
1B4	1E-11	2.9577
2B9	9E-13	3.7909
3B14	2E-12	3.5872
4B19	3E-12	3.419
4B20	2E-12	3.6463

Table 9 – Constants of Paris law for each specimen

There is not a substantial variation in the constants apart from specimens 1B4 and 2B9. But the determination of the da/dN curve for these specimens is not as reliable as the others: specimen 1B4 is smaller and specimen 2B9 the crack lengths differed by as much as 9 mm during pre-cracking.
Figure 21 shows a graph with all the curves.

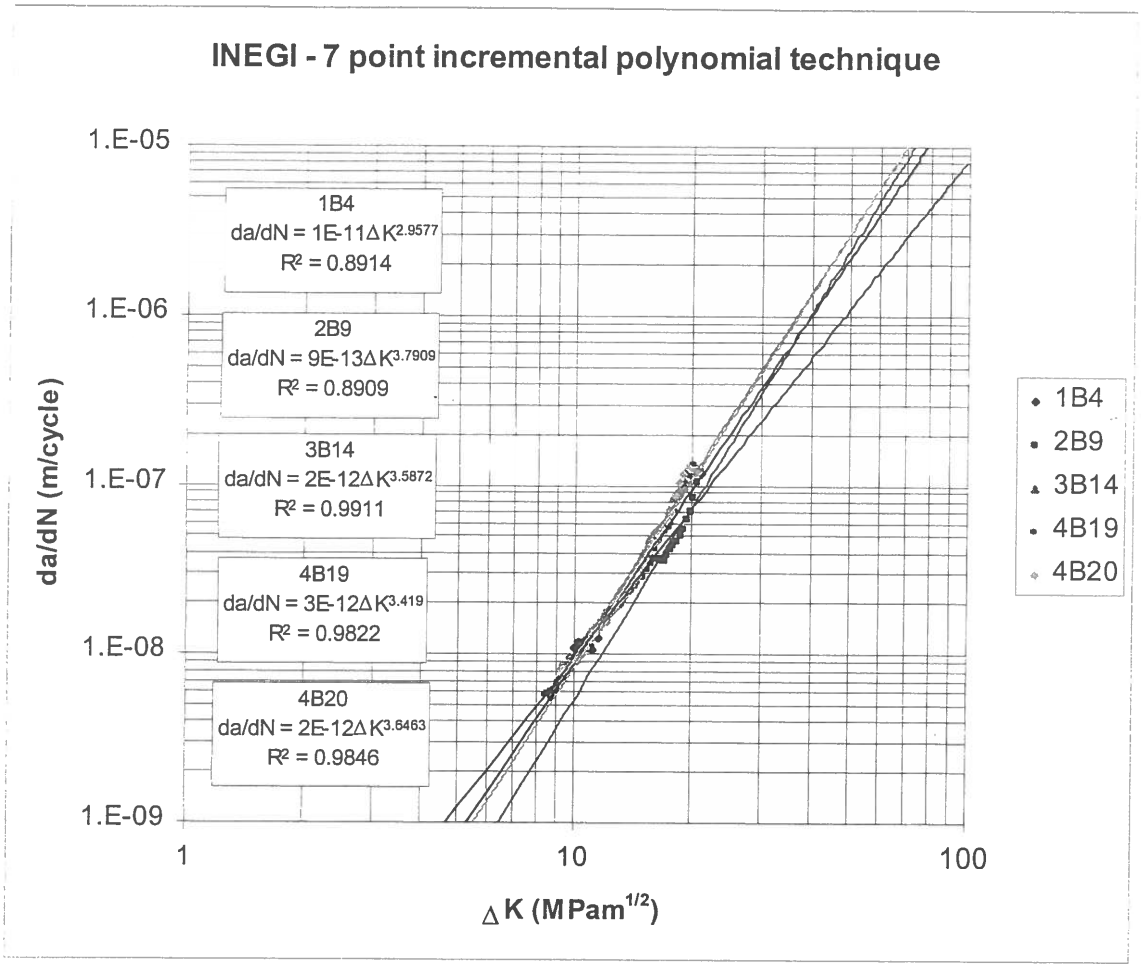

Figure 30 - Comparison of da/dN *vs* ΔK curves

An estimate of K_{Ic} was done for specimens 2B9, 3B14 and 4B19. Table 10 presents the K_Q values for these specimens.

	K_Q MPam$^{1/2}$
2B9	53
3B14	43
4B19	42

Table 10 – Estimate of K_{Ic}

Annex 1 - A basic computer program that utilises the seven point incremental polynomial technique

```
10 Cls
20 Rem SEVEN POINT INCREMENTAL POLYNOMIAL TECNIQUE
30 Dim A(200), N(200), BB(3), DADN(200), ID(7), DELK(100)
40 Dim AA(10), NN(10)
50 Print "SEVEN POINT INCREMENTAL POLYNOMIAL TECNIQUE METHOD
FOR DETERMINING DA/DN"
60 Print: Print: Print: Print
70 INPUT "PROVETE NUMERO "; NO
80 INPUT "NUMERO DE OBSERVACOES="; NPTS
160 Print "TIPO DE PROVETE....3PB"
161 INPUT "M   DIA DE Rp0,2 E Rm (MPa)="; SF
170 INPUT "LARGURA= (mm)"; W
180 INPUT "ESPESSURA= (mm)"; B
190 INPUT "FENDA= (mm)"; AN: AN = AN / 1000
200 Print "LARGURA.....W="; W, "ESPESSURA.....B="; B, "FENDA.....AN=";
AN: Print: Print
210 INPUT "PMIN(KN)="; PMIN
220 INPUT "PMAX(KN)="; PMAX
230 R = PMIN / PMAX
240 Print: Print: Print: Print "PMIN="; PMIN, "PMAX="; PMAX, "R="; R
250 Print
260 Print
270 Print
280 Print "CICLOS"
290 For I = 1 To NPTS
300 PRINT "N("; I; ")=": INPUT N(I)
310 Next
320 Print: Print: Print: Print "AVANCO DO ENTALHE"
330 Print
340 For I = 1 To NPTS
350 PRINT "A("; I; ")=": INPUT A(I)
360 Next
370 For I = 1 To NPTS
380 A(I) = A(I) / 1000
390 A(I) = A(I) + AN
400 Next
401 INPUT "INTRODUZA O NOME DO FICHEIRO-", FICH$
402 Open "C:\" + FICH$ + ".DAT" For Output As #1
410 Print "OBSno  CICLOS  A(MEAS)  A(REG)  MCC  DELK  DADN"
415 Print #1, "OBSno  CICLOS  A(MEAS)  A(REG)  MCC  DELK
DADN"
420 K = 0
430 PI = 3.1416
440 PP = PMAX - PMIN
```

```
450 For I = 1 To 3
460 Rem PRINT I, N(I), A(I) PRINT #1, I, N(I), A(I)
470 Print Tab(3); USING; "##"; I;: Print Tab(11); USING; "#######"; N(I);: Print
Tab(24); USING; "#.#####"; A(I)
471 Print #1, Tab(3); USING; "##"; I;: Print #1, Tab(11); USING; "#######"; N(I);:
Print #1, Tab(24); USING; "#.#####"; A(I)
480 Next
490 NPTS = NPTS - 6
500 For I = 1 To NPTS
510 L = 0
520 K = K + 1
530 K1 = K + 6
540 For J = K To K1
550 L = L + 1
560 AA(L) = A(J)
570 NN(L) = N(J)
580 Next
590 C1 = 0.5 * (NN(1) + NN(7))
600 C2 = 0.5 * (NN(7) - NN(1))
610 SX = 0
620 SX2 = 0
630 SX3 = 0
640 SX4 = 0
650 SY = 0
660 SYX = 0
670 SYX2 = 0
680 For J = 1 To 7
690 X = (NN(J) - C1) / C2
700 YY = AA(J)
710 SX = SX + X
720 SX2 = SX2 + X ^ 2
730 SX3 = SX3 + X ^ 3
740 SX4 = SX4 + X ^ 4
750 SY = SY + YY
760 SYX = SYX + YY * X
770 SYX2 = SYX2 + YY * X ^ 2
780 Next
790 DEN = 7 * (SX2 * SX4 - SX3 ^ 2) - SX * (SX * SX4 - SX2 * SX3) + SX2 * (SX *
SX3 - SX2 ^ 2)
800 T2 = SY * (SX2 * SX4 - SX3 ^ 2) - SYX * (SX * SX4 - SX2 * SX3) + SYX2 *
(SX * SX3 - SX2 ^ 2)
810 BB(1) = T2 / DEN
820 T3 = 7 * (SYX * SX4 - SYX2 * SX3) - SX * (SY * SX4 - SYX2 * SX2) + SX2 *
(SY * SX3 - SYX * SX2)
830 BB(2) = T3 / DEN
840 T4 = 7 * (SX2 * SYX2 - SX3 * SYX) - SX * (SX * SYX2 - SX3 * SY) + SX2 *
(SX * SYX - SX2 * SY)
850 BB(3) = T4 / DEN
```

```
860 YB = SY / 7
870 RSS = 0
880 TSS = 0
890 For J = 1 To 7
900 X = (NN(J) - C1) / C2
910 YHAT = BB(1) + BB(2) * X + BB(3) * X ^ 2
920 RSS = RSS + (AA(J) - YHAT) ^ 2
930 TSS = TSS + (AA(J) - YB) ^ 2
940 Next
950 R2 = 1 - RSS / TSS
960 DADN(I) = BB(2) / C2 + 2 * BB(3) * (NN(4) - C1) / C2 ^ 2
970 X = (NN(4) - C1) / C2
980 AR = BB(1) + BB(2) * X + BB(3) * X ^ 2
981 S = 0
1010 QQ = I + 3
1040 T = AR / (W / 1000)
1050 FT = Sqr(1000) * 6 * Sqr(T) * (1.99 - T * (1 - T) * (2.15 - 3.93 * T + 2.17 * T ^
2)) / ((1 + 2 * T) * (1 - T) ^ 1.5)
1080 DELK(I) = (FT * PP) / (B * Sqr(W))
1081 SP = PMAX * 1000 / (2 * SF * B)
1082 S = 1 - SP / W
1083 If (S.GE.T) Then GoTo 1160
1160 Print Tab(3); USING; "##"; QQ;: Print Tab(11); USING; "#######"; N(QQ);:
Print Tab(24); USING; "#.#####"; A(QQ);: Print Tab(35); USING; "#.#####"; AR;:
Print Tab(46); USING; "#.######"; R2;
1165 Print #1, Tab(3); USING; "##"; QQ;: Print #1, Tab(11); USING; "#######";
N(QQ);: Print #1, Tab(24); USING; "#.#####"; A(QQ);: Print #1, Tab(35); USING;
"#.#####"; AR;: Print #1, Tab(46); USING; "#.######"; R2;
1170 Print Tab(59); USING; "###.##"; DELK(I);: Print Tab(70); USING; "#.###^^^^";
DADN(I)
1175 Print #1, Tab(59); USING; "###.##"; DELK(I);: Print #1, Tab(70); USING;
"#.###^^^^"; DADN(I)
1180 Next
1190 J = NPTS + 4
1200 K = NPTS + 6
1210 For I = J To K
1220 Print Tab(3); USING; "##"; I;: Print Tab(11); USING; "#######"; N(I);: Print
Tab(24); USING; "#.#####"; A(I)
1225 Print #1, Tab(3); USING; "##"; I;: Print #1, Tab(11); USING; "#######"; N(I);:
Print #1, Tab(24); USING; "#.#####"; A(I)
1230 Next
```

Annex 2 – Tensile and hardness testing

Tensile testing

For each specimen, a tensile specimen was machined from the broken pieces in order to get the yield strength, the tensile strength, the elongation and the reduction of area. Figure A1 shows the localisation of the tensile specimens in the broken pieces:

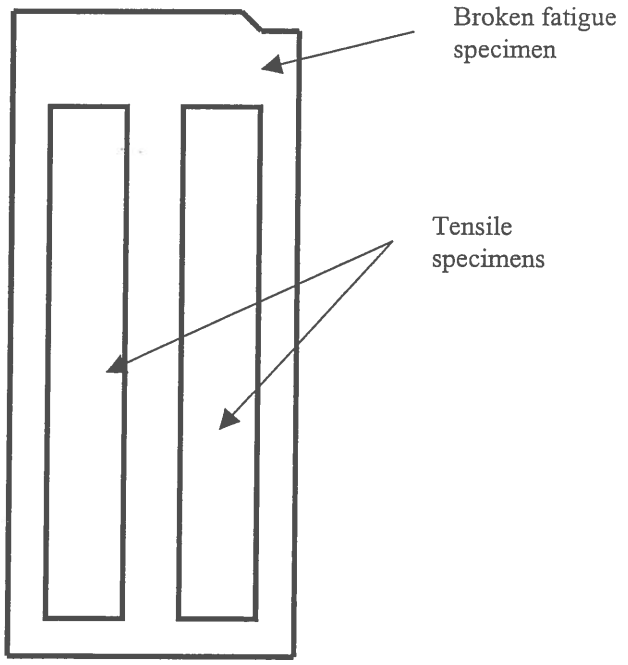

Figure A1 – Localisation of the tensile test specimens

The tensile specimen geometry is presented in figure A2.

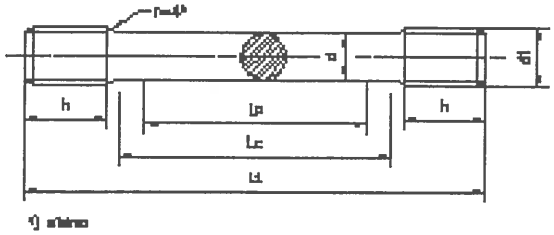

d	d1	h	Lo	Lc	Lt
10	M16	12	50	70	102

Figure A2 – Tensile specimen geometry (in mm)

Next, the stress-strain curve is presented for each specimen with the corresponding microstructure next to the curve. For all the specimens, the structure is perlitic.

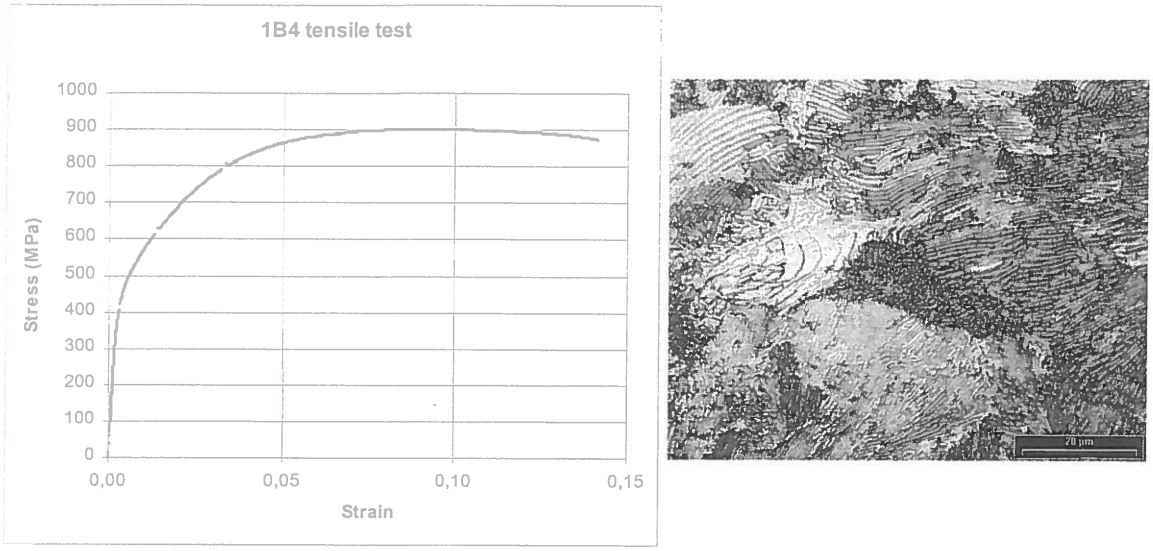

Figure A3 – Tensile curve and microstructure for specimen 1B4

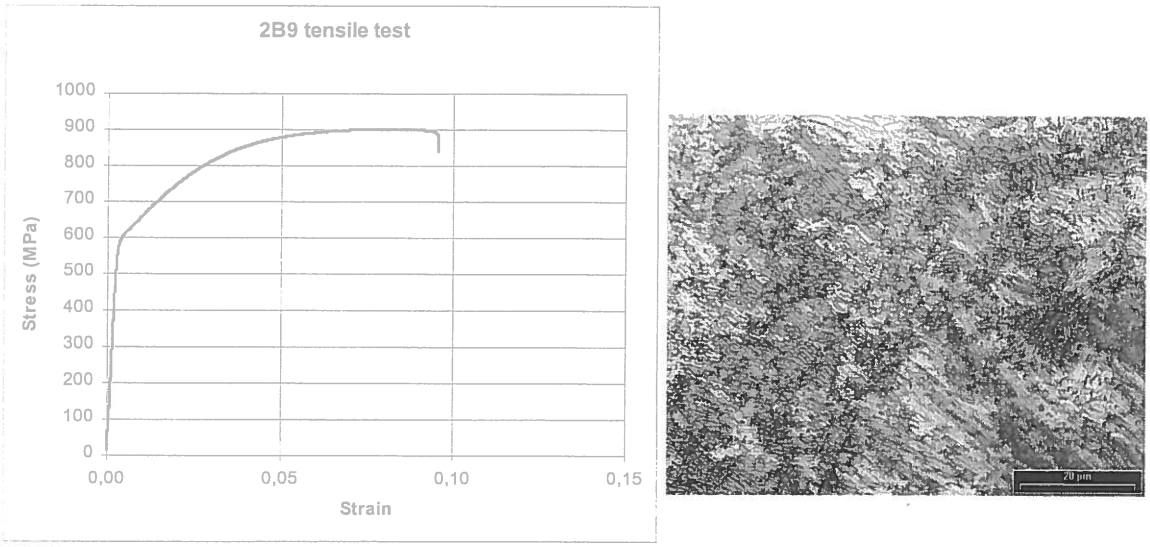

Figure A4 – Tensile curve and microstructure for specimen 2B9

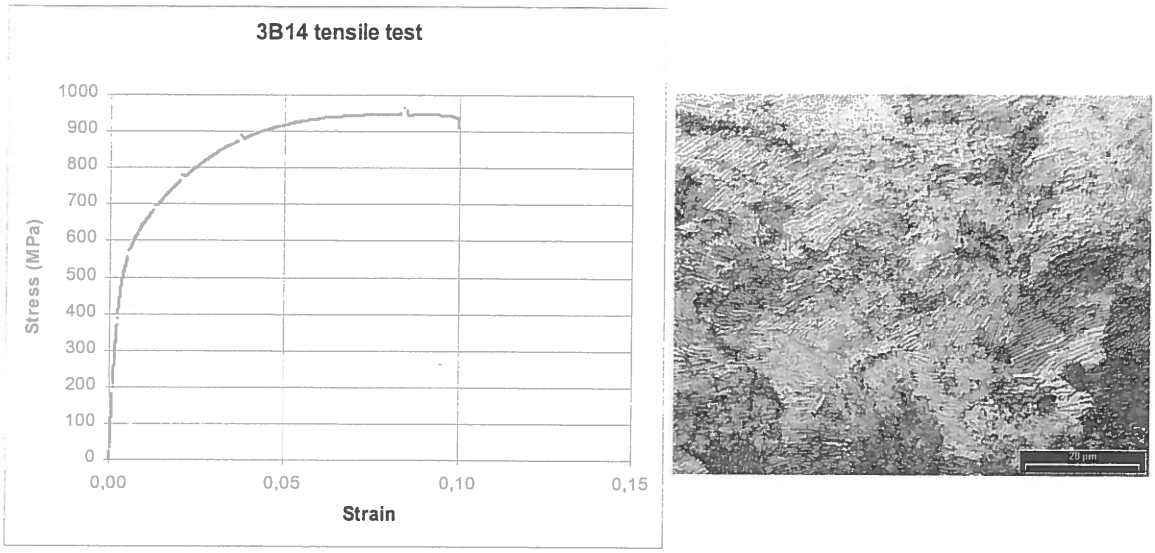

Figure A5 – Tensile curve and microstructure for specimen 3B14

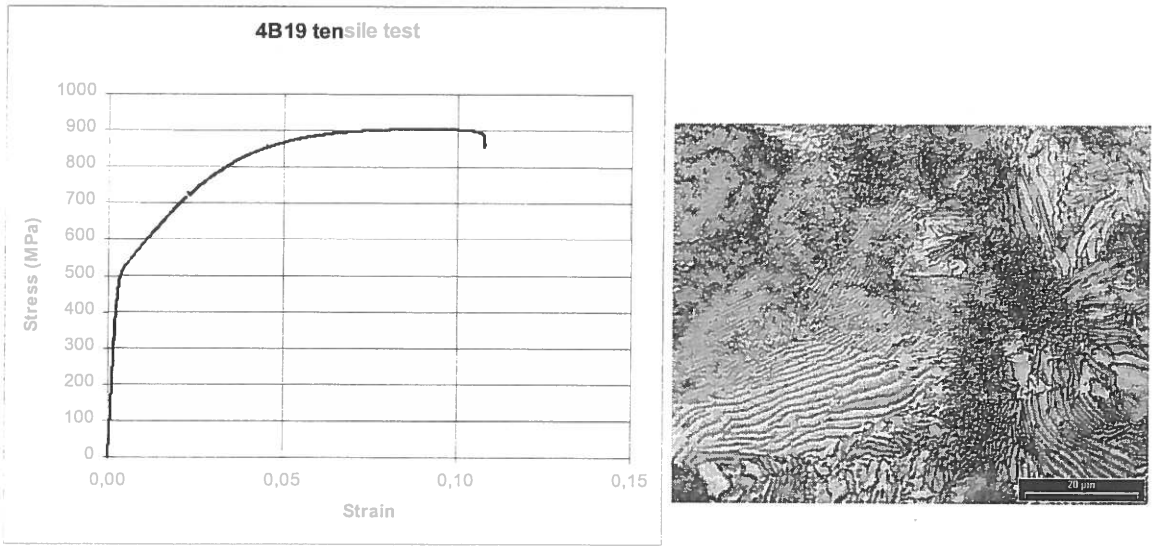

Figure A6 – Tensile curve and microstructure for specimen 4B19

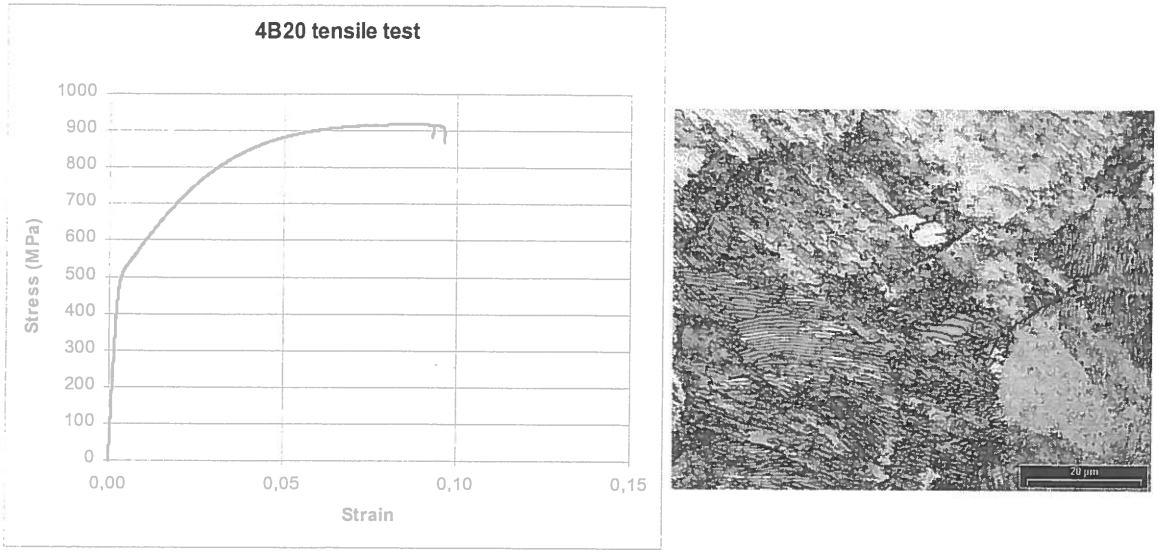

Figure A7 – Tensile curve and microstructure for specimen 4B20

Table A1 gives the yield strength, the tensile strength, the elongation and the reduction of area for each specimen. The values are those found in the literature.

	Offset 0,2% yield strength (MPa)	Tensile strength (MPa)	Elongation (%)	Reduction of area (%)
1B4	480	901	13	16
2B9	615	901	10	20
3B14	565	964	11	14
4B19	530	904	12	21
4B20	525	918	11	20

Table A1 - Yield strength, tensile strength, elongation and reduction of area for each specimen

One way of looking at toughness is to consider that it is the total area under the stress-strain curve (U_T). This area is an indication of the amount of work per unit volume which can be done on the material without causing it to rupture. Several mathematical approximations for the area under the stress-strain curve have been suggested. For ductile metals the area under the curve can be approximated by the following equation:

$$U_T = \frac{\text{Yield strength} \times \text{Tensile strength}}{2} \times \text{Elongation}$$

Table A2 presents gives the toughness based on the tensile curve for each specimen.

	Yield strength (MPa)	Tensile strength (MPa)	Elongation	U_T (MPa)
1B4	480	901	0,13	90
2B9	615	901	0,10	76
3B14	565	964	0,11	84
4B19	530	904	0,12	86
4B20	525	918	0,11	79

Table A2 - Toughness based on the tensile curve for each specimen

From this table specimen 2B9 is the one having the lower toughness whereas table 10 indicates that specimen 2B9 has a higher stress intensity factor than specimens 3B14 and 4B19. However, in any case the values are just rough estimates.

Hardness testing

Table A3 presents the hardness in Vickers for each specimen.

1B4	276 HV30
2B9	278 HV30
3B14	270 HV30
4B19	265 HV30
4B20	268 HV30

Table A3 – Hardness

It is interesting to note that the trend is the same as for the yield strength except for specimen 1B4.

Summary Report
visit to University of California, Berkeley

by

Paulo M S Tavares de Castro

Professor, Faculdade de Engenharia
da Universidade do Porto, Portugal;
Visiting Fulbright Scholar, UCBerkeley.

April 1, 2000 - June 30, 2000

Index

Activities 2
Literature surveys 2
Discussions and consultations 3
Seminar presentation 3
Short course 3
Paper submission 3
Other activities 3
Visits to Porto, Portugal, in the period 4
People 4
Events: conferences, lectures, seminars, etc. 5
Annex 1: flyer of seminar at UCB 9
Annex 2: copy of certificate of ASME short course in New York city 10
Annex 3: events attended, listed by broad topics 11
Education 11
Engineering 11
Ethics 11
Exhibitions 12
Fulbright activities 12
INTERNET and eBusiness 12
Management, Economics 12
Music 13
Philosophy, Psychology 13
Sociology, Politics, etc. 14

Activities

Literature surveys

Literature surveys of several areas of interest were prepared. Areas were chosen taking into consideration current and likely future activities at the *Universidade do Porto*, Portugal, in teaching, research and consulting. Reasons for the choice of areas included:

- a European r&d project on aging aircraft was concluded in 1999 (BRITE BE95-1053), and a new, related proposal (GRD1-2000-25069) is currently under consideration in the European Commission, Brussels;
- a European r&d project on fatigue crack propagation on steel for rails for railways was concluded in 2000 (SMT4-CT98-2240);
- a r&d proposal on adhesive connections (PCTI/1999EME35975) was recently submitted to the *Fundação para a Ciência e Tecnologia – FCT* (a Portuguese government agency for financing r&d activities);
- a PhD thesis on diffusion bonding (BD3388/94) is reaching its conclusion;
- research on composites structures, including interlaminar fracture toughness;
- consulting on aging steel structures, including bridges.

Other current areas of interest include

- new product development, and terminology and machine translation (justified by the launching in 2000 of MSc programs on industrial design (together with ESAD-Porto), and on technical terminology and translation (an initiative of the Faculty for Humanities - *Faculdade de Letras da Universidade do Porto*);
- professional ethics, with current membership of the ASME (American Society of Mechanical Engineers) Board on Professional Practice and Ethics.

In list form, topics surveyed were:

- Structural integrity
  - Aging aircraft (*bem* and *fem* stress analysis; fatigue crack propagation; multiple site damage; residual strength; equivalent initial flaw size concepts; …..)
  - Concrete structures (retrofit; use of composite materials; pultruded rebar reinforcements)
  - Steel structures (connections; bridges)
- Adhesive connections
- Materials
  - Diffusion bonding
  - Fatigue (short crack behaviour; ….)
  - Emerging materials (foams, ….)
  - Composites damage (interlaminar toughness; impact behaviour, ….)
- Design
  - Mechanical and engineering design
  - Industrial design
- New product development
- Management of technology
- Professional ethics
- Terminology (technical translation, machine translation, etc. ….)

The papers obtained correspond to approximately 1.9 Gbytes of information downloaded from the University of California Digital Library (*www.cdlib.org*).

Discussions and consultations

Among others, on:

- *Visit of Hari Dharan to the Universidade do Porto in September – December 2000* was discussed and prepared.
- *Fracture Mechanics and structural integrity* – contacts and discussions with A Mal, C K H Dharan, I Finnie, R Ritchie et al. took place; relationship manufacture procedure/fatigue behaviour was discussed with D Dornfeld.
- *Universities management* – with Loris Davanzo, on UCB planning activities and planning support services;
- *Faculty development* – with Steve Tollefson, on recognition of exceptional performance in teaching at a research university - the 'Distinguished Teaching Award' program of the Committee on Teaching, Berkeley Division of the Academic Senate, University of California;
- *Educational technology* – with Janio Itiro Akamatsu and Alice Agogino; the possibility of involvement of the *Universidade do Porto*, Portugal, on a educational technology research project recently submitted to NSF and Brazilian authorities (*Projeto Edital ProTeM-CC/NSF 02/99*) will be analised;

Seminar presentation

A seminar was presented at the UCB Mechanical Engineering Department the 15th June, well attended by academic staff and graduate students. The seminar information flyer is attached as Annex 1.

Short course

A short course of the American Society of Mechanical Engineers – ASME Professional Development Program was attended in New York city, June 5-7, 2000: *'The art of project management for engineers'* (instructor: David Adkins, PhD, Business Management Consultants, Ventura, California). A copy of the certificate is attached as Annex 2.

Paper submission

A paper based on work carried out in Porto was finished at the UCB, and submitted for possible presentation at the ASME International Mechanical Engineering Congress, Orlando, USA, Nov. 5-10, 2000.

Other activities

A working draft of new departmental rules for the *Departamento de Engenharia Mecânica e Gestão Industrial, Faculdade de Engenharia da Universidade do Porto,* Portugal, was prepared at the request of the department's Chairman.

Visits to Porto, Portugal, in the period

During the three-months stay at Berkeley (March 31, 2000 to June 30, 2000) two one-week visits to Porto, Portugal, took place as planned. The respective dates were:

- First visit: April 25 – May 2;
- Second visit: May 25 – June 2.

People

Contacts, discussions or consultations with the following (among others) took place:

- *Ajit Mal* (Professor, Mechanical and Aerospace Engineering Department, University of California, Los Angeles, and Visiting Scholar, University of California, Berkeley)
- *Alice M Agogino* (UCB Roscoe and Elizabeth Hughes Chair of Mechanical Engineering, and Faculty Assistant to Executive Vice Chancellor Carol Christ: Educational Development and Technology)
- *C K Hari Dharan* (Professor, UCB Mechanical Engineering Department)
- *Carlos A Gomes* (graduate of Universidade do Porto, Portugal; ICEP trainee at Hibbitt, Karlsson & Sorensen (West) Inc, California)
- *David A Dornfeld* (Professor and Director, Engineering Systems Research Center, UCB Department of Mechanical Engineering)
- *David E Adkins* (Principal Consultant, Business Management Consultants, Ventura, California)
- *Emanuel Almeida* (graduate of Universidade do Porto, Portugal; Mechanical Engineering MSc student, Stanford University)
- *Frank E Hauser* (Professor Emeritus, UCB Department of Mechanical Engineering);
- *Iain Finnie* (The James Fife Chair Professor Emeritus, UCB Department of Mechanical Engineering)
- *J Miguel Villas-Boas* (Associate Professor, UCB Haas School of Business)
- *Janio Itiro Akamatsu* (Professor, Department of Electrical Engineering, UNESP, Guaratinguetá campus, Brasil)
- *José Ferreira Dias* (Managing Director and Trade Commissioner, ICEP – Investimentos, Comércio e Turismo de Portugal, San Francisco)
- *Loris P Davanzo* (Assistant Director, Planning and Analysis, UCB Office of the Chancellor)
- *Mel Kanninen* (MFK Consulting Services, San Antonio, Texas)
- *Nuno Rebelo* (Hibbitt, Karlsson & Sorensen (West) Inc, California)
- *Pedro Pereira* (graduate of Universidade do Porto, Portugal; IÇEP trainee at CISCO, California)
- *Robert N Peirce* (Counsellor, British Embassy, Washington DC)
- *Robert O Ritchie* (Professor, UCB Department of Materials Science and Mineral Engineering)
- *Steve Tollefson* (UCB Office of the Assistant Vice Chancellor, Student Life: Educational Development. Coordinator: Faculty Development)

Fulbright Program staff or related

- *Marilyn N Herand* (Fulbright Visiting Scholar Enrichment Program, Institute of International Education, San Francisco Area Program Coordinator)
- *Rita Bacelar* (Fulbright Program Coordinator, Comissão Cultural Luso-Americana, Lisbon, Portugal)
- *Sone Loh* (Senior Program Coordinator, Visiting Scholar Division, Council for International Exchange of Scholars – CIES, Washington DC)

Administrative support at UCB

- *Ada O Carty* (Administrative Assistant, UCB Mechanical Engineering Department)
- *Rebecca Margosian* (Visiting Scholar Program Coordinator, UCB Department of Mechanical Engineering)

Events: conferences, lectures, seminars, etc.

1) April 6, 2000, Conference sponsored by the Berkeley Center for Law and Technology, Berkeley Technology Law Journal, et al., University of California, Berkeley (UCB) Boalt Hall School of Law, Berkeley – *'Music to whose ears? The debate over digital music'*; speakers: Peter Menell (Professor, UCB Boalt Hall School of Law), Chuck D (Rapstation.com) et al.
2) April 6, 2000, Fulbright Visiting Scholars Enrichment Program, *'The US Presidential Elections of 2000'*, Bruce Cain (UCB Professor of Political Science, Director of the UCB Institute of Governmental Studies)
3) April 10, 2000, Conference cosponsored by the UCB Institute of Governmental Studies (IGS) and American University Center for Congressional and Presidential Studies *'e-Campaigning: Ethics and the Internet'*; speakers: Bill Jones (California Secretary of State), Peter Lyman (Professor, UCB School of Information Management and Systems) et al.
4) April 10, 2000, UCB Electrical Engineering and Computer Sciences Depart. seminar: *'Bridging search engines and databases'* Roy Goldman (Stanford University), Soda Hall
5) April 10, 2000, Symposium *'What about economic rights: a symposium on wealth, poverty and the human rights legacy'*, UCB International House Auditorium; speakers: Laurel Fletcher (UCB Boalt Law School and UCB International Human Rights Clinic), Charles Henry (UCB African American Studies), Cheri Honkala (Director, Kensington Welfare Rights Union), Anuradha Mittal (Policy Director, Food First) et al.
6) April 11, 2000, Panel *'The future of the professoriate: a report from the Harvard project on faculty appointments'*, UCB Faculty Club; speakers: Richard Cheit (Harvard School of Education), Robert Post (Professor, UCB Boalt School of Law and Chair, American Association of University Professors) et al.
7) April 11, 2000, UCB Graduate Council of the Academic Senate lecture: *'Cities in civilization: culture, innovation and urban order'*, by Sir Peter Hall (Chair of Planning at the Bartlett School of Planning, University College, London)

8) April 11, 2000, UCB Avenali Lectures, *'The end of nature as a way to organize our polity'* (first of a two lecture series – *'Politics of nature'*), speaker: Bruno Latour (Professor, *Centre de Sociologie de l'Innovation, Ecole des Mines de Paris*)
9) April 12, 2000, UCB Depart of Mechanical Engineering seminar *'Structural health monitoring of aging aircraft'*; speaker: Ajit Mall (Professor, Mechanical and Aerospace Engineering Department, University of California, Los Angeles)
10) April 12, 2000, UCB Engineering Alumni Society and Engineers' Joint Council panel *'Anatomy of a startup'*, speakers from venture capital funds and CEOs of startup companies
11) April 13, 2000, UCB Institute of International Studies, The Rockefeller Foundation Communities in Crisis Lecture Series: *'Justice, tolerance and accountability in South Africa'*, speaker: Albie Sachs (Justice of the Constitutional Court of South Africa)
12) April 13, 2000, UCB 8th Annual Lecture on Energy and the Environment, *'Cogs and wheels aren't enough: conserving biodiversity in the 21st century'*, speaker: Deborah Jensen (Vice President, The Nature Conservancy)
13) April 14, 2000, UCB Center for Studies in Higher Education lecture *'Teaching Physics at a distance'*, Jocelyn Burnell (Open University, UK), CSHE Library, South Hall Annex
14) April 15, 2000, *'Mechanical Engineering - the program'*, speaker: Arun Majumdar (UCB Depart. of Mech. Engineering Associate Professor and Vice-Chairman – Instruction) et al., UCB Northgate Hall (part of Cal Day 2000)
15) April 15, 2000, Panel *'Commemorating the 25 years of the student regent position'*; speakers: David Saxon (former UC President) et al. (part of Cal Day 2000)
16) April 17, 2000, UCB Institute of International Studies panel: *'Controlling nuclear weapons: where are we'*, UCB Alumni House; panellists: Alan Cranston (former US Senator), Michael Nacht (Dean, UCB Richard and Rhoda Goldman School of Public Policy), Wolfgang Panofsky (Director Emeritus, Stanford Linear Accelerator Center) et al.
17) April 17, 2000, UCB School of Social Welfare, Friedlander Lecture *'Privatising social security – an international perspective'*; speaker: Dalmar Hoskins (Secretary General, International Social Securities Association)
18) April 17-18, 2000, Berkeley-Yomiuri Conference *'Envisioning a triangular relationship in the pacific: China, Japan and the US at the millennium'*; speakers: Walter Mondale (former US Vice-President and Ambassador to Japan), James Sasser (former US Senator and Ambassador to PRChina), Peter Tarnoff (former US Under Secretary of State for Political Affairs, lecturer UCB) et al.
19) April 18, 2000, UCB Center for Slavic and East European Studies lecture *'A case of post-communist bewilderment: culture, media and culture politics in Hungary'*; speaker: Balint Rozsnyai
20) April 18, 2000, UCB Townsend Center for the Humanities, and the Commonwealth Club of California, panel *'Immigration issues and the new right in Europe'*; speakers: Richard Mitten (Associate Professor of History, Central European University, Budapest), Richard Webster (Professor Emeritus of Contemporary Italian History, UCB), et al.

21) April 18, 2000, UCB Avenali Lectures, *'Bringing the sciences into democracy'* (second of a two lecture series – *'Politics of nature'*), speaker: Bruno Latour (Professor, *Centre de Sociologie de l'Innovation, Ecole des Mines de Paris*)

22) April 19, 2000, UCB Depart of Mechanical Engineering seminar *'Fracture Mechanics and the nation's aging aircraft problem'*; speaker: Melvin Kanninen (engineering consultant, San Antonio, Texas, former research scientist, Southwest Research Institute)

23) April 20, 2000, UCB Institute of International Studies, The Rockefeller Foundation Communities in Crisis Lecture Series: *'Swallowing injustice to rebuild community: Latin America after the era of state terror'*, speaker: Thomas Farer (Dean, Graduate School of International Affairs, University of Denver, member Inter-American Commission on Human Rights 1976-83)

24) April 20, 2000, UCB, The Bancroft Library roundtable: *'Envoys of the empire: California engineers and the common world destiny'*, speaker: Bancroft fellow Jessica Teisch

25) April 21, 2000, UCB *Undergraduate Symposium on Ethics and Research*; speakers: Deni Elliot (Professor of Ethics and Director of the Practical Ethics Center, University of Montana) et al.

26) April 24, 2000, UCB Institute of Governmental Studies, UCExtension, New York Times and the Berkeley Alumni Association, *'The annual review of the presidency'*, panellists: Laura Capps (former speechwriter for President Clinton), Thomas Mann (The Brookings Institution), Nelson Polsby (UCB Department of Political Science), Richard Berke (New York Times), et al.

27) May 4, 2000, UCB, California Association of Scholars (an affiliate of the National Association of Scholars), lecture by Alan Charles Kors (University of Pennsylvania Professor of History, coauthor *'The Shadow University: the Betrayal of Liberty at American Campuses'* and President, Fire: Foundation for Individual Rights in Education Inc)

28) May 4, 2000, The 6th Annual Aaron Wildavsky Forum for Public Policy, UCB Richard and Rhoda Goldman School of Public Policy: *'Competing models of the human agent: implications for policy making'*; speaker: Daniel Kahneman (Eugene Higgins Professor of Psychology, Princeton University)

29) May 5, 2000, UCB IGS Lecture: *'Modern Britain: an examination of devolution and the revitalization of Britain's external relationships – Europe, US and the Commonwealth'*; speaker: Robert Peirce (Counsellor, British Embassy, Washington DC)

30) May 8, 2000, Symposium *'After Seattle: politics, trade and culture in the new North America'*, UCB Boalt School of Law, Canadian Studies Program; speakers: Michael Hawes (Professor, Queen's University), Vinod Aggarwal (UCB), John Wirth (Stanford University) et al.

31) May 9, 2000, UCB School of Social Welfare lecture *'Wealth, Poverty and Alan Greenspan: Social policy and macro economic policy'*; speaker: Robert Reich (Maurice B Hexter Professor of Social and Economic Policy, Brandeis University, and former US Secretary of Labor)

32) May 10, 2000, UCB, Panel *'Making large lectures seem small through the use of technology'*; speakers: Alice Agogino (Professor, UCB Depart of Mechanical Engineering) et al.

33) May 14, 2000, Fulbright Visiting Scholar Enrichment Program, Yerba Buena Gardens, Visual Arts Gallery

34) May 17, 2000, Scholar information meeting, organised by University of California SISS – Services for International Students and Scholars, International House

35) June 3-4, 2000, American Society of Mechanical Engineers, Board on Professional Practice and Ethics - BPPE meeting, Providence, Rhode Island

36) June 5-7, 2000, American Society of Mechanical Engineers – ASME Professional Development Program *'The art of project management for engineers'*; instructor: David Adkins, PhD, Business Management Consultants. New York city

37) June 13-14, 2000, *'eBusiness Conference and Expo'*, San Jose Convention Center, San Jose

38) June 15, 2000, UCB Depart of Mechanical Engineering seminar *'Multiple site fatigue damage in aircraftt'*; speaker: Paulo M S T de Castro (Professor, *Departamento de Engenharia Mecânica e Gestão Industrial, Universidade do Porto*)

39) June 18, 2000, Moscone Center, San Francisco: exhibition of NEXPO2000, Newspaper Association of America

Fracture Mechanics Seminar

University of California, Berkeley
Department of Mechanical Engineering

Presents

"Multiple-Site Fatigue Damage in Aircraft"

By

Paulo M.S.T. de Castro
Department of Mechanical Engineering and Industrial Management
University of Porto, Portugal

Thursday, June 15, 2000
6153 Etcheverry Hall
4:00 pm
(Coffee & Cookies served at 3:30 pm)

ABSTRACT

This seminar concerns fatigue processes in aircraft structures and is related to the recent seminars in the department on aging aircraft, a subject by Professor Ajit Mal and Dr. Melvin Kanninen. The work to be presented here, conducted by the University of Porto, Portugal for a project on the fatigue behavior of aging aircraft, was funded by the European Union (project leader: DASA/Airbus). It concerns the multiple-site damage phenomenon exemplified by the behavior of 2024-T3 alclad aluminum riveted lap-joints, a common design feature in aircraft structures.

The study involves fatigue testing under constant amplitude loading of 1.6-mm-thick riveted lap-joints, and includes examination of the specimens during and subsequent to testing (post-mortem analysis of the fracture surface using scanning electron microscopy) in order to determine the time of occurrence, location and extent of fatigue damage. Crack growth rates were determined from periodic crack length measurements with a traveling microscope. Stress measurements were made using extensometry and the SPATE infrared technique to determine loading distribution on the lap-joints and redistribution due to cracking of fastener holes. Data on the initiation and growth of cracks and on residual static strength was used to assess the predictive model based on the finite element method.

Hosted by Professor David Dornfeld, 5100A Etcheverry Hall, (510) 642-0906, dornfeld@me.berkeley.edu & by Professor Hari Dharan, 5135 Etcheverry Hall, (510) 642-4933, dharan@me.berkeley.edu

THE AMERICAN SOCIETY OF MECHANICAL ENGINEERS

FOUNDED 1880

THIS CERTIFICATE IS AWARDED TO

PAULO DE CASTRO, PH.D.

FOR ATTENDING THE COURSE

THE ART OF PROJECT MANAGEMENT FOR ENGINEERS

June 5, 2000
New York, NY
2.1 CEU

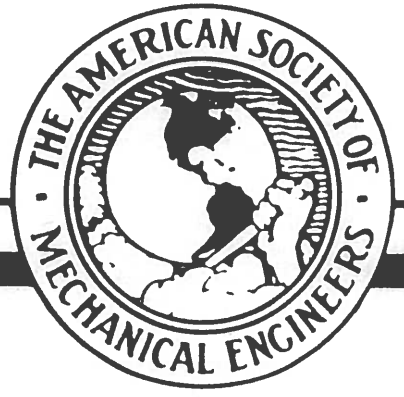

Vice President
Professional Development

ANNEX 2

Annex 3

Education

- April 11, 2000, Panel *'The future of the professoriate: a report from the Harvard project on faculty appointments'*, UCB Faculty Club; speakers: Richard Cheit (Harvard School of Education), Robert Post (Professor, UCB Boalt School of Law and Chair, American Association of University Professors) et al.
- April 14, 2000, UCB Center for Studies in Higher Education lecture *'Teaching Physics at a distance'*, Jocelyn Burnell (Open University, UK), CSHE Library, South Hall Annex
- April 15, 2000, *'Mechanical Engineering - the program'*, speaker: Arun Majumdar (UCB Depart. of Mech. Engineering Associate Professor and Vice-Chairman – Instruction) et al., UCB Northgate Hall (part of Cal Day 2000)
- April 15, 2000, Panel *'Commemorating the 25 years of the student regent position'*; speakers: David Saxon (former UC President) et al. (part of Cal Day 2000)
- May 4, 2000, UCB, California Association of Scholars (an affiliate of the National Association of Scholars), lecture by Alan Charles Kors (University of Pennsylvania Professor of History, coauthor *'The Shadow University: the Betrayal of Liberty at American Campuses'* and President, Fire: Foundation for Individual Rights in Education Inc)
- May 10, 2000, UCB, Panel *'Making large lectures seem small through the use of technology'*; speakers: Alice Agogino (Professor, UCB Depart of Mechanical Engineering) et al.

Engineering

- April 10, 2000, UCB Electrical Engineering and Computer Sciences Depart. seminar: *'Bridging search engines and databases'* Roy Goldman (Stanford University), Soda Hall
- April 12, 2000, UCB Depart of Mechanical Engineering seminar *'Structural health monitoring of aging aircraft'*; speaker: Ajit Mall (Professor, Mechanical and Aerospace Engineering Department, University of California, Los Angeles)
- April 14, 2000, lecture *'Teaching Physics at a distance'*, Jocelyn Burnell (Open University, UK), UCB Center for Studies in Higher Education, CSHE Library, South Hall Annex
- April 15, 2000, *'Mechanical Engineering - the program'*, speaker: Arun Majumdar (UCB Depart. of Mech. Engineering Associate Professor and Vice-Chairman – Instruction) et al., UCB Northgate Hall (part of Cal Day 2000)
- April 19, 2000, UCB Depart of Mechanical Engineering seminar *'Fracture Mechanics and the nation's aging aircraft problem'*; speaker: Melvin Kanninen (engineering consultant, San Antonio, Texas, former research scientist, Southwest Research Institute)
- June 15, 2000, UCB Depart of Mechanical Engineering seminar *'Multiple site fatigue damage in aircraftt'*; speaker: Paulo M S T de Castro (Professor, *Departamento de Engenharia Mecânica e Gestão Industrial, Universidade do Porto*)

Ethics

- April 10, 2000, Symposium *'What about economic rights: a symposium on wealth, poverty and the human rights legacy'*, UCB International House Auditorium; speakers: Laurel Fletcher (UCB Boalt Law School and UCB International Human Rights Clinic), Charles Henry (UCB African American Studies), Cheri Honkala (Director, Kensington Welfare Rights Union), Anuradha Mittal (Policy Director, Food First) et al.
- April 21, 2000, UCB *Undergraduate Symposium on Ethics and Research*; speakers: Deni Elliot (Professor of Ethics and Director of the Practical Ethics Center, University of Montana) et al.
- June 3-4, 2000, American Society of Mechanical Engineers, Board on Professional Practice and Ethics - BPPE meeting, Providence, Rhode Island

Exhibitions

- San Francisco Museum of Modern Art – SFMOMA: René Magritte exhibition; Sol Lewitt retrospective; San Francisco, May 6, 2000
- Yerba Buena Center for the Arts, San Francisco, May 14, 2000
- Corbis – The Bettmann Archive 'The living lens', Metreon, San Francisco, May 14, 2000
- 17th Himalayan Fair, Live Oak Park, Berkeley, May 20, 2000
- Photo Exhibit by Horst Hamann, Vanderbilt Hall, Grand Central Terminal, New York city, June 7, 2000
- 6th Biennial Berkeley Festival and Exhibition; exhibition - UCB King Student Union Building, June 11, 2000
- California Academy of Sciences, San Francisco, June 18, 2000
- 'The Golden Age of Chinese Archaeology', Asian Art Museum, San Francisco, June 25, 2000

Fulbright activities

- April 6, 2000, Fulbright Visiting Scholars Enrichment Program, *'The US Presidential Elections of 2000'*, Bruce Cain (UCB Professor of Political Science, Director of the UCB Institute of Governmental Studies)
- May 14, 2000, Fulbright Visiting Scholar Enrichment Program, Yerba Buena Gardens, Visual Arts Gallery
- May 17, 2000, Scholar information meeting, organised by University of California SISS – Services for International Students and Scholars, International House

INTERNET and eBusiness

- April 6, 2000, Conference sponsored by the Berkeley Center for Law and Technology, Berkeley Technology Law Journal, et al., UCB (University of California, Berkeley) Boalt Hall School of Law, Berkeley – *'Music to whose ears? The debate over digital music'*; speakers: Peter Menell (Professor, UCB Boalt Hall School of Law), Chuck D (Rapstation.com) et al.
- April 10, 2000, Conference cosponsored by the UCB Institute of Governmental Studies (IGS) and American University Center for Congressional and Presidential Studies *'e-Campaigning: Ethics and the Internet'*; speakers: Bill Jones (California Secretary of State), Peter Lyman (Professor, UCB School of Information Management and Systems) et al.
- June 13-14, 2000, *'eBusiness Conference and Expo'*, San Jose Convention Center, San Jose

Management, Economics

- April 6, 2000, Conference sponsored by the Berkeley Center for Law and Technology, Berkeley Technology Law Journal, et al., UCB (University of California, Berkeley) Boalt Hall School of Law, Berkeley – *'Music to whose ears? The debate over digital music'*; speakers: Peter Menell (Professor, UCB Boalt Hall School of Law), Chuck D (Rapstation.com) et al.
- April 10, 2000, Symposium *'What about economic rights: a symposium on wealth, poverty and the human rights legacy'*, UCB International House Auditorium; speakers: Laurel Fletcher (UCB Boalt Law School and UCB International Human Rights Clinic), Charles Henry (UCB African American Studies), Cheri Honkala (Director, Kensington Welfare Rights Union), Anuradha Mittal (Policy Director, Food First) et al.
- April 12, 2000, UCB Engineering Alumni Society and Engineers' Joint Council panel *'Anatomy of a startup'*, speakers from venture capital funds and CEOs of startup companies
- April 17, 2000, UCB School of Social Welfare, Friedlander Lecture *'Privatising social security – an international perspective'*; speaker: Dalmar Hoskins (Secretary General, International Social Securities Association)
- April 17-18, 2000, Berkeley-Yomiuri Conference *'Envisioning a triangular relationship in the pacific: China, Japan and the US at the millennium'*; speakers: Walter Mondale (former US Vice-President and Ambassador to Japan), James Sasser (former US Senator and Ambassador to PRChina), Peter Tarnoff (former US Under Secretary of State for Political Affairs, lecturer UCB) et al.
- April 20, 2000, UCB, The Bancroft Library roundtable: *'Envoys of the empire: California engineers and the common world destiny'*, speaker: Bancroft fellow Jessica Teisch

- May 5, 2000, UCB IGS Lecture: *'Modern Britain: an examination of devolution and the revitalization of Britain's external relationships – Europe, US and the Commonwealth'*; speaker: Robert Peirce (Counsellor, British Embassy, Washington DC)
- May 8, 2000, Symposium *'After Seattle: politics, trade and culture in the new North America'*, UCB Boalt School of Law, Canadian Studies Program; speakers: Michael Hawes (Professor, Queen's University), Vinod Aggarwal (UCB), John Wirth (Stanford University) et al.
- May 9, 2000, UCB School of Social Welfare lecture *'Wealth, Poverty and Alan Greenspan: Social policy and macro economic policy'*; speaker: Robert Reich (Maurice B Hexter Professor of Social and Economic Policy, Brandeis University, and former US Secretary of Labor)
- June 5-7, 2000, American Society of Mechanical Engineers – ASME Professional Development Program *'The art of project management for engineers'*; instructor: David Adkins, PhD, Business Management Consultants. New York city
- June 13-14, 2000, *'eBusiness Conference and Expo'*, San Jose Convention Center, San Jose

Music

- April 5, 2000, UCB Department of Music noon concert, Jolie Lin, piano solo. UCB Hertz Hall
- April 9, 2000, Midsummer Mozart Chamber Players. Old First Church, Sacramento and Van Ness, San Francisco
- April 12, 2000, UCB Department of Music noon concert, Ivan Ilic; Yi-Fang Tsai; Brian Christian. UCB Hertz Hall
- April 15, 2000, UCB University Symphony Orchestra, David Milnes, conductor. UCB Hertz Hall (part of the Cal Day 2000)
- April 15, 2000, University Chorus; Mozart: Requiem. UCB Hertz Hall
- April 19, 2000, UCB Department of Music noon concert, Yong-In University Art Troup, Korea. UCB Hertz Hall
- May 3, 2000, pianist Jolie Lin. UCB Hertz Hall
- May 7, 2000, UC Davis Concert Band and UC Berkeley Wind Ensemble. UCB Hertz Hall
- May 12, 2000, Oakland East Bay Symphony, Michael Morgan, Director. Paramount Theatre, Oakland
- May 13, 2000, The Berkeley Community Chorus and Orchestra, Arlene Sagan, Director; J S Bach Mass in B Minor. St Joseph the Worker Church, Berkeley
- June 10, 2000, San Francisco Symphony, San Francisco Symphony Chorus. San Francisco Davies Symphony Hall

Philosophy, Psychology

- April 11, 2000, UCB Avenali Lectures, *'The end of nature as a way to organize our polity'* (first of a two lecture series – *'Politics of nature'*), speaker: Bruno Latour (Professor, Centre de Sociologie de l'Innovation, Ecole des Mines de Paris)
- April 18, 2000, UCB Avenali Lectures, *'Bringing the sciences into democracy'* (second of a two lecture series – *'Politics of nature'*), speaker: Bruno Latour (Professor, Centre de Sociologie de l'Innovation, Ecole des Mines de Paris)
- May 4, 2000, The 6th Annual Aaron Wildavsky Forum for Public Policy, UCB Richard and Rhoda Goldman School of Public Policy: *'Competing models of the human agent: implications for policy making'*; speaker: Daniel Kahneman (Eugene Higgins Professor of Psychology, Princeton University)

Sociology, Politics, etc.

- April 6, 2000, Fulbright Visiting Scholars Enrichment Program, *'The US Presidential Elections of 2000'*, Bruce Cain (UCB Professor of Political Science, Director of the UCB Institute of Governmental Studies)
- April 10, 2000, Conference cosponsored by the UCB Institute of Governmental Studies (IGS) and American University Center for Congressional and Presidential Studies *'e-Campaigning: Ethics and the Internet'*; speakers: Bill Jones (California Secretary of State), Peter Lyman (Professor, UCB School of Information Management and Systems) et al.

- April 10, 2000, Symposium *'What about economic rights: a symposium on wealth, poverty and the human rights legacy'*, UCB International House Auditorium; speakers: Laurel Fletcher (UCB Boalt Law School and UCB International Human Rights Clinic), Charles Henry (UCB African American Studies), Cheri Honkala (Director, Kensington Welfare Rights Union), Anuradha Mittal (Policy Director, Food First) et al.
- April 11, 2000, UCB Graduate Council of the Academic Senate lecture: *'Cities in civilization: culture, innovation and urban order'*, by Sir Peter Hall (Chair of Planning at the Bartlett School of Planning, University College, London)
- April 13, 2000, UCB Institute of International Studies, The Rockefeller Foundation Communities in Crisis Lecture Series: *'Justice, tolerance and accountability in South Africa'*, speaker: Albie Sachs (Justice of the Constitutional Court of South Africa)
- April 13, 2000, UCB 8th Annual Lecture on Energy and the Environment, *'Cogs and wheels aren't enough: conserving biodiversity in the 21st century'*, speaker: Deborah Jensen (Vice President, The Nature Conservancy)
- April 17, 2000, UCB Institute of International Studies panel: *'Controlling nuclear weapons: where are we'*, UCB Alumni House; panellists: Alan Cranston (former US Senator), Michael Nacht (Dean, UCB Richard and Rhoda Goldman School of Public Policy), Wolfgang Panofsky (Director Emeritus, Stanford Linear Accelerator Center) et al.
- April 17, 2000, UCB School of Social Welfare, Friedlander Lecture *'Privatising social security – an international perspective'*; speaker: Dalmar Hoskins (Secretary General, International Social Securities Association)
- April 17-18, 2000, Berkeley-Yomiuri Conference *'Envisioning a triangular relationship in the pacific: China, Japan and the US at the millennium'*; speakers: Walter Mondale (former US Vice-President and Ambassador to Japan), James Sasser (former US Senator and Ambassador to PRChina), Peter Tarnoff (former US Under Secretary of State for Political Affairs, lecturer UCB) et al.
- April 18, 2000, UCB Center for Slavic and East European Studies lecture *'A case of post-communist bewilderment: culture, media and culture politics in Hungary'*; speaker: Balint Rozsnyai
- April 18, 2000, UCB Townsend Center for the Humanities, and the Commonwealth Club of California, panel *'Immigration issues and the new right in Europe'*; speakers: Richard Mitten (Associate Professor of History, Central European University, Budapest), Richard Webster (Professor Emeritus of Contemporary Italian History, UCB), et al.
- April 20, 2000, UCB Institute of International Studies, The Rockefeller Foundation Communities in Crisis Lecture Series: *'Swallowing injustice to rebuild community: Latin America after the era of state terror'*, speaker: Thomas Farer (Dean, Graduate School of International Affairs, University of Denver, member Inter-American Commission on Human Rights 1976-83)
- April 24, 2000, UCB Institute of Governmental Studies, UCExtension, New York Times and the Berkeley Alumni Association, *'The annual review of the presidency'*, panellists: Laura Capps (former speechwriter for President Clinton), Thomas Mann (The Brookings Institution), Nelson Polsby (UCB Department of Political Science), Richard Berke (New York Times), et al.
- May 4, 2000, UCB, California Association of Scholars (an affiliate of the National Association of Scholars), lecture by Alan Charles Kors (University of Pennsylvania Professor of History, coauthor *'The Shadow University: the Betrayal of Liberty at American Campuses'* and President, Fire: Foundation for Individual Rights in Education Inc)
- May 4, 2000, The 6th Annual Aaron Wildavsky Forum for Public Policy, UCB Richard and Rhoda Goldman School of Public Policy: *'Competing models of the human agent: implications for policy making'*; speaker: Daniel Kahneman (Eugene Higgins Professor of Psychology, Princeton University)
- May 5, 2000, UCB IGS Lecture: *'Modern Britain: an examination of devolution and the revitalization of Britain's external relationships – Europe, US and the Commonwealth'*; speaker: Robert Peirce (Counsellor, British Embassy, Washington DC)
- May 8, 2000, Symposium *'After Seattle: politics, trade and culture in the new North America'*, UCB Boalt School of Law, Canadian Studies Program; speakers: Michael Hawes (Professor, Queen's University), Vinod Aggarwal (UCB), John Wirth (Stanford University) et al.
- May 9, 2000, UCB School of Social Welfare lecture *'Wealth, Poverty and Alan Greenspan: Social policy and macro economic policy'*; speaker: Robert Reich (Maurice B Hexter Professor of Social and Economic Policy, Brandeis University, and former US Secretary of Labor)

Mixed Mode Stress Intensity Factor Determination Using Trefftz Complex Functions

J. Sabino Domingues[1], A. Portela[2] and P. M. S. T. de Castro[3]

[1] Instituto Superior de Engenharia, Instituto Politécnico do Porto
Rua Dr. António Bernardino de Almeida, 4200-072 Porto, Portugal
[2] Faculdade de Ciências e Tecnologia, Universidade Nova de Lisboa
Monte de Caparica, 2825-114 Caparica, Portugal
[3] Faculdade de Engenharia, Universidade do Porto
Rua Dr. Roberto Frias, 4200-465 Porto, Portugal

***ABSTRACT**: This communication presents a method to determine the mode one and two stress intensity factors (K_I and K_{II}) in single and mixed mode situations based upon the use of Trefftz functions. These Trefftz functions inherently satisfy the Elasticity conditions in the domain, and, simultaneously, satisfy the free edge conditions of the crack. The series of functions that determine the stress-field are obtained from Kolosov-Muskhelishvili complex potentials using the complex variable notation. The coefficients of each term of the series are obtained using Galerkin method for minimisation of residues on the boundary of each problem. Some results obtained using the method developed are presented: a plate with a slant edge crack and a plate with two non-collinear parallel cracks. The accuracy of the results is discussed and compared with data available in the literature. An advantage of the method developed consists on the fact that stress intensity factor values are primary variables of the problem, directly determined.*

INTRODUCTION

Some different numerical methods have been developed in the past recent, issuing for an accurate determination of stress intensity factor (sifs) at the crack tips for complex geometry and stress-field.

When using Finite Element Method, a very refined domain mesh must be used at the neighborhood of the crack tip to achieve suitable sif values. Therefore, for crack growth analysis, where remeshing is needed, this method denotes high consuming of computer resources, see Shephard *et al.* [1]. The Dual Boundary Element Method, implemented by Portela [2] for crack problems, drastically reduces the remeshing effort, since only the boundaries must be discretized into elements. However, special care must be

taken with integrations along the crack line near the tip, as the method uses functions that are singular and hipersingular at that point. Moreover, in this technique sifs are evaluated by post-processing methods, as for example is the case of J-integral technique.

A boundary element method based upon the use of Trefftz functions is presented in this communication. Like any other boundary method, this method has the advantage of an easy discretization, enhanced by the fact that sifs are determined directly as primary unknowns. In addition, numerical integrations are always regular which leads to no boundary layer effect present in the other boundary methods.

The idea of using trial functions automatically satisfying the governing equations in the domain of a body was first presented by Trefftz [3] in 1926, who introduced them for the analysis of shear stress distribution in a section of a bar in torsion. From the 80's on, many researchers [4-6] have followed the idea of Trefftz for the analysis of different phenomena, basically within the framework of the finite element method.

Functions of a complex variable were first introduced in plane Elasticity by Kolosov [8] and were extensively used in the classical book of Muskhelishvili [8]. After the Introduction, this communication presents the Elasticity equations through complex variable representation. Next section presents the series expansions for the complex potentials from which the displacement and stress fields are obtained. Then, the Galerkin weighted residual formulation is applied to approximate boundary conditions. Finally, the efficiency and accuracy of the method is shown by presenting some numerical results.

ELASTICITY EQUATIONS IN COMPLEX VARIABLE

We consider an homogeneous and isotropic plane body occupying a domain Ω bounded by Γ in the complex plane represented by the complex variable $z = x + iy$. We also consider that Ω can be a multiply connected domain such that all points interior to internal closed contours Γ_k (k=1, 2, ..., m) do not belong to the body.

For this case, it can be shown [9,10] that Navier's equations can be expressed by

$$\frac{\partial}{\partial \bar{z}}\left(\lambda \frac{\partial U}{\partial z}+\overline{\frac{\partial U}{\partial z}}\right)=0 \tag{1}$$

where $U=u+iv$ is the complex displacement and λ is a parameter that depends on the type of plane problem and Poisson's ratio, ν, as follows:

$$\lambda=\begin{cases}3-4\nu & \text{(plane strain)}\\ (3-\nu)/(1+\nu) & \text{(plane stress)}\end{cases} \tag{2}$$

The general solution of differential Eq. 1 is

$$2G\,U=\lambda\,\psi(z)-z\overline{\psi'(z)}-\overline{\omega(z)} \tag{3}$$

where G is the shear modulus and $\psi(z)$ and $\omega(z)$ are multiple-valued functions - called complex potentials - with a general representation of the form

$$\begin{aligned}\psi(z)&=\psi^{*}(z)+\sum_{k=1}^{m}\gamma_k\log(z-z_k)\\ \omega(z)&=\omega^{*}(z)-\sum_{k=1}^{m}\lambda\bar{\gamma}_k\log(z-z_k)\end{aligned} \tag{4}$$

where $\psi^{*}(z)$ and $\omega^{*}(z)$ are analytic functions, z_k is an arbitrary point interior to the closed contour Γ_k and γ_k are complex constants.

Stresses can now be obtained by the following expressions:

$$\begin{aligned}\sigma_x+\sigma_y&=\psi'(z)+\overline{\psi'(z)}\\ \sigma_y-\sigma_x+2i\tau_{xy}&=\bar{z}\psi''(z)+\omega'(z)\end{aligned} \tag{5}$$

COMPLEX POTENTIALS EXPANSIONS

In general, the analytical functions $\psi^{*}(z)$ and $\omega^{*}(z)$ in Eq.s 4 can be represented by uniformly convergent power series of the form

$$\psi^*(z) = \sum_k a_k (z - z_0)^k ; \omega^*(z) = \sum_k b_k (z - z_0)^k \qquad (6)$$

where z_k is a fixed point and a_k and b_k are complex constants. In Eq.s 6 subscript k can range from 0 to $+\infty$ for interior regions, from $-\infty$ to 1 for exterior regions and from $-\infty$ to $+\infty$ for ring regions.

Expansions that automatically satisfy some specific boundary conditions can be derived from Eq.s 6. One of them, which is of a special interest for Fracture Mechanics, is the crack tip Williams problem. Considering a reference system centered at the crack tip and aligned with the crack edges as shown in Figure 1, the special expansions for the complex potentials of this case are obtained when the traction free condition is imposed along the rays $\theta = \pm\pi$. These crack expansions, see Piltner [11], are given by

$$\psi(z) = \sum_{k=0}^{\infty} a_k z^{k/2} ; \quad \omega(z) = -\sum_{k=0}^{\infty} \left[\frac{k}{2} a_k + \bar{a}_k (-1)^k \right] z^{k/2} \qquad (7)$$

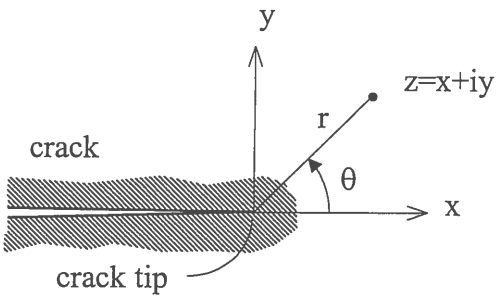

Figure 1: The crack tip Williams problem.

We must observe that when k=1 the complex coefficient a_1 in Eq.s 7 gives us the stress intensity factors for the opening mode (K_I) and for the sliding mode (K_{II}). The two stress intensity factors can be defined in the complex form by

$$K_I + i K_{II} = \sqrt{2\pi} \lim_{\substack{z \to 0 \\ \theta = 0}} \left(\sigma_y + i \tau_{xy} \right) z^{1/2} \qquad (8)$$

from where we can find, considering Eq.s 5, the important relation

$$K_I + i K_{II} = \sqrt{2\pi}\ \bar{a}_1 \tag{9}$$

BOUNDARY CONDITIONS AND WEIGHTED RESIDUALS FORMULATION

The weak formulation of the weighted residuals method corresponding to the Elasticity problem can be expressed by

$$\int_{\Gamma_u} \omega_i^u (\mathbf{u} - \mathbf{u}^*)\, d\Gamma + \int_{\Gamma_t} \omega_i^t (\mathbf{t} - \mathbf{t}^*)\, d\Gamma = 0 \tag{10}$$

where $\mathbf{u} = \sum c_i \mathbf{u}_i$ and $\mathbf{t} = \sum c_i \mathbf{t}_i$ are the displacement and traction vectors, $\mathbf{u}^*$ and $\mathbf{t}^*$ the corresponding boundary values, and ω_i^u and ω_i^t are arbitrary weighting vector functions. According to the Galerkin formulation, by conveniently selecting $\omega_i^u = \mathbf{t}_i$ and $\omega_i^t = -\mathbf{u}_i$ we can obtain the system of equations

$$\mathbf{K}\,\mathbf{c} = \mathbf{f} \tag{11}$$

where

$$K_{ij} = \int_{\Gamma_u} \mathbf{t}_i \mathbf{u}_j\, d\Gamma - \int_{\Gamma_t} \mathbf{u}_i \mathbf{t}_j\, d\Gamma \tag{12}$$

$$f_i = \int_{\Gamma_u} \mathbf{t}_i \mathbf{u}^*\, d\Gamma - \int_{\Gamma_t} \mathbf{u}_i \mathbf{t}^*\, d\Gamma \tag{13}$$

The system of Eq.s 11 allows, in general, the determination of all the unknown coefficients of vector **c**. It can be shown, by using Betti's work reciprocal theorem, that square matrix K is a symmetric one.

Eq.s 11-13 were derived considering that a specific expansion for only one simple region is used to describe the displacement and stress fields in the whole body. For complex geometry, the Continuation Theorem from complex analysis can be applied to consider the elastic body divided into several regions, each one with its own expansion, see Domingues *et al.* [10].

EXAMPLE 1: PLATE WITH A SLANT EDGE CRACK

A rectangular plate with a slant edge crack in uniaxial tension was analyzed by using crack expansions, Eq.s 7. Figure 2 shows the geometry under consideration. Figures 3 and 4 shows stress intensity factor for modes I and II calculated for different relative crack lengths and different crack slopes. In those figures, the results obtained with 100 expansion terms are compared with those published by Murakami [12] and those obtained with the Dual Boundary Element Method by Portela [2].

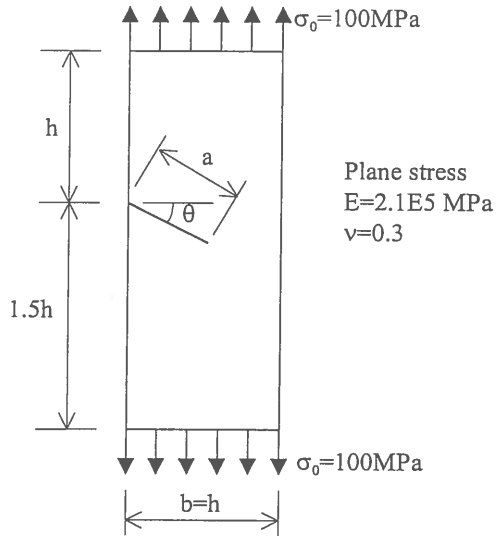

Figure 2: Plate in uniaxial tension with a slant edge crack.

EXAMPLE 2: PLATE WITH TWO OFFSET PARALLEL CRACKS

This is a problem of the multiple site damage type. The configuration of the two offset parallel cracks in the infinite plate under consideration is shown in Figure 5(a). Figure 5(b) shows the domain division into five regions considered in the analysis. Eq.s 7 specific for crack expansions were used for the first four regions, while Eq.s 6 for exterior regions were used for region #5. Table 1 shows the stress intensity factors for tips A and B, calculated with 5x98 expansion terms, and the corresponding values obtained by Rooke and Cartwright [13].

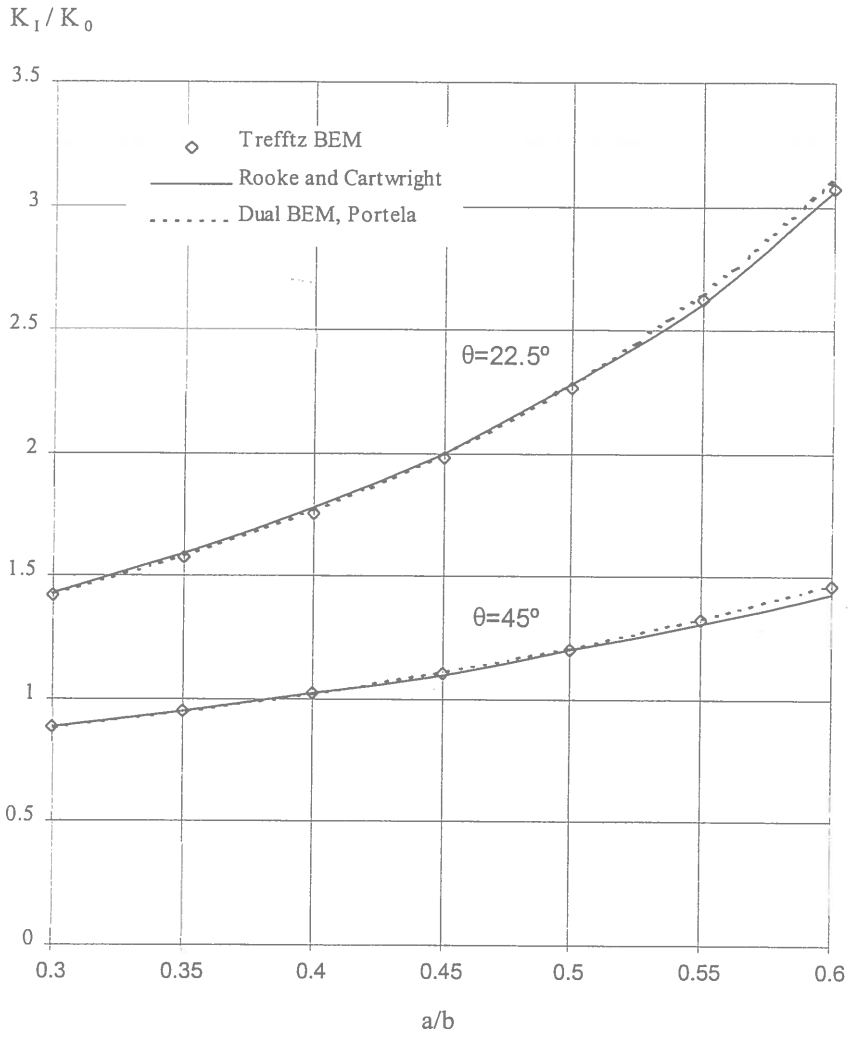

Figure 3: K_I for a slant edge crack in uniaxial tension. $K_0 = \sigma_0 \sqrt{\pi a}$

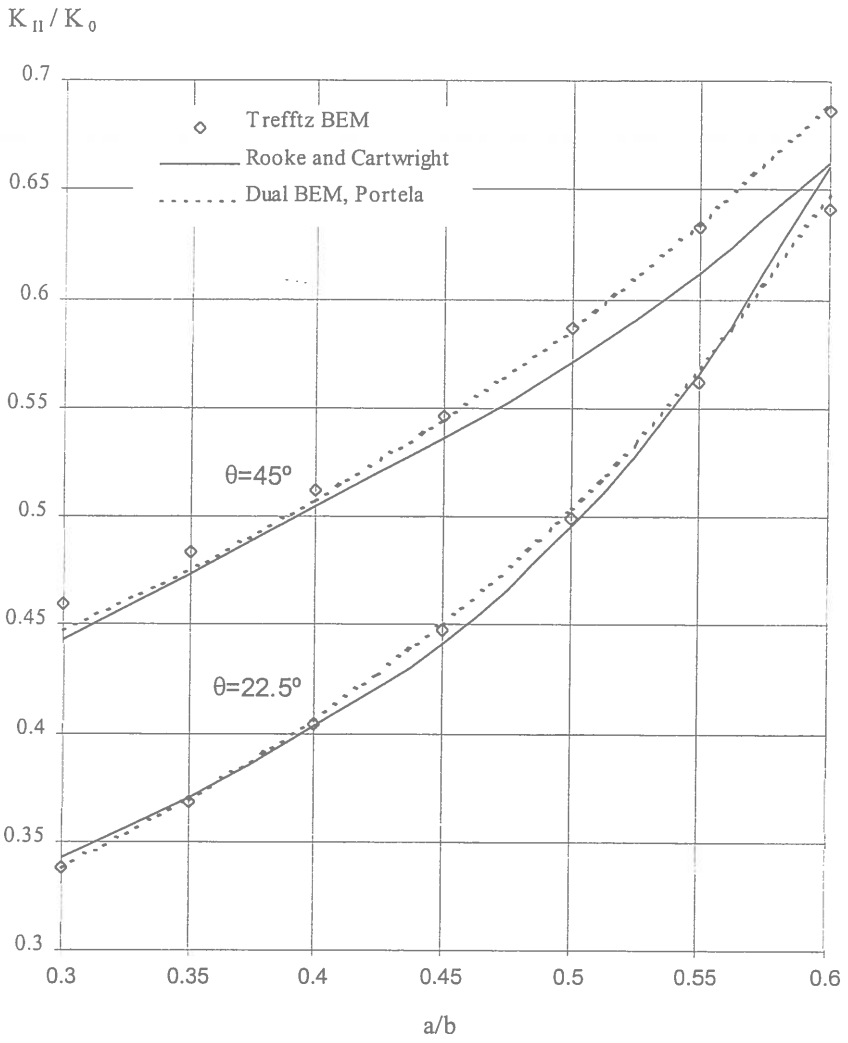

Figure 4: K_{II} for a slant edge crack in uniaxial tension. $K_0 = \sigma_0 \sqrt{\pi a}$

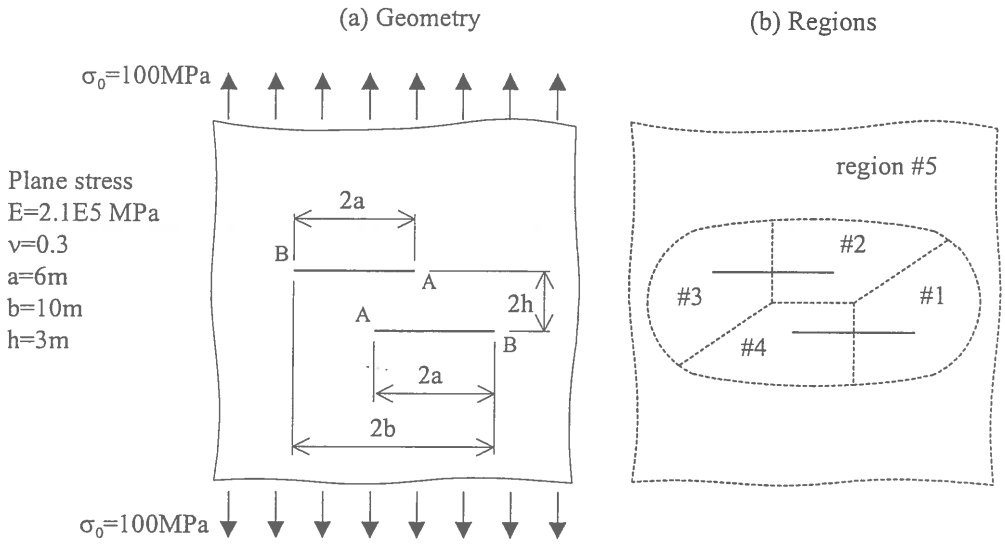

Figure 5: Two offset parallel cracks in an infinite plate.

TABLE 1: STRESS INTENSITY FACTORS (MPa $m^{1/2}$) FOR TWO OFFSET PARALLEL CRACKS

	Tip A		Tip B	
	K_I	K_{II}	K_I	K_{II}
Trefftz complex functions	107.7	33.3	156.3	6.96
Rooke and Cartwright [13]	107.1	35.7	155.1	7.69
Difference	0.6%	-6.7%	0.8%	-9.5%

CONCLUSIONS

Results obtained with Trefftz complex functions compare favourably with those available in the literature, as well as with those obtained with a Dual Boundary Element software.

The accuracy of the results presented here lead to the conclusion that the method is a simple and efficient tool to solve linear elasticity plane problems and it is specially useful for Linear Elastic Fracture Mechanics

where the stress intensity factors are determined directly as primary unknowns.

REFERENCES

1. Shephard, M. S., Yehia, N. A. B., Burd, G. S. and Weidner, T. J. (1985) *Automatic Crack Propagation Tracking*, Comput. Struct. **20**, 211-223.
2. Portela, A., Aliabadi, M. H. and Rooke, D. P. (1992) *The Dual Boundary Element Method: Effective Implementation for Crack Problems*, Int. J. for Num. Methods in Engineering **33**, 1269-1287.
3. Trefftz, E. (1926) *Ein Gegenstück zum Ritzschen Verfahren*, Proc. 2nd Int. Congress on Applied Mechanics, Zürich, 131-137.
4. Jirousek, J. (1987) *Hybrid-Trefftz plate bending elements with p-method capabilities*, Int. J. for Num. Methods in Engineering, **24**, 1367-1393.
5. Piltner, R. (1992) *A quadrilateral hybrid Trefftz plate bending element for the inclusion of warping based on a three-dimensional plate formulation*, Int. J. for Num. Methods in Engineering **33**, 387-408.
6. Herrena, I. (1984) *Trefftz method*, in C. A. Brebbia (ed.), Topics in Boundary Element Method, Chap. 10, Springer.
7. Kolosov, G. V. (1909) *On an application of complex function theory to a plane problem of the mathematical theory of Elasticity*, Yuriev.
8. Muskhelishvili, N. I. (1953) *Some basic problems of the mathematical theory of Elasticity*, Noordhoof, Groningen.
9. England, A. H. (1971) *Complex variable methods in Elasticity*, Wiley-Interscience.
10. Domingues, J. S., Portela, A. and de Castro, P. T. (1999) *Trefftz boundary element method applied to fracture mechanics*, Eng. Fracture Mechanics **64**, 67-86.
11. Piltner, R. (1995) *Recent developments in the Trefftz method for finite element and boundary element applications*, Advances in Engineering Software **24**, 107-115.
12. Murakami, Y. et al. (1987) *Stress intensity factor handbook*. Oxford: Pergamon Press.
13. Rooke, D. P. and Cartwright D. J. (1976) *Compendium of stress intensity factors*, 1st Ed., HMSO, The Hillingdon Press, Uxbridge.